DOE Award #: DE-EE0007798

Final Scientific/Technical Report

Ian P. Brown (Illinois Institute of Technology)

Wound Field and Hybrid Synchronous Machines for EV Traction with Brushless Capacitive Rotor Field Excitation

Ian P. Brown
Illinois Institute of Technology
Electrical and Computer Engineering Dept.
3301 S Dearborn St. #103
Chicago, IL 60616
Email: ibrown1@iit.edu
Phone: 312-567-5981

Team Organizations:

University of Wisconsin – Madison
Lucid Motors (Atieva, Inc.)

1.1 Executive Summary

This project focused on the development of wound field synchronous machines (WFSMs) and hybrid excitation synchronous machines (HESMs) with brushless capacitive power transfer for the field excitation. The target application for the machines developed is the main traction motor in electric vehicles. The magnetization in these types of machines is provided by a field winding on the rotor which is excited with DC current. The magnetization level in the machine can be varied by changing the magnitude of the field current. The variable magnetization or field is one of the key features of WFSMs.

WFSMs are commonly used as generators however they have several attractive features for automotive traction applications.
1) No use of permanent magnet: Rare earth permanent magnets are primarily mined and processed in China. They have been subject to large price and supply variations and their export may be restricted during times of geopolitical tension.

2) Easy field weakening: Wound field synchronous machines have complete control of their field excitation. With proper design, this type of machine can electromagnetically have an infinite constant power speed range.

3) High power factor: With proper choice of the field excitation, WFSMs may be operated with high or even unity power factor. This potentially allows for the inverter connected to the stator winding to be downsized. In comparison induction machines and interior permanent magnet synchronous machines must supply reactive power to the stator increasing the kVA rating and cost of the inverter.

4) Reduced iron losses at high speed: By reducing the field excitation, the iron loss in the stator can be reduced. This is in comparison to interior permanent magnet synchronous machines which must use stator current to buck or reduce the flux produced by the permanent magnets. Generally, WFSMs have their highest efficiency at high speed.

5) Torque output at high temperatures: The magnetization provided by the field winding only depends on the field current and not on the field winding temperature. This is in contrast to permanent magnet machines where the permanent magnet flux decreases as the magnet temperature increases.

Historically a number of approaches have been developed to provide DC current to the rotating field winding in WFSM's including brushes and slip rings, low frequency brushless exciters, and high frequency rotary transformers and rectifiers. In this project, a different approach was used: brushless capacitive power transfer. Brushless capacitive power transfer uses two sets of rotating capacitors or electrodes in which an AC electric field is established by a high frequency inverter. A displacement current can flow through the airgap in the rotating capacitors which is rectified on the rotor using a diode bridge. The basic concept is illustrated in Fig. 1.1-1 and the application for field excitation in a WFSM in Fig. 1.1-2.

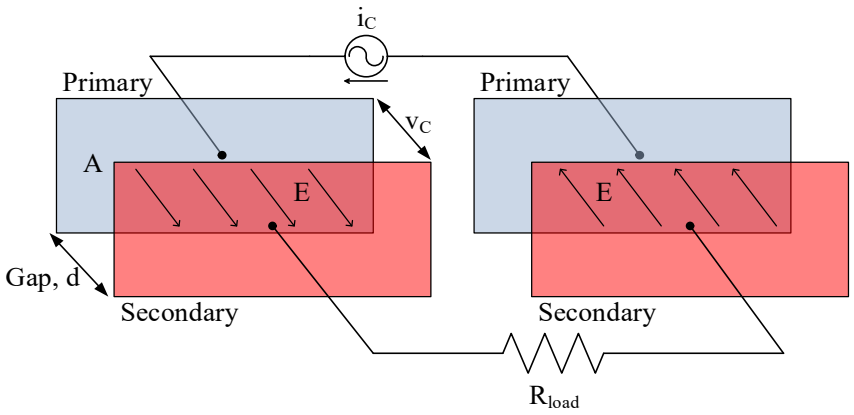

Fig. 1.1-1. Basic capacitive power transfer concept.

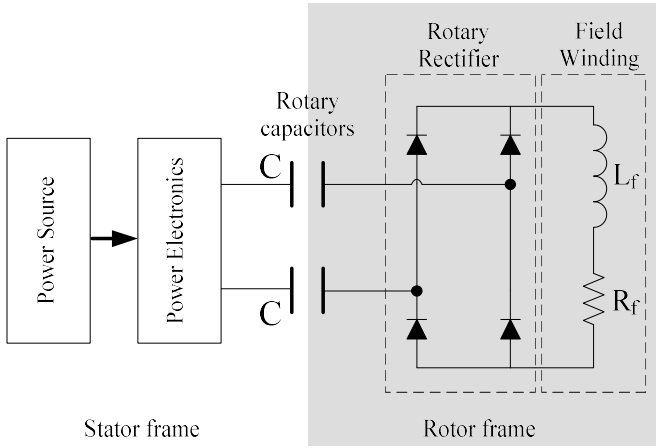

Fig. 1.1-2. Concept of capacitive power transfer for wound field synchronous machines.

The potential advantage of capacitive power transfer is that there is no need for heavy iron to guide magnetic flux. The electric flux lines terminate on the charges on the rotary capacitor surfaces. This should also limit the electric field outside the rotary capacitor airgaps. The main challenge with capacitive power transfer is that the capacitance and surface area of the rotating capacitors is small. Because capacitive power transfer systems are essentially a dual of a magnetic system, an Ampere per Hertz relationship is characteristic versus a Volts per Hertz relationship. A very high frequency power inverter must be used to provide sufficient excitation to the field winding.

The concept of using capacitive power transfer to excite a high performance WFSM was initially developed in a previous U.S.A. Dept. of Energy project, DE-EE0006829. This project focused on increasing the power density of the WFSMs and reducing the cost and manufacturing complexity of the capacitive power transfer system. Specific items that were developed as part of this project include the following.

1) An improved WFSM rotor based on the previous project's WFSM. This WFSM had a random wound rotor. This is termed the generation I WFSM.

2) A WFSM rotor with a rectangular die compressed field winding to increase the field copper slot fill. This is termed the generation II WFSM.

3) A third generation WFSM with distributed winding hairpin stator and high slot fill rotor. Three high slot fill field winding technologies were explored: bobbin wound square magnet wire, twisted square magnet wire, and a non-rectangular die compressed winding. Rotors with bobbin wound and twisted square magnet wire were produced. A 12 slot 10 pole WFSM with die compressed stator and rotor windings was also designed.

4) Journal bearing capacitive power transfer system.

5) Integrated magnetic and capacitive power transfer system based on printed circuit boards.

6) Large gap printed circuit board capacitive power transfer system in single phase and three phase variants.

7) Kilowatt level, megahertz switching frequency, single and three phase high frequency Gallium Nitride inverters for excitation in the capacitive power transfer system.

8) Current measurement and phase lock loop control systems for the capacitive power transfer system. A rotating buck converter with a fixed duty cycle was used for impedance transformation to match the field winding to the high frequency inverter.

9) Two radial flux dual rotor hybrid excitation synchronous machine rotors with combined permanent magnet and wound field excitation to reduce the field power transfer requirements.

10) New control techniques for WFSMs including deadbeat direct torque and flux controllers.

11) A new approach to the design of WFSMs using multi-material, magneto-structural topology optimization.

The generation I and III WFSMs were dynamometer tested with the single-phase large gap capacitive power transfer system. The overall system was tested to the limit of the stator supply inverter. The measured performance of the generation III WFSM correlated well with the predicted performance.

This project has demonstrated that WFSMs with brushless capacitive field power transfer can provide a high-power density and low-cost automotive powertrain technology.

2.1 Generation I Wound Field Synchronous Machine

2.1.1 Introduction

Based on the design tools developed as part of a previous Dept. of Energy project, a revised wound field synchronous machine rotor was developed. The finite element-based design tools were revised based on the prototype construction and dynamometer testing from the previous project. These tools were used to design a rotor with a longer stack length; 106 mm versus 92 mm used in previous prototypes. The rotor is shown in Fig. 2.1.1-1. This rotor was used with two stators, one of 106 mm stack length and the other of 92 mm stack length. The rotor was dynamometer tested at the University Wisconsin-Madison with the 92 mm stack length stator. A peak torque output of 196 Nm at 4,000 RPM corresponding to a power output of 83 kW was measured. Simulations with the 106 mm stator stack length indicate a 270 Nm torque output at 4,000 RPM corresponding to a power output of 112 kW.

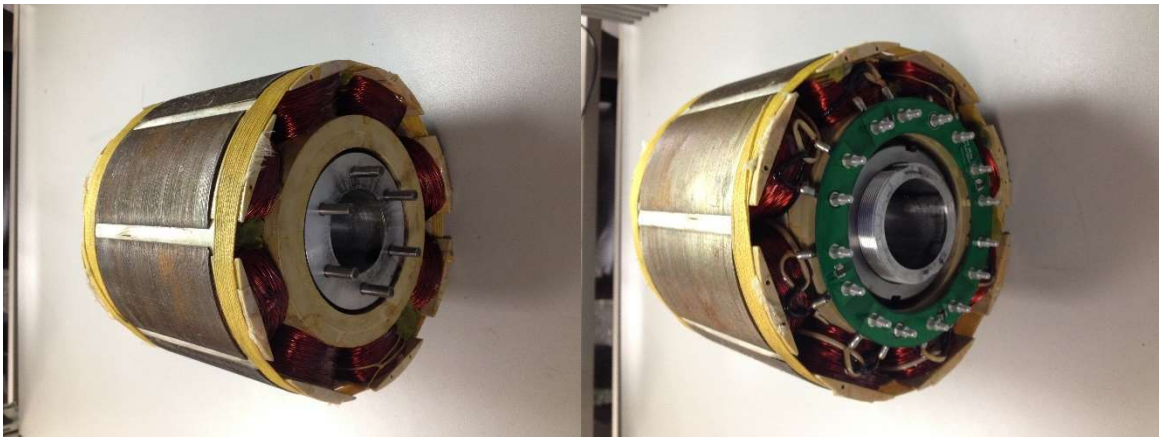

Fig. 2.1.1-1. Generation I WFSM Rotor

2.1.2 Topology Optimization Design Tools for WFSMs

In addition to the geometric template based finite element-based design tools used for the design of the generation I prototypes, a new approach to the design of WFSMs was developed based on topology optimization. Topology optimization allows for the free form optimal distribution of material in a design domain. A topology optimization approach was developed which distributes iron, copper, or air in the rotor. The topology optimization considers both magnetic and structural mechanical phenomena. The concept of virtual regions was developed to emulate the mechanical boundary conditions between the copper containing regions and the iron. The developed technique is explained in detail in the following paper.

F. Guo, M. Salameh, M. Krishnamurthy, I.P. Brown, “Multimaterial Magneto-Structural Topology Optimization of Wound Field Synchronous Machine Rotors”, IEEE Transactions on Industry Applications, Vol. 56, No. 4, 2020, DOI: 10.1109/TIA.2020.2989682.

An example multi-material, magneto-structural WFSM rotor topology optimization is shown in Fig. 2.1.2-1. The topology optimization approach discovers small features such as the flux barriers near the pole surface which might not be intuitively obvious to electric machine designers.

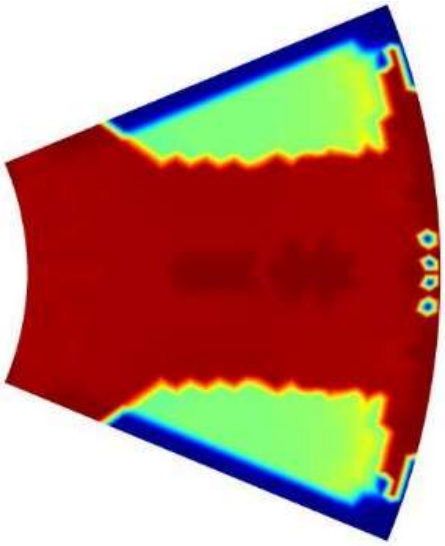

Fig. 2.1.2-1. Representative multi-material, magneto-structural WFSM rotor topology optimization. Iron is represented by the color red, copper by the light green color, and air by blue.

2.2 Generation II WFSM

2.2.1 Introduction

Ideally the field ampere turns in a WFSM needs to match or preferably exceed the stator ampere turns. In an inner rotor radial flux machine, the area available for the field winding is however smaller than the stator winding area because the field winding is located in a region with smaller diameters. Therefore, to match or exceed the ampere turns of the stator winding, the current density in the field winding must be higher, leading to loss and cooling concerns or its slot fill must be increased. To increase the field winding slot fill, a die compressed field winding was created. A rectangular shape for the field coil was used as it is the simplest form to create a die compressed winding. As a die compressed winding is an integral unit, a joint must be introduced in the rotor lamination to allow its insertion.

Additional details regarding the design, optimization, and prototyping of the generation II WFSM are contained in the following paper.

M. Salameh, T. Spillman, M Krishnamurthy, I.P. Brown, D.C. Ludois, "Wound Field Synchronous Machine with Segmented Rotor Laminations and Die Compressed Field Winding," 2019 IEEE Energy Conversion Congress and Exposition (ECCE), Baltimore, MD, Sept. 29th – Oct 3rd, 2019.

2.2.2 Design of WFSM Rotor with Die Compressed Field Winding

The same stator as used for the proof of concept hybrid excitation synchronous machine was assumed for the design process with its 106 mm stack length, Table 2.2.2-1. Several large-scale optimization studies were carried out using the in-house WFSM design software. The optimization objectives and constraints are listed in Table 2.2.2-2. The optimization study which provided the final selected design for prototyping is shown in Fig. 2.2.2-1. The rotor has been designed assuming a die compressed coil with a high slot fill factor, 0.8. An additional Pareto front with an assumed 0.45 field slot fill is also shown. The rotor design will also work with a bobbin wound coil of lower fill factor though this will reduce the torque output.

The selected design is on the Pareto front of designs with the best tradeoff between electromagnetic torque production and losses. This particular design is predicted to give the maximum torque production. Given the levels of saturation in the machine it is likely that the output torque will be substantially lower. The selected design cross-section is shown in Fig. 2.2.2-2. The predicted performance of this design is listed in Table 2.2.2-3 column (a).

TABLE 2.2.2-1. WFSM BASIC MACHINE PARAMETERS

Parameter	Value
Stator Slots	48
Number of poles	8
Stator Outer Diameter	254 mm
Stator Inner Diameter	178 mm
Axial Stack Length	106 mm
Base Speed	4000 RPM
Maximum Speed / CPSR	12 kRPM / 3:1
Cooling	ATF Spray

TABLE 2.2.2-2. OPTIMIZATION OBJECTIVES AND CONSTRAINTS

Objectives	**Goal**
Average torque	Maximize
Total Loss	Minimize
Constraints	**Value**
Torque ripple	< 5%
Average torque	> 180 Nm
Rotor loss	< 2,000 W
Stator loss	< 6,500 W
Rotor current density	5-20 A/mm^2

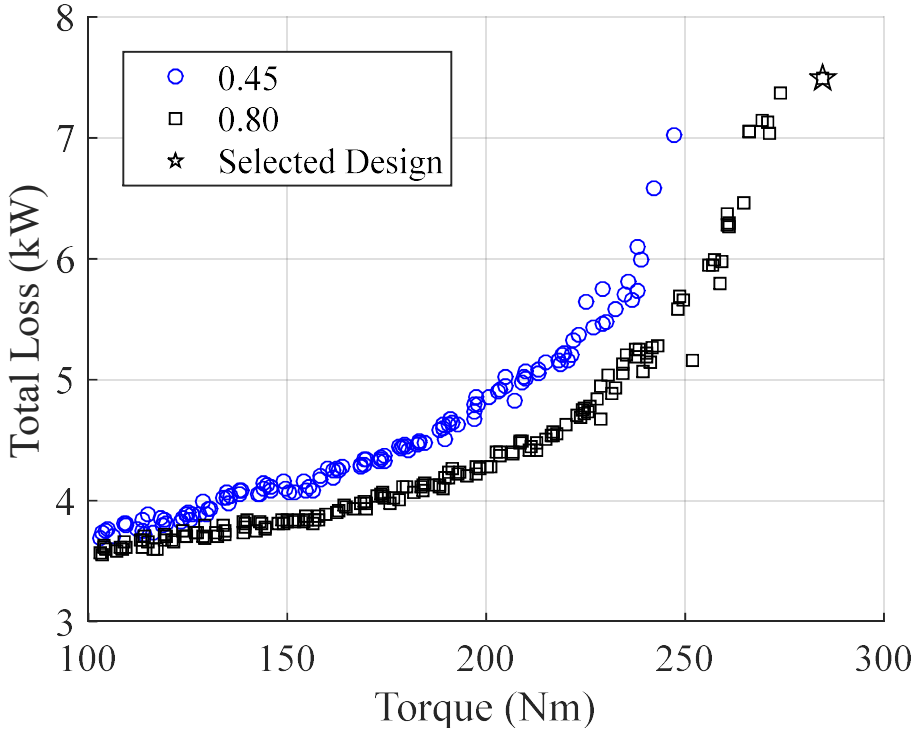

Fig. 2.2.2-1. Optimization of Pareto fronts of WFSM assuming a die compressed winding with a slot fill of 0.8 or a random winding with a slot fill of 0.45. The selected design for prototyping is indicated by the star.

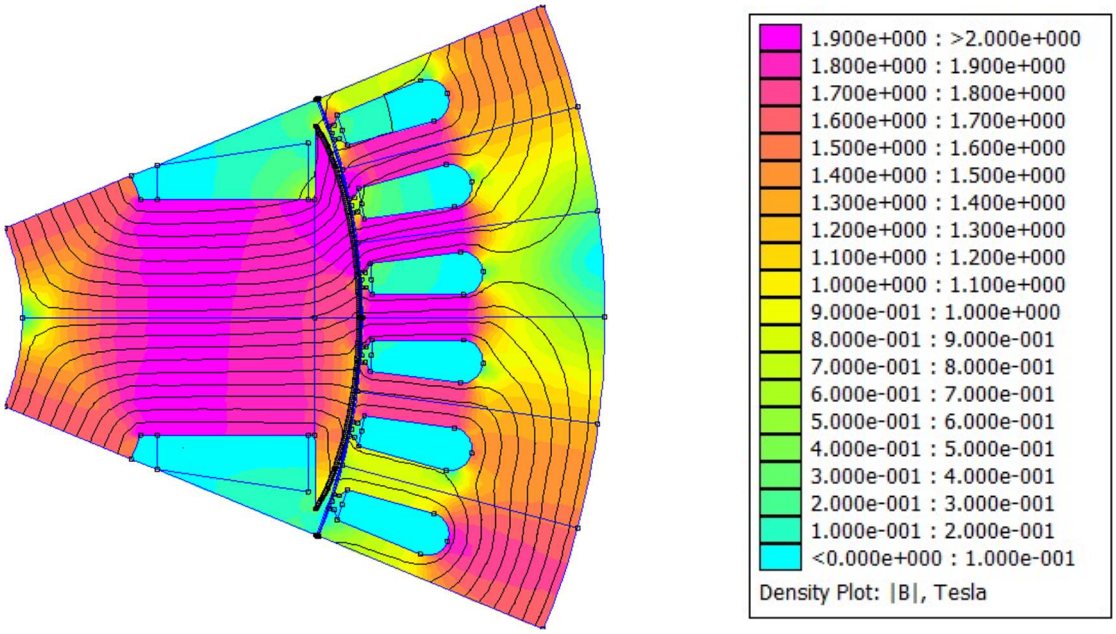

Fig. 2.2.2-2. Magnetic flux density cross-section of the selected Pareto front member for prototyping. The stator is the same as used for the proof of concept hybrid excitation synchronous machine. The rotor slot fill is assumed to be 0.8.

TABLE 2.2.2-3. PREDICTED PERFORMANCE OF WFSM ROTOR DESIGN REFINEMENTS

Design	**Fig. 2.2.2-2 (a)**	**Fig. 2.2.2-2 with modified slot fill (b)**	**Fig. 2.2.2-4 (c)**	**Fig. 2.2.2-5 (d)**
Rotor Slot Fill	0.8	0.7	0.7	0.7
Joint Gap Length (in/mm)	-	-	0.006/ 0.1524	0.006/ 0.1524
Average Torque (Nm)	284.8	278.0	271.1	253.8
Torque Ripple (%)	8.6	9.5	11.0	10.7
Rotor Copper Loss (W)	3969	3472	3472	2879
Stator Iron Loss (W)	743	703	674	626
Stator Copper Loss (W) [Common for all]			2781	
Total Losses (W)	7493	6956	6927	6286
Rotor Coil Area (mm^2)	167.3	167.3	167.3	138.7
Rotor Ampere-turns	2676	2342	2342	1942

Modifications were made to the WFSM optimization environment geometry template to account for the additional airgap introduced by dovetail or fir tree style joint in the rotor, Fig. 2.2.2-3. An example of the modeling of the impact of a dovetail in the pole cap is shown in Fig. 2.2.2-3. Because of the DC flux, the location of the dovetail, in either the pole cap or between the pole neck and yoke, does not have a large impact. The gap distance however has a significant effect on the performance of the WFSM.

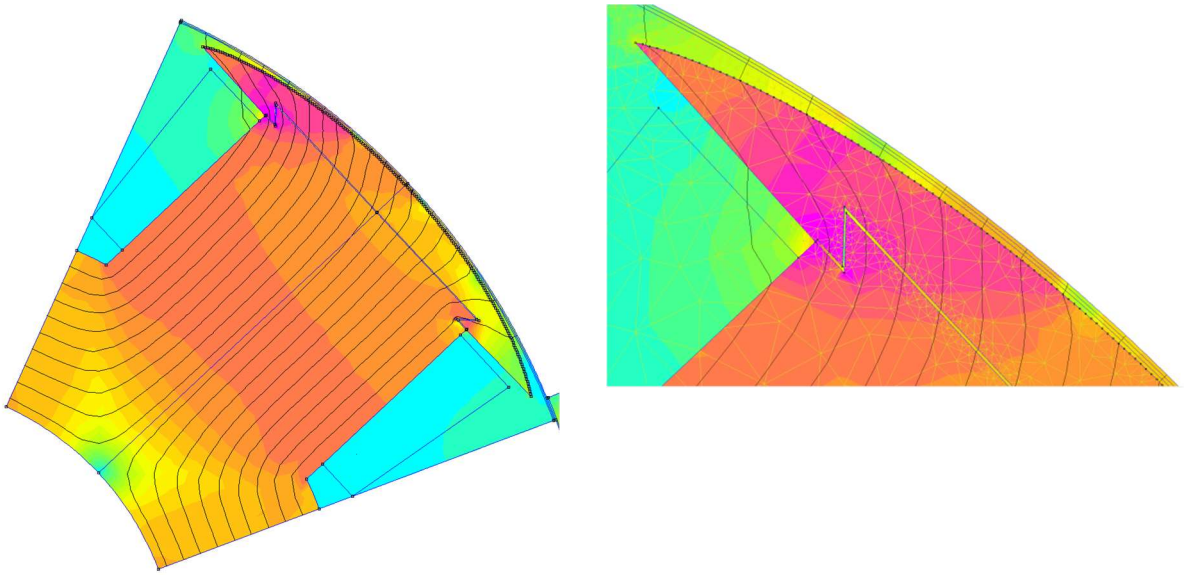

(a) (b)

Fig. 2.2.2-3. Example dovetail joint inserted into rotor geometry to study the impact of the additional airgap introduced by the magnetic joint, (a) full rotor geometry, (b) zoomed in view of dovetail airgap including the mesh.

To ease the assembly of this first prototype, a large nominal joint gap of 0.006” was specified to ensure clearance between the rotor pole and yoke pieces, assuming a laser cut lamination stackup tolerance of +/-0.003” for each stack. A 0.006” gap was introduced in the magnetic model, Fig. 2.2.2-4. The predicted performance reduction due to the introduction of the segmentation gap is listed in column (c) of Table 2.2.2-3.

To ease the construction of the die to compress the field coil, the coil shape was altered to a rectangle and the pole neck shortened to reduce the MMF drop over it, Fig. 2.2.2-5, Table 2.2.2-3, column (d). The reduction of the die compressed coil cross-section area due to the change in the coil shape, causes the largest percentage drop in the average torque. The design in Fig. 2.2.2-5 serves as a basis of the actual prototype except that the location of the joint has been moved.

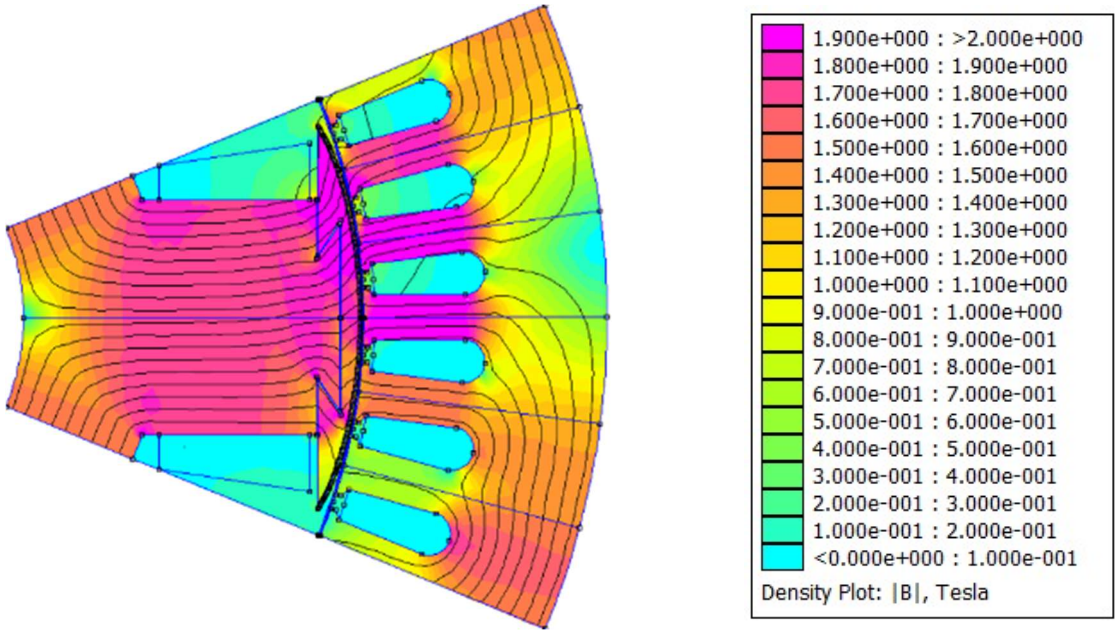

Fig. 2.2.2-4. Magnetic modeling of 0.006” segmentation gap in WFSM rotor. The gap is modeled in the pole cap but actually implemented between the pole neck and yoke.

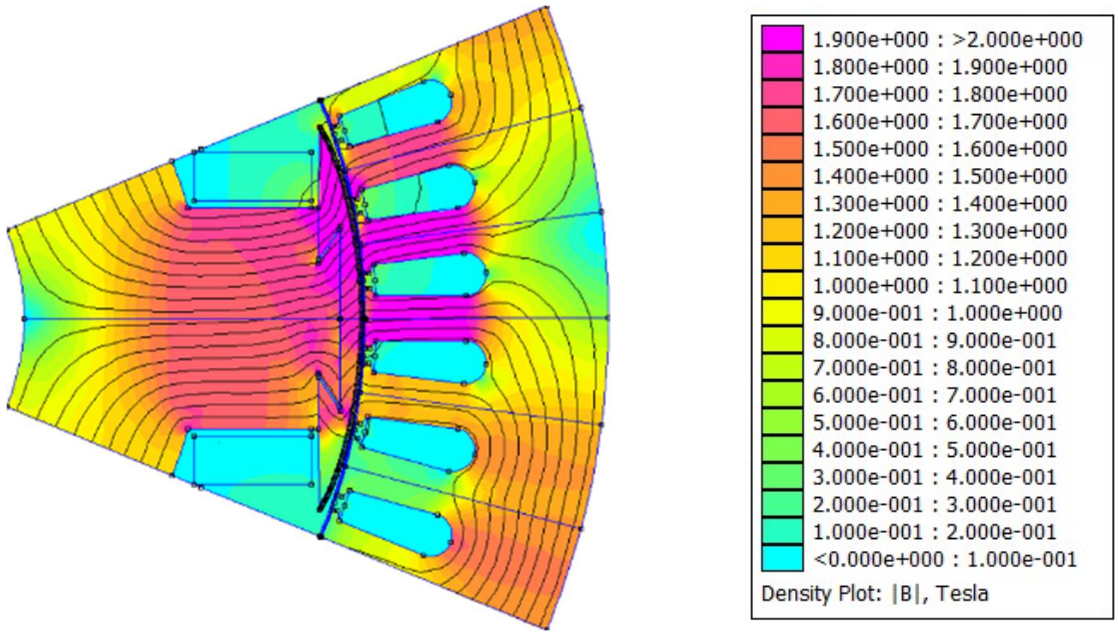

Fig. 2.2.2-5. Magnetic modeling of WFSM with rectangular field coil, shortened pole neck, and 0.006” segmentation gap. The gap is modeled in the pole cap but actually implemented between the pole neck and yoke.

Slight adjustments to the pole cap and winding were made in anticipation of constructing a die for the compression of the rotor field winding. Multiple lamination joint designs have been studied, including a dovetail joint in the pole cap, Fig. 2.2.2-6, and dovetail, fir tree, and T-slot style joints between the pole neck and the rotor yoke, Fig. 2.2.2-7. A range of dovetail joint styles and sizes were simulated in Abaqus, Fig. 2.2.2-7. The pole cap joint was found to be the least desirable structurally. A pole neck to yoke dovetail joint was found to have adequate structural strength and was the easiest to manufacture given the relatively loose tolerances of laser cut lamination stacks.

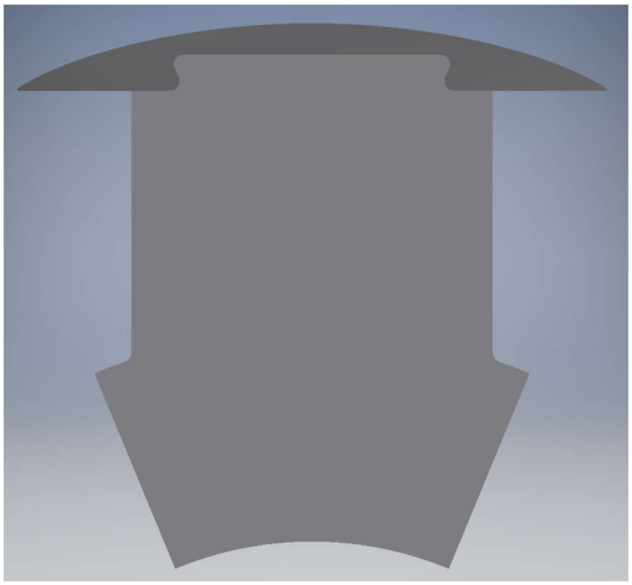

Fig. 2.2.2-6. Representative dovetail magnetic joint located in the pole cap.

The final lamination design is shown in Fig. 2.2.2-8 along with the entire rotor assembly. The rotor pole pieces are axially constrained by a lip on the drive end hub, Fig. 2.2.2-8(b), and on the non-drive end by a nut on a rotor hub, Fig. 2.2.2-8(c). The end turns of the die compressed field windings are protected from lamination stack corners by polyether-ether-ketone (PEEK) end caps epoxied to each end. The end caps also serve to support the end turns at high speeds. To retain the PEEK endcaps at high speeds a PEEK ring interlocks with all eight dovetails; green rings in Fig. 2.2.2-8 (b) and Fig. 2.2.2-8(c). The field poles are connected electrically using a PCB which integrates onto the non-drive end green PEEK ring.

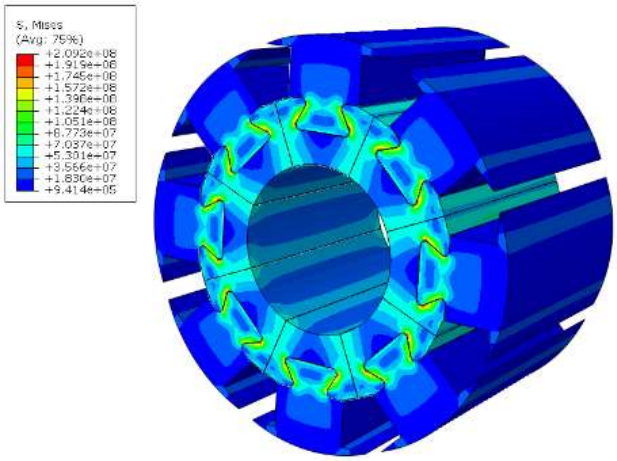

(a)

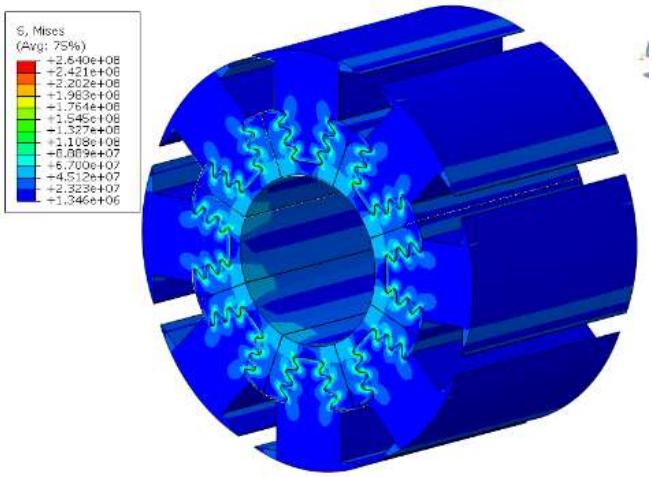

(b)

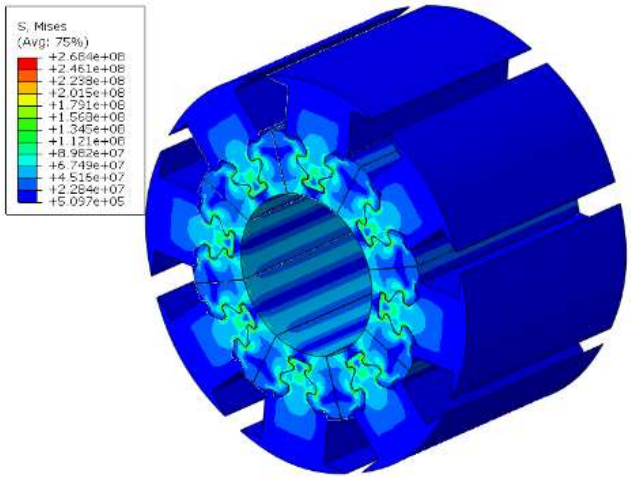

(c)

Fig. 2.2.2-7. Abaqus stress analyses at 12 kRPM of three rotor lamination joints: (a) dovetail, (b) fir-tree, and (c) T-slot.

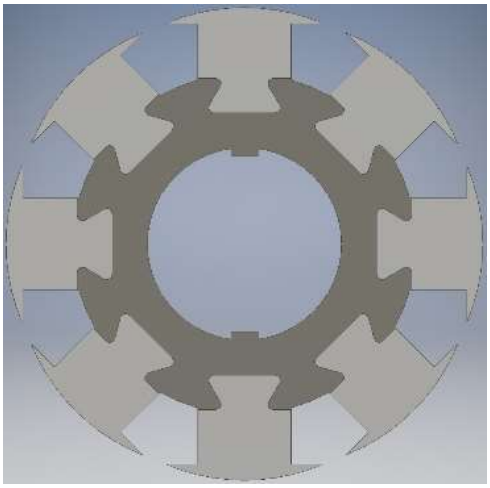

(a)

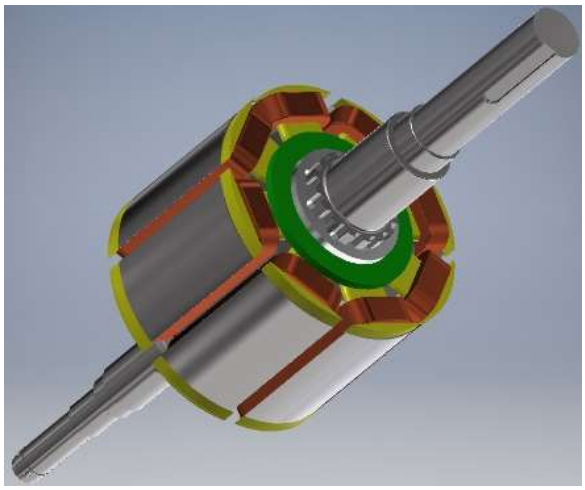

(b)

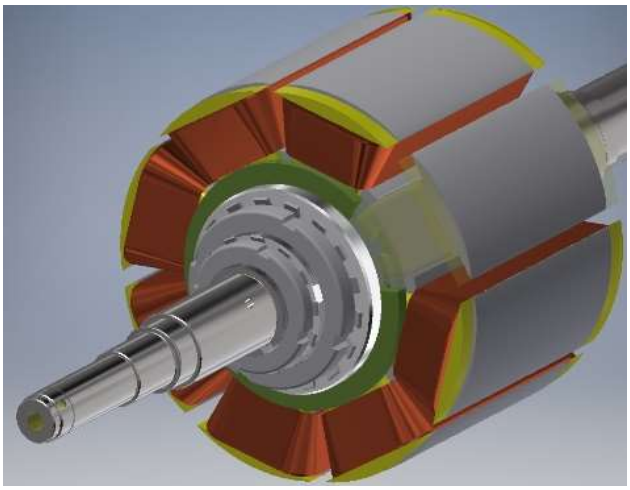

(c)

Fig. 2.2.2-8. Final segmented lamination design (a), and overall rotor assembly (b) and (c) showing the drive end (b) and non-drive end (c).

2.2.3 Construction of Generation II WFSM Rotor with Die Compressed Field Winding

The design of the die for the compression of the field winding was updated several times after visits to tool and die makers. The initial die design to produce the die compressed field coil is shown in Fig. 2.2.3-1. An aluminum bobbin to trial the field winding process before compression was also constructed, Fig. 2.2.3-2. After several revisions to the design the die set for producing die compressed field coils for this prototype is shown in Fig. 2.2.3-3. The die was manufactured by EDM wire cutting hardened A2 steel blocks.

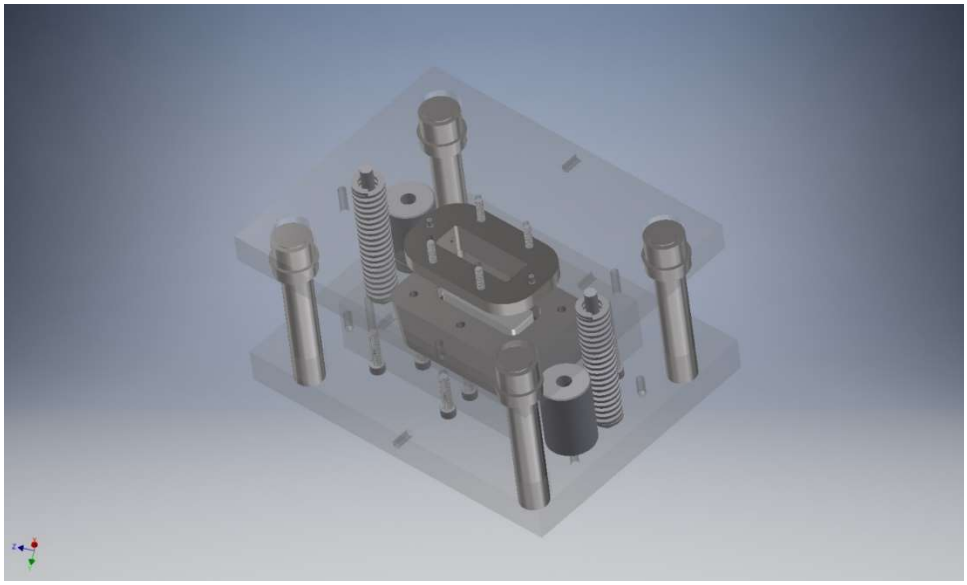

Fig. 2.2.3-1. Initial design of punch, die, yoke, bobbin, and Danly die set for field winding coil compression.

Fig. 2.2.3-2. Aluminum bobbin for trial winding of coil before compression.

Fig. 2.2.3-3. Die used to produce compressed field coils for generation II WFSM.

The field turns are wound on the bobbin in the orthocyclic manner with the bottom bobbin and punch providing support. Figure 2.2.3-4 shows the coil precompression wound on the bobbin. Two presses were utilized in the initial trial compressed coils; a 800,000 lb Riehle press and 400,000 lb Tinius Olsen press, Fig. 2.2.3-5.

Die compressed coils for the eight poles of a segmented rotor were constructed from 21 AWG magnet wire with ~250 turns. The coils were pressed in two stages. In the final stage, the press was held at the peak force of ~780,000 lbs for ~2 minutes. A representative die compressed coil is shown in Fig. 2.2.3-6.

As shown in Fig. 2.2.3-7, 0.012" Nomex 410 insulation paper was used to cover the coil sides. The length of the Nomex covering is 111 mm to extend slightly beyond the laminations but still leave the end turns exposed for oil-spray cooling. PEEK axial retainment pieces were bonded to the rotor pole laminations using Hysol 120 adhesive epoxy. Retainment hubs with negative dovetails were also machined from PEEK to capture the retainment pieces from each pole. A single rotor pole is shown in Fig. 2.2.3-7(a) and inserted into the rotor yoke Fig. 2.2.3-7(b). The entire rotor assembly is shown in Fig. 2.2.3-8.

Fig. 2.2.3-4. Coil wound on bobbin precompression.

(a)

(b)

Fig. 2.2.3-5. Presses used for initial trial die compressed coils. (a) 800,000 lb Riehle press, (b) 400,000 lb Tinius Olsen press.

Fig. 2.2.3-6. Representative die compressed coil for generation II WFSM

Fig. 2.2.3-7 Segmented rotor pole and pole mounted on rotor yoke.

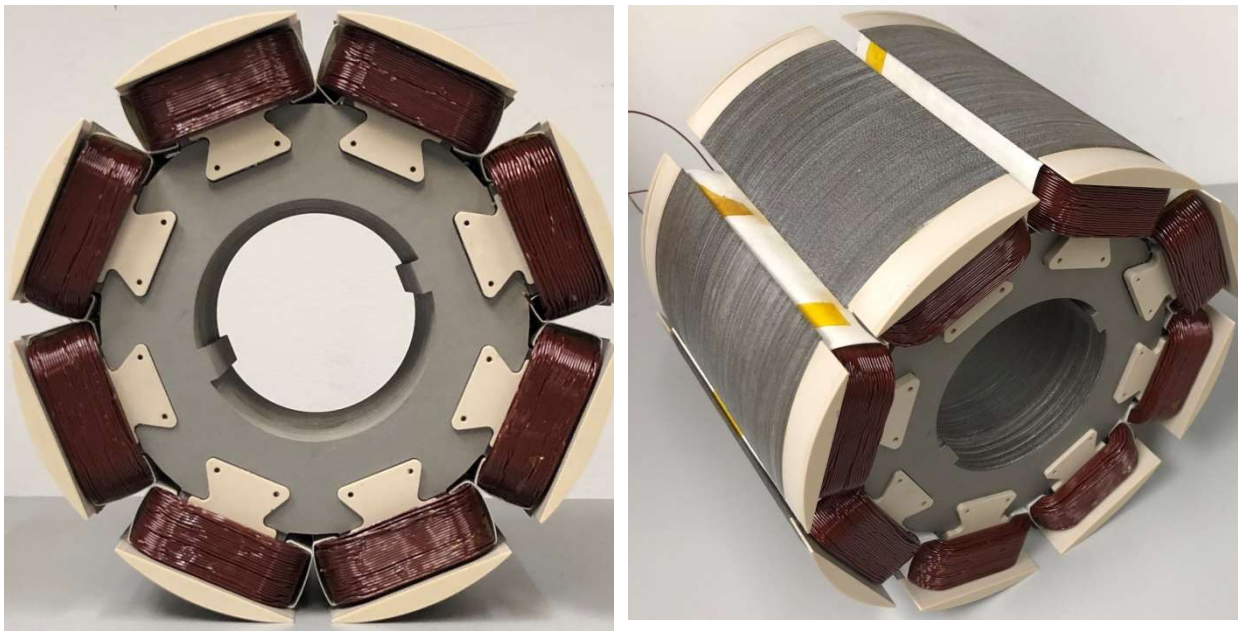

(a) (b)

Fig. 2.2.3-8. Assembled segmented WFSM with die compressed windings; (a) drive end view, (b) isometric view.

Spring Back Measurements:

In order to estimate the spring back effect once the coil is removed from the die, the dimensions of the pressed coil were measured, as shown in Fig. 2.2.3-9. This will help in evaluating the co-design of the lamination and insulation systems and the increased design tolerances around the coil to accommodate the spring back effects in the low scrap WFSM. The average measured spring back of the coil dimensions was less than 5%.

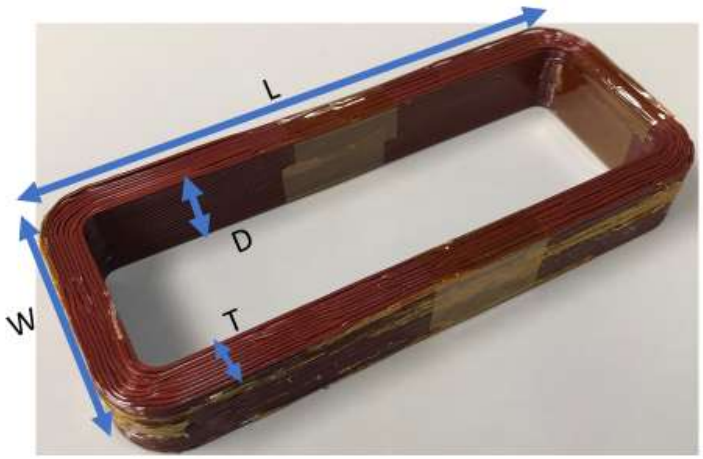

Fig. 2.2.3-9 Die compressed coil measured dimensions to evaluate spring back after removal from compression die.

Different measurements of each dimension were taken for each coil, Table 2.2.3-IV, including the average, minimum and maximum of the dimensions of pressed coils. A summary of the dimensional measurements is shown in Table 2.2.3-V.

TABLE 2.2.3-IV. DIMENSIONAL COIL MEASUREMENTS AFTER REMOVAL FROM COMPRESSION DIE

Coil	W (mm)	L (mm)	T (mm)			D (mm)		
			Min	Average	Max	Min	Average	Max
1	51.8	129.6	7.8	8	8.2	18.8	19.4	19.7
2	52.3	129.7	8.1	8.25	8.6	18.4	18.9	19.5
3	52.2	129.7	8.1	8.1	8.3	18.1	18.3	18.6
4	52.2	129.3	7.9	7.9	8.1	17.8	18	18.2
5	52.25	129.6	7.9	8.15	8.45	18.2	18.6	19.2
6	52.25	129.9	8.1	8.4	8.6	18.2	18.5	18.8
7	52.3	130	8.1	8.3	8.4	18.6	19	19.3
8	52.13	130	7.8	8	8.3	17.8	18.3	18.4
9	51.9	129.3	7.6	7.7	7.9	17.1	17.3	17.6

TABLE 2.2.3-V: SUMMARY OF COIL DIMENSION MEASUREMENTS

	W (mm)	L (mm)	T(mm)	D (mm)
Average	52.1	129.7	8.09	18.47
Minimum	51.8	129.3	7.6	17.6
Maximum	52.3	130	8.6	19.7

Coil Testing:

To verify the integrity of the pressed coils, the coil terminals were extracted, and continuity checks and surface insulation resistance checks were carried out. The surface insulation of the coils was tested using HIPOT insulation test, as shown in the Fig. 2.2.3-10. A Megger MIT420 Hi-Pot tester was used to measure the insulation resistance. A voltage of 0.5-1 kV was applied across one of the coil terminals and the coil surfaces were placed on a copper sheet and the other test lead attached, as shown in Fig. 2.2.3-10. Coils with an insulation resistance less than 10 MΩ were discarded.

Fig. 2.2.3-10. HIPOT and surface insulation tests of die compressed coils.

2.3 Generation III Wound Field Synchronous Machine

2.3.1 Introduction

To increase the performance of the traction oriented wound field synchronous machines being developed for this project, topologies and technologies for high slot fill windings on both the rotor and stator were investigated. To reduce cost, topologies and designs that could reduce the lamination punching scrap and progressive die tooling cost were examined. To achieve a high slot fill stator winding, two potential stator topologies were investigated.

1) 12 slot 10 pole fractional slot concentrated die compressed winding
2) Distributed hairpin winding as commonly used to automotive traction motors presently.

For the rotor field winding high slot fill die compressed windings and windings using square profile conductors were also investigated.

A 12 slot 10 pole WFSM with die compressed stator and field windings was designed. To match the stator inverter voltage supply a relatively moderate number of turns are needed and multiple "strands in hand" or conductors per turn are necessary to reach a high slot fill given the size of the stator slot. Techniques for approximate orthocyclic winding of the multiple strands in hand on a bobbin before compression in a die were investigated. However, it was decided that it would be too difficult to ensure defect free coils given the time remaining for the project.

Distributed hairpin winding WFSMs which also have high stator slot fill, albeit probably slightly less than a die compressed coil, were also optimized. Because it is very difficult to prototype a hairpin winding in an academic setting the hairpin wound stator from a General Motors Chevy Volt Gen 1 Motor B was used. The rotor lamination was designed to be segmented such that the field winding could be die compressed, bobbin wound with square/rectangular conductor magnet wire, or bobbin wound with a square conductor twisted at a 45-degree angle. Two of the three potential field winding techniques were prototyped. The bobbin wound square conductor and the twisted bobbin wound square conductor. The version with the bobbin wound square conductor was dynamometer tested with brushes and slip rings and two generations of the single phase GaN inverters with a printed circuit board (PCB) based capacitive power coupler.

2.3.2 Initial Distributed Hairpin Stator and Rectangular Die Compressed Field Winding Designs

Initial design studies were carried out to assess the potential of a WFSM with a hairpin stator and a rotor with a die compressed field winding. An open slot hairpin stator template was created in the in-house created optimization suite. A rectangular die compressed field winding similar to that used in the Generation II WFSM, was assumed.

Dimensional optimization was performed on the stator and rotor, using a differential evolution algorithm, implemented within the WFSM design environment. The dimensional variables included the stator and rotor yoke thickness, and stator tooth width. The rest of the rotor dimensional variables, which includes the pole neck and pole shoe were kept the same, to match the design of the rectangular die compressed winding, which was previously optimized for in the

Generation II WFSM. A variable current density optimization was first carried out to infer a reasonable ratio of the stator/rotor excitation to be used in a second optimization with peak constant current densities. The optimization objectives were maximizing the average torque and minimizing the total losses. Furthermore, optimization constraints were applied to the torque ripple to find designs with less than 10% ripple. Figure 2.3.2-1 shows an overview of all evaluated design candidates with a single layer stator winding. The design candidates which meet the torque ripple constraint are shown in Fig. 2.3.2-2. As can be observed in Fig. 2.3.2-2 the torque ripple constraint has a significant impact on the Pareto front and the torque densities which can be reached.

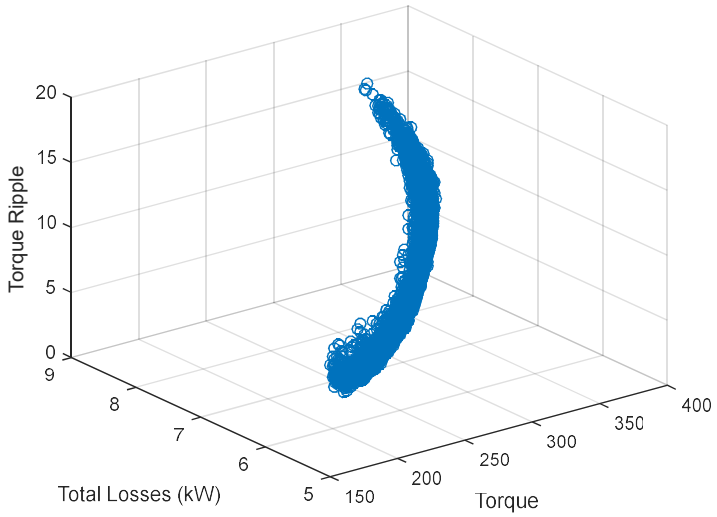

Fig. 2.3.2-1. All open slot hairpin stator and rectangular die compressed field winding optimization candidate designs, with fixed peak rotor and stator current densities

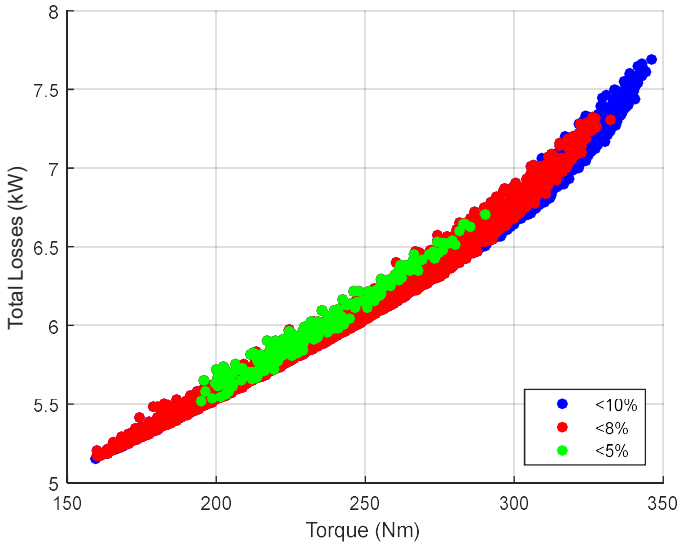

Fig. 2.3.2-2. Total losses versus torque for fixed current density WFSM designs which meet the torque ripple constraint.

The performance of the promising design candidates is listed in Table 2.3.2-I. The flux density cross-sections of the promising designs are shown in Fig. 2.3.2-3.

TABLE 2.3.2-I. PROMISING DESIGNS – RECTANGULAR COPPER DIE-COMPRESSED WINDING ROTOR AND OPEN SLOT SINGLE LAYER WINDING STATOR

Members	Torque (Nm)	Total Losses (kW)	Torque Ripple (%)		Stator (At)	Rotor (At)	At's ratio	Stator Slot Opening (mm)	Stator Yoke Thickness (mm)	Shaft Radius (mm)	Torque / Loss (Nm/kW)	Goodness (Nm/W$^{1/2}$)
			24	48								
M1(3045)	267.5	6.2	6.5	7.1	910	1942	0.47	3.29	18.9	37.6	42.94	3.39
M2(4027)	267.9	6.4	4.8	5.9	937	1942	0.48	3.09	16.6	39.6	42.19	3.36
M3(4455)	276.5	6.3	7.1	7.4	950	1942	0.49	3.46	18.8	37.3	43.68	3.48
M4(0142)	280.1	6.5	4.9	5.7	994	1942	0.51	3.14	16.3	39.8	43.02	3.47
M5(2774)	287.4	6.5	7.5	8.2	1000	1942	0.52	3.59	18.9	41.0	44.43	3.57
M6(1079)	285.4	6.6	5.0	6.5	1033	1942	0.53	3.19	15.7	37.5	43.05	3.51
M7(3068)	290.5	6.7	4.9	5.9	1061	1942	0.55	3.22	15.5	39.7	43.31	3.55
M8(1623)	295.2	6.6	7.8	8.1	1046	1942	0.54	3.67	18.0	38.6	44.60	3.63
M9(1590)	297.9	6.6	9.5	11.1	1060	1942	0.55	3.96	18.9	38.8	45.06	3.66
M10(2022)	307.1	6.8	7.7	8.7	1104	1942	0.57	3.77	17.9	36.5	45.33	3.73
M11(2552)	316.8	6.9	9.8	10.4	1161	1942	0.60	4.15	18.6	38.3	45.94	3.81
M12(0534)	317.3	7.0	7.1	8.2	1188	1942	0.61	3.79	16.3	40.0	45.12	3.78
M13(0889)	326.2	7.3	7.2	8.6	1272	1942	0.65	3.87	15.4	36.2	44.91	3.83
M14(3668)	340.5	7.4	10.0	10.9	1350	1942	0.70	4.39	16.7	43.5	45.77	3.95
M15(3927)	344.2	7.6	9.8	10.5	1412	1942	0.73	4.46	15.9	40.3	45.23	3.95

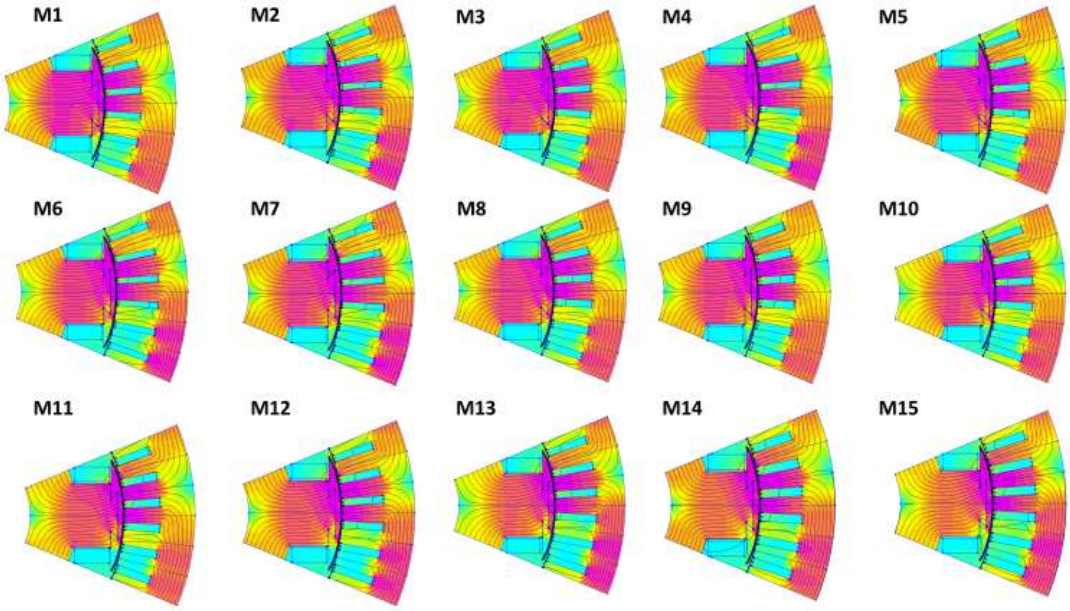

Fig. 2.3.2-3 Flux density cross-sections of promising designs with rectangular copper die-compressed winding rotor and open slot single layer winding stator.

2.3.3 Design of 12 Slot 10 Pole WFSM with Die Compressed Windings

A template for a 12 slot 10 pole fractional slot concentrated winding (FSCW) was developed in the in-house WFSM design environment, as shown in Fig. 2.3.3-1(a). Variations of 12 slot 10 pole FCSW were considered to achieve a low space-harmonic content and a higher fundamental winding factor including combined star-delta designs that act like a six-phase winding. The template was verified with a model built in Infolytica Magnet as shown in Fig. 2.3.3-1(b).

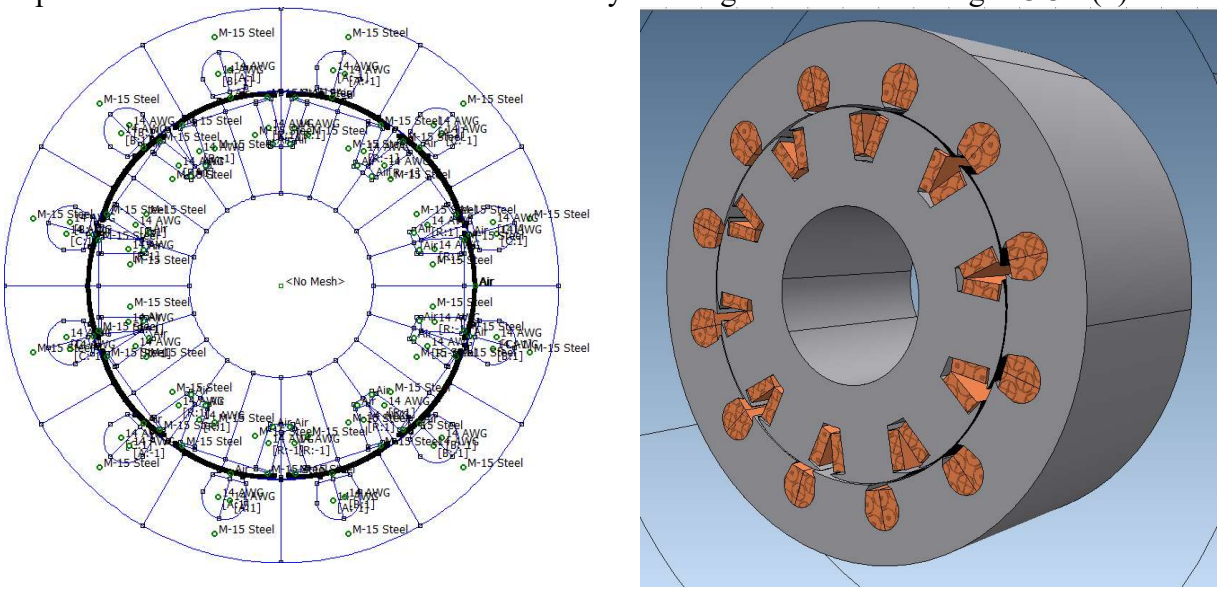

(a) . (b).

Fig. 2.3.3-1. Initial 12 slot 10 pole template developed for IIT's in-house optimization suite (a), and verification model developed in Infolytica Magnet (b).

The electromagnetic design optimization of a WFSM with die compressed windings on both the stator and rotor has been completed. Segmentation is used on both the stator and the rotor for reduced scrap during punching. The die compressed coil must be inserted as a single unit, unlike classical distributed windings where turns may be inserted one by one. The use of a die compressed winding in the stator most likely necessitates the use of a fractional slot concentrated winding (FSCW) layout. Normally, FSCWs are used in low speed machines because of their large space harmonic content. Electric vehicle traction motors are trending towards higher speeds to increase their power density. To reduce the space harmonic content of the FSCW used in the new WFSM prototype, with the targeted maximum speed of 12,000 RPM, a 12 slot 10 pole configuration with two winding subsets was adopted. The two winding subsets are displayed spatially and also wound in a combined star-delta configuration to achieve a 30-degree phase shift in the excitation between windings. This winding configuration emulates a six-phase machine and eliminates a number of harmonic orders. Electromagnetic optimization was carried out at 4,000 RPM for two different stator to rotor current density ratios: 24 A/mm2 to 20 A/mm2 and 33 A/mm2 to 30 A/mm2. The Pareto fronts of the optimized designs are shown in Figure 2.3.3-2. Designs indicated by a solid circle were then down-selected for re-simulation at the opposite current densities. The re-simulated designs at the opposite current density are indicated by the diamond mark. The down-selected

designs are the solid red-dot and solid red diamond which correspond to the same design at two different current density ratios.

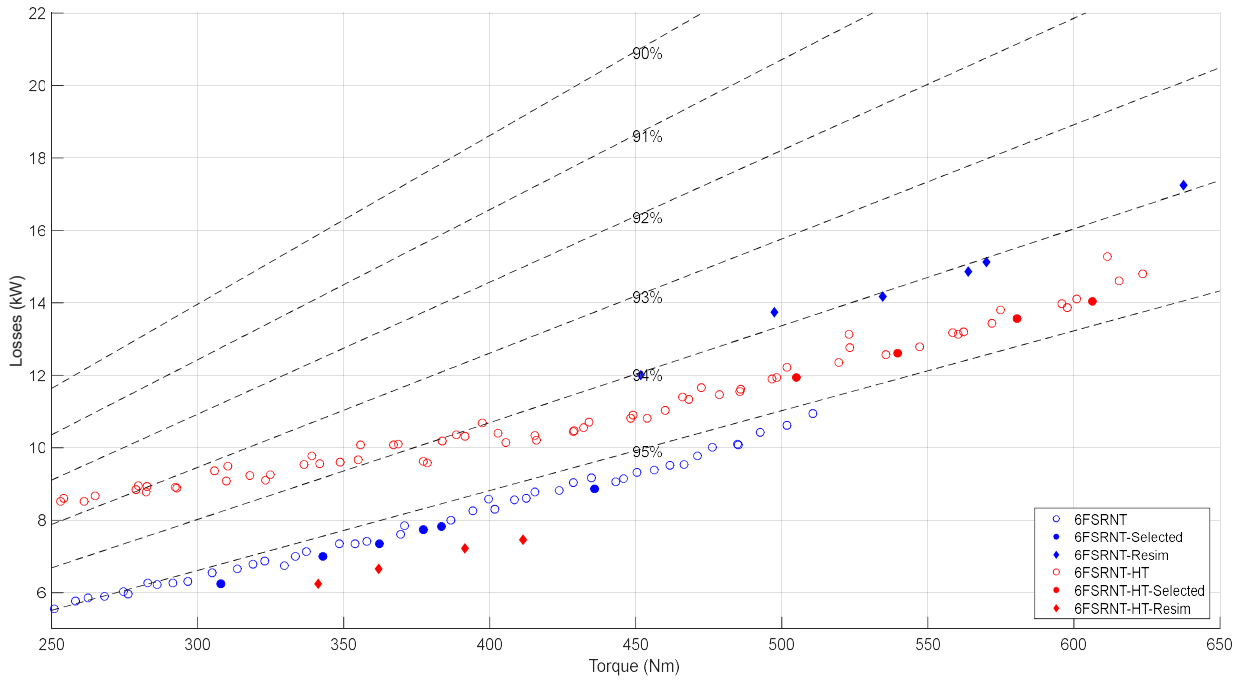

Fig. 2.3.3-2. Electromagnetic optimization Pareto fronts of 12 slot 10 pole star-delta designs for two different current density ratios at 4,000 RPM. Down-selected designs from original simulations are solid dots. Corresponding designs re-simulated at the opposite current density are indicated by a diamond mark.

The down-selected designs are listed in Table 2.3.3-1 and Table 2.3.3-2. The high current density (high torque) designs show better performance at both high current densities and moderate current densities. The M72 design (Table 2.3.3-2) was selected as the design for prototype construction.

TABLE 2.3.3-1. MODERATE CURRENT DENSITY PARETO FRONT SELECTED DESIGNS PERFORMANCE

	Stator Winding Area	Rotor Winding Area	Min Air gap Length	G	M	Original Current Densities (24/20)				New Current Densities (33/30)			
						T (Nm)	Losses (kW)	Torque Ripple (%)	Nm/kW	T (Nm)	Losses (kW)	Torque Ripple (%)	Nm/kW
M9	259	139.3	0.53	02	64	308.0	6.25	3.9	49.23	451.9	12.0	2.0	37.67
M14	274.6	171.2	0.82	50	23	343.0	7.0	1.7	48.94	497.4	13.7	1.1	36.19
M16	306.5	163.8	0.79	25	09	362.2	7.36	1.7	49.24	534.6	14.2	0.9	37.71
M19	340.6	164.2	0.85	21	09	377.3	7.73	2.0	48.80	563.8	14.9	1.0	37.92
M20	341.3	170.4	0.83	20	23	383.4	7.82	2.0	49.02	570.0	15.1	0.9	37.69
M25	387.9	194.9	0.72	25	60	435.9	8.88	0.9	49.11	637.6	17.2	0.5	36.96

TABLE 2.3.2-2. HIGH CURRENT DENSITY PARETO FRONT SELECTED DESIGNS PERFORMANCE

	Stator Winding Area	Rotor Winding Area	Min Air gap Length	G	M	Original Current Densities (33/30)				New Current Densities (24/20)			
						T (Nm)	Losses (kW)	Torque Ripple (%)	Nm/kW	T (Nm)	Losses (kW)	Torque Ripple (%)	Nm/kW
M52	246.8	135.8	0.66	39	32	504.9	11.94	1.6	42.30	341.3	6.2	2.3	54.62
M58	272.0	136.2	0.58	39	51	539.5	12.60	1.1	42.81	361.9	6.7	1.8	54.31
M67	288.6	147.7	0.52	38	71	580.5	13.56	0.9	42.82	391.6	7.2	1.5	54.31
M72	299.1	156.6	0.51	38	40	606.4	14.04	0.9	43.18	411.5	7.4	1.5	55.25

Comparison of Down-Selected Design with Other WFSM Topologies

A large number of dimensional optimizations were performed for WFSM different templates and excitation levels. The design templates included two templates for the 12 slot 10 pole machine, for three phase and six phase winding configurations with copper and aluminum windings. Additional stator topologies and winding types considered include open and semi-open hairpin/bar wound, classical random wound distributed windings, and distributed mixed layer windings. The different design optimizations are listed in Table 1. An “S”, “R”, or “SR” in the design optimization name indicates whether variables in the stator, rotor, or stator and rotor were optimization parameters.

The differential evolution was used as the optimization algorithm, where the average torque and the total losses were set as the optimization objectives. Optimization constraints included maximum torque ripple and losses and minimum average torque. Generally, each optimization consisted of 50 generations of 96 members.

For each design, optimizations were performed with variable current densities to determine the appropriate current density ratio between rotor and stator. Afterwards, optimizations were performed with the fixed current densities indicated by the “F” in the optimization name. A “-HT” in the optimization name corresponds to optimizations carried out with a nominally high current ratio and corresponds to high torque.

A comparison of the new selected design predicted performances with past designs are indicated by the blue black and red stars in Fig. 2.3.2-2. The blue star corresponds to the predicted performance of the 6 phase equivalent 12 slot 10 pole at high current densities (33 A/mm^2 stator and 30 A mm^2 rotor). The black star corresponds to the predicted performance of the Generation II segmented rotor prototype and the red star the experimentally measured performance of the Generation I classical wound field rotor using the shorter stack length UW-Madison stator. The down-selected design offers quite high predicted performance.

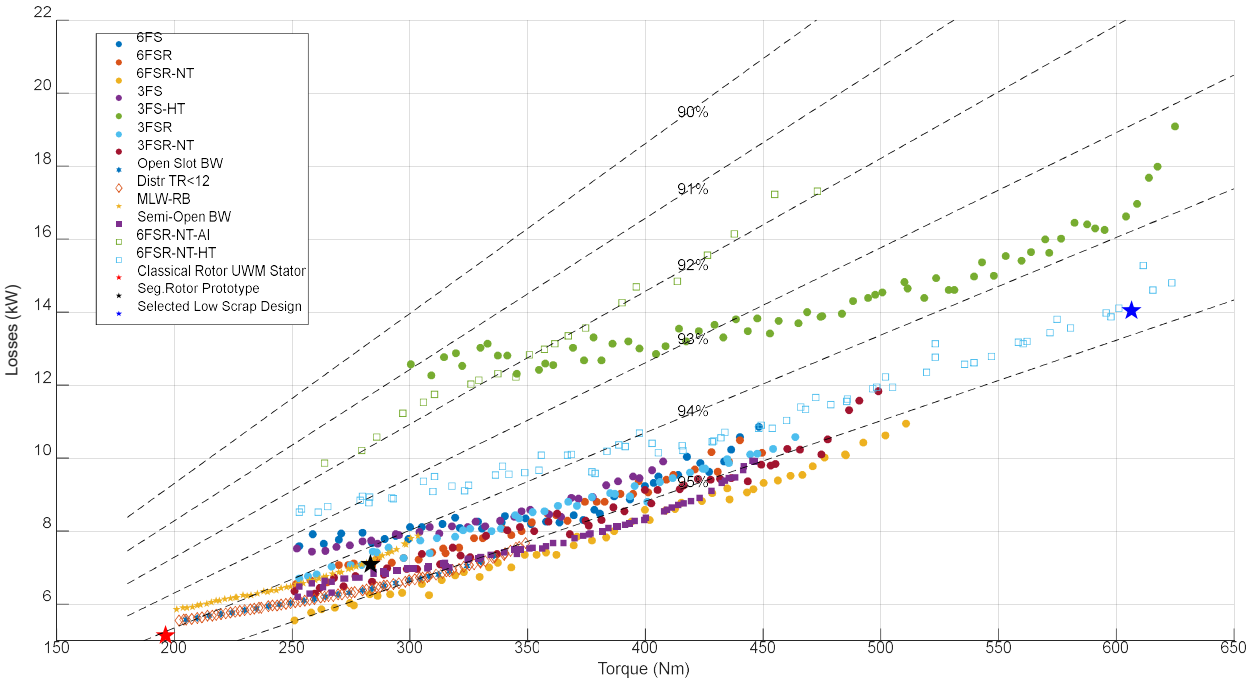

Fig. 2.3.2-2. Comparison of Pareto fronts of wound field synchronous machine topologies.

TABLE 2.3.2-3: CONSIDERED DESIGN OPTIMIZATIONS

Optimization Name	Phases	Slots	Poles	Optimization Variables	Stator Current Density A/mm²	Rotor Current Density A/mm²	Stator Winding Fill Factor	Rotor Winding Fill Factor
6FS	6	12 – Template 1	10	Stator	24	20	0.7	
6FSR	6	12– Template 1	10	Stator& Rotor	22.4	20	0.7	
6FSR-NT	6	12 - Template 2	10	Stator & Rotor	24	20	0.7	
3FS	3	12	10	Stator	24	20	0.7	
3FS-HT	3	12 - High Torque	10	Stator	30	28.8	0.7	
3FSR	3	12	10	Stator & Rotor	22.4	20	0.7	
3FSR-NT	3	12 -Template 2	10	Stator & Rotor	24	24	0.7	0.7
Open Slot BW	3	48 - Open Slot Bar Wound	8	Stator	21.4	20	0.7	
Distrib.	3	48 - Distributed Round Bottom	8	Stator	27.4	18	0.4	
MLW-RB	3	48 - Mixed Layer Round Bottom	8	Stator	26	19.3	0.4	
Semi-Open BW	3	48 - Semi-Open Slot Bar Wound	8	Stator & Rotor	24	20	0.7	
6FSR-NT-AL	6	12 – Template 2 - Aluminum	10	Stator & Rotor	26	20	0.7	
6FSR-NT-HT	6	12 – Template 2 - High Torque	10	Stator & Rotor	33	30	0.7	

Performance Mapping of Down-Selected 12 Slot 10 Pole Design with Die Compressed Stator and Field Windings

A series of FEA simulations, using Infolytica MagNet, were done in order to map the performance of the selected design of the 12 slot 10 pole machine, shown in Fig. 2.3.2-3. The simulations considered the windings actual 6 phase equivalent star delta connection, shown in Fig. 2.3.2-4, which is used to obtain the 30 degrees phase angle difference between the two sets of the three-phase windings used in the machine reducing the space harmonics. These mappings are also used to design the number of turns in the windings of the machine.

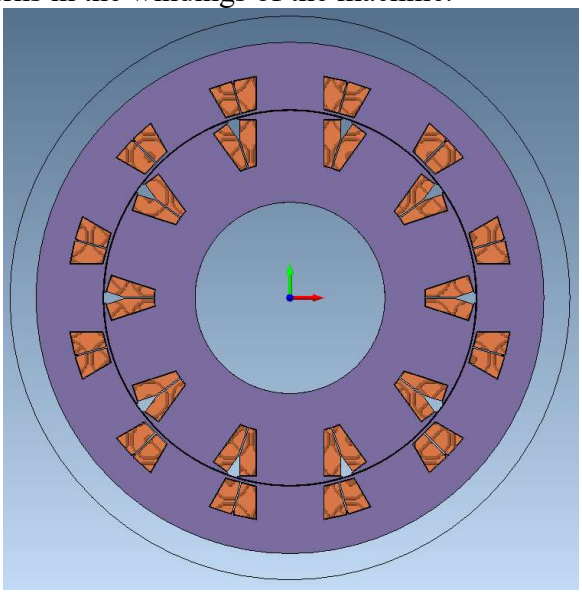

Fig. 2.3.2-3 Finalized lamination and coil shape design of 12 slot 10 pole WFSM.

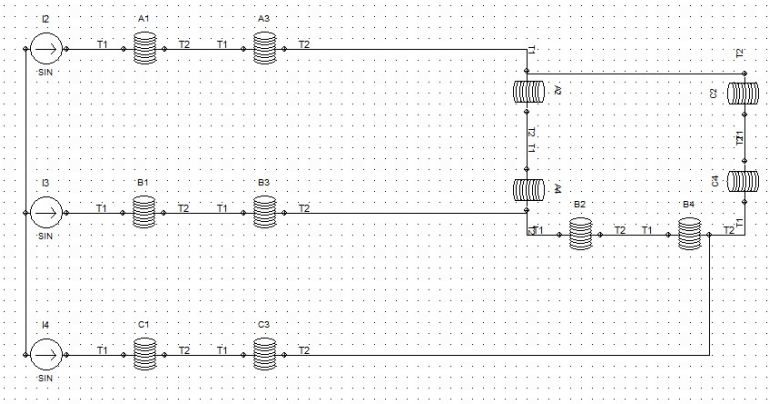

Fig. 2.3.2-4 Current driven star delta winding connection in Infolytica MagNet for 12 slot 10 pole machine.

The mapping was used to evaluate the machine performance for different rotor and stator current densities, number of stator winding turns and stator current phase advance angles to ensure that the operation is within the voltage and current requirements of the large Semikron drive used for dynamometer testing at UW-Madison. Selected mapping results are shown below in Fig. 2.3.2-5 through Fig. 2.3.2-7 for the average electromagnetic torque, peak line voltage and power factor. The figure legend indicates the number of coil turns in the wye and delta connected coils and the phase advance. Two phase advance angles are shown, -15° and -30°. Please note that the phase

advance angle is shifted compared to its normal reference of the rotor field axis. The DC voltage limitation into the Semikron drive is 600 V, restricting the number of turns. The power factor mapping also demonstrates the importance of having sufficient rotor field winding ampere turns to achieve a unity power factor. Future designs should consider increased field conductor areas or cooling solutions to achieve higher current densities in the field winding. As can be observed from the terminal voltage waveforms, the harmonic content significantly improves with an over-excited machine. Fig. 2.3.2-8 to Fig. 2.3.2-11. The sinusoidal nature of the currents in the delta connected coils also substantially improves if the machine is over-excited, Fig. 2.3.2-12 to Fig. 2.3.2-15. To be compatible with the maximum DC link voltage the number of turns, wye = 8, and delta = 14 were selected. To fill the entire stator slot area and keep the number of strands in hand reasonable, a relatively thick wire gauge was selected. More details about this selection are provided in the following subsection.

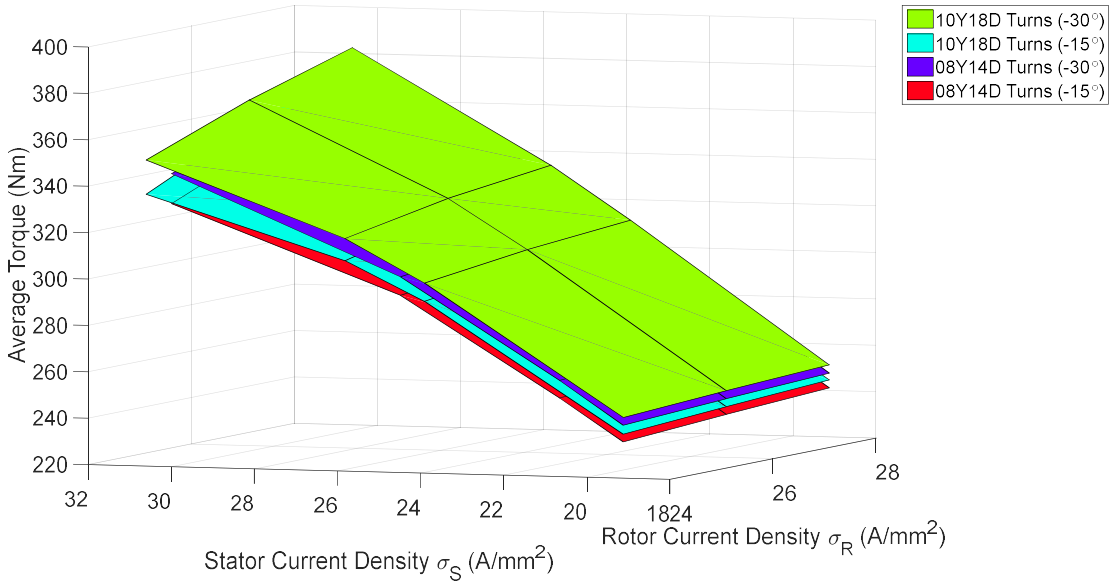

Fig. 2.3.2-5 Average electromagnetic torque mapping for the finalized 12 slot 10 pole design for two different wye and delta turn combinations and current angles.

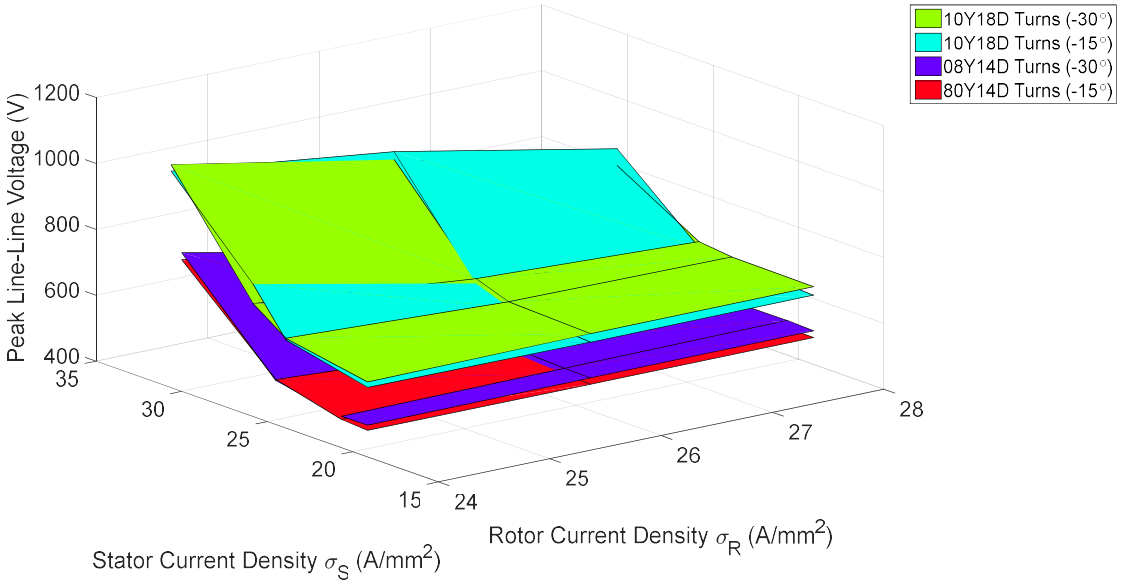

Fig. 2.3.2-6 Peak line to line voltage mapping for the finalized 12 slot 10 pole design for two different wye and delta turn combinations and current angles.

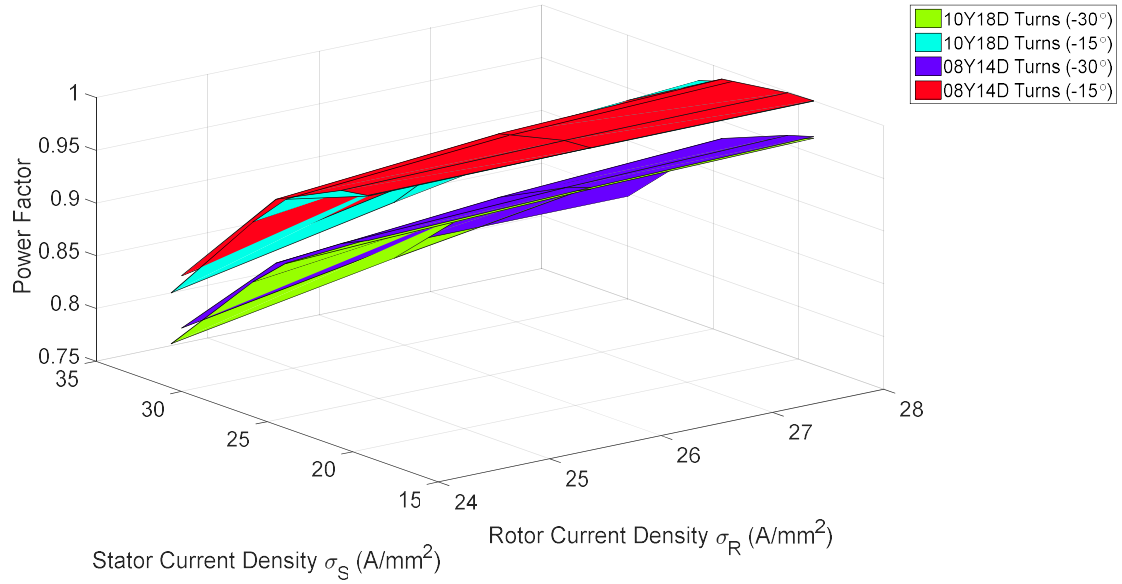

Fig. 2.3.2-7 Power factor mapping for the finalized 12 slot 10 pole design for two different wye and delta turn combinations and current angles.

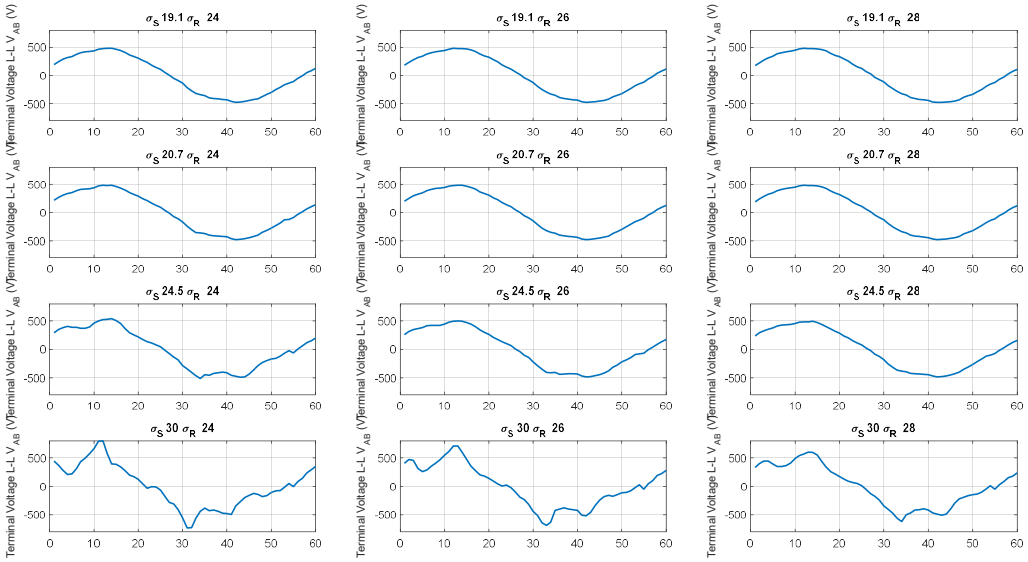

Fig. 2.3.2-8. Predicted line to line terminal voltage waveforms as a function of stator and rotor current densities for a phase advance angle of -15° with 8 turns in the wye connected coils and 14 turns in the delta connected coils.

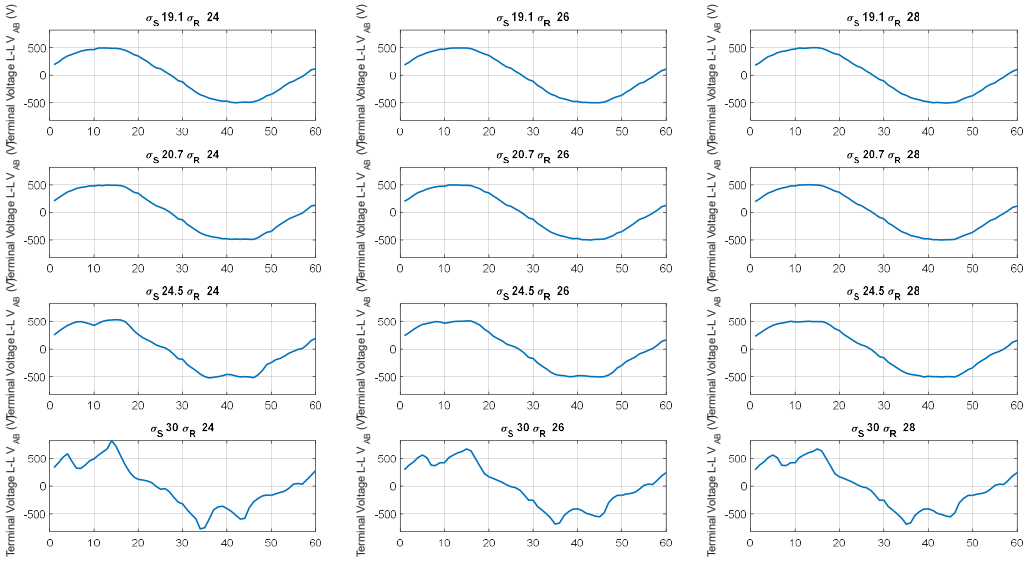

Fig. 2.3.2-9. Predicted line to line terminal voltage waveforms as a function of stator and rotor current densities for a phase advance angle of -30° with 8 turns in the wye connected coils and 14 turns in the delta connected coils.

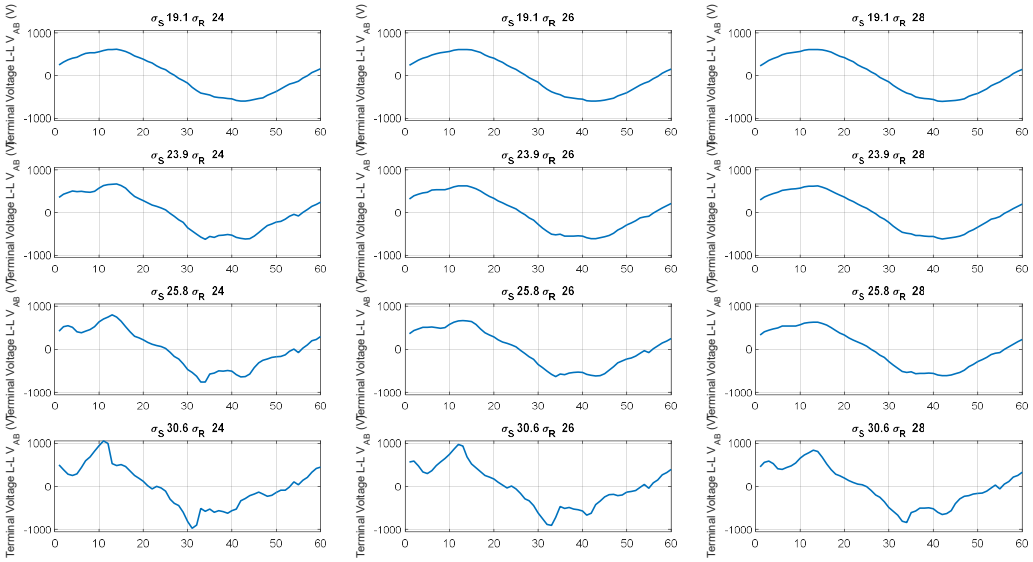

Fig. 2.3.2-10. Predicted line to line terminal voltage waveforms as a function of stator and rotor current densities for a phase advance angle of -15° with 10 turns in the wye connected coils and 18 turns in the delta connected coils.

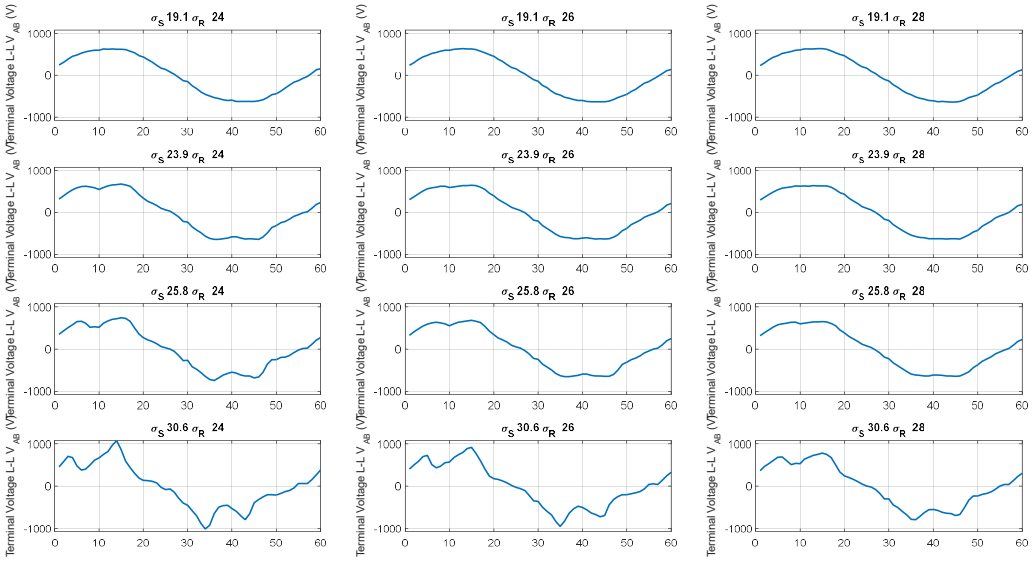

Fig. 2.3.2-11. Predicted line to line terminal voltage waveforms as a function of stator and rotor current densities for a phase advance angle of -30° with 10 turns in the wye connected coils and 18 turns in the delta connected coils.

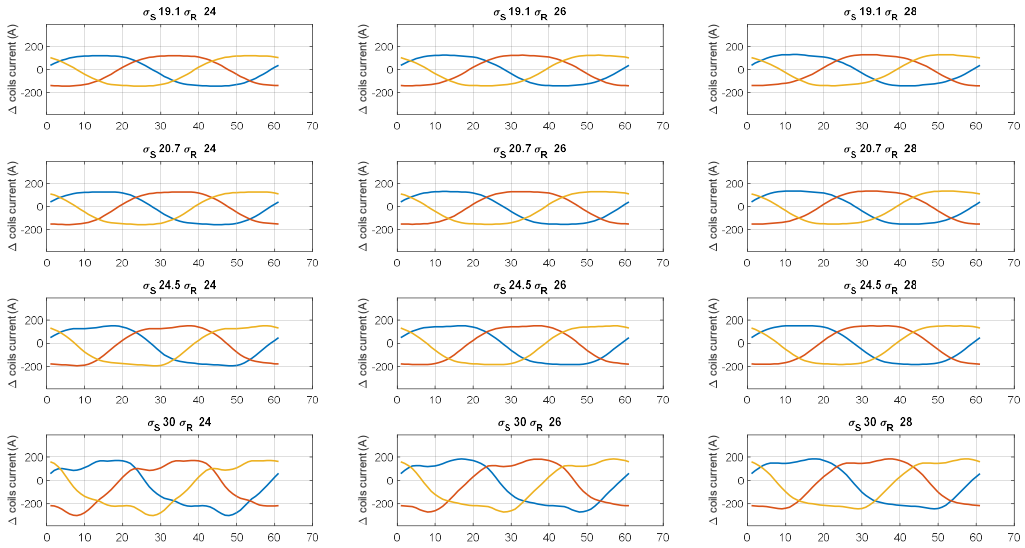

Fig. 2.3.2-12. Predicted delta connection coil current waveforms as a function of stator and rotor current densities for a phase advance angle of -15° with 8 turns in the wye connected coils and 14 turns in the delta connected coils.

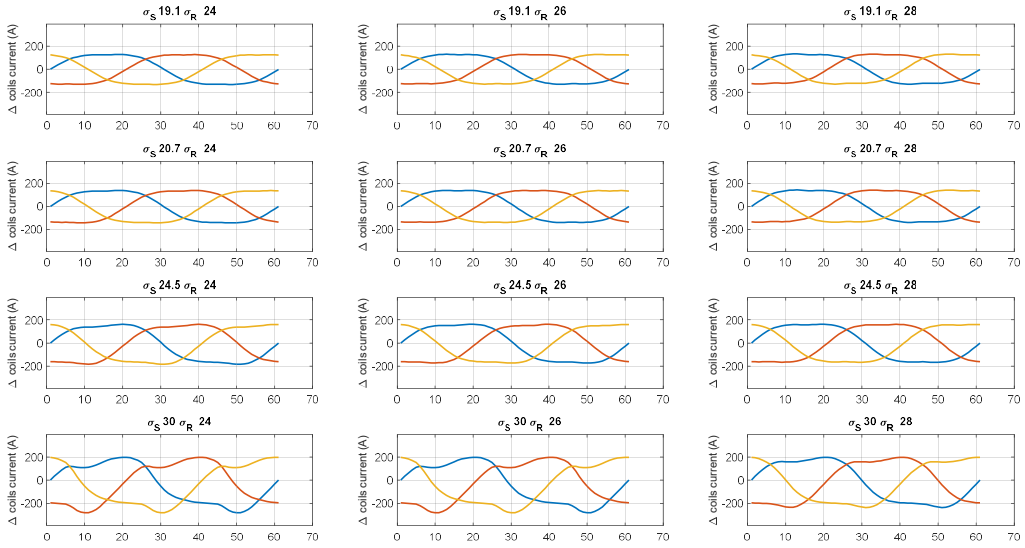

Fig. 2.3.2-13 Predicted delta connection coil current waveforms as a function of stator and rotor current densities for a phase advance angle of -30° with 8 turns in the wye connected coils and 14 turns in the delta connected coils.

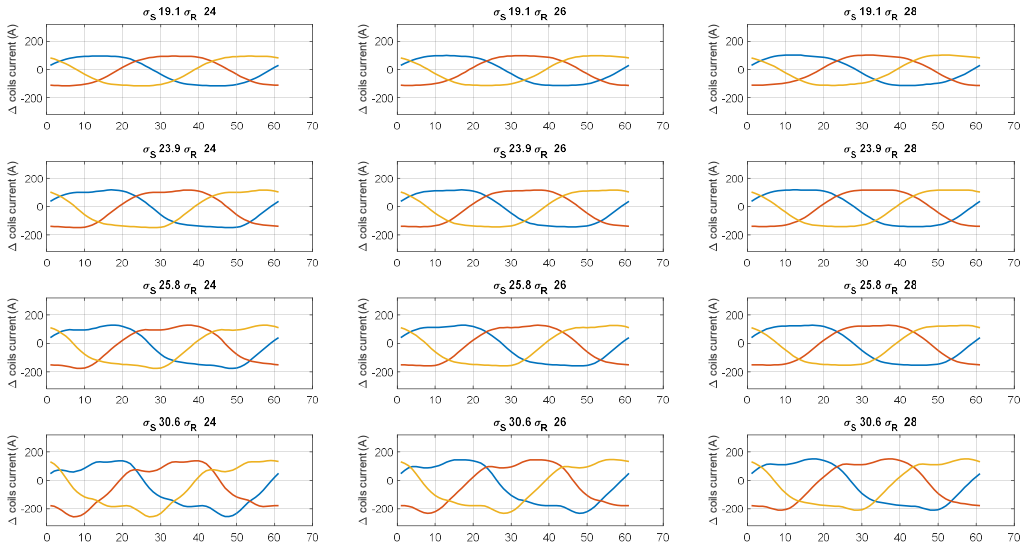

Fig. 2.3.2-14. Predicted delta connection coil current waveforms as a function of stator and rotor current densities for a phase advance angle of -15° with 10 turns in the wye connected coils and 18 turns in the delta connected coils.

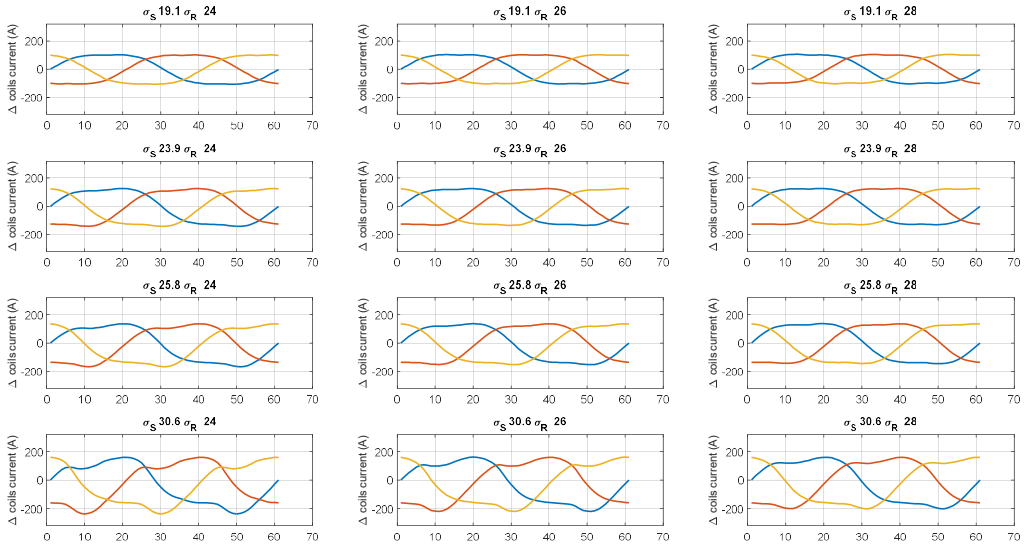

Fig. 2.3.2-15. Predicted delta connection coil current waveforms as a function of stator and rotor current densities for a phase advance angle of -30° with 10 turns in the wye connected coils and 18 turns in the delta connected coils.

2.3.4 Challenges of Die Compressed Windings for 12 Slot 10 Pole WFSM

The construction of prototype die compressed stator coils for the down-selected 12 slot 10 pole machine was undertaken to verify the initial design ideas for the die. In the previous subsection, the selection of the number of turns was detailed for the Wye-Delta two subset winding (Wye = 8 turns; Delta = 14 Turns) based on the anticipated current loadings and corner point speed. Because of the low number of stator turns to reach a high slot fill, either a very large wire diameter (low gauge) needs to be used or multiple strands in hands with smaller wire diameters (higher gauge). The is no literature or public reports about die compression of large diameter wires and their potentially extreme deformation. Alternatively, if multiple strands in hand are used, how to wind the bobbin layers and fix the turns during winding are unknowns with no public literature or reports. Some investigations into winding these cases were undertaken. The rotor number of turns and winding is similar to previous prototypes and the design of the rotor winding die was relatively low risk.

Using multiple strands in hand (multiple turns of magnet wire) in each turn of the stator winding can allow a better slot fill and make the winding and die compression process easier, especially if wires with smaller diameter are used. The wire sizes/diameters of the stator winding and the corresponding number of strands in each turn were determined for the designed stator winding window, as shown in Fig. 2.3.4-1. A balance is sought between restricting the number of turns to ease the winding process, reducing the deformation of the copper and magnet wire insulation, and maximizing the fill factor for the designed slot size. The Y connected winding subset with the lowest number of turns is the winding most likely to cause difficulty and was the focus of the investigation. Table 2.3.4-1 shows the number of strands to be used with different AWG sizes of the magnetic wires and the corresponding slot fill for eight turns. For initial trial windings, a wire gauge of AWG 11 was selected with 4 strands in hand. This wire gauge was selected to achieve a high theoretical slot fill of 0.893.

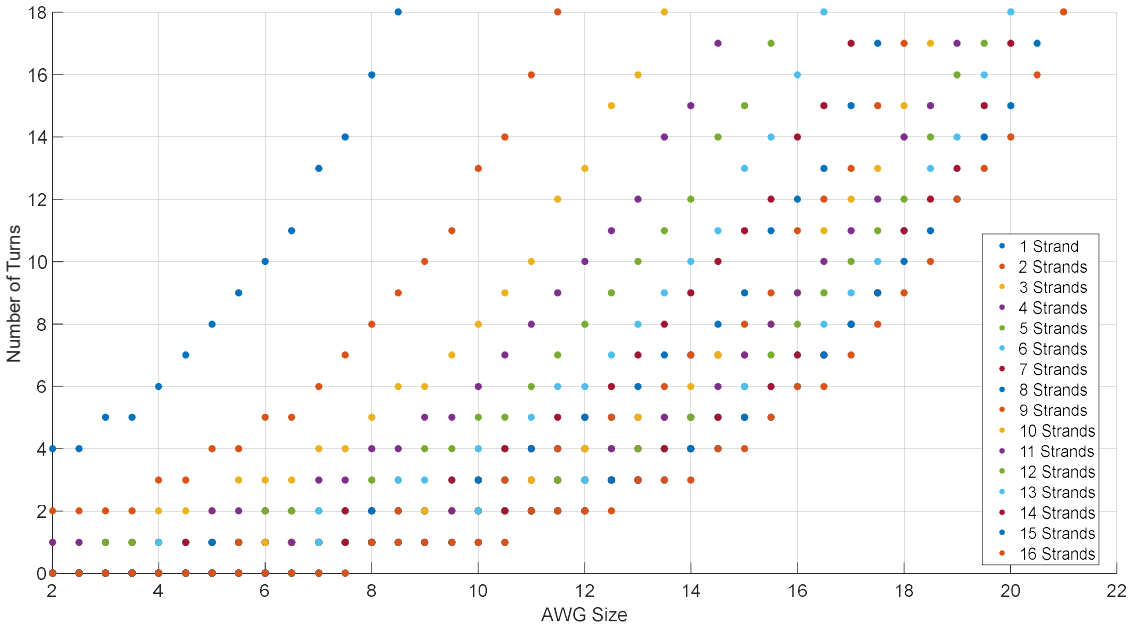

Fig. 2.3.4-1. Number of turns for different AWG size and number of strands.

TABLE 2.3.4-1. NUMBER OF STRANDS AND SLOT FILL FACTOR FOR DIFFERENT WIRE SIZES

AWG Size	# Strands	Fill Factor (including Insulation)	Fill Factor (Copper)
5	1	0.952	0.898
8	2	0.963	0.896
10	3	0.922	0.845
11	4	0.984	0.893
12	5	0.984	0.886
13	6	0.944	0.844
13.5	7	0.985	0.876
14.5	8	0.903	0.795
15	9	0.908	0.796
15.5	10	0.907	0.788
15.5	11	0.997	0.867
16	12	0.967	0.840
16.5	13	0.940	0.813
17	14	0.905	0.780
17	15	0.970	0.836
17.5	16	0.926	0.792

The AWG 11 wire is very stiff and work hardens very easily. The previous winding setup used for winding the rectangular die compressed winding, was suitable for only winding with one strand in hand as tension could only be applied on the single strand. A new winding setup was designed to facilitate winding multiple strands of the magnetic wire and to obtain the required number of turns imposed by the voltage requirement of operation. The winding device shown in Fig. 2.3.4-2 was constructed using aluminum T-slotted rails. It includes multiple stages in order to level the wires, apply tension (using the device shown in Fig. 2.3.4-3), and to group and guide the wires using a sleeve bearing carriage with an eye-bolt. Finally, the manual coil winding device is attached to the assembly with an aluminum mounting plate.

In order to check the winding process for multiple strands and a relatively large diameter magnet wire, a trial coil was made using AWG 11 and two strands per turn. As shown in Fig. 2.3.4-4, the lead-in to the winding area is much more difficult with the thicker gauge wire and the multiple strands in hand. The large bending radius of the lead in distorts the initial position of the base layer of the winding, making subsequent layers have cross-overs. Cross-overs in the compression process can lead to insulation damage. Two new lead-in techniques were investigated to avoid the issues described. A number of layering designs for winding on the bobbin were also investigated for non-rectangular die cavities or stator slots. The layout pre-compression is critical for avoiding excessive strain on the magnet wires.

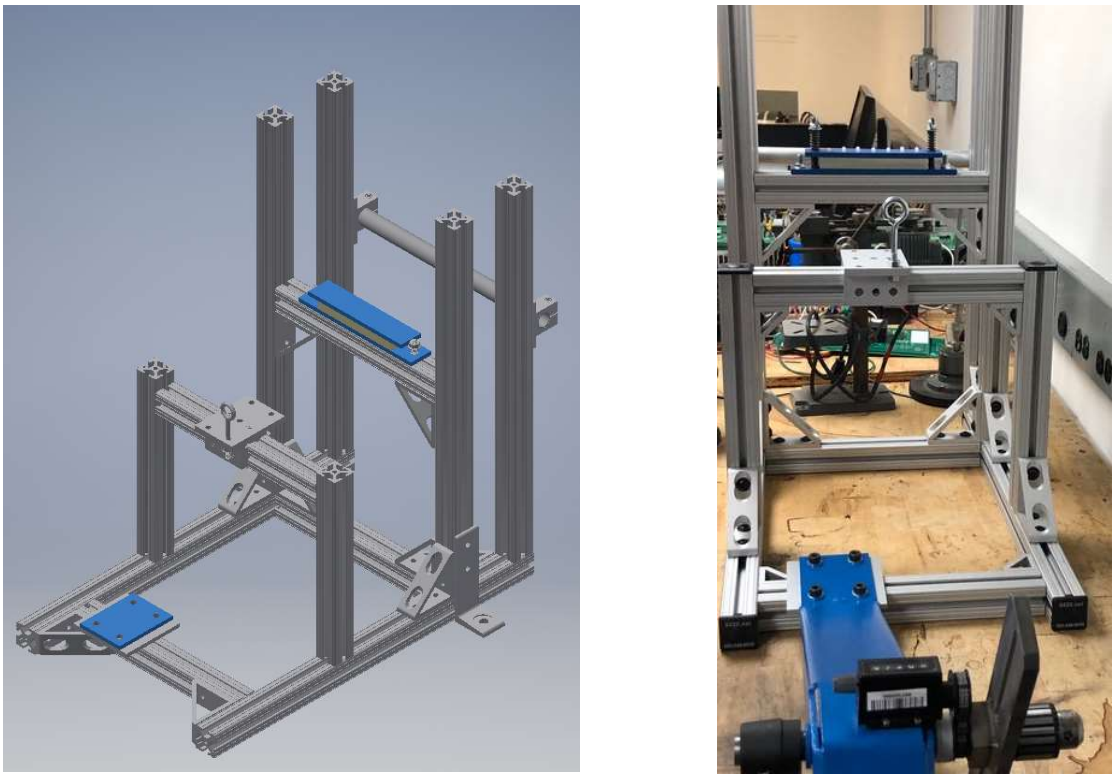

Fig. 2.3.4-2. Winding setup, CAD model (left), actual built setup (right)

Fig. 2.3.4-3. Tension device used in the setup

Fig. 2.3.4-4. Initial trial coil with two strands per turn of 11 AWG magnet wire.

The custom winding machine setup was fully overhauled in order to improve the accuracy in the positioning of the strands as they are wound on the bobbin. Fig. 2.3.4-5 shows the full setup. Wire first goes through the tensioner at the right, where it is pinched between two UHMW plastic surfaces. It then passes through the 2-axis wire straightener, which has been designed to apply the concepts used for straightening single wires to multiple wires simultaneously. The horizontal section is designed to flex all strands at the same time, and in the same direction, while keeping them in one plane, trapped between UHMW sheets. The vertical section then flexes the wires vertically before outputting the wires in the flat bundle desired. It is able to straighten even very wavy wires, and allows the winding to be much more precise.

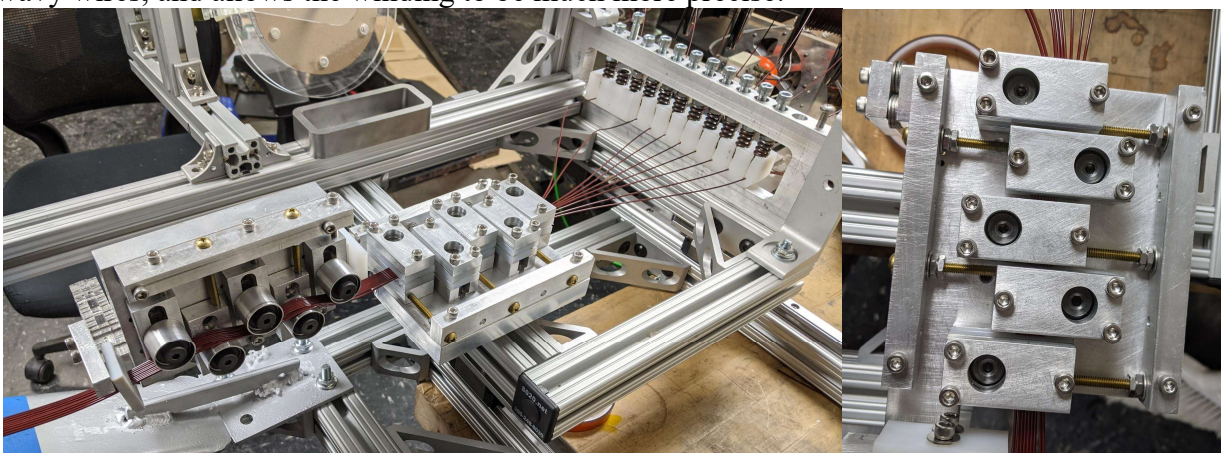

Fig. 2.3.4-5: Overhauled custom winding machine for improved strand positioning accuracy.

Multiple methods to minimize the number of crossovers by laying the strands as parallel as possible, permit easier access to the wire ends, and eliminate the cross-over bump, were investigated. A method was found that resulted in a reasonably orthocyclic layout before compression. It however still had a relatively high failure rate and would likely have taken too long to perfect for the timeline of the 12 slot 10 pole prototype construction which would have required 24 perfect coils. An example of the compressed coil cross-sections resulting from this process are shown in Fig. 2.3.4-6. Both proper levels of deformation and over-deformation can be seen.

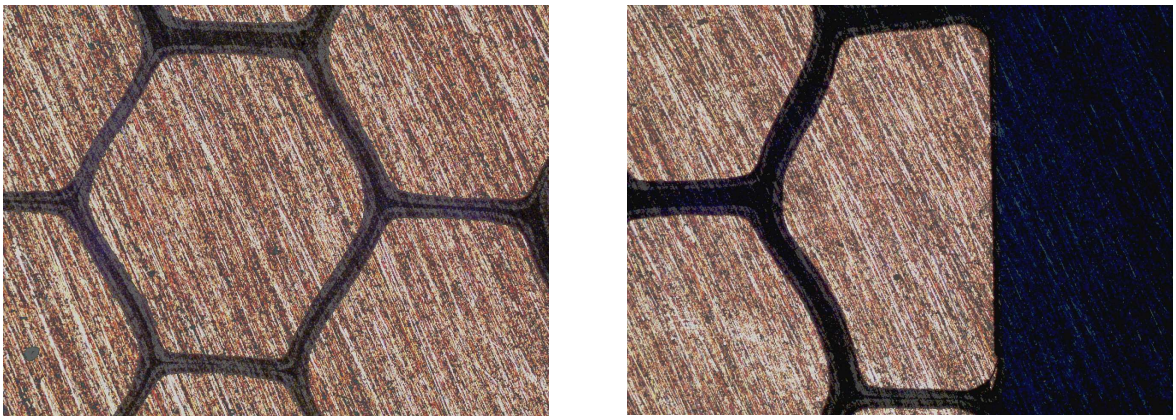

(a) (b)

Fig. 2.3.4-6. Compressed coil cross-sections, (a) typical cross-section, (b) over-deformed.

AC losses in fractional slot concentrated windings operating at high fundamental frequencies are a concern because of the relatively high space harmonic content of the fractional slot concentrated windings. This concern is partially mitigated in wound field synchronous machines because of their variable field excitation, and in this particular prototype because of the use of the star-delta connected dual three phase winding which eliminates some of the space harmonics. An experiment to reduce the AC losses in die compressed stator windings by twisting or transposing the strands in hand similar to Litz wire was attempted.

Twisted strands in hand are easier to wind, as it can be wound in one layer and does not have multiple strands to manage during winding. It also offers potential electromagnetic benefits in terms of reduced AC copper losses at the expense of lower slot fills. A machine was made to wrap wire around itself, shown in Fig. 2.3.4-7(a), and the coil wound on the bobbin shown in Fig. 2.3.4-7(b). Twisted wire coils suffer from having a great many crossovers. Careful control of the compression process and design of the bobbin radii are needed to avoid excessive insulation failures during the compression process.

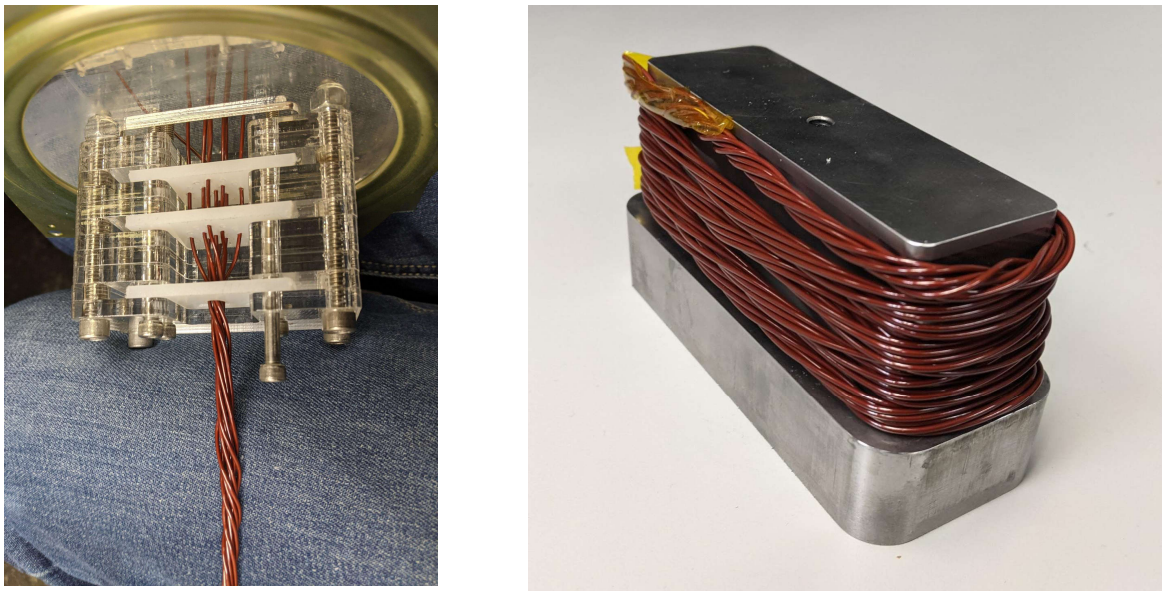

(a) (b)

Fig. 2.3.4-7. (a) wire twisting jig, and twisted wire with fine pitch on bobbin.

To improve the probability of achieving an orthocyclic winding on the bobbin before compression, the tooth tip angle of the stator lamination was been increased to 120 degrees between the tooth side and the slot top (side closer to the airgap). The lamination and bobbin design for the field winding were also suitably modified to improve the probability of achieving an orthocyclic winding. Both the die for the stator and the field winding would require a non-rectangular cavity increasing the difficulty of the machining/wire EDM/sinker EDM. To keep the design simpler, inserts were considered. but they increase the probability of shearing the magnet wire insulation as there will always be some gap between the insert and the side wall of the straight die cavity and the bottom bobbin.

As the die compressed windings are formed as an integral unit, a segmented lamination structure must be used. While segmented laminations are relatively commonly used in the manufacture of servo motors using stamping dies with interlocking features, there is essentially no public information about the tolerances required for assembly if a prototype scale laser cutting and stack bonding manufacturing process is used. In the previous Generation II WFSM prototype with only the field winding die compressed, the assumption was made that the stack up tolerance of the pole tip and rotor lamination yoke were +/-0.003" on each bonded stack. To ensure assembly, a 0.006" gap was specified between each part. While this allowed the poles to be inserted into the yoke with ease it also significantly increases the equivalent airgap reducing the airgap flux density for a given field winding MMF.

Lamination laser cutters will not typically guarantee a stack tolerance and the surface roughness can be substantial. To better determine proper tolerances for slip, press, and shrink fit lamination assembly, a series of positive and negative dovetails into a part to be laser cut was designed. To keep costs reasonable, the part is laser cut as a single piece lamination, stacked, bonded, Fig. 2.3.4-8. Tolerances step between 0.0005" to 0.005" between the positive and negative dovetails. The individual dovetails were then cut from the single stack, Fig. 2.3.4-9.

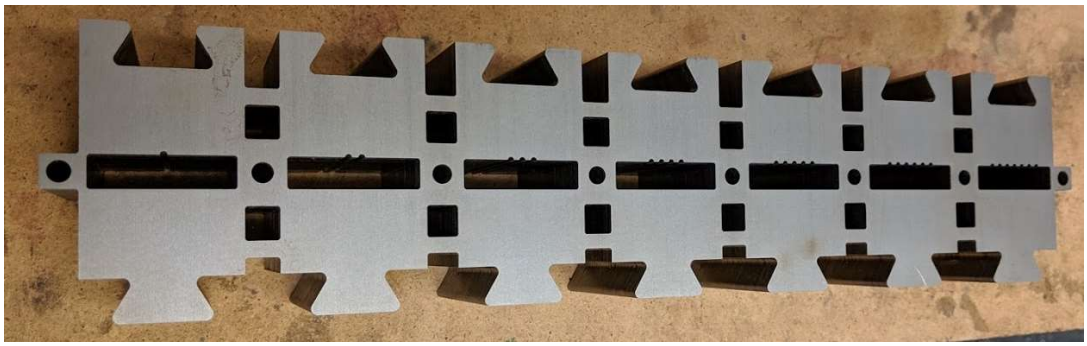

Fig. 2.3.4-8. Laser cut, stacked, and bonded laminations with positive and negative dovetail features with different nominal gap distances.

Fig. 2.3.4-9. Cut apart positive and negative dovetail pieces.

Insertion of the positive dovetails into the corresponding negative dovetails was first tried with both at room temperature. Different temperature differentials were then tried including using oven heating to ~80 Deg. C for the negative dovetails and dry ice and liquid nitrogen for the positive dovetails. The most reliable assembly with the minimum gap was using the oven and liquid nitrogen combination along with pressing. An example of a shrink fit dovetail is shown in Fig. 2.3.4-10.

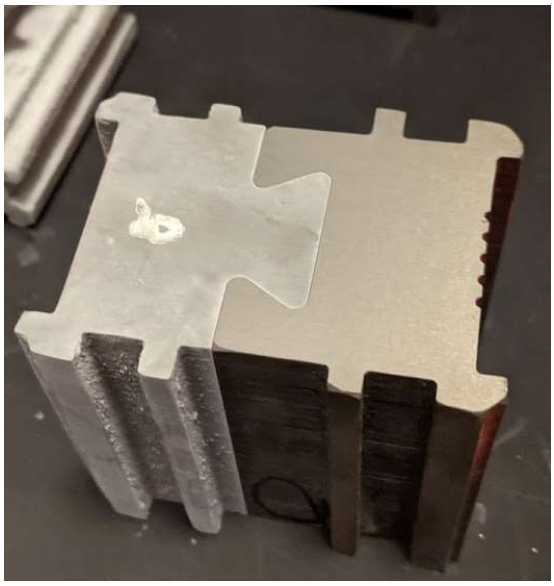

Fig. 2.3.4-10. Representative shrink fit dovetail joint with laser cut, stacked, and bonded laminations.

This did not work very well, as it was not able to generate a sufficient temperature differential to allow a slip fit. Two solutions were tested: Increasing the precision of the dovetail joint, and grinding the joint to fit. EDM machining was tested using a subscale dovetail design cut into the side of one of the prototype dovetails, Fig. 2.3.4-11. It cut well, despite the layers of adhesive holding the stack together, but was not able to be shrink fitted because of the insufficient temperature differential - most shrink fits are affected using high heat that would degrade the adhesive in the lamination. It could, however, be pressed together. The other option was to precisely grind the joints to smooth down the high spots inherent in small-scale prototype laminations, and a machine was built to do this. After a very small amount of grinding, the joints could be assembled using an arbor press and without any loss of lamination layers, Fig. 2.3.4-12. As it avoids the expense and uncertainty (relative to the established laser-cut lamination supply chain) of EDM machining, this technique would be preferential for final assembly of prototype quantities. The precision of stamped laminations should avoid most of the issues associated with segmented laser cut laminations.

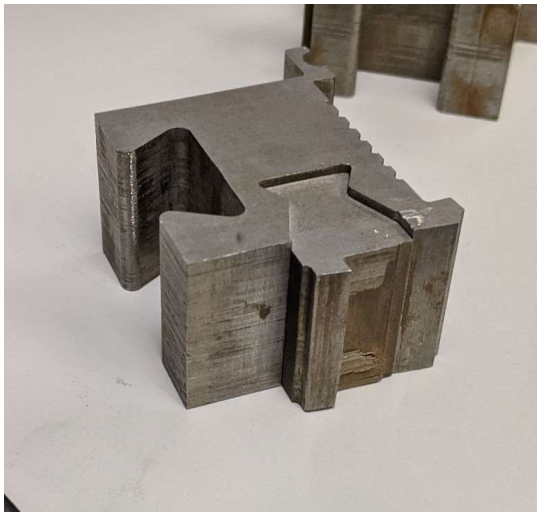

Fig. 2.3.4-11. Trial dovetail wire EDM cut into a bonded lamination stack.

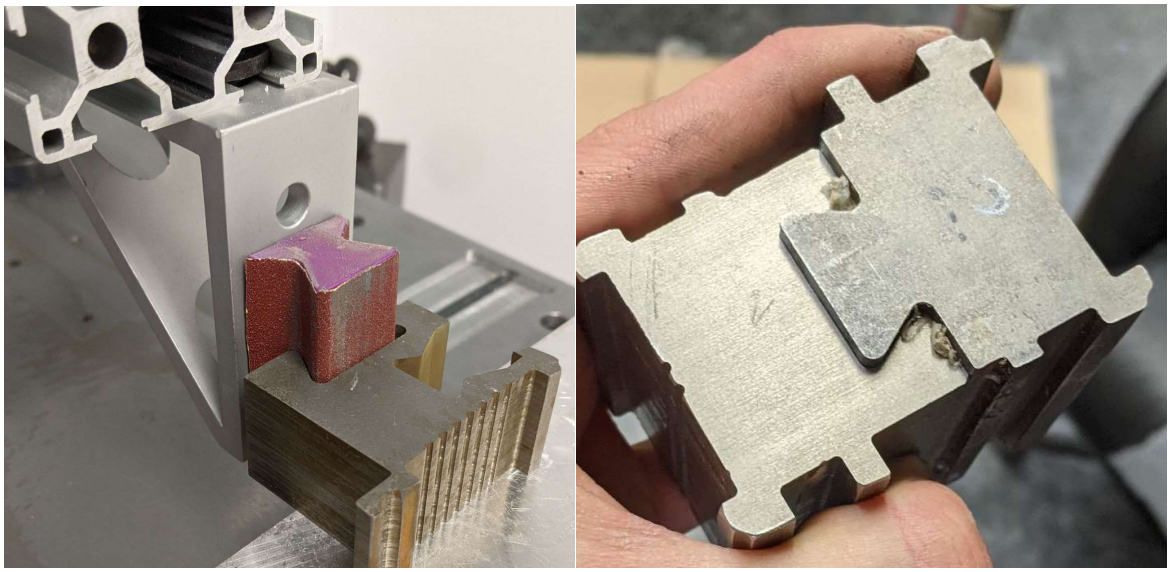

Fig. 2.3.4-12. Portion of reciprocating grinding jib (left) and light press fit of ground joint (right).

2.3.5 12 Slot 10 Pole WFSM Design Modifications

In addition to the small modifications to the stator and field winding slots, further optimization of the field winding for die compression with a non-rectangular shape was carried out. Design studies on the number of turns, different AWG wire sizes, and strands in hand (parallel conductors), were performed assuming that with dual brush packs on the slip rings would allow a maximum of 20 A terminal current to the field winding. A rotor slot area of 158.5 mm^2 was also assumed after modifications to the field slot. The resulting fill factor design space is shown in Fig. 2.3.5-1. Projections along two axes are shown in Fig. 2.3.5-2 and Fig. 2.3.5-3.

Based on the range of anticipated number of turns, wire size, and strands in hand, a die with a non-rectangular cavity was designed. The CAD model of the target coil and die set components is shown in Fig. 2.3.5-4.

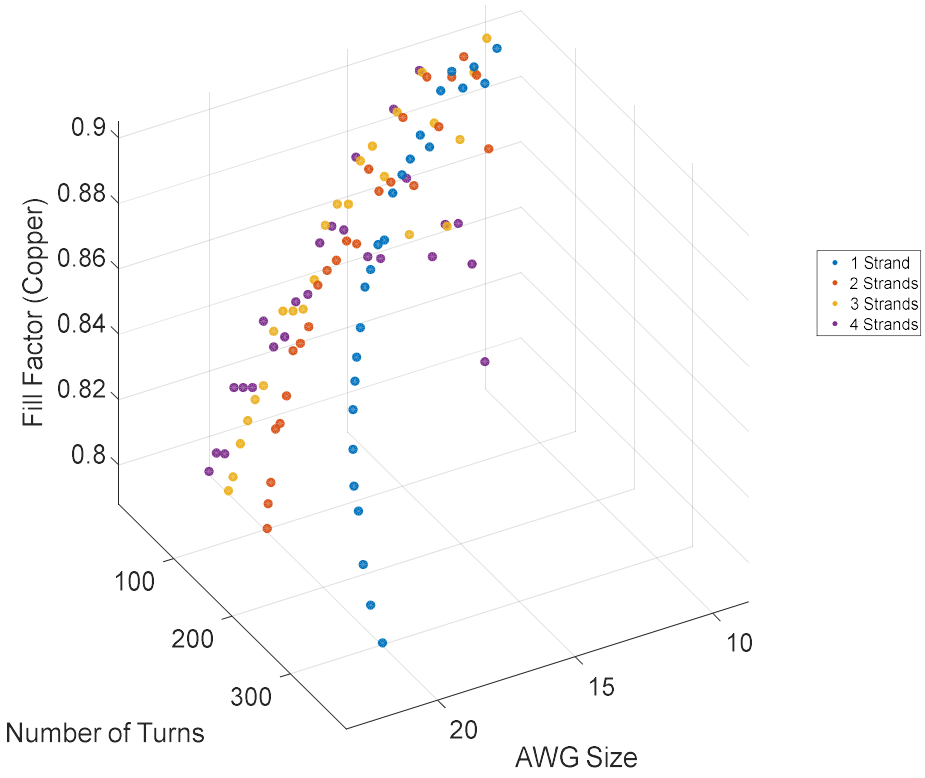

Fig. 2.3.5-1. Estimated die compressed fill factor as a function of the number of turns, AWG wire size, and strands in hand.

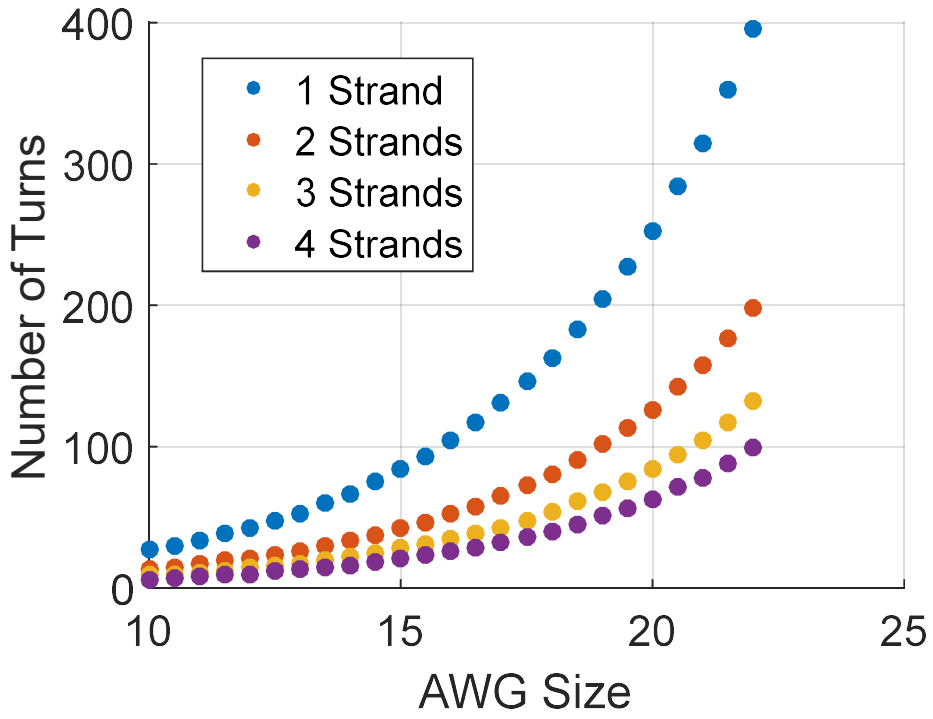

Fig. 2.3.5-2. Projection of Fig. 2.3.5-1 along the fill factor axis.

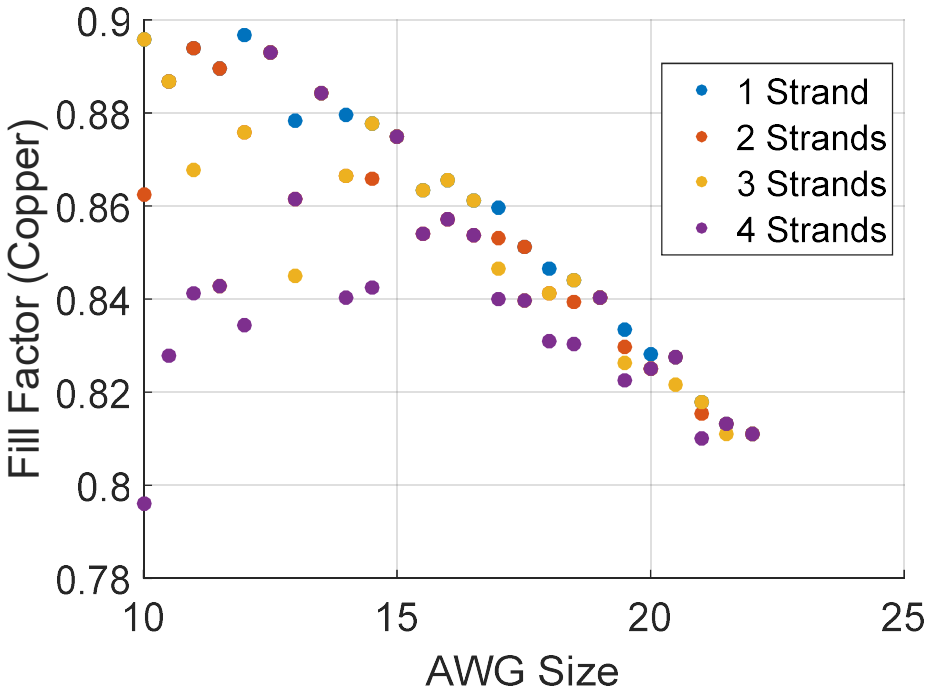

Fig. 2.3.5-3. Projection of Fig. 2.3.5-1 along the number of turns axis.

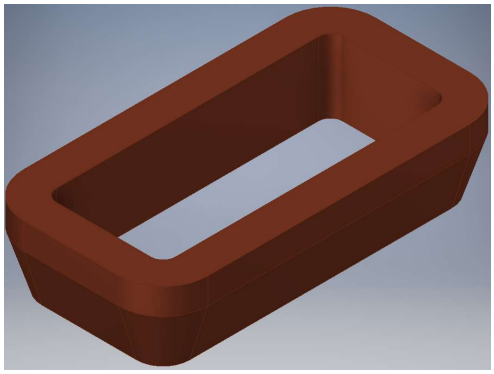

(a) Target field coil

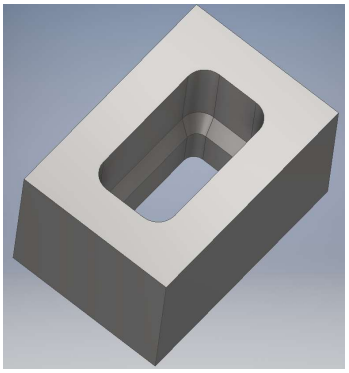

(a) Outer die and cavity

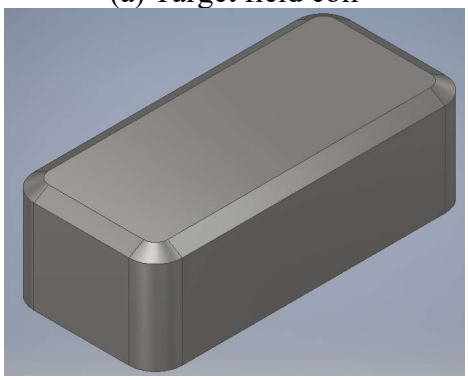

(b) Bottom bobbin

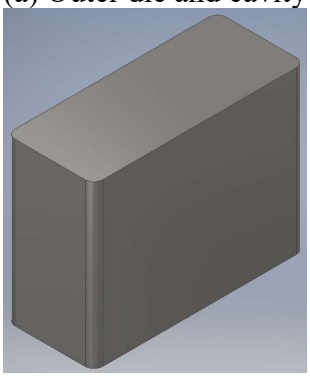

(c) Top bobbin

Fig. 2.3.5-4. Compression die design for rotor field coil.

Performance Mapping of 12 Slot 10 Pole WFSM with Die Compressed Stator and Field Windings after Design Modifications

The actual machine is intended to be operated with a single three phase inverter with a star-delta connection of the winding subsets in each phase. To emulate this, a 6 phase machine model with dual independent 3 phase Y windings with a 30 electrical degree offset between phases was utilized. With the emulated 6 phase machine, a DC link voltage of 300 V corresponds to the three phase machine DC link voltage of 600 V. All the coils in the 6 phase machine model had 8 turns which corresponds to the star portion of the winding in the 3 phase star-delta winding. For the loss calculations, a temperature of 40 Deg. C was assumed for both the stator and rotor windings. Losses that we included in the mapping include DC stator and rotor copper loss and stator iron losses. AC winding and bearing/windage losses were not considered.

The model used for the mapping evaluation, allowed for peak stator currents up to 325 A_{peak} which corresponds to the Semikron drive capability that we have utilized for dynamometer testing. The rotor current was limited to 20 A. This current level will likely require two sets of brushes and slip rings. This rotor excitation level is beyond the current capabilities of the capacitive power coupler. A speed range of 0 RPM to 12,000 RPM with a target base speed of 4,000 RPM was assumed. The predicted performance maps are shown in Fig. 2.3.5-5 to Fig. 2.3.5-14. The predicted performance should easily meet the DOE USDRIVE 2020 targets. The final lamination and die compressed coil designs in the CAD model are shown in Fig. 2.3.5-15

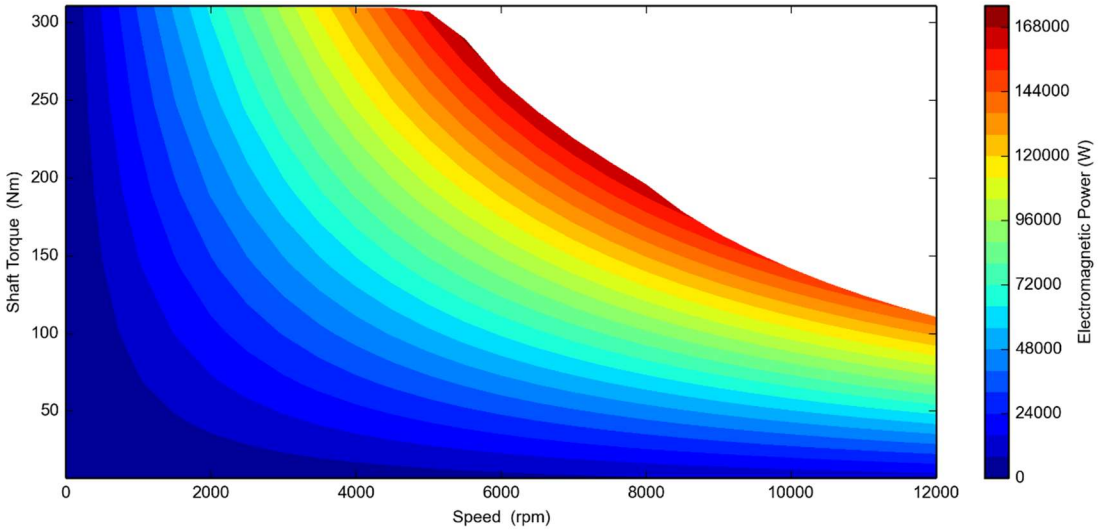

Fig. 2.3.5-5. Predicted final WFSM prototype electromagnetic power map.

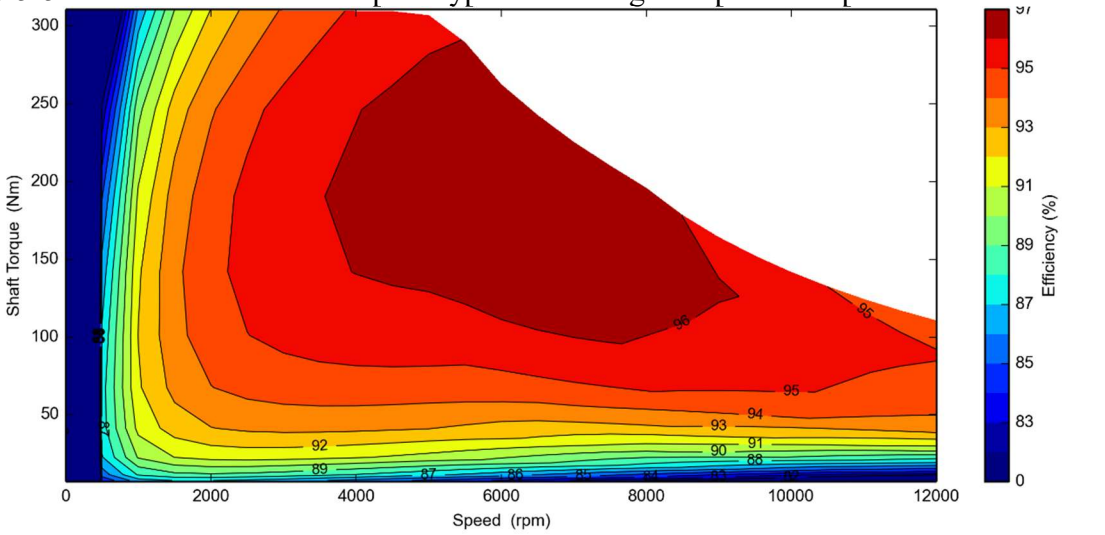

Fig. 2.3.5-6. Predicted final WFSM prototype efficiency map.

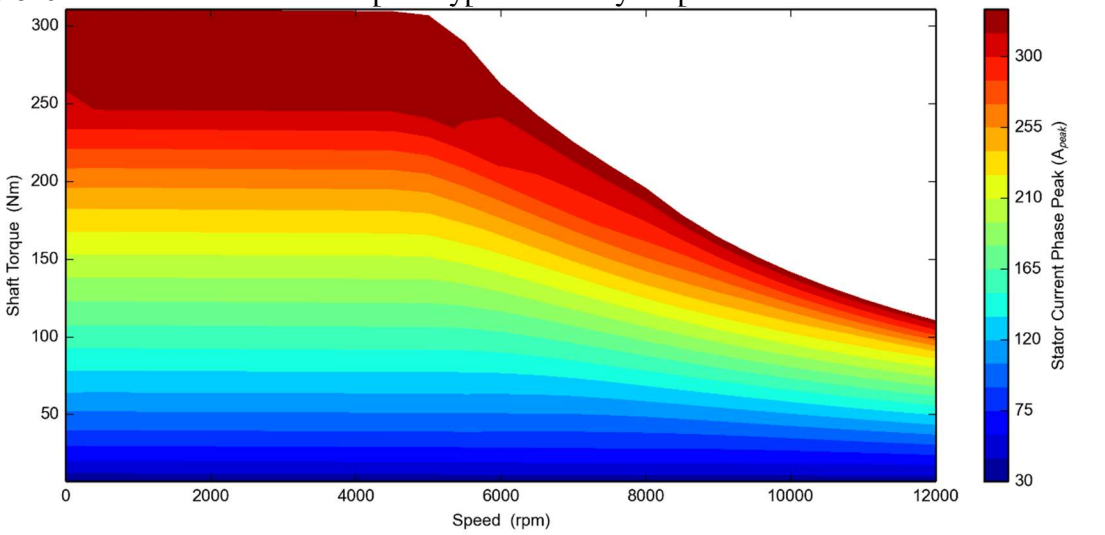

Fig. 2.3.5-7. Predicted final WFSM prototype peak stator phase current.

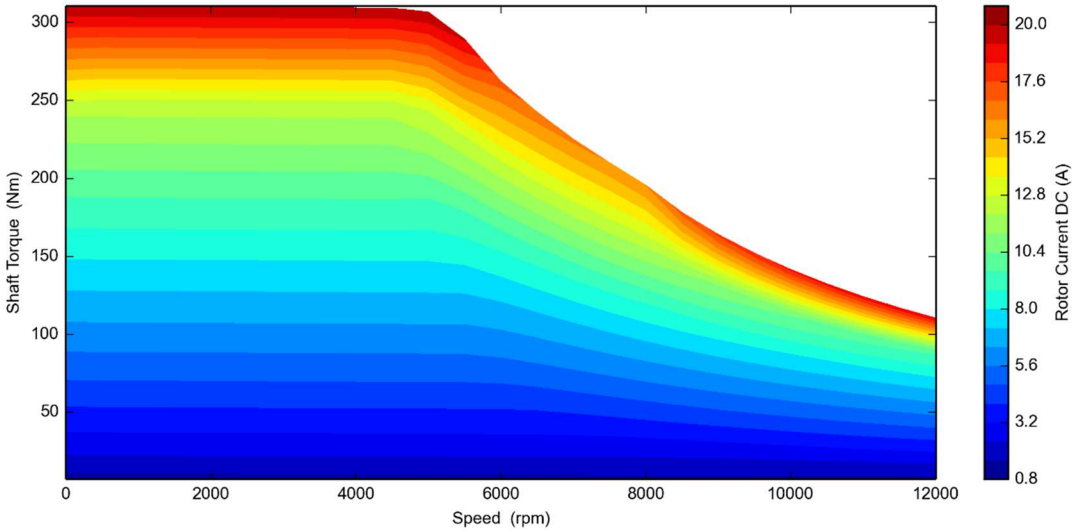

Fig. 2.3.5-8. Predicted final WFSM prototype rotor current.

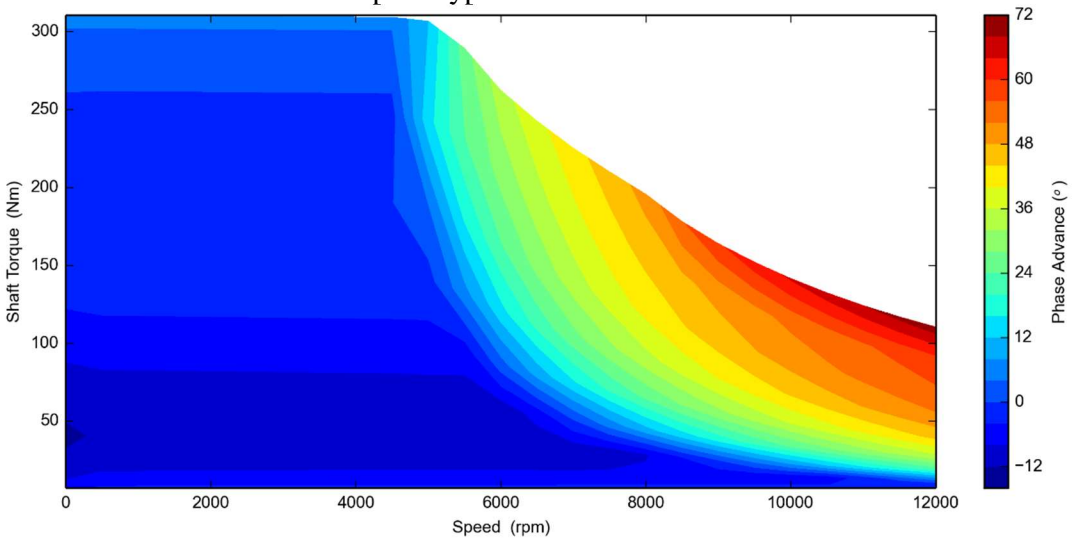

Fig. 2.3.5-9. Predicted final WFSM prototype rotor phase advance. Note 15º initial shift.

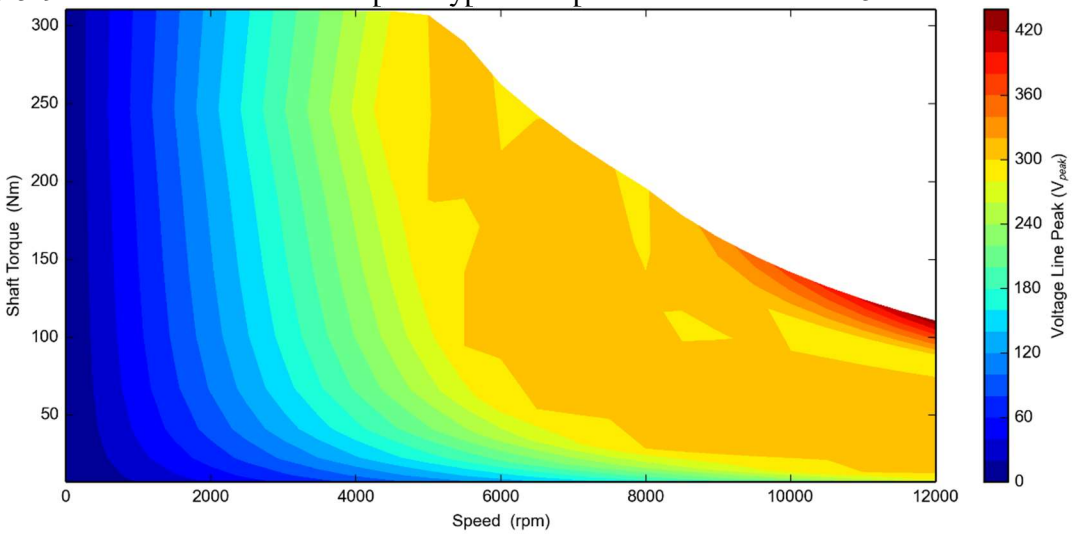

Fig. 2.3.5-10. Predicted final WFSM prototype peak line to line voltage.

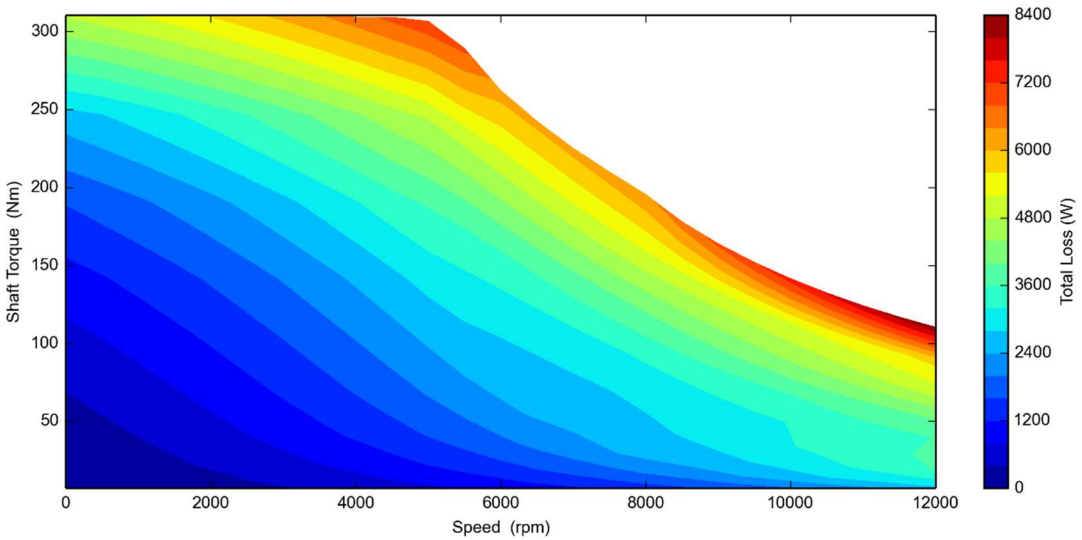

Fig. 2.3.5-11. Predicted final WFSM prototype total loss.

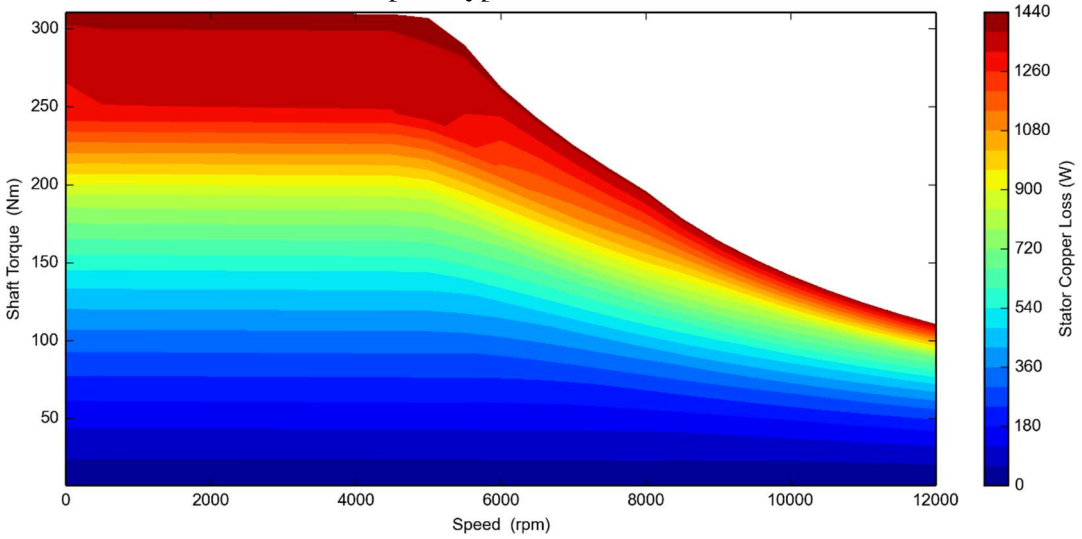

Fig. 2.3.5-12. Predicted final WFSM prototype stator copper loss.

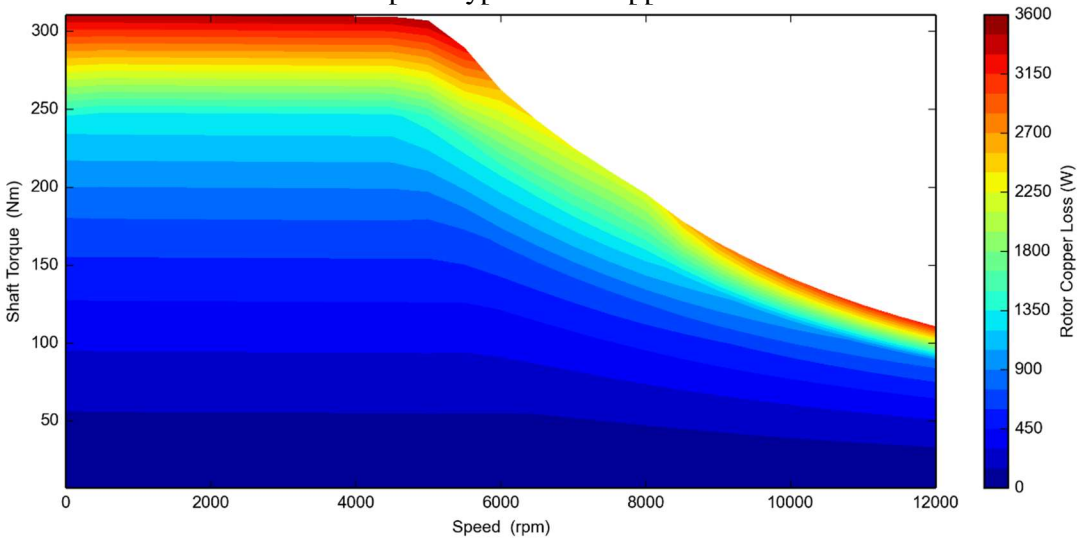

Fig. 2.3.5-13. Predicted final WFSM prototype rotor copper loss.

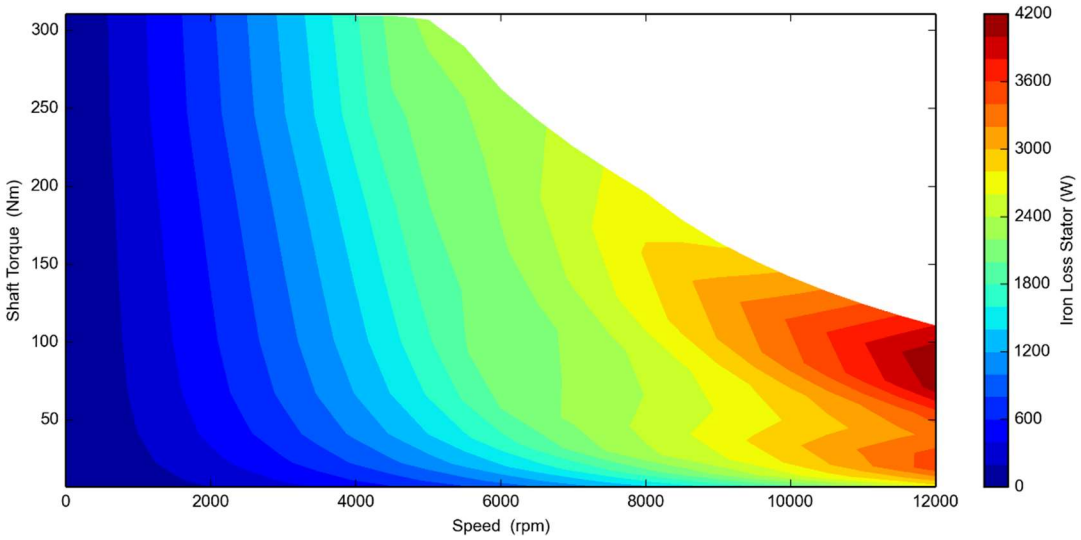

Fig. 2.3.5-14. Predicted final WFSM prototype stator iron loss.

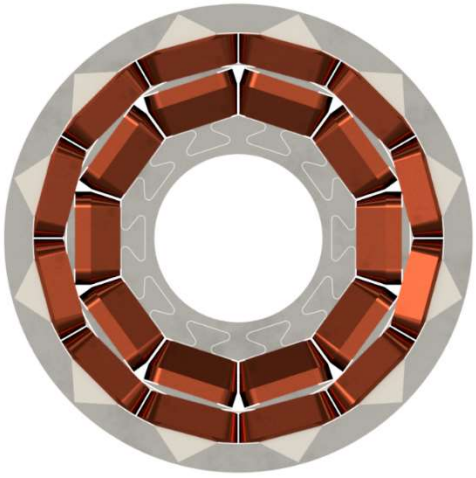
Fig. 2.3.5-15. Final lamination and die compressed coil design for 12 slot 10 pole WFSM.

2.3.6 Design of a WFSM with Distributed Hairpin Stator and Die Compressed Field Winding

A generation III WFSM with a distributed hairpin stator winding was designed as an alternative to the 12 slot 10 pole WFSM machine with the die compressed stator and field windings. Previous WFSM optimizations have been carried out for distributed hairpin winding topologies in subsection 2.3.6 for the peak operating point. The previous WFSM optimizations with distributed hairpin windings did not restrict the hairpin conductor dimensions to a commercially available rectangular magnet wire. It is difficult and expensive to prototype a hairpin winding stator in an academic setting. For this reason, an off the shelf stator with hairpin windings was utilized, specifically the stator from a General Motors Chevy Volt Generation 1 B Motor, as shown in Fig. 2.3.6-1. This is a 72-slot 12-pole design with 4 hairpin conductors per slot. The number of stator poles is larger than ideal for a high speed, high power density machine as the electrical frequency will be high, increasing the iron losses and control difficulties. The stator's large inner diameter

also limits the maximum speed of the rotor lower than would be perhaps chosen otherwise. More modern hairpin winding designs also typically use 6 or 8 conductors per slot compared to the 4 conductors in the stator that was used. The increase in the number of conductors per slot can significantly reduce AC copper loss in the stator. The stator laminations are shrunk fit into a steel sleeve with mounting tabs. The sleeve likely increases the iron losses in the stator laminations because of the increased compressive stress in the laminations. The steel sleeve with the tabs also presents some challenges for mechanical integration into the overall housing. The measured outer diameter of the steel shell is not sufficiently consistent along the axis of the machine to easily use a machined outer cylindrical housing. The tabs also present challenges for designing a motor housing. A stator without the sleeve would have been preferred.

Fig. 2.3.6-1. GM Chevy Volt Gen 1 motor B stator.

In previous WFSM distributed hairpin winding optimizations, the rotor was assumed to be essentially the same as the generation II rectangular die compressed winding and rotor lamination. For the generation III WFSM, the rotor is still a salient pole wound field rotor configuration that is electrically excited and free of PM materials. For an optimum design, the magneto-motive force (MMF) of the field winding at the rated operating point must be equal to or exceed the MMF per pole of the stator winding. Given the smaller diameter of the field winding compared to the stator winding, the slot area available is smaller necessitating a high slot fill. The number of turns per pole of the field winding must also be high for a reasonable terminal current, and compatibility with slip ring, inductive, or capacitive field supplies. In this generation III machine, the rotor lamination was designed to be flexible in terms of the high slot fill field winding technology used. The rotor lamination was segmented to enable the use of a die compressed, bobbin wound square magnet wire, or twisted square magnet wire field winding. The field winding window in the lamination is non-rectangular to maximize the field winding conductor cross-section area in the overall available rotor area. Two final prototype rotors were constructed with the bobbin wound square magnet wire and the twisted square magnet wire field windings. A non-rectangular die for a die compressed version was manufactured but because of the project timeline it was decided to use the two square magnet wire field winding versions for the final prototype as their technology readiness is significantly higher.

Initial Electromagnetic Design

The prototype WFSM is designed and optimized using a metamodel-based approach to maximize its efficiency over a custom set of five load points, Table 2.3.6-1, while utilizing a fully per-unitized geometric template, Fig. 2.3.6-2. The design that was prototyped was selected from a large set of designs generated during sensitivity studies and during optimizations. The predicted peak power density of the down-selected design is listed in Table 2.3.6-3.

The overall objective of the design optimization presented here is to maximize the volumetric power density and efficiency of a WFSM prototype which will be constructed. The dynamometer available for testing, fixes several aspects of the design. To stay within the absolute peak torque and power capability of the dynamometer, a peak power output of 190 kW and corner speed of 4,000 RPM were selected. A 3:1 constant power speed field weakening range for a maximum speed of 12,000 RPM is also desired. To match the available absorber DC voltage supply interface, a prototype machine drive DC link voltage of 600 V is used. The prototype drive (Semikron inverter) peak output current is also limited to less than 325 A_{peak}. From the open literature, the peak current of the GM Chevy Volt Gen 1 motor B when used with the vehicle cooling system and drive in the Volt automobile is 608 A_{peak}. Because of this, the generation III WFSM prototype machine could not be dynamometer tested to its full predicted peak power capability. However, the predicted performance of the prototype at other operating points can be compared and correlated to dynamometer measurements to lend evidence to the accuracy of the predicted performance.

The load points listed in Table 2.3.6-1 were selected to ensure that the generation III WFSM prototype is able to reach likely desired operating points without violating terminal voltage or current constraints. An overall weighted efficiency for a particular design is found by weighting the contribution of the efficiency at each load point. Load points 1 and 2 represent the required 55 kW continuous power output required of this project. Load point 3 is a low speed moderate torque 25 kW operating point. Lead point 4 is the peak output operating point with a target power output of 190 kW. To ensure a constant speed range of 3:1 for the peak power output, load point 5 also has a target output power of 190 kW. With a 600 V DC link input, the base speed could be increased to 6,000 RPM, which for the same target torque of 454 Nm, corresponds to an output power of 285 kW. The constant power speed range however would need to be limited to 2:1, keeping the maximum operational speed at 12,000 RPM for structural reasons.

The optimization objectives and constraints are listed in Table 2.3.6-2. The objective of the optimization is to maximize the weighted efficiency of all five load points. Except the field power constraint at load point 1, all other constraints are on the maximum or minimum values of all the five load points, as listed in Table 2.3.6-1. The field power at load point 1 was constrained to be less than 750 W to ensure operation with the capacitive power transfer system for the 55 kW power output point. The peak voltage constraint is to ensure the required voltage can be supplied with the 600 V DC bus voltage combined with a 0.94 maximum modulation index. The 0.985 p.u. threshold for the output torque is used to check if a design can deliver the required amount of torque across all load points. It is intentionally made to be slightly less than 1 p.u. due to the iterative nature of the load point calculation and it is not very likely to be exactly at 1 p.u. or above each time.

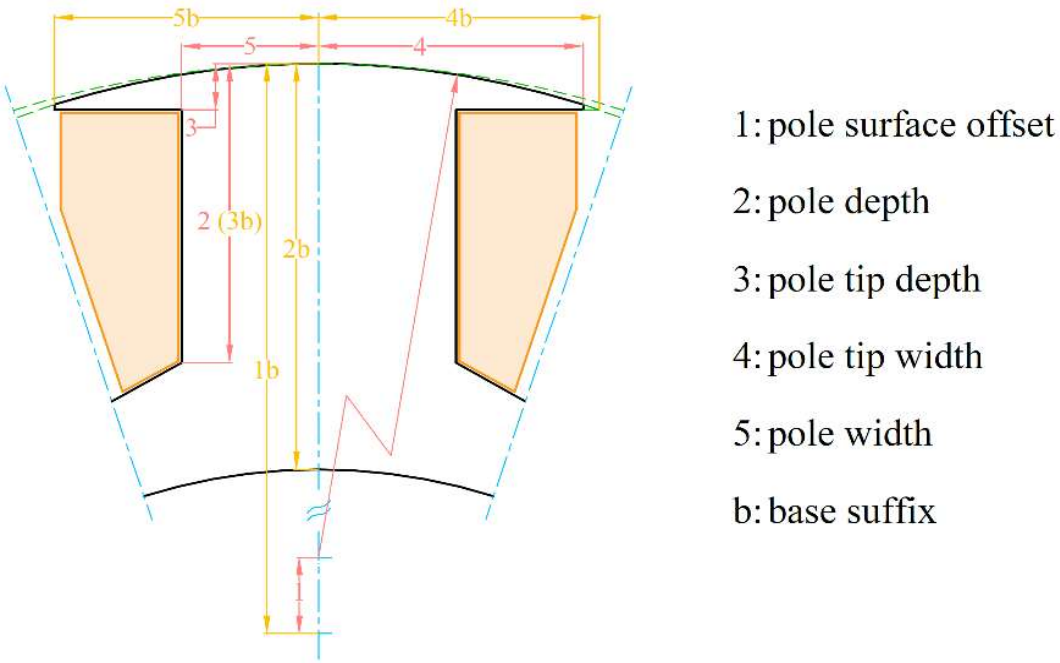

Fig. 2.3.6-2. Parametric rotor geometry for generation III WFSM optimization.

TABLE 2.3.6-1. GENERATION III WFSM OPTIMIZATION LOAD POINTS

Operating Points	Speed (RPM)	Torque (Nm)	Output Power (kW)	DC Link Voltage (Vdc)
1	4,000	131.3	55	600
2	8,000	65.65	55	600
3	2,000	119.4	25	600
4	4,000	453.59	190	600
5	12,000	151.2	190	600

TABLE 2.3.6-2. OPTIMIZATION OBJECTIVES AND CONSTRAINTS

Quantity	Type	Expression
Weighted Efficiency	Objective	Maximize
Torque at all Load Points (p.u.)	Constraint	≥ 0.985
Peak Voltage at all Load Points (p.u.)	Constraint	≤ 0.94
Stator Current Density at all Load Points (A_{rms}/mm^2)	Constraint	≤ 25
Field Current Density at all Load Points (A_{rms}/mm^2)	Constraint	≤ 20
Field Power (W), at LP1	Constraint	≤ 750
Field Power at all Load Points (W)	Constraint	≤ 3500
Torque Ripple at all Load Points (pk2pk, %)	Constraint	≤ 10

TABLE 2.3.6-3. PREDICTED PEAK VOLUMETRIC POWER DENSITIES

	4000 RPM Base Speed	6000 RPM Base Speed
Active Material Volume	37.7 kW/l	57.6 kW/l
Volume Including End Turns	24.0 kW/l	36 kW/l

Because of the variable field excitation and finite element analysis predicted performance at multiple load points, a metamodeling based optimization process was developed versus using a direct optimization process. A direct optimization, like was used for the generation I and generation II prototype designs, would be too computationally expensive as thousands of designs would typically need to be evaluated. A metamodeling based approach instead, samples the design space during a sensitivity study phase to create response surfaces of output variables as a function of input variables. A representative metamodel for the overall weighted efficiency output is shown in Fig. 2.3.6-3. A comparison of the metamodel predicted and finite element predicted overall weighted efficiency for sample designs is shown in Fig. 2.3.6-4.

Instead of directly solving finite element models for each design that the optimization algorithm evaluates, the metamodel is instead evaluated. This approach can be orders of magnitude more computationally efficient. Additionally, the optimization objectives and constraints can be changed and the optimization rerun without having to regenerate the metamodel.

The metamodel optimization process begins with a sensitivity analysis. Sample designs with input parameters set to explore the design space are evaluated through finite element simulations. Metamodels are formed which best predict the output variable behavior. The optimization algorithm then evaluates potential designs using the metamodel. Down-selected optimization designs are then verified through finite element analysis. The overall process chain is shown in Fig. 2.3.6-5.

For the metamodeling based optimization, a combination of ANSYS optiSLang and Motor-CAD were used. An extensive Python script is called by optiSLang to control Motor-CAD to perform finite element analysis of a design at each load point with iterations to ensure that the load points can be reached, Fig. 2.3.6-5 and Fig. 2.3.6-6. Each sample design during the sensitivity analysis stage and the best designs picked for validation at the final stage, will go through a sequence of operations that are controlled by a Python script. The electromagnetic calculations performed in Motor-CAD are an iterative chain of load point prediction and finite element verification in accordance with the exact torque demand and voltage limit, followed by AC loss calculations and corrections. Multiple Python and Motor-CAD instances can be run in parallel.

For the metamodeling optimization, the field slot fill in the achievable winding window was assumed to be 70% as a realistic target compromise among the potential winding techniques (die compression, bobbin wound square magnet wire, twisted square magnet wire). This assumed slot fill is based on previous experience with die compressed windings.

A design from the sensitivity samples was selected as the design for prototyping. The cross-section of the initial rotor design is shown in Fig. 2.3.6-6.

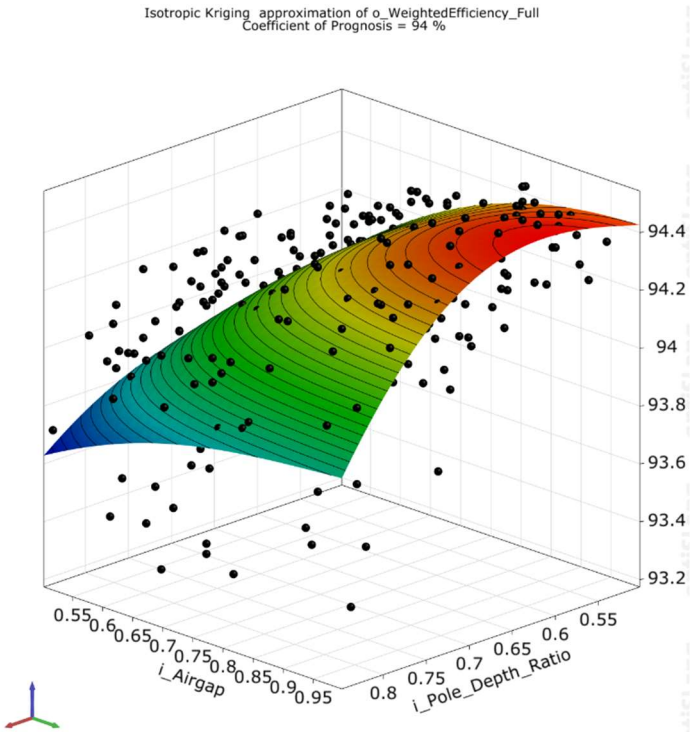

Fig. 2.3.6-3. Representative metamodel surface of the overall weighted efficiency as a function of the airgap and pole depth ratio, while other all other input design variables are held at their mid-point values. Sample sensitivity designs are indicated by the black dots.

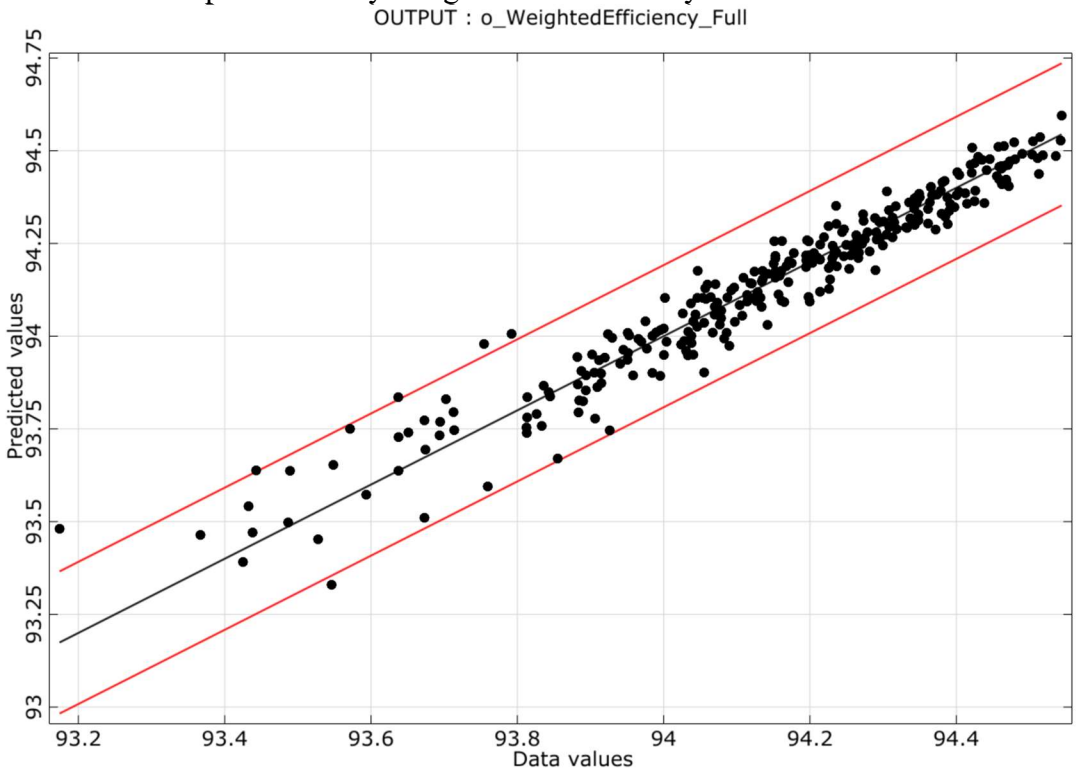

Fig. 2.3.6-4. Representative comparison of the metamodel predicted and the finite element simulated overall weighted efficiency.

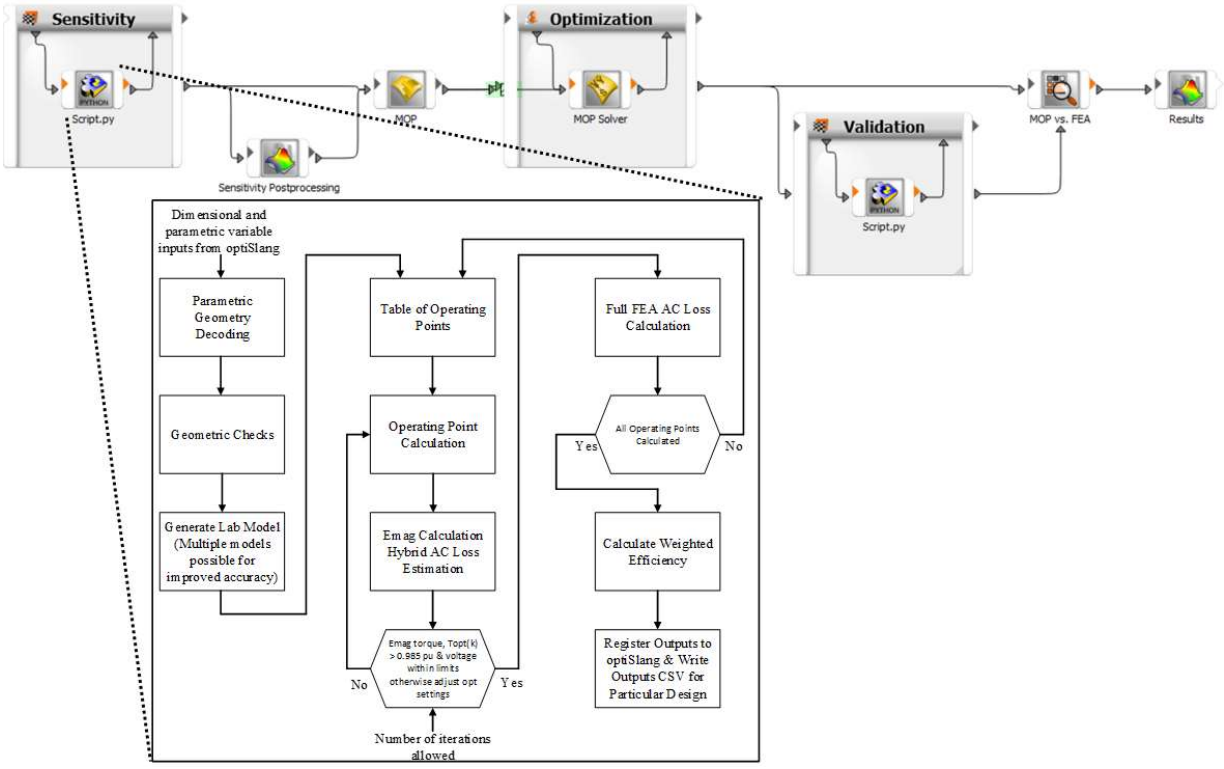

Fig. 2.3.6-5. Representative metamodeling optimization process.

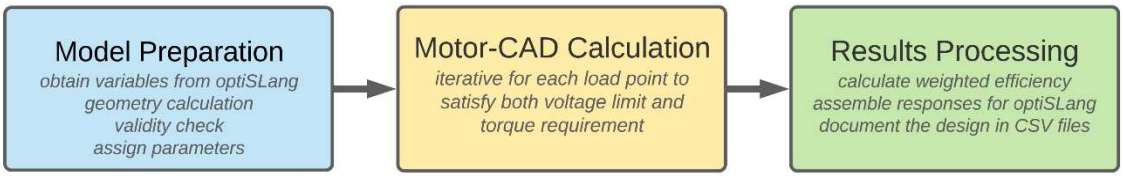

Fig. 2.3.6-6. Communications, calculations, and results processing performed by the Python script.

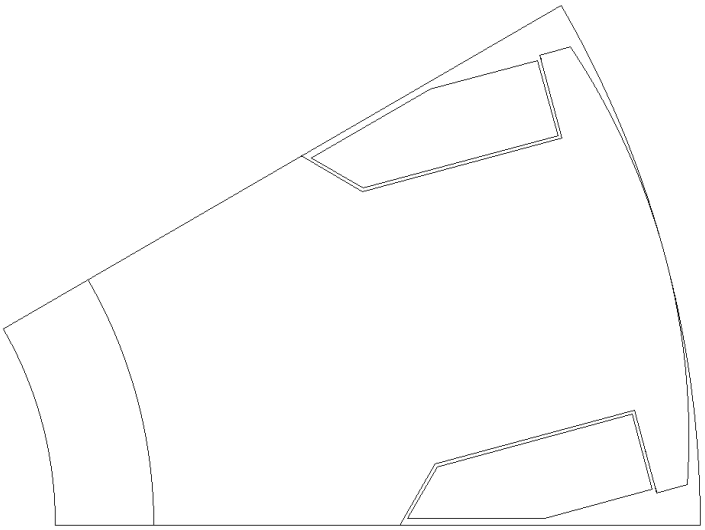

Fig. 2.3.6-6. Initial rotor design from metamodeling optimization.

Structural Refinement of Pole Tip and Dovetail Optimization

The motor is designed to operate at up to 12,000 RPM, and should therefore survive an overspeed up to 14,400 RPM. Multiple iterations of structural and electromagnetic finite element analysis were performed to optimize the pole tip thickness and fillet between the pole tip and pole neck. In the end the pole tip thickness was increased slightly and a small fillet was added between the pole tip and pole neck to reduce the stress concentration there. The fillet is small enough to only remove one turn's worth of cross-section from the field winding. A representative ANSYS Mechanical simulation from the structural refinement process is shown in Fig. 2.3.6-7.

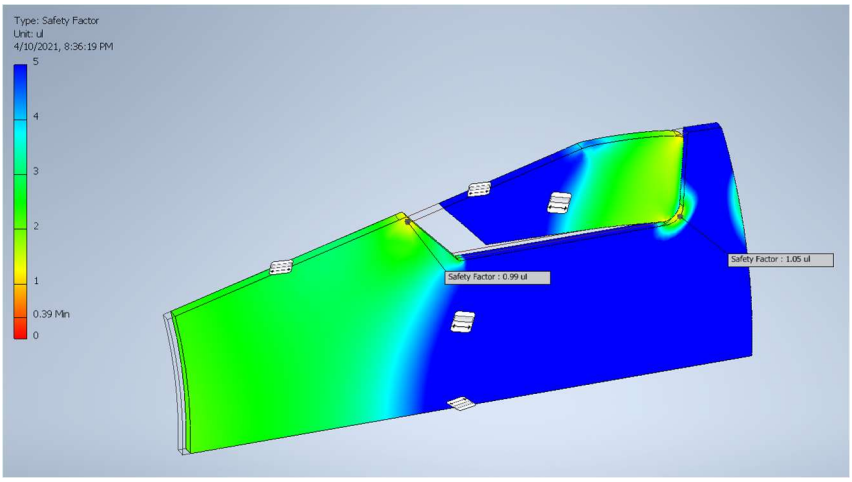

Fig. 2.3.6-7. ANSYS Mechanical structural simulation of WFSM design at 14,400 RPM.

Both the bobbin wound square magnet wire and die compressed coil windings require a joint be put into the lamination. Die compressed coils must be physically assembled onto the machine as solid units, and so cannot fit over a pole tip. Bobbin wound square magnet wire windings must be wound very precisely, and the complexity involved in winding so precisely on a solid rotor would be prohibitive. A joint must therefore be designed capable of withstanding the very high rotational speeds involved. If the pole with the field winding is to be inserted into the yoke the bottom of the field winding must clear the yoke. Because of this, the field winding slot bottom angle was adjusted from 120 Deg. to 90 Deg. and the total field slot areas made to be approximately equal. After the structural revisions, the initial winding layout of the field turns was completed before to roughly estimating the number of field turns and the field winding terminal current, Fig. 2.3.6-8.

Once the slot geometry was finalized, it became possible to run an evolutionary optimization in ANSYS to find the ideal dovetail geometry, varying the tip width, side angle, overall length, and tip and root radii, Fig. 2.3.6-9. In the dovetail optimization, the winding region was represented by a material with density equivalent to 70% that of copper to model the expected packing density. Because the winding turns are not a solid body and the mechanical properties of the impregnation varnish are unknown, a very low elastic modulus was used to allow the level of bulk deformation expected in a coil. To aid convergence, all dovetail joint contacts were frictional contacts preloaded by overlapping the faces 0.01mm.

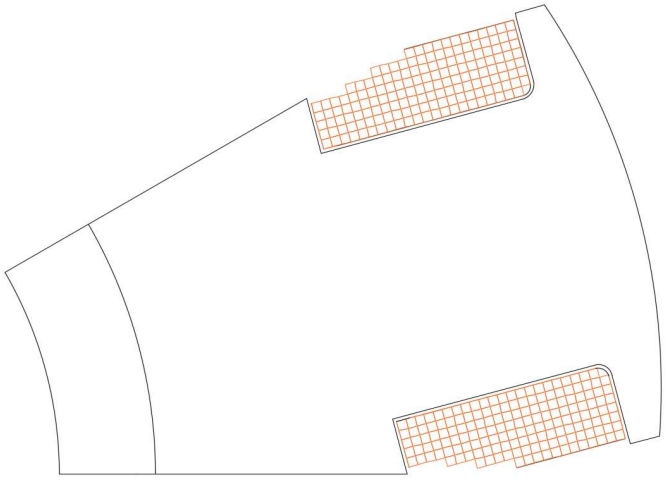

(a)

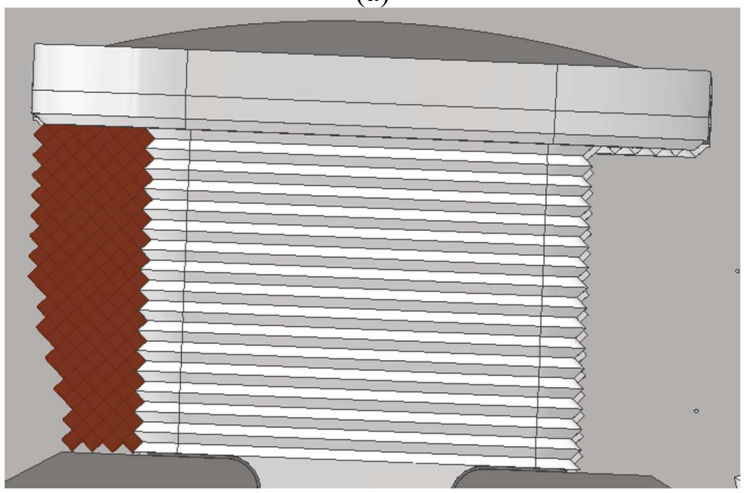

(b)

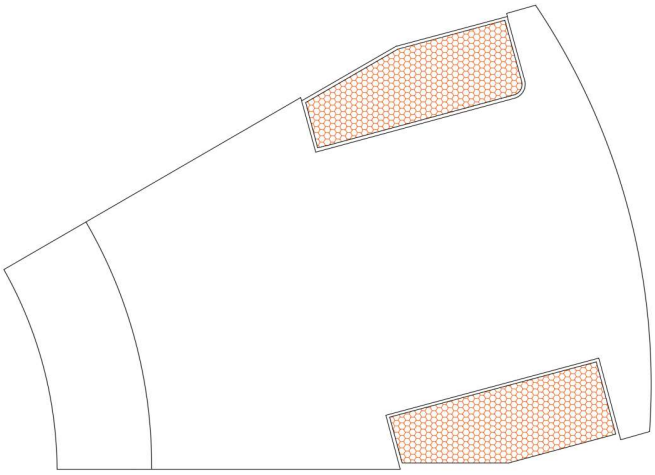

(c)

Fig. 2.3.6-8. Initial field winding turn layouts for (a) bobbin wound square magnet wire, (b) twisted square magnet wire, (c) die compressed.

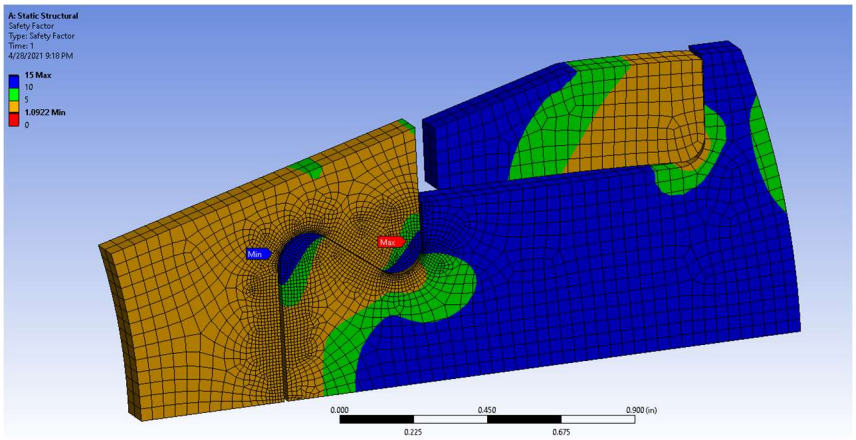

Fig. 2.3.6-9. Dovetail joint structural optimization in ANSYS.

Predicted Performance of the Generation III WFSM Prototype Design

The refined generation III WFSM design was re-simulated at the five load points to predict the prototype performance, Table 2.3.6-4. The losses and efficiency of the design are estimated based on assumed 120 Deg. C winding temperatures, two times iron loss build factors, and full FEA evaluation of the stator AC copper loss. The current densities in the stator and field are reasonable for the planned ATF spray cooling. The predicted efficiency map of the prototype design is shown in Fig. 2.3.6-10. The AC loss in the predicted efficiency map may be overestimated, as it uses a hybrid FEA technique versus a full FEA evaluation as was used for the load point calculations. The power factor of the design can also be maintained at close to unity over the majority of the operating space, Fig. 2.3.6-11.

TABLE 2.3.6-4. PREDICTED PERFORMANCE OF GENERATION III WFSM WITH BOBBIN WOUND SQUARE MAGNET WIRE FIELD WINDING

Load Point	Speed (RPM)	Torque (Nm)	Torque Ripple (pk2pk %)	I_s (A_{peak})	J_s (A_{rms}/mm^2)	I_f (A_{dc})	J_f (A_{rms}/mm^2)	Power Factor	Eff*, **, *** (%)	Total Loss*, **, *** (W)
1	4000	131.65	6.83	205.48	8.26	6.07	7.62	0.97	95.26	2741
2	8000	65.38	5.08	144.27	5.80	4.00	5.02	1.00	95.59	2525
3	2000	119.68	6.72	190.28	7.65	5.66	7.10	0.95	93.85	1642
4	4000	454.34	0.55	608.00	24.44	13.00	15.67	0.98	93.59	13,035
5	12000	151.27	6.83	412.82	16.60	5.97	7.20	0.99	94.66	10,722

*Winding temperatures of 120 Cº assumed; ATF spray cooling of end turns
**AC losses in stator conductors included through full FEA evaluation of conductors
*** 2 x iron loss build factor included
**** Stator with 6 or 8 conductors would significantly improve efficiency at high speed

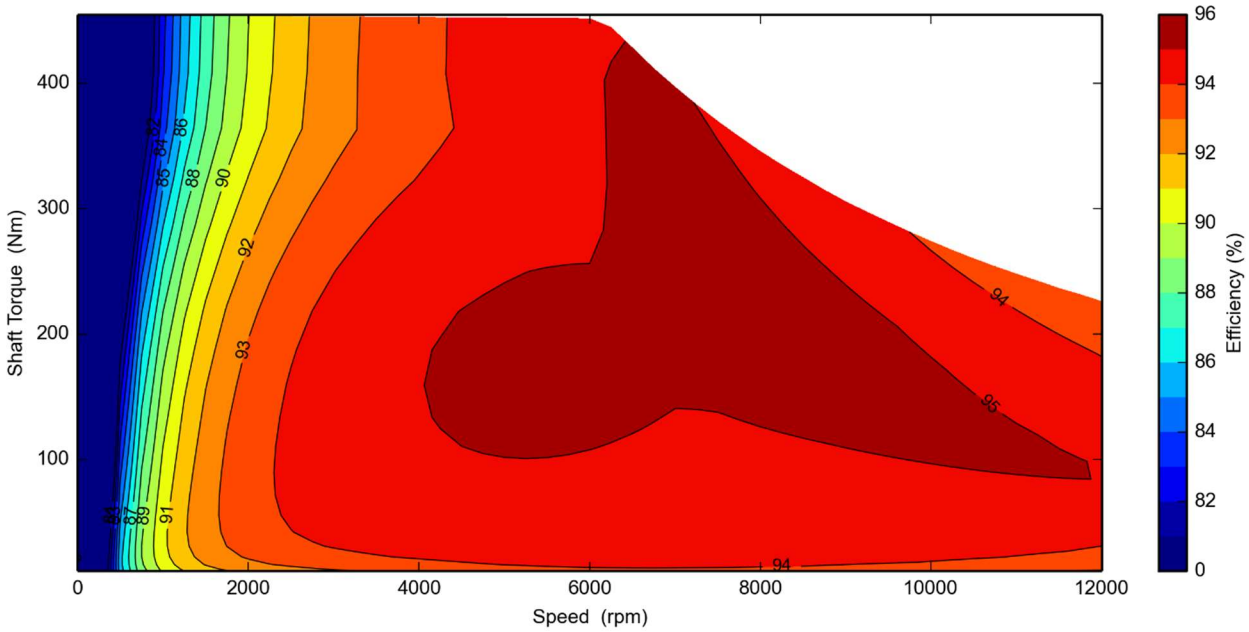

Fig. 2.3.6-10. Predicted efficiency map of generation III WFSM prototype with bobbin wound square conductor field winding with V_{dc} = 600 V and $I_{s\text{-}max}$ = 608 A_{peak}.

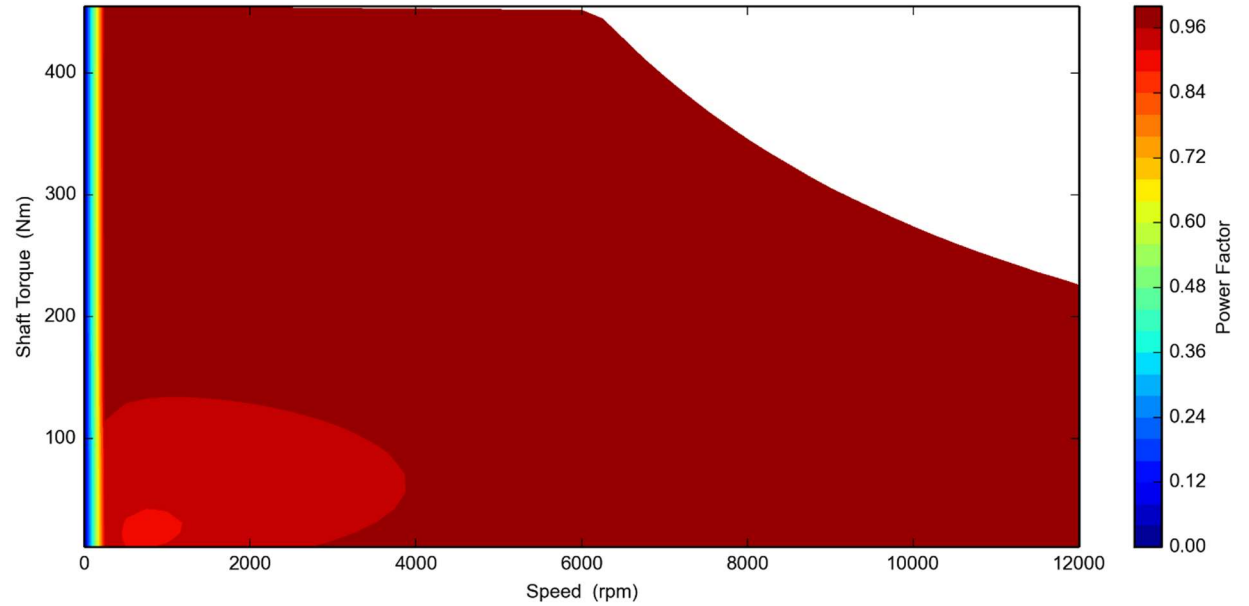

Fig. 2.3.6-11. Predicted power factor map of generation III WFSM prototype with bobbin wound square conductor field winding with V_{dc} = 600 V and $I_{s\text{-}max}$ = 608 A_{peak}.

2.3.7 Construction of WFSM Prototypes with Distributed Hairpin Stator and Bobbin Wound Square Magnet Wire Field Winding

Overall Mechanical Design of the Generation III WFSM Prototype

As described previously, the steel sleeve with tabs that is shrunk over the stator laminations poses challenges for the design of housing for the prototype generation III WFSM prototype. To accommodate the sleeve tabs and accurately locate the shaft along the centerline of the stator bore, a non-standard box/cubic housing structure was designed and manufactured. The box/cubic structure is cost effective and enabled in-house production of many of the housing components. The overall design of the housing can be seen in Fig. 2.3.7-1 in a half section view, with the drive end side to the right of the figure. A quarter section view from the non-drive end is shown in Fig. 2.3.7-2.

A large end bell located the stator sleeve tabs, relative to the front bearing bore on the drive end side, Fig. 2.3.7-3. The stator sleeve tabs are also used to transmit the reaction torque to the housing. The rear end bell bearing bore is located by precision alignment of the four plates between the two end bells. The housing is designed with a flexible spray cooling system to direct jets of ATF at both the stator and field windings. The spray plates have been designed such that they can be changed without having to disassemble the housing. The terminal box is also spray cooled to allow for testing with very high terminal currents. The white terminal box design also allows for two terminals to be mounted to reach higher terminal currents than the single terminal is rated (single terminal rating ~200 Arms continuous). The Chevy Volt Gen 1 motor B stator has been installed in the housing and aligned to within 0.001 inches, shown in Fig. 2.3.7-4. A wireless borescope was also installed to be able to partially observe the ATF spray during operation.

The shaft for this prototype, Fig. 2.3.7-5, is over designed and its weight could be considerably lessened, but it was relatively easy to manufacture. The shaft allows for interchange of different rotors, e.g. the bobbin wound square magnet wire rotor with the twisted square magnet wire version. The non-drive end of the shaft allows for the field terminal leads to be brought out to connect to brushes and slip rings.

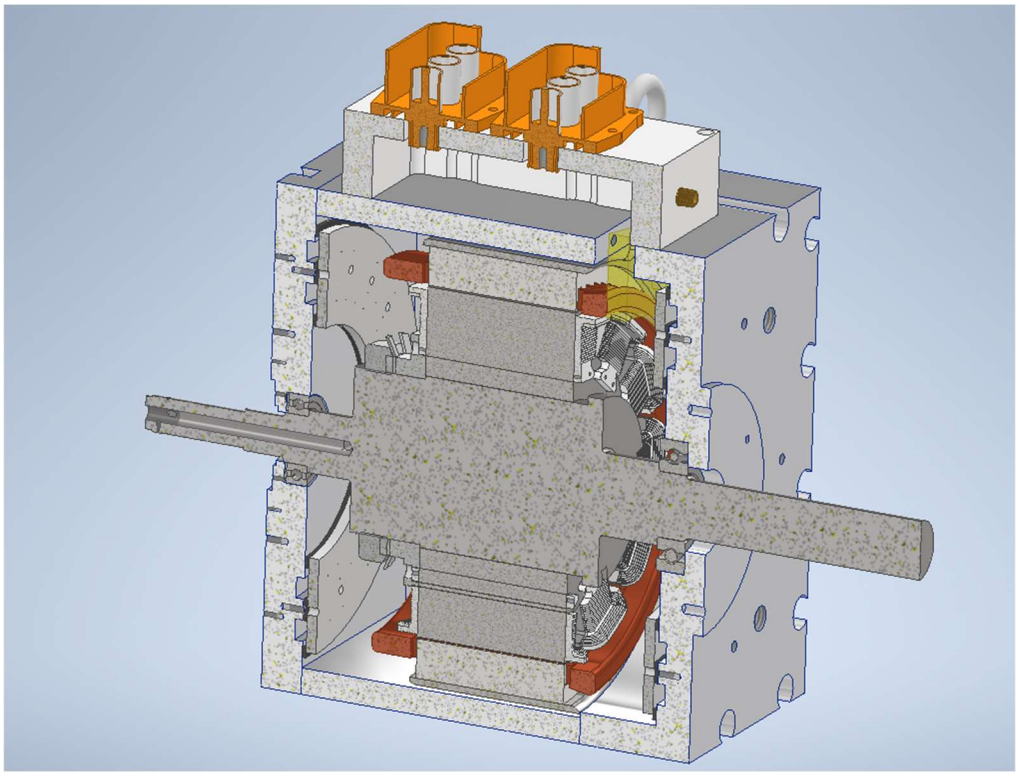

Fig. 2.3.7-1. Housing design for generation III WFSM prototype half section view. The drive end of the shaft is on the right-hand side.

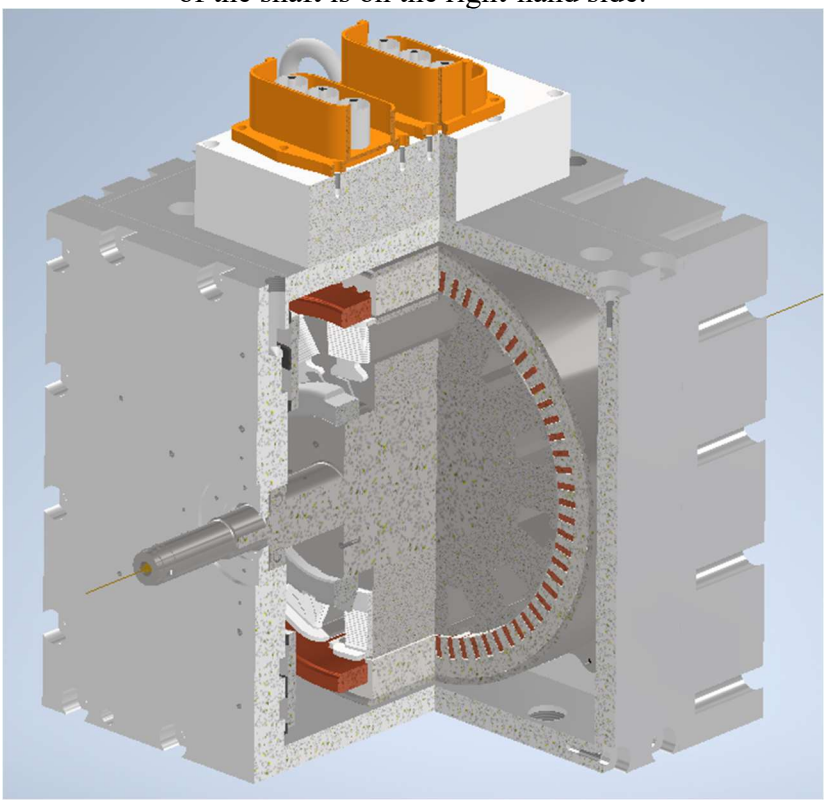

Fig. 2.3.7-2. Housing design for generation III WFSM prototype quarter section view. The non-drive end is shown.

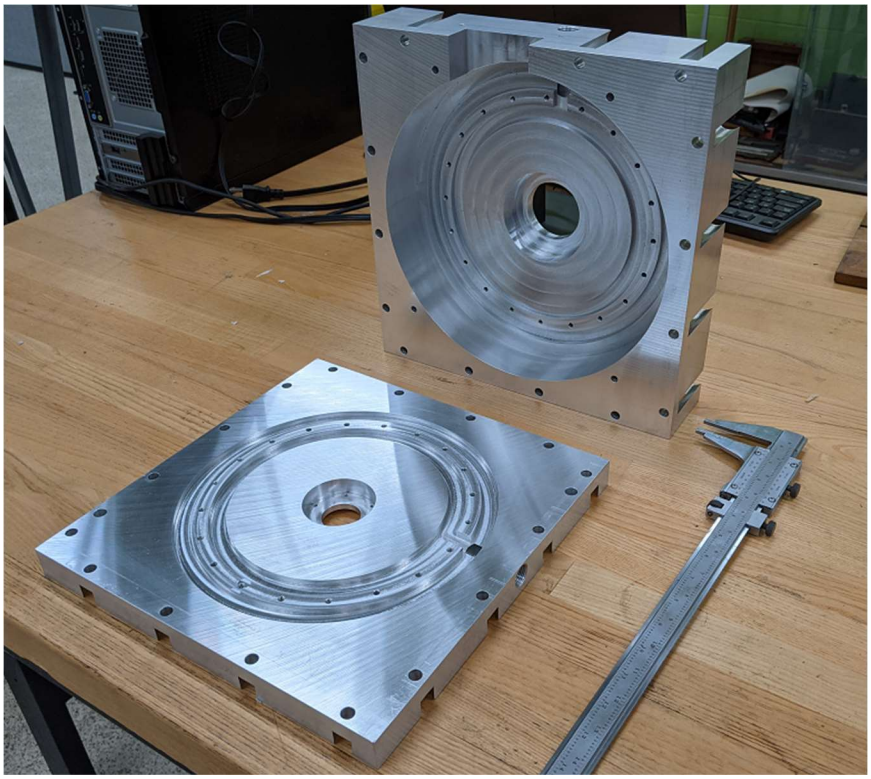

Fig. 2.3.7-3. Machined housing end bells. The non-drive end is in the foreground.

A shaft for all prototypes has been designed and is currently undergoing final review before fabrication.

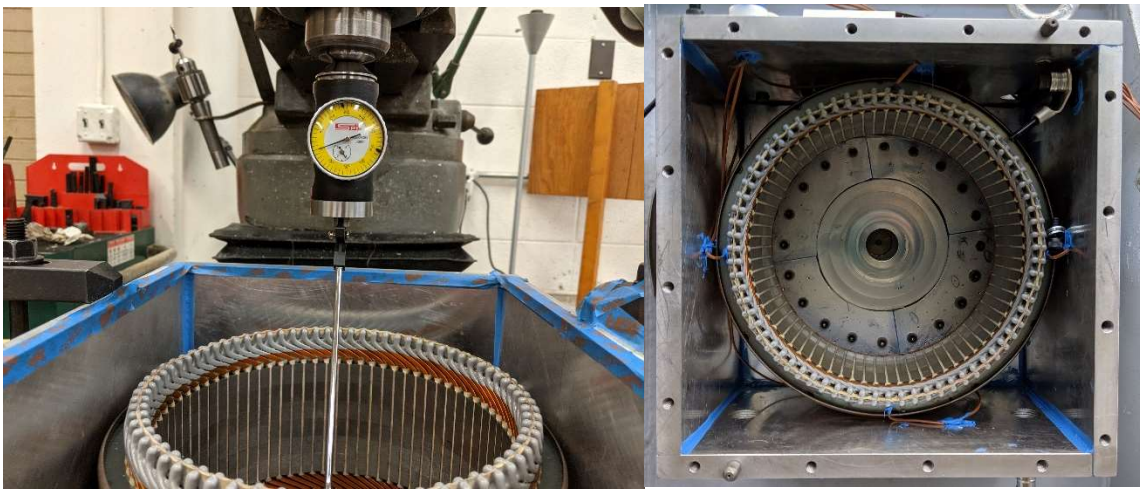

Fig. 2.3.7-4. Stator insertion and alignment in housing.

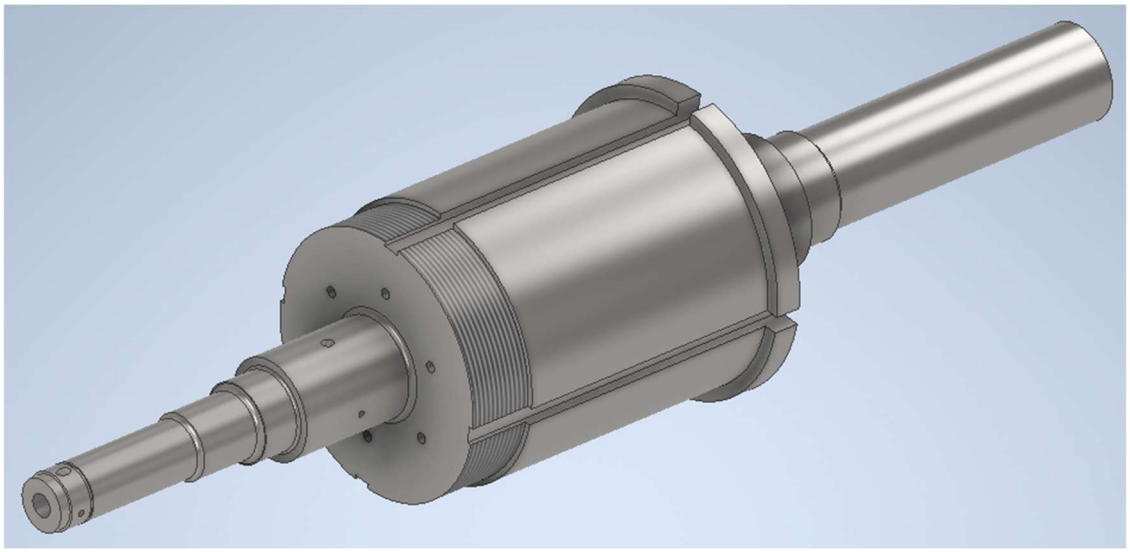

Fig. 2.3.7-5. Shaft for generation III WFSM which allows for rotor changes.

Rotor Lamination Stacks

Rotor lamination stacks have been sourced from an outside vendor. The rotor is designed with a dovetail joint at the root of each pole, enabling bobbin winding of square magnet wire, bobbin winding of twisted square magnet wire as well as the insertion of die compressed windings. This joint means that, rather than one large lamination stack, the rotor is assembled from twelve smaller lamination stacks pressed into one larger yoke. Three sets of bonded lamination stacks were procured so that three rotors could potentially be made to test winding with both straight and twisted square wire as well as die compressed coils. Unfortunately, the smaller pole lamination stacks were inadequately bonded and suffered from a great deal of breakage, both in transit and in handling. A procedure was developed to repair a number of broken stacks using high-temperature epoxy, and the twenty-four stacks considered to be in the best shape were repaired to be used with square and twisted square magnet wire windings. Fig. 2.3.7-6 shows the lamination stacks prior to repair, and Fig. 2.3.2-4 shows the repair process.

Fig. 2.3.7-6. Damaging poles from shipment and repair thereof.

It has been found that acceptably tight dovetail joints can be formed without advanced manufacturing techniques such as EDM, however, the sharp edges of the individual lamination

layers sticking up to 0.002 inches proud of the surface can catch on dovetail assembly. Mass production of pole pieces using a stamping die and interlocking should avoid this issue.

After repair, the stacks were lightly hand ground to allow them to be pressed into the yoke, as the layers were not perfectly stacked on top of each other due to the small size of the prototype lamination stacks and the repair process. The misalignment of the pole layers by manufacturer also caused insertion difficulties. Grinding was first performed with a high-precision 3d printed block with abrasive paper adhered to it shown in Fig. 2.3.7-7 to refine the dovetail shape. This was performed until around half of all layers exhibited a ground surface, and followed by a brief hand-sanding to slightly round over all edges to help prevent further breakage.

Fig. 2.3.7-7. Dovetail grinding using precision 3D printed hand grinding block.

Machined PEEK endcaps were epoxied to the lamination stacks to support the ends of the winding, using 3d printed jigs, shown in Fig. 2.3.7-8. The PEEK endcaps for the square magnet wire are shown in Fig. 2.3.7-8. The twisted square magnet wire winding endcaps have additional features to provide a base layer for the twisted square winding.

Fig. 2.3.7-8. Alignment and epoxying of PEEK endcaps onto pole piece lamination stacks.

Bobbin Wound Square Magnet Wire Rotor

Nomex slot liners were laser cut to fit the pole lamination stacks. Square 19 AWG equivalent wire was then wound to form 161 turns onto each pole stack to form the salient pole pieces, shown in Fig. 2.3.7-9 to Fig. 2.3.7-11. The complete salient pole with the bobbin wound square wire is shown in Fig. 2.3.7-11. The wire was found to lay a few degrees from flat, and this had the effect of making winding difficult. It is expected that process optimizations could reduce this. The target winding pattern was completed on all pole pieces. After winding, the number of turns on each coil was verified using high-precision resistance measurement. Prior to assembly, windings were consolidated using a 3d printed die and arbor press, Fig. 2.3.7-12, to ensure that the windings in adjacent poles did not interfere during the pressing of the pole pieces into the yoke. The salient poles were pressed into the yoke using an arbor press, Fig. 2.3.7-13.

Aluminum rings with negative dovetail pockets were bonded on to the PEEK endcaps to ensure their retention against centrifugal forces, Fig. 2.3.7-14. The connection PCB was also trial fitted. The rotor stack was then vacuum pressure impregnated (VPI) as is shown in Fig. 2.3.7-15. After inserting the shaft, the connection PCB was reattached and connected to the field windings on the poles. The terminal leads were brought through the shaft to the connection PCB, Fig. 2.3.7-16. The slip rings and coupler hub were pressed onto the shaft before balancing. The complete rotor assembly after balancing and with the bearings shrunk fit on, is shown in Fig. 2.3.7-17. This rotor assembly was dynamometer tested at UW-Madison with brushes and slip rings and the capacitive power coupler.

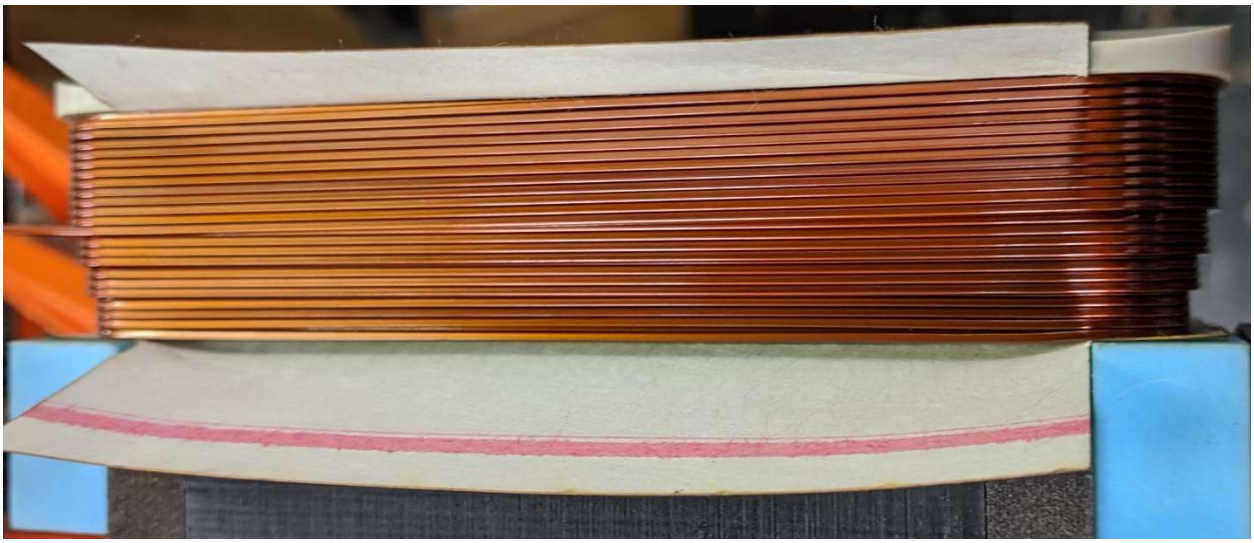

Fig. 2.3.7-9. Winding of square 19 AWG equivalent magnet wire onto pole stack.

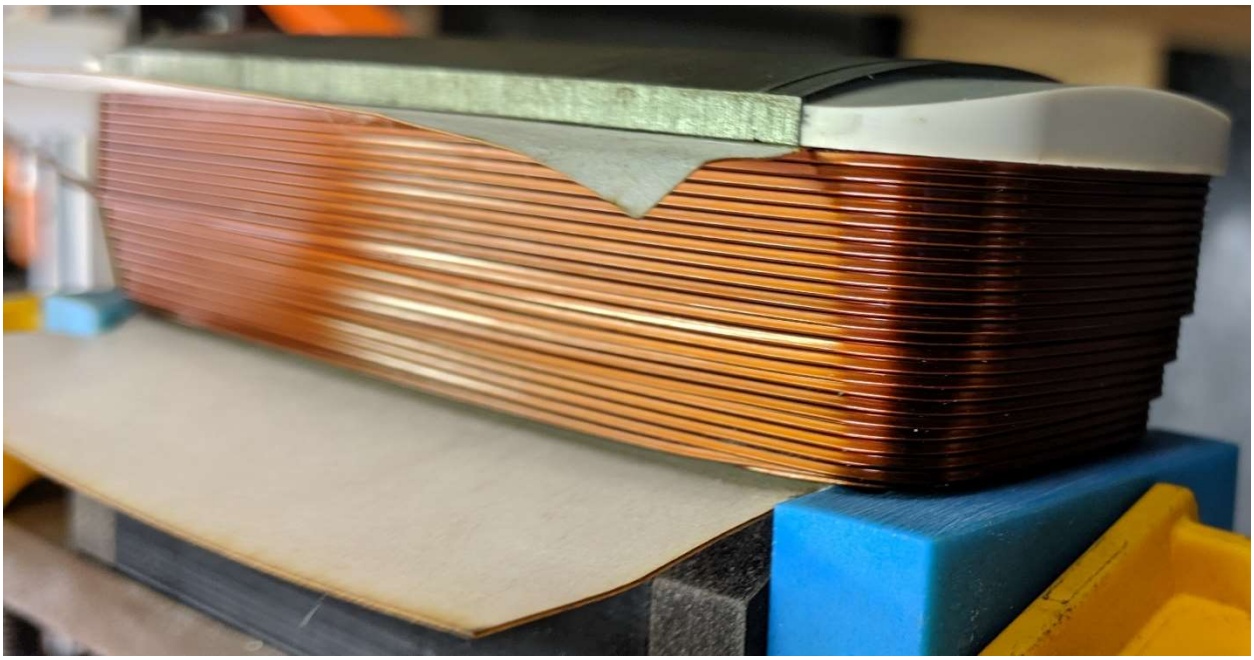

Fig. 2.3.7-10. Alternative view of winding of square 19 AWG equivalent magnet wire onto pole stack.

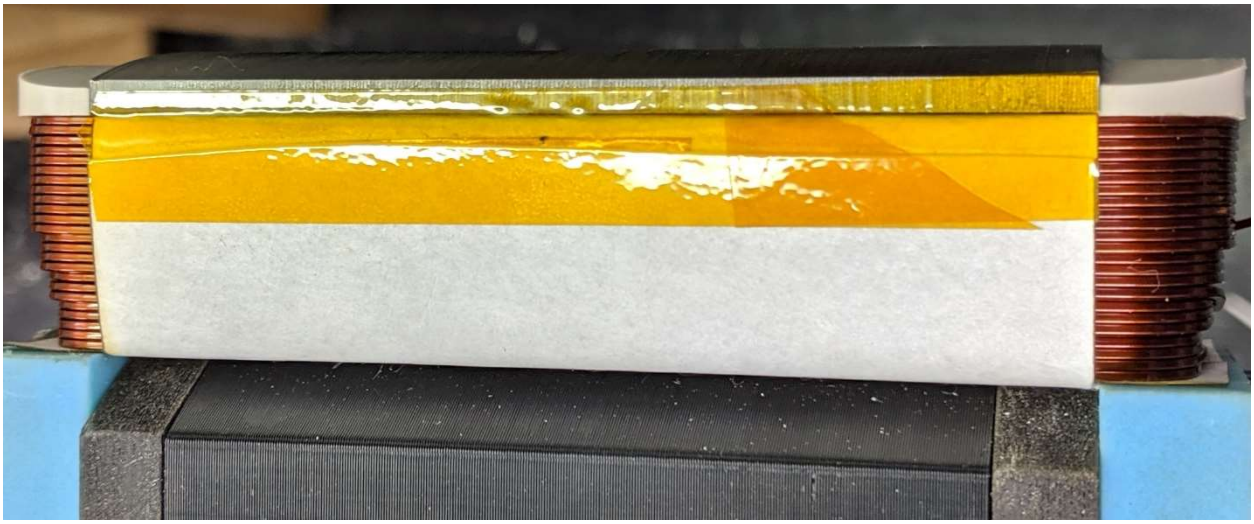

Fig. 2.3.7-11. Bobbin wound salient pole with square magnet wire.

Fig. 2.3.7-12. Winding consolidation on salient pole.

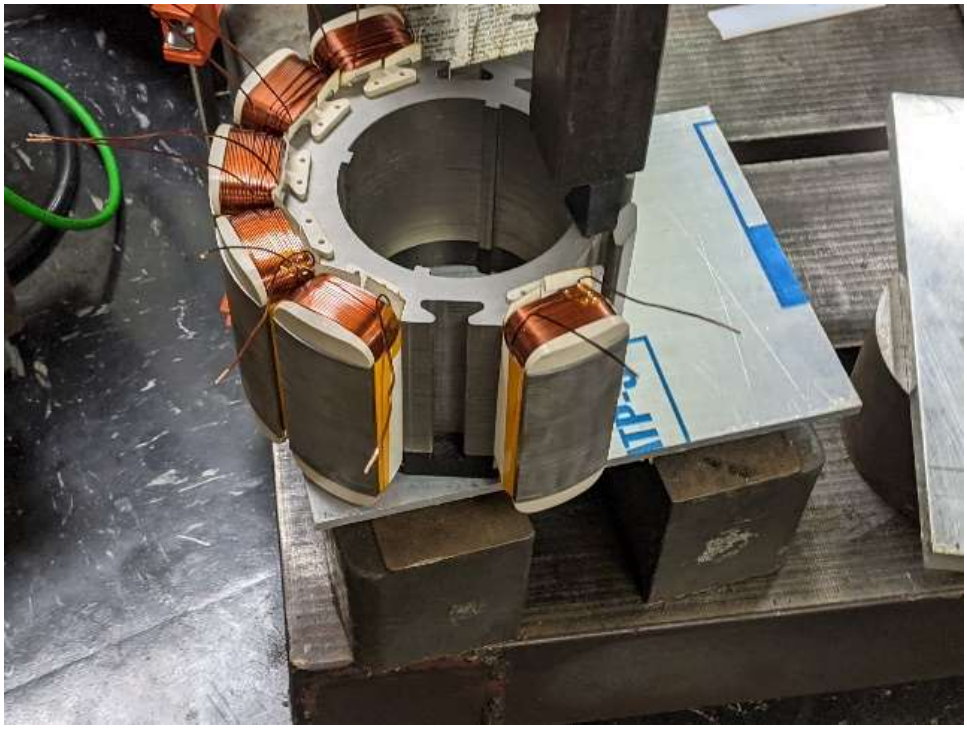

Fig. 2.3.7-13. Pressing of salient poles into yoke.

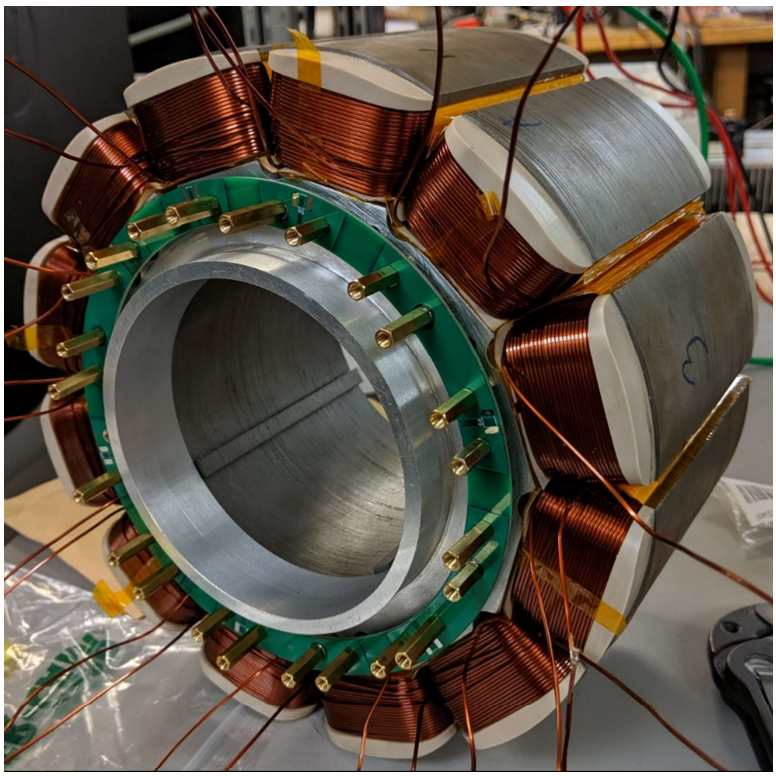

Fig. 2.3.7-14. Aluminum retention rings for end caps bonded on and trial fitting of the connection PCB.

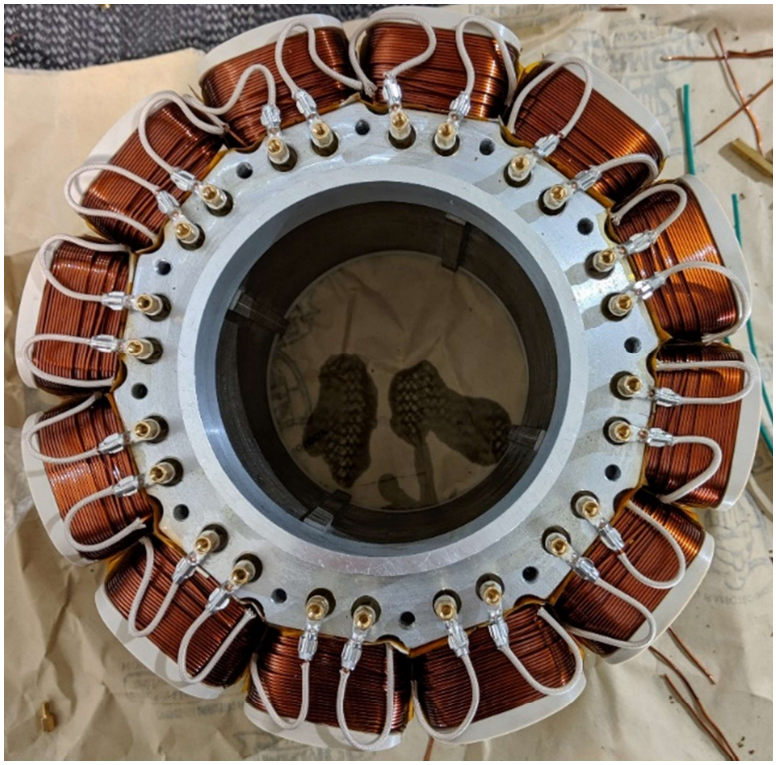

Fig. 2.3.7-15. View of complete rotor after vacuum pressure impregnation without the shaft.

Fig. 2.3.7-16. Rotor mounted on shaft with connection PCB.

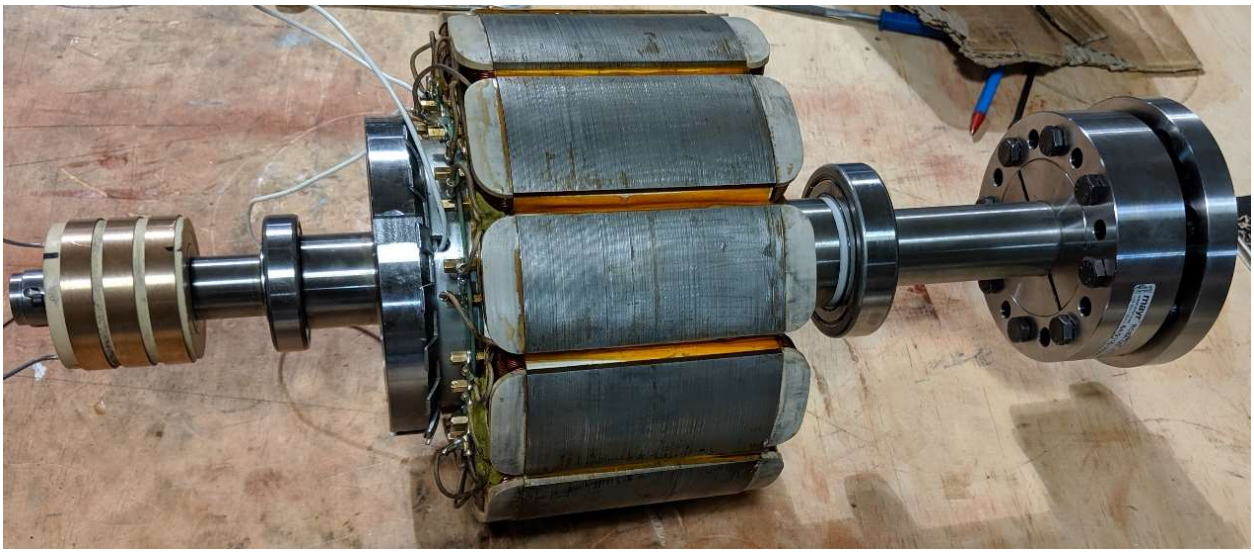

Fig. 2.3.7-17. Complete rotor assembly after balancing.

Twisted Square Magnet Wire Rotor

A second rotor using the repaired pole lamination stacks was also constructed, but with the field wound using a twisted square magnet wire approach. If rotated 45 degrees, the square wire can be wound pseudo-orthocyclically, with each layer interlocking with the layer below. This requires a grooved support to position the first layer, and several such supports were tested. Adequate performance was attained with supports only present under the end turns.

This approach has a lower slot fill than the die compressed winding or regular square wire winding but is significantly easier to wind. It also likely resists centripetal forces more than the regular square magnet wire or die compressed windings because of its self-locking nature. While the twisted square magnet wire rotor prototype manufactured in this project was wound directly as a bobbin, it does seem feasible to potentially needle wind if the entire rotor was a single stack and not individual pole pieces. A custom winding needle and program would need to be developed however.

The initial base layer winding guides are shown in Fig. 2.3.7.

An example initial base winding layer end turn guide model is shown in Fig. 2.3.7-18. Base winding layer guide configurations covering the entire bobbin are shown in Fig. 2.3.7-18(a) and only the end turns in Fig. 2.3.7-18(b). An example square winding with a pseudo orthocyclic winding is shown in Fig. 2.3.7-19.

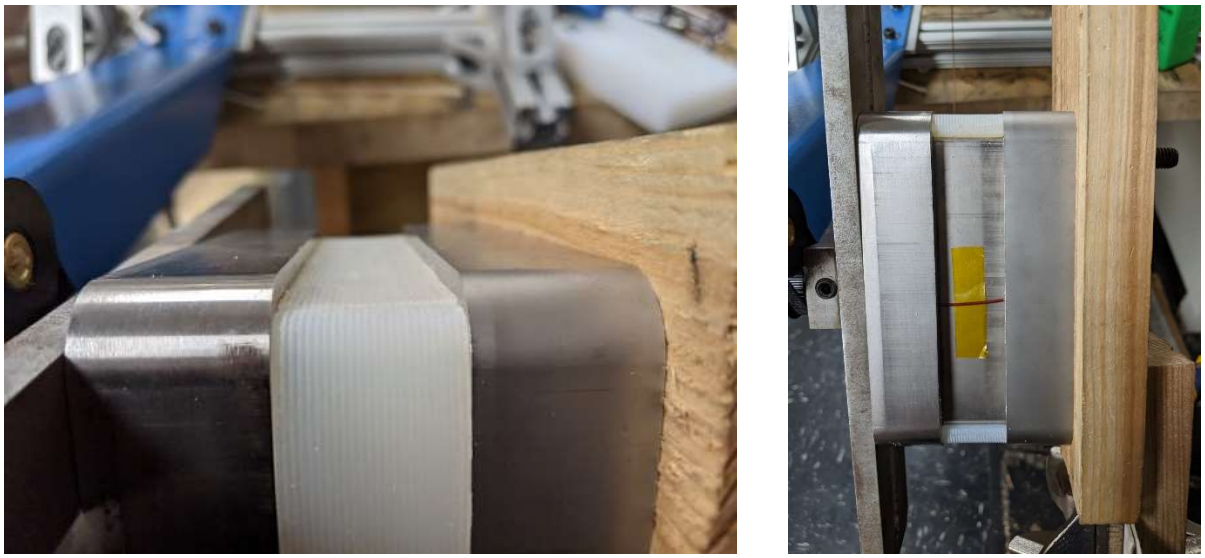

(a) (b)

Fig. 2.3.7-18. Square wire base winding layer guides covering the entire bobbin (a) or just the end turn regions (b).

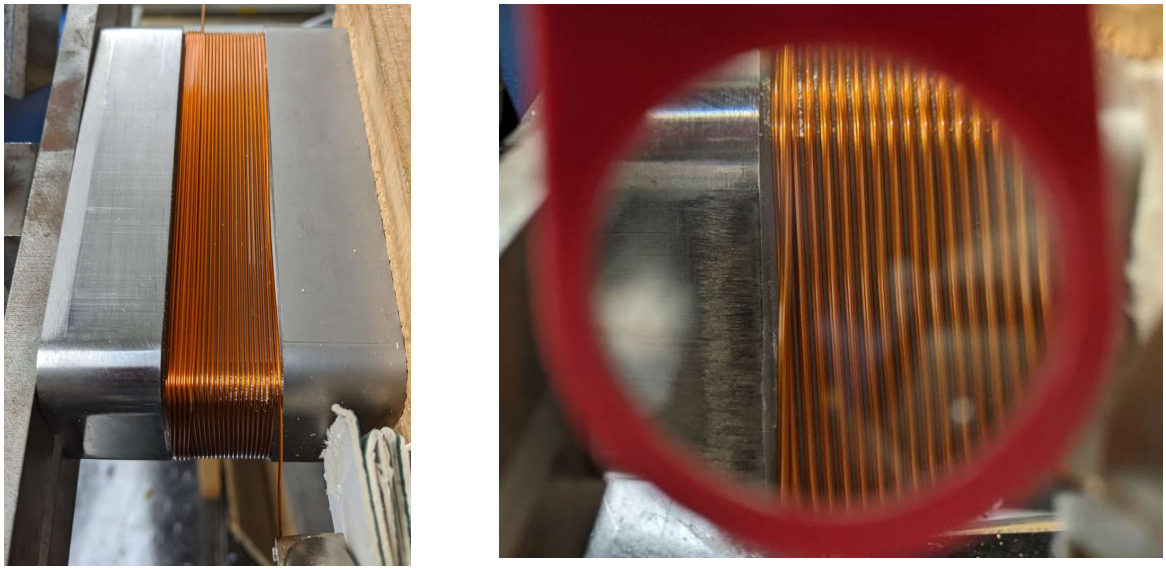

(a) (b)

Fig. 2.3.7-19. Example initial square wire winding with pseudo orthocyclic layout.

Several modifications to the end turn guides were made to ensure that all the wires stay on edge. These changes have been incorporated into the final PEEK endcap design. The straightener in the in-house designed winding machine was also modified for use with the twisted square wire, Fig. 2.3.7-20. After the design modifications, prototype coils were wound for sectioning and adjustment of the process. A representative trial coil is shown in Fig. 2.3.7-21 and sectioned in Fig. 2.3.7-22. The section in Fig. 2.3.7-22 is taken through the middle of one end support. The wires can clearly be seen to be diagonal, and they are supported on the bottom and sides by the support geometry. They also have a very high degree of slot fill. Further improvements to the final endcap design and winding process were made.

The winding of the first base layer, guided by the PEEK endcaps is shown in Fig. 2.3.7-23 and continuing through the end of the 2nd layer in Fig. 2.3.7-24. The completed winding of one pole with the twisted square magnet wire is shown in Fig. 2.3.7-25 on the transition end. The wound poles were then inserted into the yoke in a similar manner as the regular square magnet wound poles, Fig. 2.3.7-26. The view of the wound pole in Fig. 2.3.7-26 is from the non-transition end of the winding. After inserting all the poles and performing a high precision resistance check to ensure that there is not a missing or additional turn on a pole, the pole connection rings were crimped on, Fig. 2.3.7-27. The sleeves and connection PCB were then attached before the vacuum pressure impregnation, Fig. 2.3.7-28.

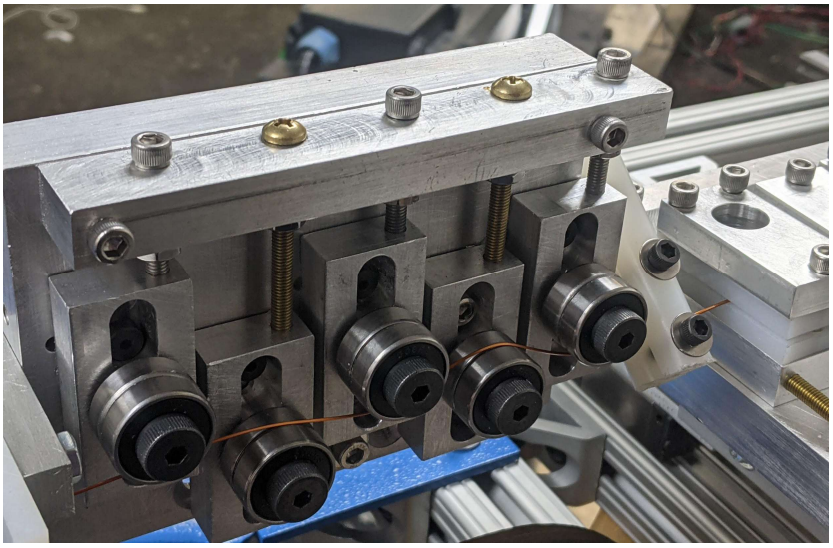

Fig. 2.3.7-20. Custom twisted square wire straightener for twisted square wire.

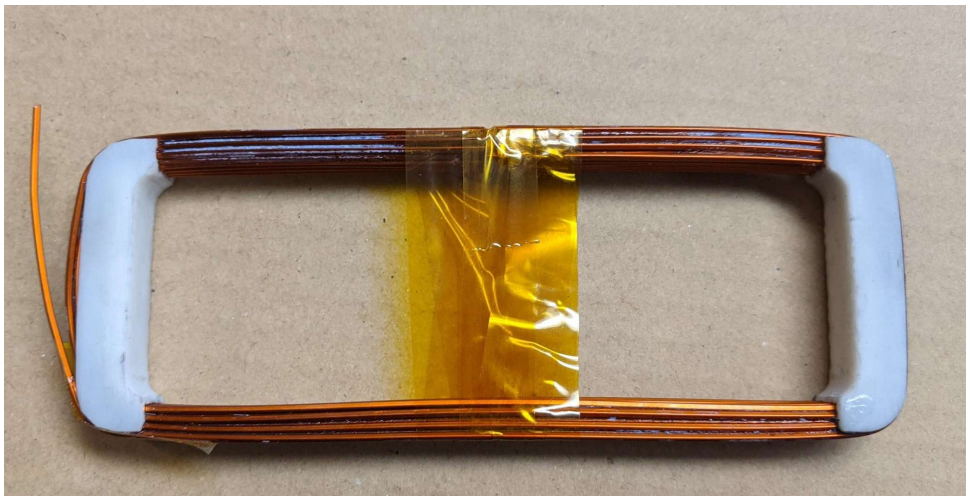

Fig. 2.3.7-21. Trial twisted square wire coil with modified endcaps.

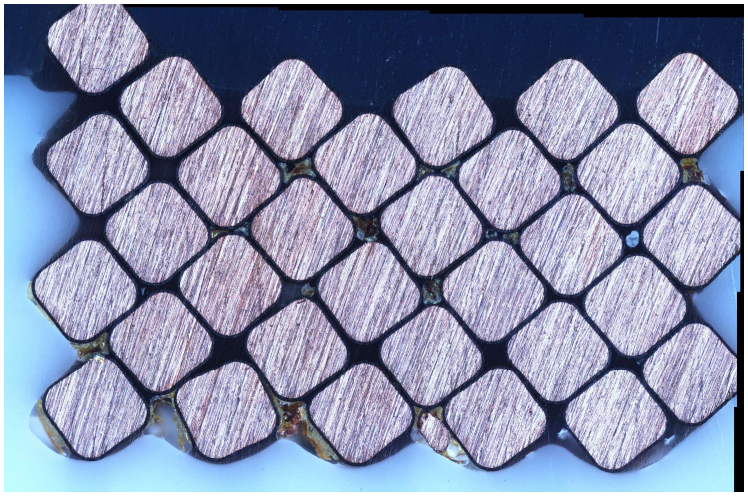

Fig. 2.3.7-22. Cross-section of trial twisted square wire coil.

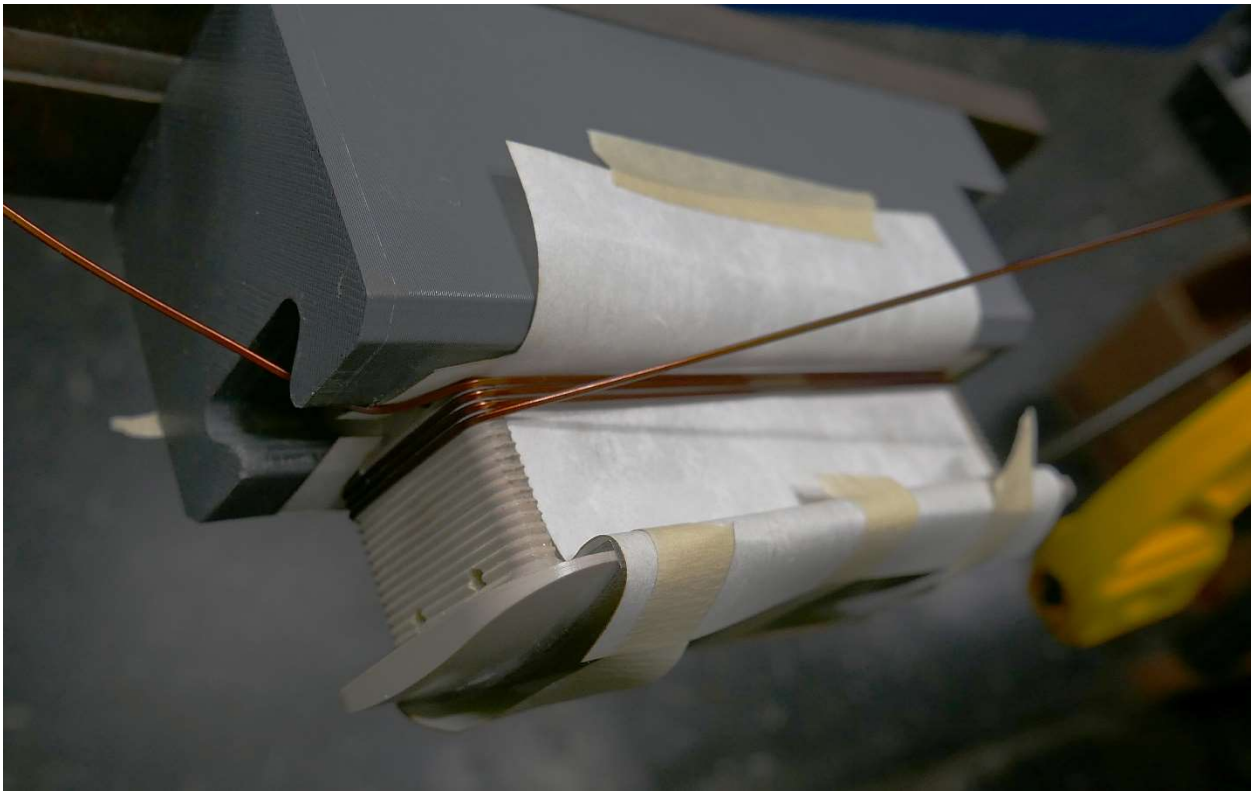

Fig. 2.3.7-23. Winding of initial layer of twisted square magnet wire on pole lamination stack.

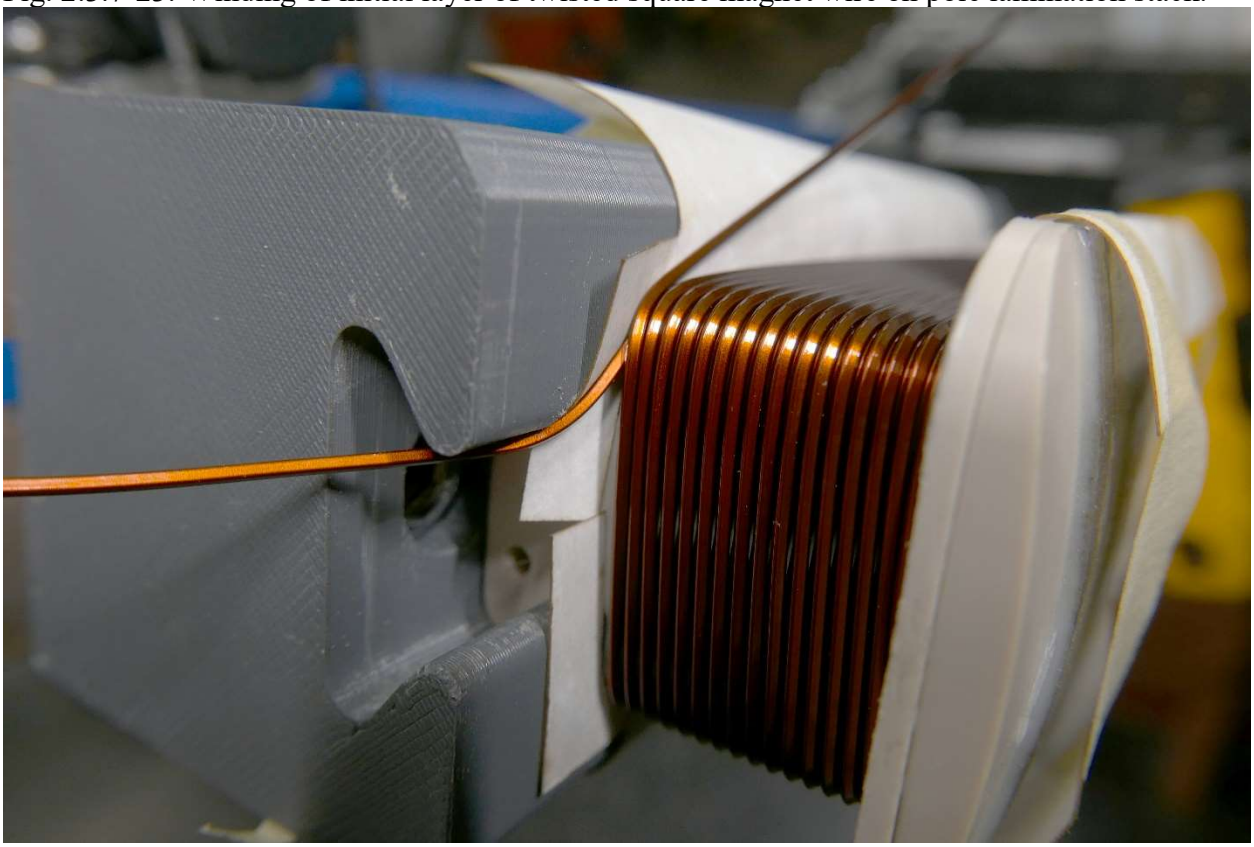

Fig. 2.3.7-24. Completion of second layer of twisted square magnet wire winding on pole stack.

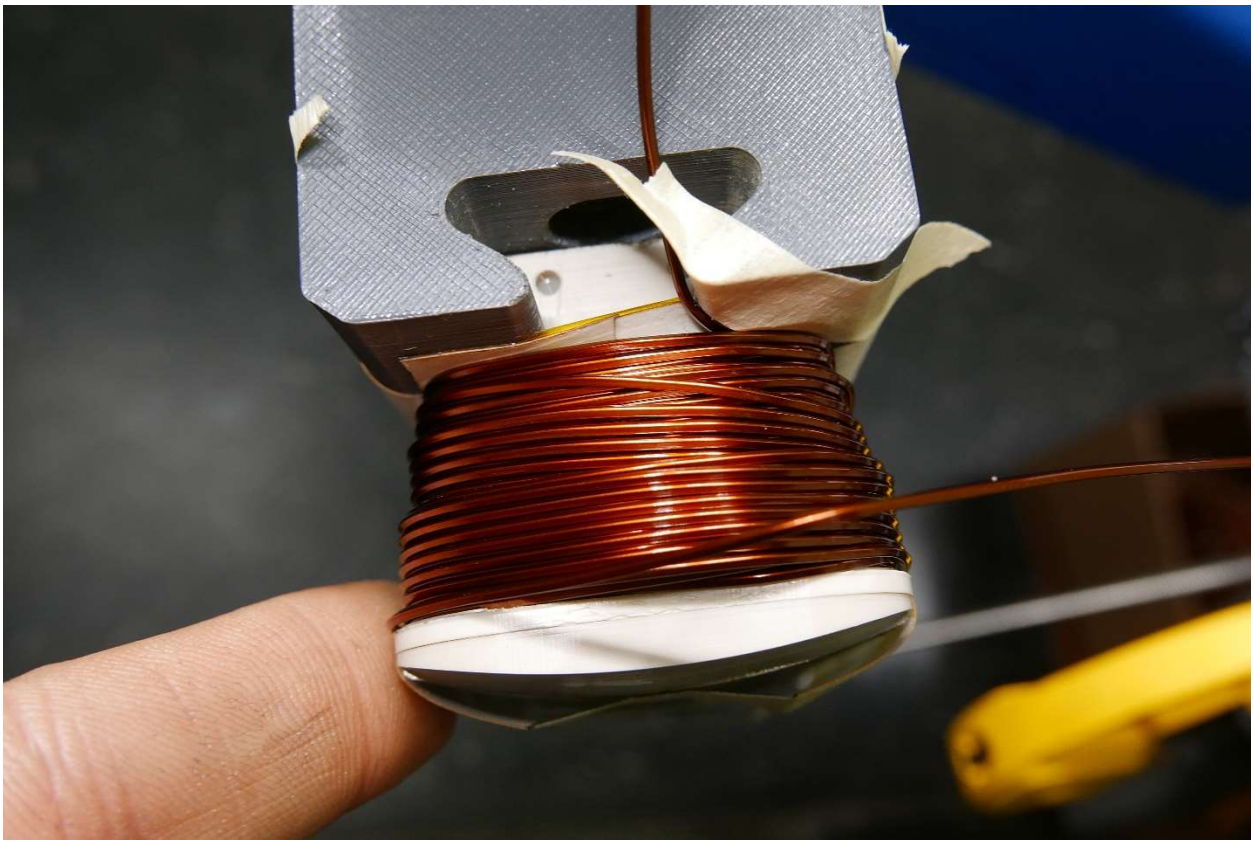

Fig. 2.3.7-25. Complete winding of twisted square magnet wire on a pole stack.

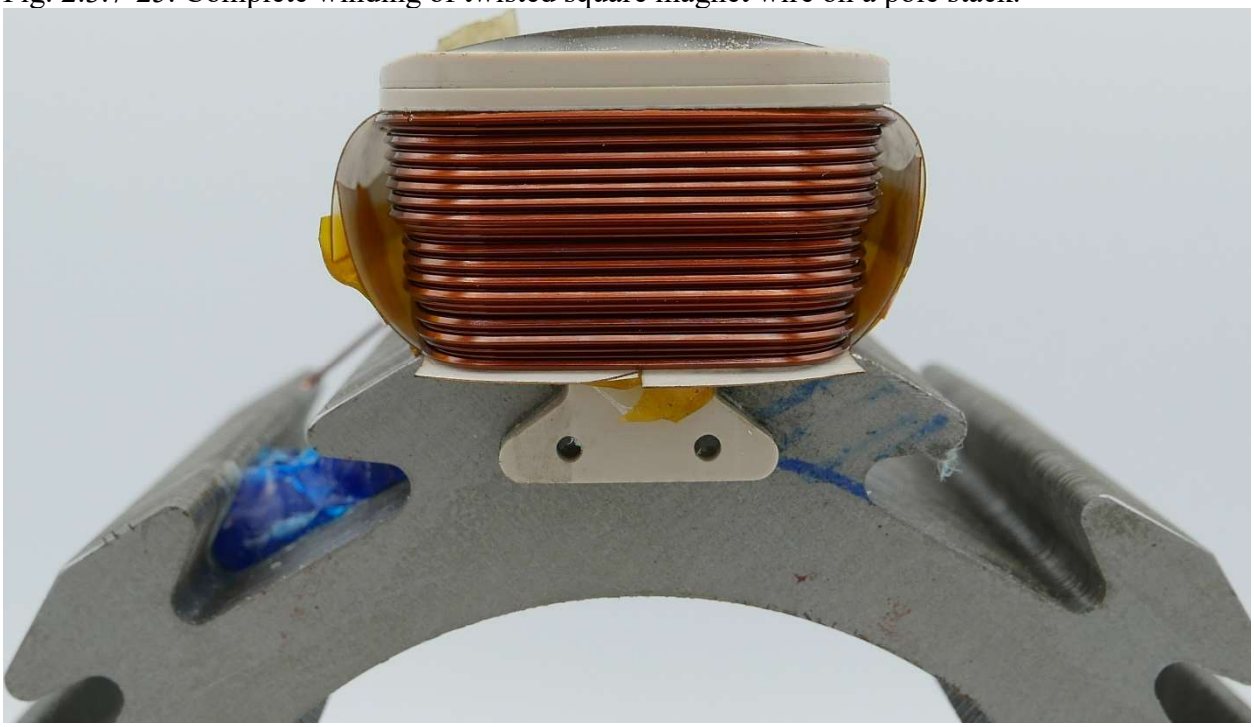

Fig. 2.3.7-26. Salient pole with twisted square wire inserted into pole stack.

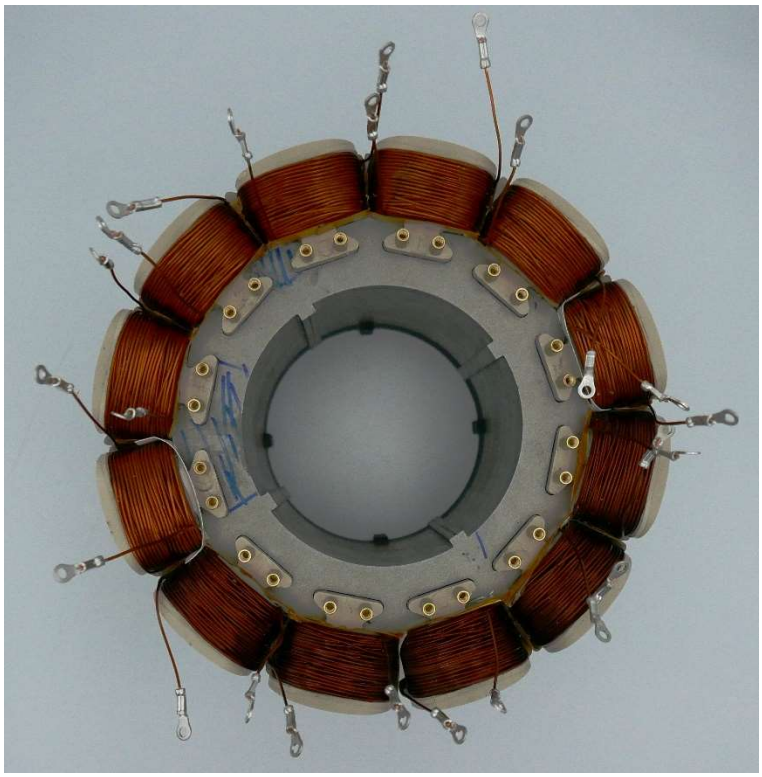

Fig. 2.3.7-27. Twisted square rotor after all poles inserted.

Fig. 2.3.7-28. Complete twisted square rotor.

Non-Rectangular Die Compressed Field Coil

A third field winding variant was planned as an option for the generation III prototype. This variant would be like the generation II WFSM using a die compressed field winding, but the coil shape would have a trapezoidal and rectangular profile unlike the generation II field coil which only had a rectangular profile. The deformation of the coil turns in the non-rectangular cavity is more complex and care must be taken during the placement of the turns on the bobbin before compression to avoid overly straining individual turns during the compression process. While non-rectangular coils were successfully produced, the manufacturing process still needs refinement and the lower risk path of using the square magnet wire was decided to be used for the final prototype that would be dynamometer tested. There was also concern that we would not be able to repair enough pole pieces for this prototype.

A CAD model of the final field winding coil geometry is shown in Fig. 2.3.7-29. To produce this shape, an outer die with a non-rectangular cavity was manufactured along with a top bobbin on which the coil was wound, a bottom bobbin to support the coil, a punch, and a backing plate. The CAD model of all the components except the backing plate, are shown in Fig. 2.3.7-30. The die components except the backing plate, were made from hardened A2 steel. An example pseudo-orthocyclic winding on the bobbin, with steppings to reduce the strain the magnet wire undergoes during compression, is shown in Fig. 2.3.7-31. A trial compressed coil is shown in Fig. 2.3.7-32. The non-rectangular shape of the coil is apparent.

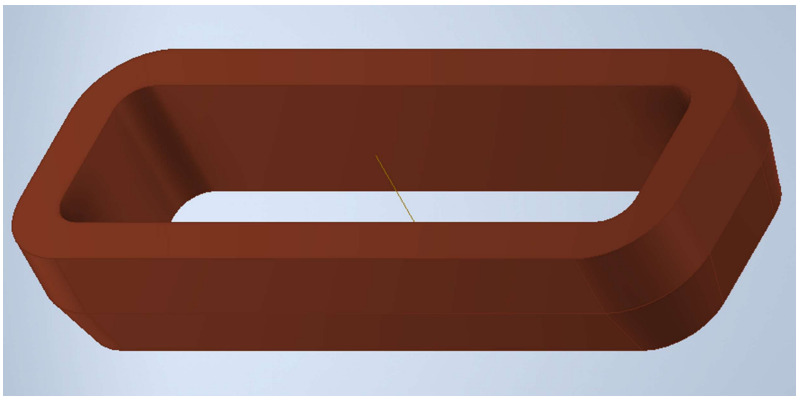

Fig. 2.3.7-29. CAD model of desired non-rectangular compressed coil field winding.

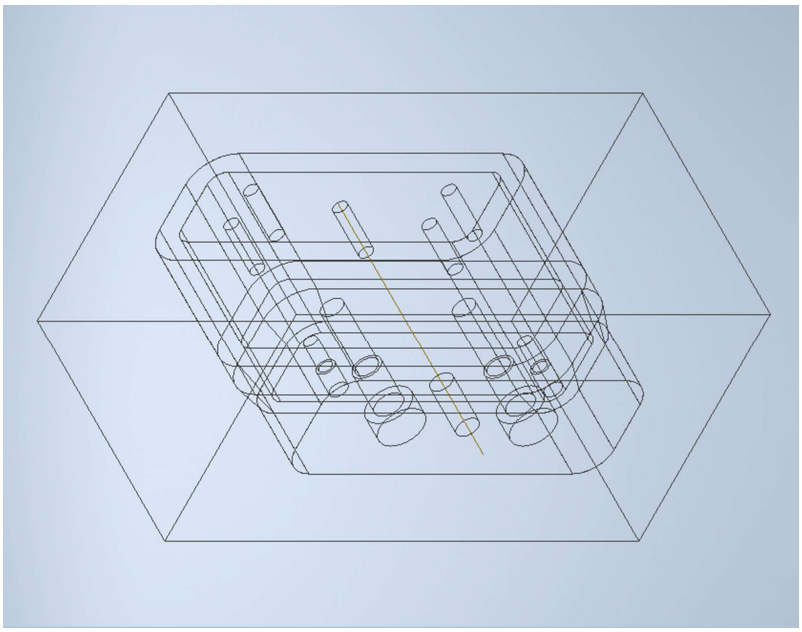

Fig. 2.3.7-30 – Non-rectangular field coil die set CAD model wireframe view.

Fig. 2.3.7-31. Winding of field turns on bobbin before insertion in die and compression.

Fig. 2.3.7-32. Compressed coil on bobbin after compression.

2.4 Brushless Capacitive Power Transfer

2.4.1 Introduction

A number of brushless capacitive power transfer technologies were developed during the course of this project. One way to group the technologies is in terms of the physical form of the capacitor which allow rotary motion and displacement current transfer across the rotary gap. Three broad approaches to capacitors which allow rotary motion are
1) Journal bearings with pressurized air or oil in the airgap
2) Printed circuit boards with inductive and capacitive transfer properties
3) Large gap printed circuit board capacitive power couplers

2.4.2 Journal Bearing Capacitive Couplers

Journal bearings with the gap filled with either pressurized air or oil were investigated for use as the rotary capacitive power coupler to transfer power to the wound field synchronous machine field winding. The journal bearings have intrinsic capacitance that enables the capacitive coupling. The proposed overall capacitive power transfer system with the rotary coupling capacitors, C_C, are shown in Fig. 2.4.2-1. A high frequency inverter on the stationary side couples to the rotary side through the rotary coupling capacitors and a matching network. The AC currents are rectified on the rotating side to supply DC current to the wound field synchronous machine field winding, L_L and R_L.

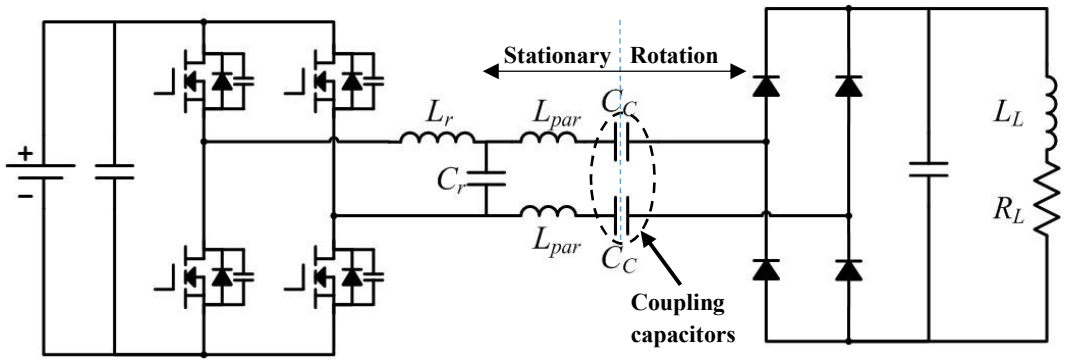

Fig. 2.4.2-1. Active bridge and matching network with journal bearing capacitive coupler for powering the rotor field winding.

Journal Bearing Capacitive Coupler with Pressurized Air

A basic design feasibility study of a capacitive power coupling was carried out which utilized a pair of externally pressurized compressed air journal bearings to realize electrical capacitors through which high frequency alternating current can pass. The advantage of pressurized air is that it allows for potentially high rotor speeds because of the low effective viscosity. The basic parameters of the design study are listed in Table 2.4.2-1.

TABLE 2.4.2-1: BASIC DESIGN PARAMETERS FOR PRESSURED AIR JOURNAL BEARING CAPACITIVE COUPLER

	Parameter	Symbol	Value	Parameter	Symbol	Value
Coupler	Total area	A_{tot}	$10in^2$ ($6.45\times10^{-3}m^2$)	Breakdown voltage	V_{pk}	700V
	Gap distance	d	2.5 mil (0.064mm)	Switching frequency	f_{sw}	2MHz
	Gap permittivity	ε_0	8.85pF/m	Load resistance	R_L	100Ω
Electronics	Resonant inductance	L_r	6.1μH	Input voltage	V_{in}	180V
	Resonant Capacitance	C_r	0.7nF	Output voltage	V_{out}	500V
	Coupling capacitance	C_C	0.9nF	Switch current stress	I_{MOS_peak}	24A
	Parasitic inductance	L_{par}	200nH	Coupling cap. RMS current	I_{C_rms}	7.2A

With the basic design parameters estimated in Table 2.4.2-1 the theoretical output power can be given as:

$$P_{out} = \frac{4R_L A_{tot}^2 f_{sw}^2 \varepsilon^2 V_{pk}^2}{d^2} = 2.54kW$$

While the use of pressurized air is attractive because it allows for high speed operation the wound field synchronous machine being developed uses automatic transmission fluid spray cooling of the stator and field winding. There is a risk of introducing automatic transmission fluid into the journal bearing airgap and a separate pressurized air supply would be needed raising cost concerns.

Journal Bearing Capacitive Coupler with Pressurized Oil

A sizing design study for externally pressurized oil journal bearings along with the power electronics to transfer power to the rotor field winding was been carried out. The overall concept is shown in Fig. 2.4.2-2. Pressurized automatic transmission fluid is injected into the gap between the journal bearings to serve as the dielectric. Two journal bearings embedded underneath the rotor allow current to be transferred on and off the rotor in a non-contact fashion. The gap dimensions, estimated coupling capacitance, and break down voltage of the capacitive coupler journal bearings are listed in Table 2.4.2-2. The power electronic component sizing and designed switching frequency are listed in Table 2.4.2-3. Simulation results for this converter are shown in Fig. 2.4.2-4 and summarized in Table 2.4.2-4.

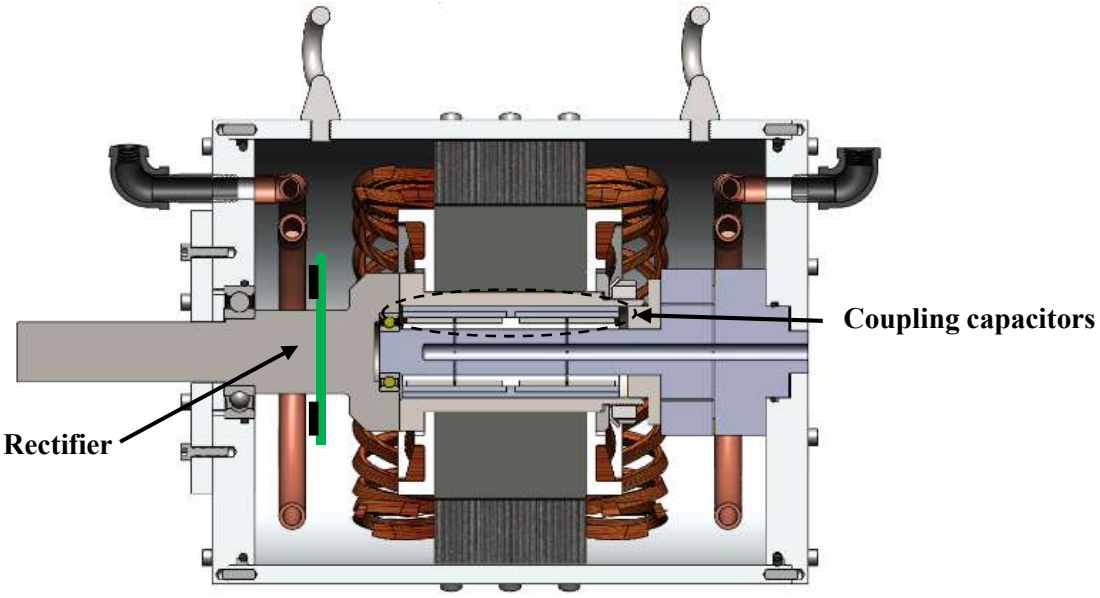

Fig. 2.4.2-2. Oil journal bearing setup for capacitive power transfer to wound field synchronous rotor field winding.

TABLE 2.4.2-2: JOURNAL BEARING SIZING AND DESIGN

Parameter	Value	Parameter	Value
Gap Diameter	41.25 mm	**Dielectric**	ATF
Gap Width	27.5 mm (per cap)	**Capacitance**	2.48 nF/cap
Gap Thickness	~40 micron	**Breakdown V**	~400V

TABLE 2.4.2-3: POWER ELECTRONICS COMPONENT SIZING AND DESIGNED SWITCHING FREQUENCY

Parameter	Symbol	Value	Parameter	Symbol	Value
Switching frequency	f_{sw}	2MHz	**Resonant Capacitance**	C_r	3.3nF
Load resistance	R_L	31Ω	**Parasitic inductance**	L_{par}	5μH
Resonant inductance	L_r	1.23μH	**Coupling capacitance**	C_C	2.49nF

TABLE 2.4.2-4: POWER ELECTRONICS SIMULATION RESULTS SUMMARY

Parameter	Symbol	Value	Parameter	Symbol	Value
Input voltage	V_{in}	100V	Coupling cap. peak voltage	V_{pk}	232V
Output Power	P_{out}	649W	Coupling cap. RMS current	I_{C_rms}	5.09A

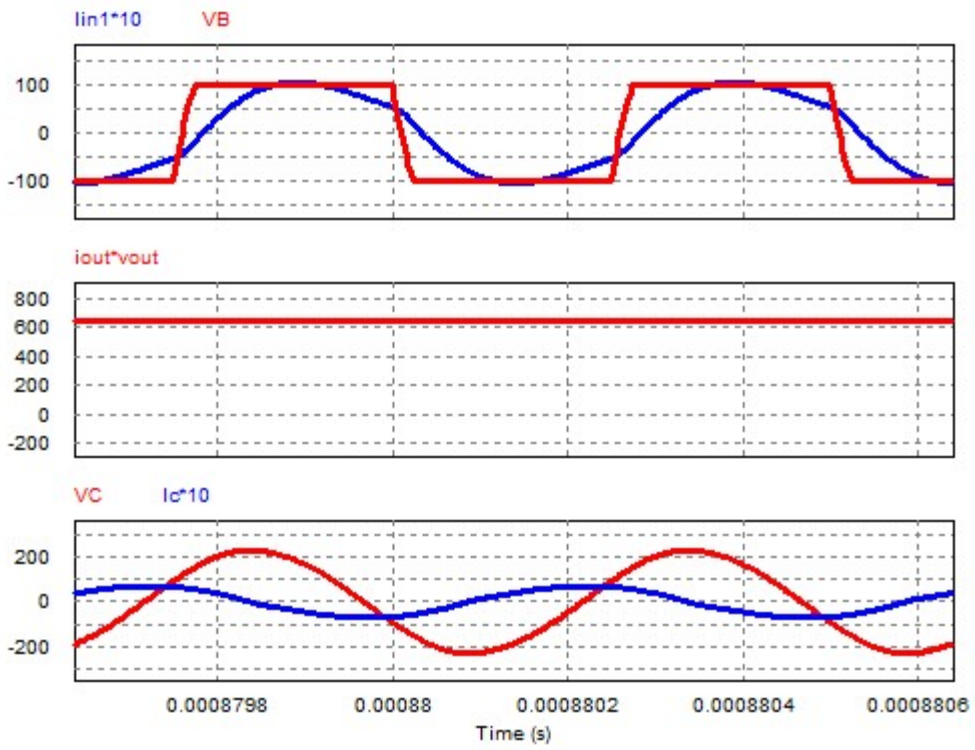

Fig. 2.4.2-3. Simulation results for active bridge and matching network with journal bearing capacitive coupler for powering the rotor field winding.

A pressurized oil journal bearing capacitive coupler was experimentally demonstrated as part of this project on a 10 kW wound field synchronous machine generator. A full description of the design and experimental results of this capacitive coupler are included in the paper.

J. Dai, S. Hagen, D. C. Ludois and I. P. Brown, "Synchronous Generator Brushless Field Excitation and Voltage Regulation via Capacitive Coupling Through Journal Bearings," in *IEEE Transactions on Industry Applications*, vol. 53, no. 4, pp. 3317-3326, July-Aug. 2017.

Two sets of pressurized oil journal bearings form the set of capacitive couplers, Fig. 2.4.2-4(a) through Fig. 2.4.2-4(e). The high frequency push-pull class E inverter providing excitation is shown in Fig. 2.4.2-4(f). The overall electrical schematic of the system is shown in Fig. 2.4.2-5. The pressurized oil journal bearings had 1.7 nF of capacitance allowing for 340 W to be transferred to the rotor field winding.

The main disadvantage of the pressurized oil journal bearing style capacitive coupler is that at high speed because of the large surface area of the journal bearings the drag losses would become excessive. To reach the required power densities for the USDRIVE 2020 and 2025 is likely to require high speed operation and would be challenging in terms of drag losses if a pressurized oil journal bearing was used.

Feedback from the auto industry indicates that there will be considerable reliability testing of the journal bearings, as they are used less frequently in automotive applications (unlike aircraft which use them frequently). Bearing systems are mechanically “sacred” and therefore slow to change. Thus, the automakers inquired if it would be possible to integrate the coupler into the rotating rectifier board. As a result, two other approaches of integrating the capacitive coupling structure based on printed circuit boards were investigated.

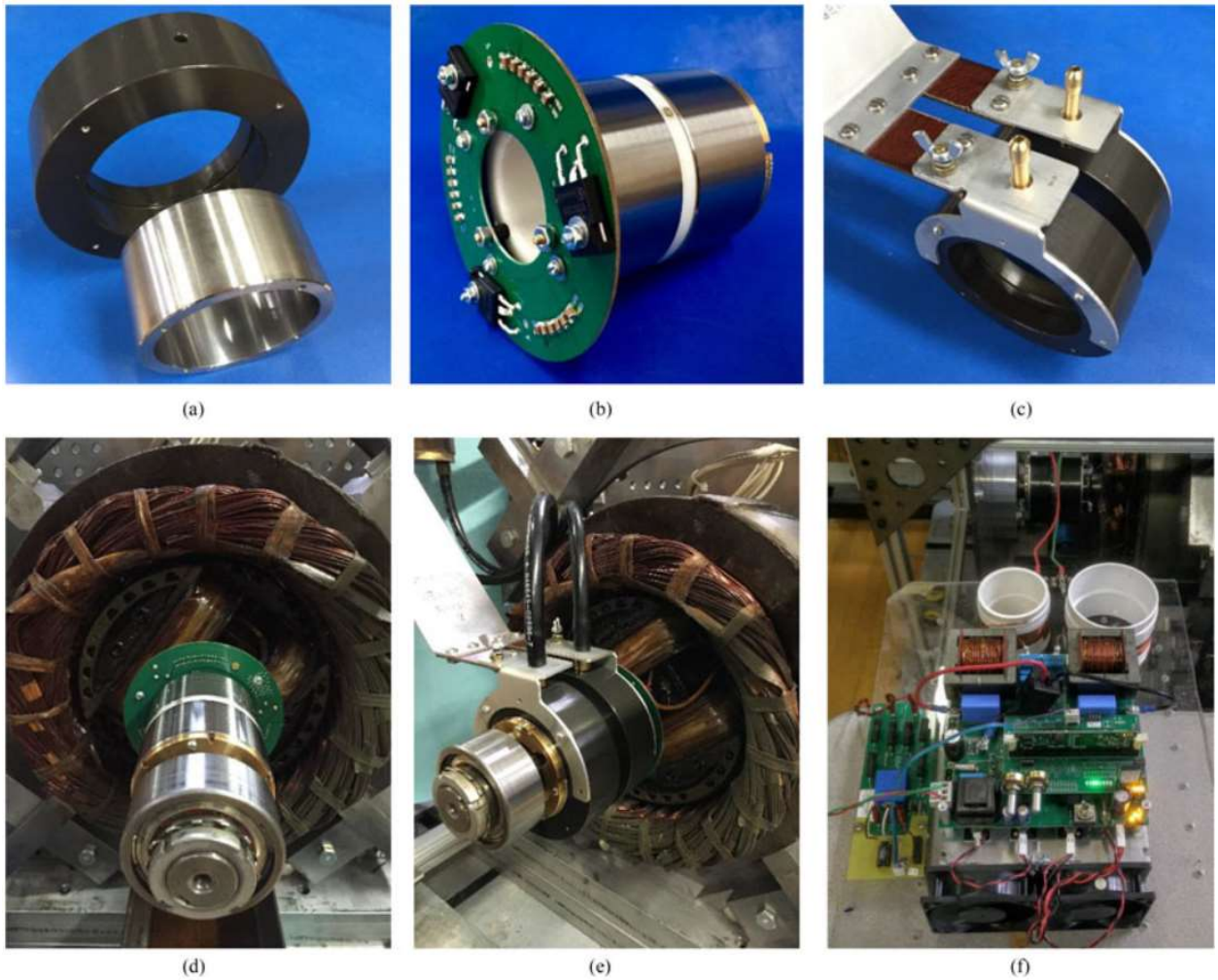

Fig. 2.4.2-4. Pressurized oil journal bearing capacitive power transfer system for wound field synchronous generator: (a) Journal bearing stator and rotor, (b) Journal bearing rotor with rotating rectifier, (c) Bearing stator assembly with pressurized oil ports, (d) Journal bearing rotor mounted on wound field synchronous generator shaft, (e) Assembled journal bearing setup, (f) Assembled push-pull class E inverter for field excitation.

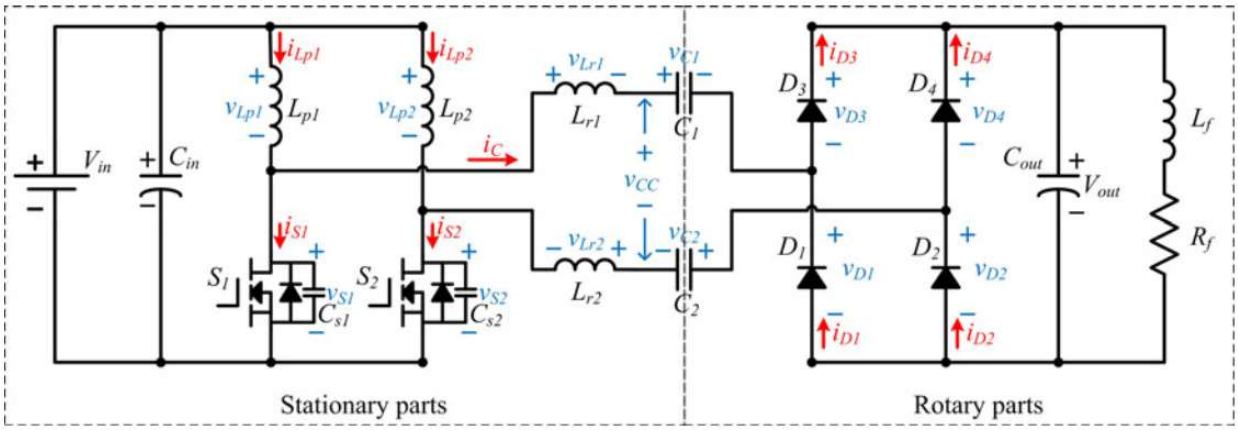

Fig. 2.4.2-5. Pressurized oil journal bearing capacitive power transfer system schematic. The L_{p1}, L_{p2} inductors provides constant current, L_{r1} , L_{r2} are resonant inductors, capacitors C_1 and C_2 form the pressurized oil journal bearing capacitive power coupler assembly, D_1–D_4 represent the rotating rectifier, and L_f, R_f are the field winding inductance and resistance, respectively.

2.4.3 Integrated LC Printed Circuit Board Coupler

A coupler approach that utilized both inductive and capacitive transfer properties was investigated. Fig. 2.4.3-1 shows two PCBs facing one another. These are 2-layer boards, i.e. top and bottom. The top and bottom layers of a board are galvanically isolated but form a parallel plate capacitor, and the layers have been cut such that current flows in a spiral as the surface's charge/discharge. This makes the PCB a coupling capacitor and coil simultaneously. Two such PCBs in close proximity have mutual capacitive and inductive coupling, forming a power transfer system. The coupling is shown in greater detail in Fig. 2.4.3-2.

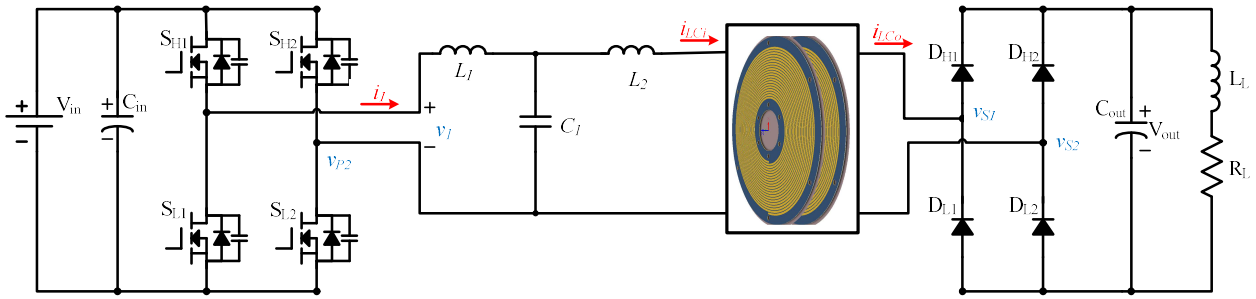

Fig. 2.4.3-1. Active bridge and matching network with integrated LC PCB coupler for powering the rotor field winding.

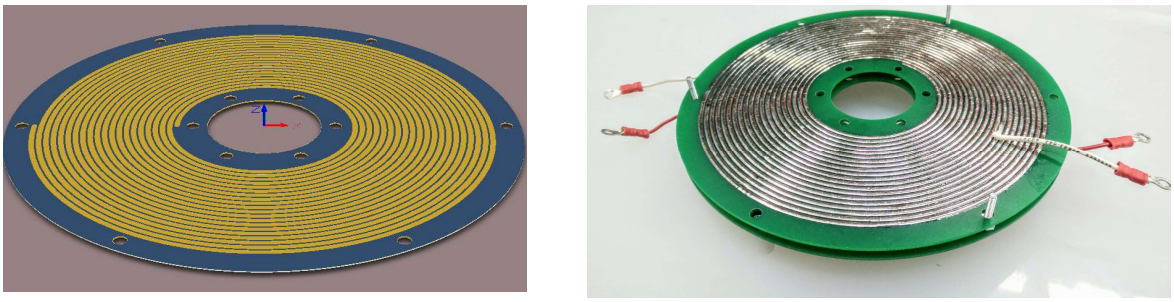

Fig. 2.4.3-2. (Left) – A single integrated LC PCB coupler drawn in Altium, (Right) Two integrated LC coupler boards separated by a 1 mm gap ready for bench testing.

Connections are made mid-spiral on either side of a coupler PCB, and the spirals on each side of a PCB go in opposite directions such that the magneto-motive force (MMF) from the azimuthal component of the current densities add constructively. Finite element models of the magnetic and electric fields, as well as the current densities are plotted in Fig. 2.4.3-3 for a single PCB. Losses are concentrated at the center of the spiral, where the current density is highest. Additionally, proximity and skin effects increase the ESR of the PCB traces.

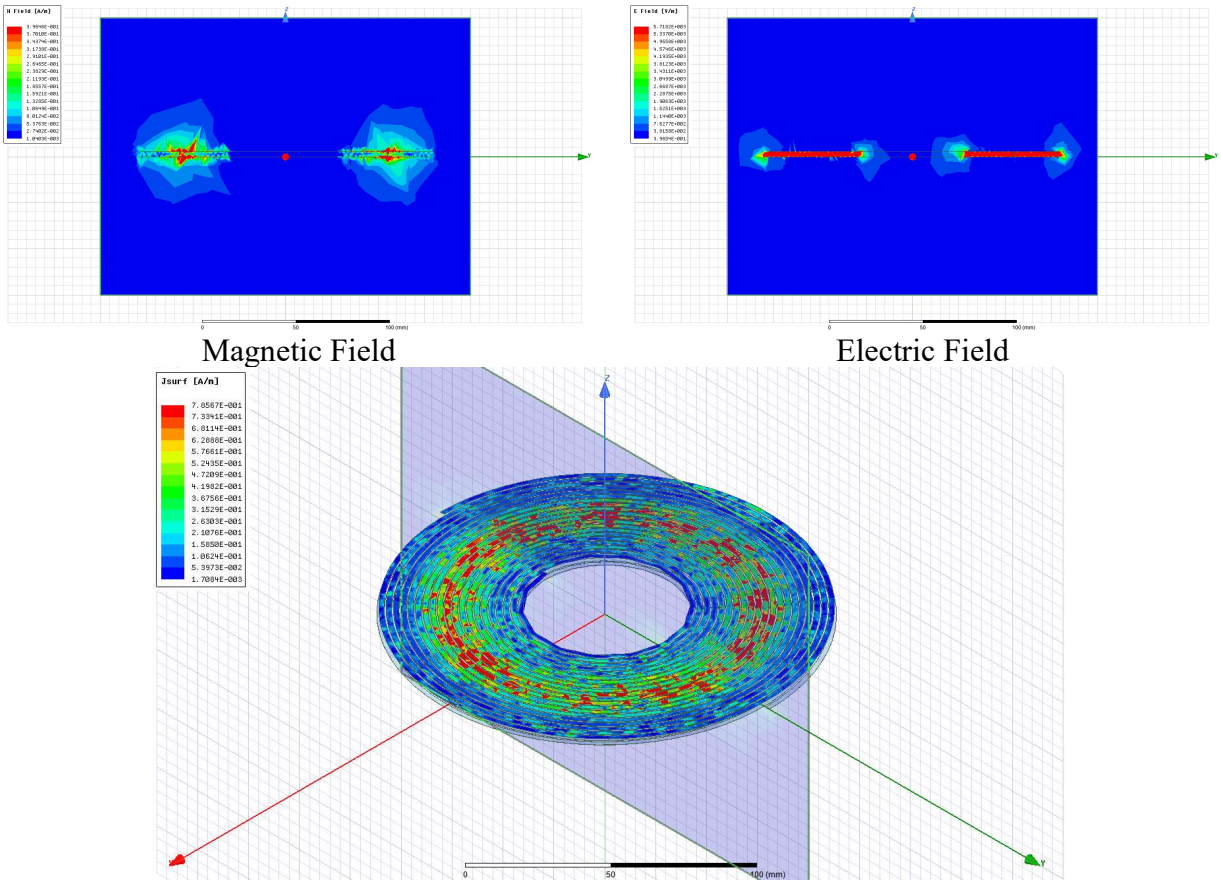

Fig. 2.4.3-3. Finite element analysis of an integrated LC PCB coupler

Theoretically, the impedance of the integrated coupling can be described as a transmission line.

$$Z_0 = \sqrt{\frac{R + j\omega L}{G + j\omega C}}$$

$$\gamma l = \sqrt{(R + j\omega L)(G + j\omega C)}$$

Transmission line model:

$$Z_{in} = Z_0 \frac{Z_L + Z_0 \tanh(\gamma l)}{Z_0 + Z_L \tanh(\gamma l)}$$

In this case,

$$Z_L = \infty$$

$$Z_{in} = \frac{Z_0}{\tanh(\gamma l)}$$

The first resonant frequency:

$$f_{res} = \frac{1}{4\sqrt{LC}}$$

The modeled Z_{in} is based on:

$$R = 5\Omega \quad G = \frac{1}{2.2k\Omega} \quad L = 12.5\mu H \quad C = 0.4nF$$

The characteristic C and L of the coupler can be calculated as lumped elements based on the dimensions and the number of turns, etc. The theoretical versus measured coupler impedance magnitude and phase are shown in Fig. 2.4.3-4.

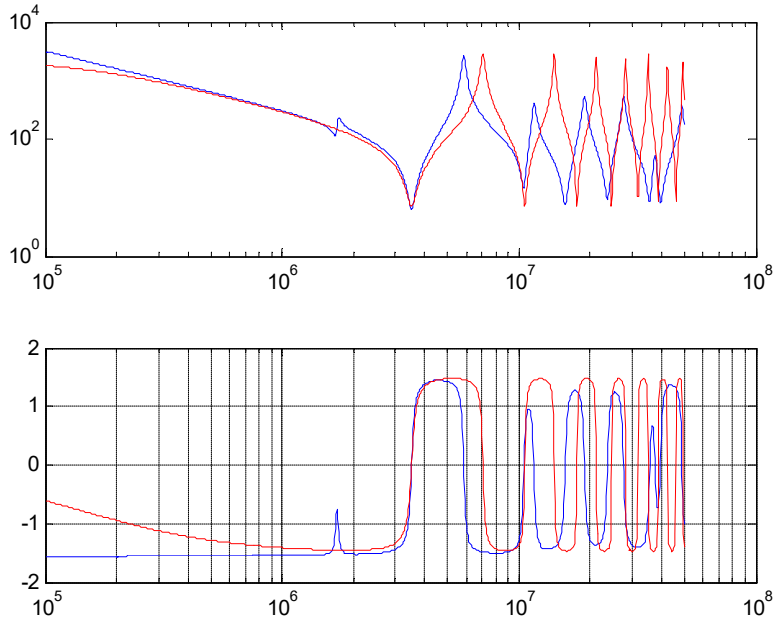

Fig. 2.4.3-4 Single coupler theoretical, red, Z_{in} impedance [magnitude – top (Ohms), phase – bottom [Radians] versus frequency (Hz) versus measured, blue.

From a power electronics and loss perspective, the resonant frequency should be the self-resonant frequency of each coupler by itself, so that the voltage and current on each of them can be sinusoidal, which makes the losses lower. To make the resonant frequency to be the self-resonant frequency, an LCL compensation circuit is needed. In Fig. 2.4.3-1, L_2 moves the resonant frequency lower while L_1 and C_1 split the resonant frequency into 2, the higher of them can be used as the self-resonant frequency.

A reduced power level (20W) bench top demonstration of this approach was constructed, with the coupler pictured in Fig. 2.4.3-2, for the purpose of model validation. Measured waveforms, corresponding to the circuit in Fig. 2.4.3-1, are plotted below in Fig. 2.4.3-5. The operational frequency is 3 MHz and peak efficiency is 65%. In general, the efficiency ranged between 56 and 64%. This efficiency is low especially if kilowatt level power transfer is the goal.

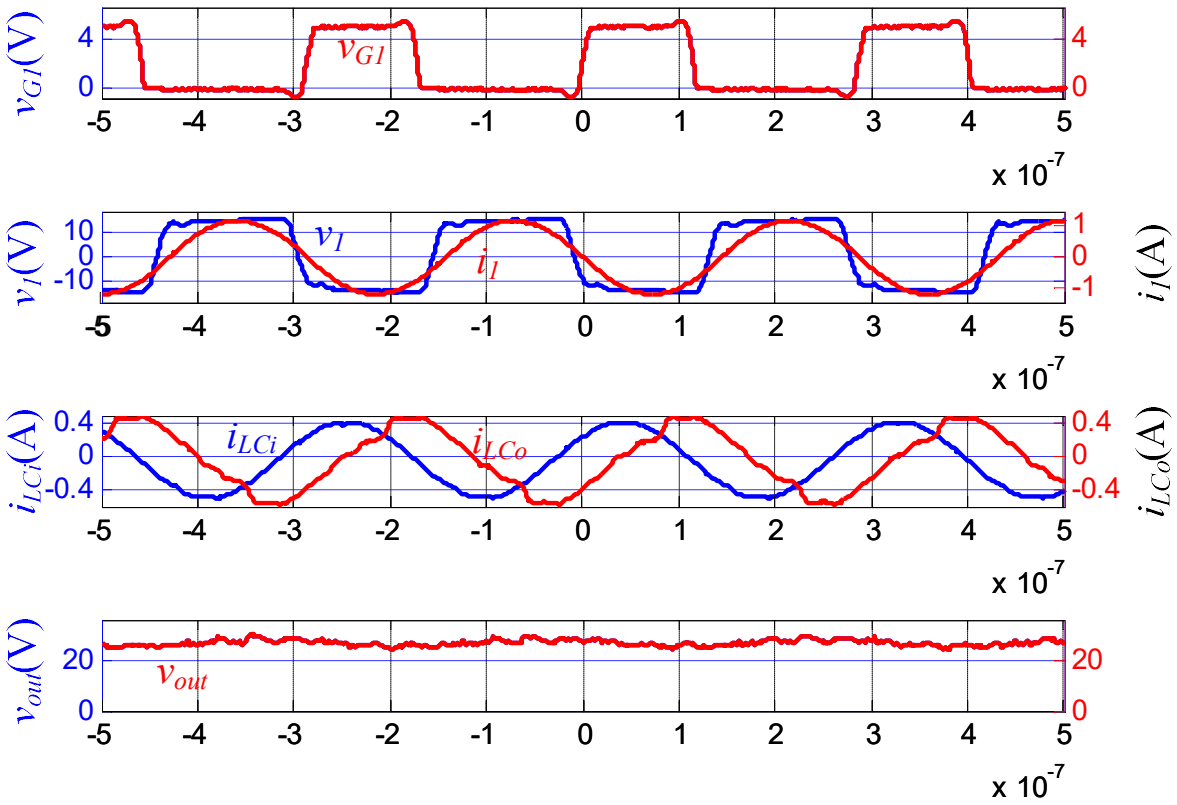

Fig. 2.4.3-5. Measured electrical signals from bench top demonstration of integrated LC printed circuit board coupler, Fig. 2.4.3-2, and the overall excitation, compensation, and rectifier in Fig. 2.4.3-1.

A separation of losses was performed for different loading conditions and switching schemes. The integrated coupler may have greater than 20% loss. Bypassing the coupling with direct connections yields ~85% efficiency, while with the coupler is the efficiency is less than 65%. No matter what the load is (resistance high or low), the efficiency cannot be higher than 70%. The coupler exhibits both series and parallel resistance brought about from the high proximity loss

caused by the integration of L and C. It was deemed that extensive finite element analysis would be required to optimize the design of this approach if needed efficiencies were at all achievable.

2.4.4 Large Gap Printed Circuit Board Capacitive Coupler

Instead of integrating the inductive aspect into the coupling structure, it is removed and remains as a separate lumped element and the printed circuit board simply has large conductive areas instead of traces. The printed circuit boards should be low cost, easy to manufacture, and mechanically simple as they are standard technology. The coupling capacitance between the circuit boards is small because of the large gap on the order of a 1 mm. The large gap printed circuit board coupler approach that was decided upon for testing with the final wound field synchronous machine prototype. Several iterations of this coupler approach were developed along with variations of the high frequency excitation inverter and resonant tank circuits.

Initial Proof of Concept Large Gap Capacitive Power Transfer System

The initial proof of concept large gap capacitive power transfer system used square boards and air core inductors in the matching network and resonant tank system, Fig. 2.4.4-1.

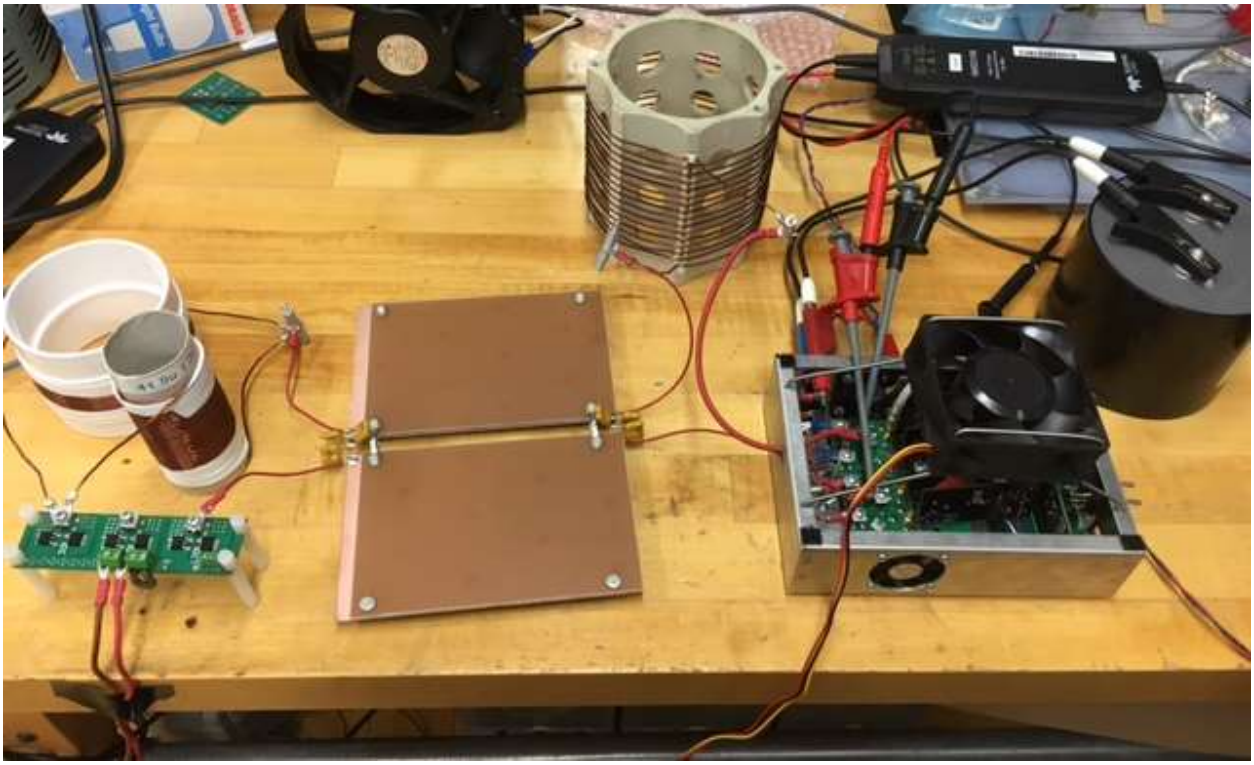

Fig. 2.4.4-1. Proof of concept large gap capacitive power transfer system with air core inductors in the matching network/resonant tank circuit.

Initial Three Phase Large Gap Capacitive Power Transfer System

The initial large gap printed circuit board used a three-phase topology. Three concentric ring traces are present on the PCBs. The double-sided rotor PCB is sandwiched between the single sided stator PCB. The rotating rectifier is located inside the inner most capacitive coupler ring. The rotor PCB would be mounted on the WFSM shaft and the two stator PCBs held parallel to the rotor PCB. This three-phase rotating capacitor has ~500nF of capacitive coupling per phase. Because of the low coupling capacitance, the excitation frequency must be high.

Double sided rotor PCB

Single sided stator PCB

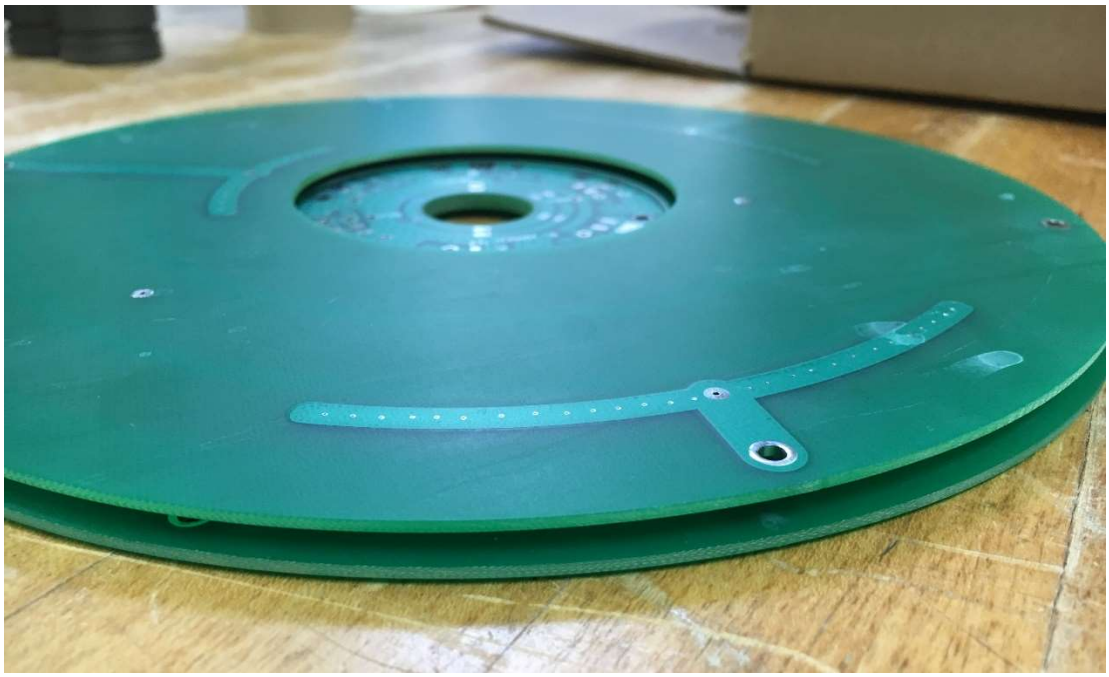

CPC coupling board stack, Rotor “sandwiched” between two PCBs

Fig. 2.4.4-2. Photographs of the initial 3 phase printed circuit board-based CPC. The pads for the rotating rectifier components are visible on rotor board.

The excitation of the three-phase capacitive power transfer system was provided by a three phase GaN based high frequency voltage source inverter (VSI), Fig. 2.4.4-3 that was developed as part of this project. This inverter is capable of switching at 3 to 5 MHz. The main challenge in developing this inverter is the extreme dV/dt induced by the switching of the semiconductors, especially when the dc bus is above 150V. During these conditions, shoot through can occur as the low side gate drive may be triggered by the switching of the high side device. Filters, damping resistors, Schmidt triggers and shielding were investigated to squelch inadvertent turn on of the low side switches.

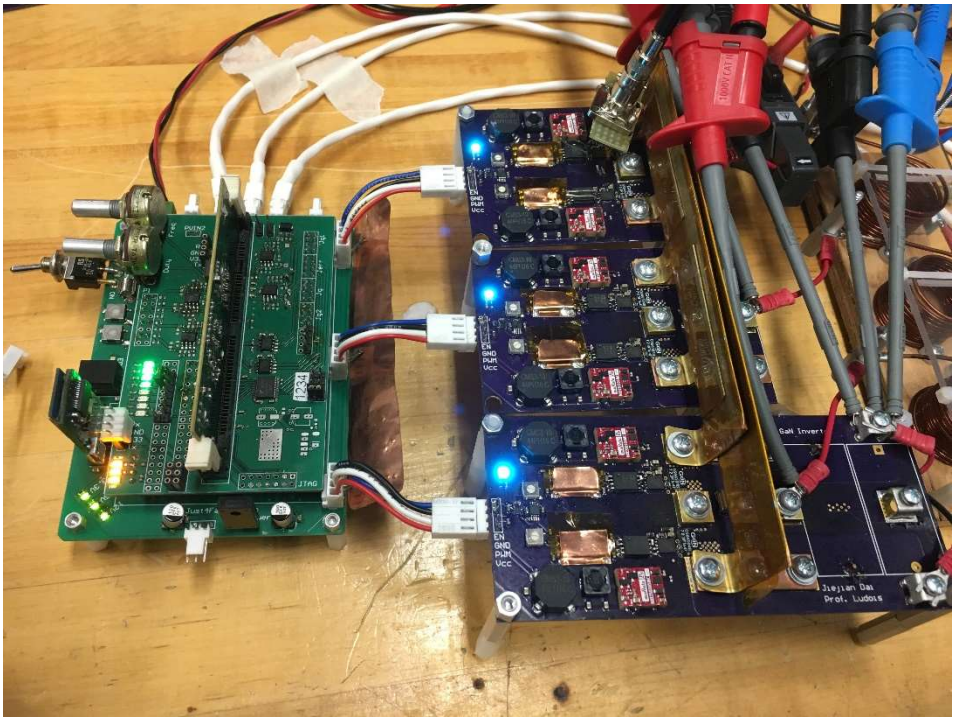

Fig. 2.4.4-3. Initial high frequency 3 phase GaN voltage sourced inverter (VSI), switching at 3 – 5MHz for exciting the three phase CPC.

A full bench assembly is pictured below that displays (from left to right) the controller, another 3.3 MHz GaN HEMT inverter, matching network, resonant inductors, and the prototype capacitive coupler, Fig. 2.4.4-4. The capacitive coupler consists of a single three phase surface rotor board sandwiched between two stator boards of identical facing area. At the center of the rotor board is the SiC rectifier, directly integrated into the coupler rotor. The entire coupler is 10 inches in diameter and 0.375 inches in axial length. It is mounted on a fixture plate that allows for precision control of the axial gap between rotors and stators, enabling study of parameter sensitivity/control. Adjustable air core inductors are used in the matching network and resonant tank circuit. Example ~120 W test results are listed in Table 2.4.4-1 and waveforms in Fig. 2.4.4-5.

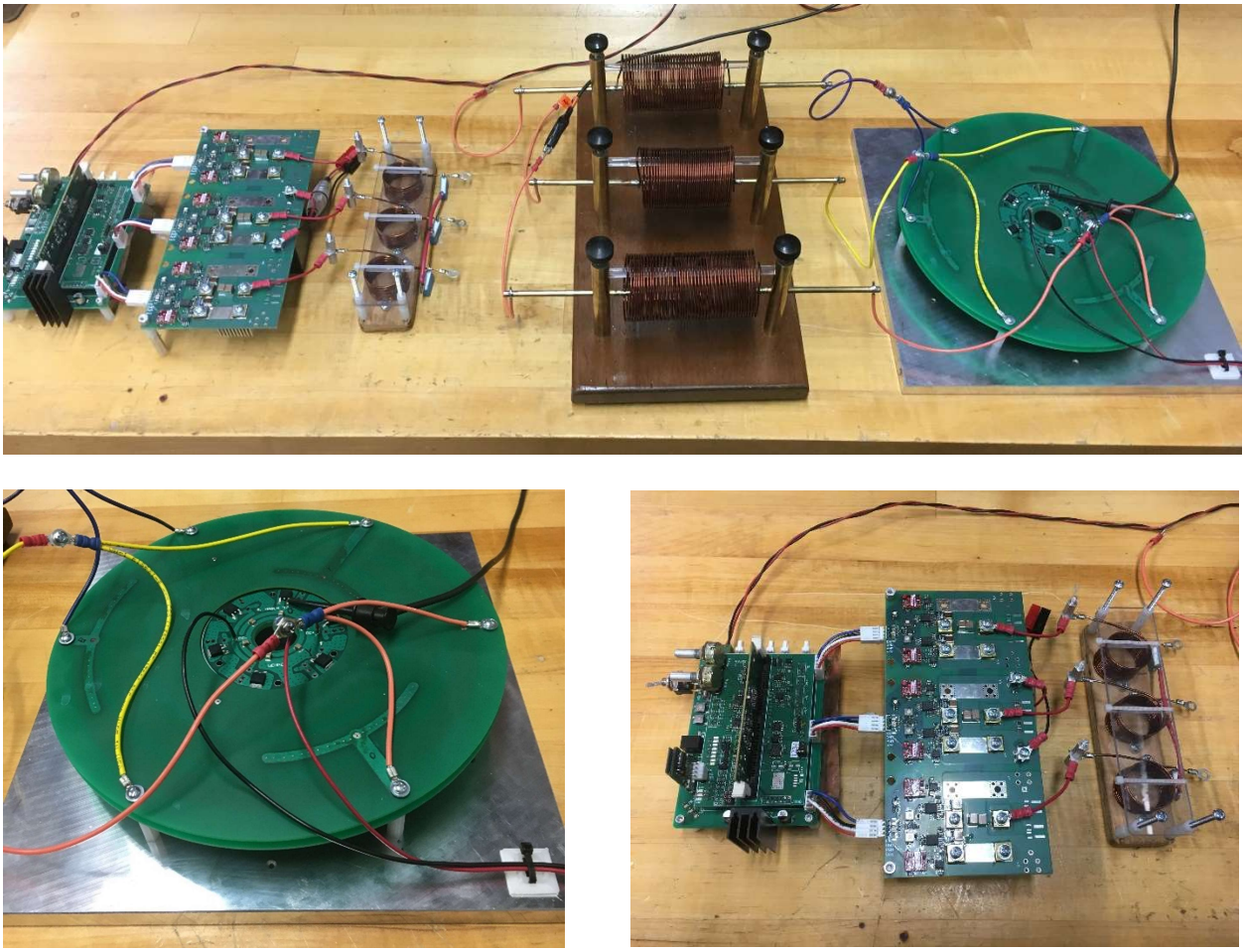

Fig. 2.4.4-4. Initial overall bench test assembly for testing 3 phase GaN inverter, adjustable matching network and resonant tank, and three phase CPC with adjustable gap fixture.

TABLE 2.4.4-1: REPRESENTATIVE INITIAL 3 PHASE CAPACITIVE POWER TRANSFER BENCH TEST ASSEMBLY POWER TRANSFER RESULTS

Parameter	**Description**	**Value**
V_{in} I_{in} P_{in}	Input voltage, current, power	100V, 1.18A, 118W
V_{out} I_{out} P_{out}	Output voltage, current, power	174.6V, 0.641A, 111.9W
η	Efficiency	95%

Parameter	**Description**	**Phase 1**	**Phase 2**	**Phase 3**
I_{r_rms}	Bearing current (rms)	0.6455A	0.5897A	0.699A
V_{C_max}	Bearing voltage (absolute peak)	118.6 V	90.7 V	95 V
V_{C_avg}	Bearing voltage offset	-11.07 V	-0.18 V	5.17 V

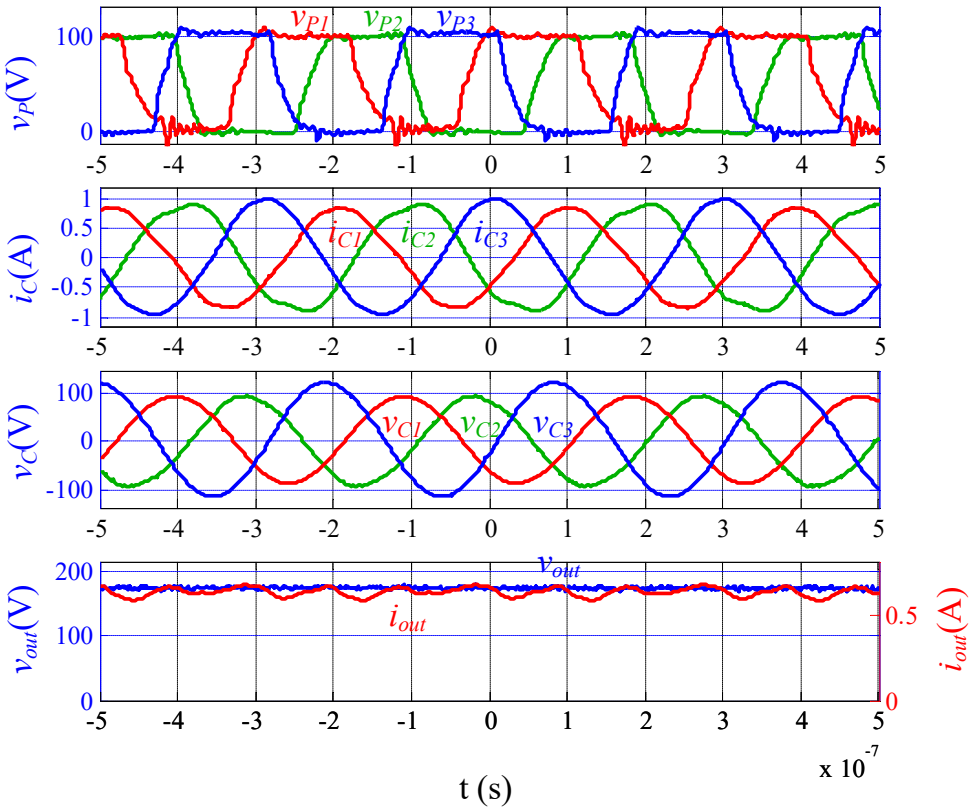

Fig. 2.4.4-5. Representative initial 3 phase capactive power transfer bench test assembly power transfer waveforms.

A burst-mode controller was developed to control throughput power, Fig. 2.4.4-6. The burst mode approach was adopted because it is impossible to regulate current directly on a switching cycle by switching cycle basis at MHz frequencies, thus a mode of control that works on an average basis was devised. Here, burst mode control is effectively controlling the average resonant current injected into the rectifier. Selected command tracking results are provided below. The burst PWM frequency is 10 kHz.

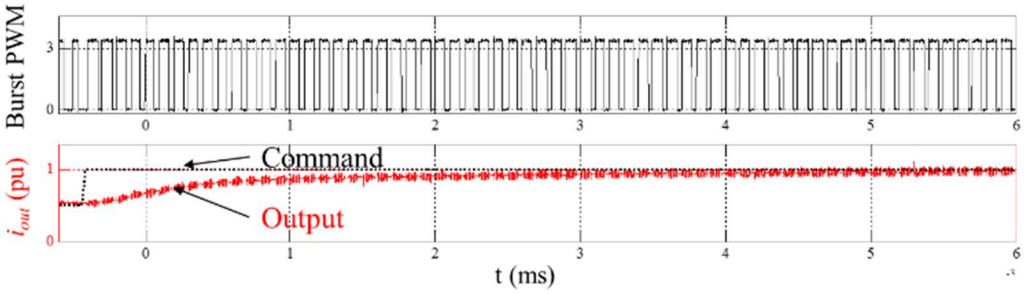

(a) Step up command tracking

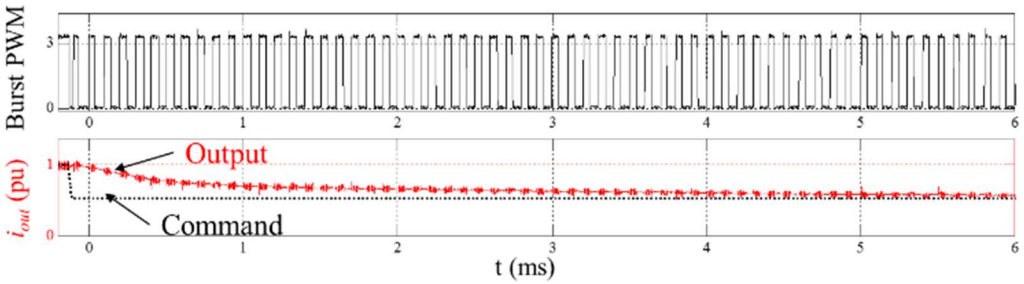

(b) Step down command tracking

Fig. 2.4.4-6. Burst mode current regulator step up and step down transients.

A press-fit rotor hub for the PCB CPC was fabricated and used to mount the printed circuit board coupler on the Generation I machine rotor shaft. Insulated standoffs to hold the PCB stator coupler boards to the non-drive end bell of the motor frame were manufactured and the non-drive end bell drilled/tapped with the mounting pattern for the PCB CPC. Photos of the PCB CPC, mounting mechanism, and overall assembly are shown in Fig. 2.4.4-7 through Fig. 2.4.4-9.

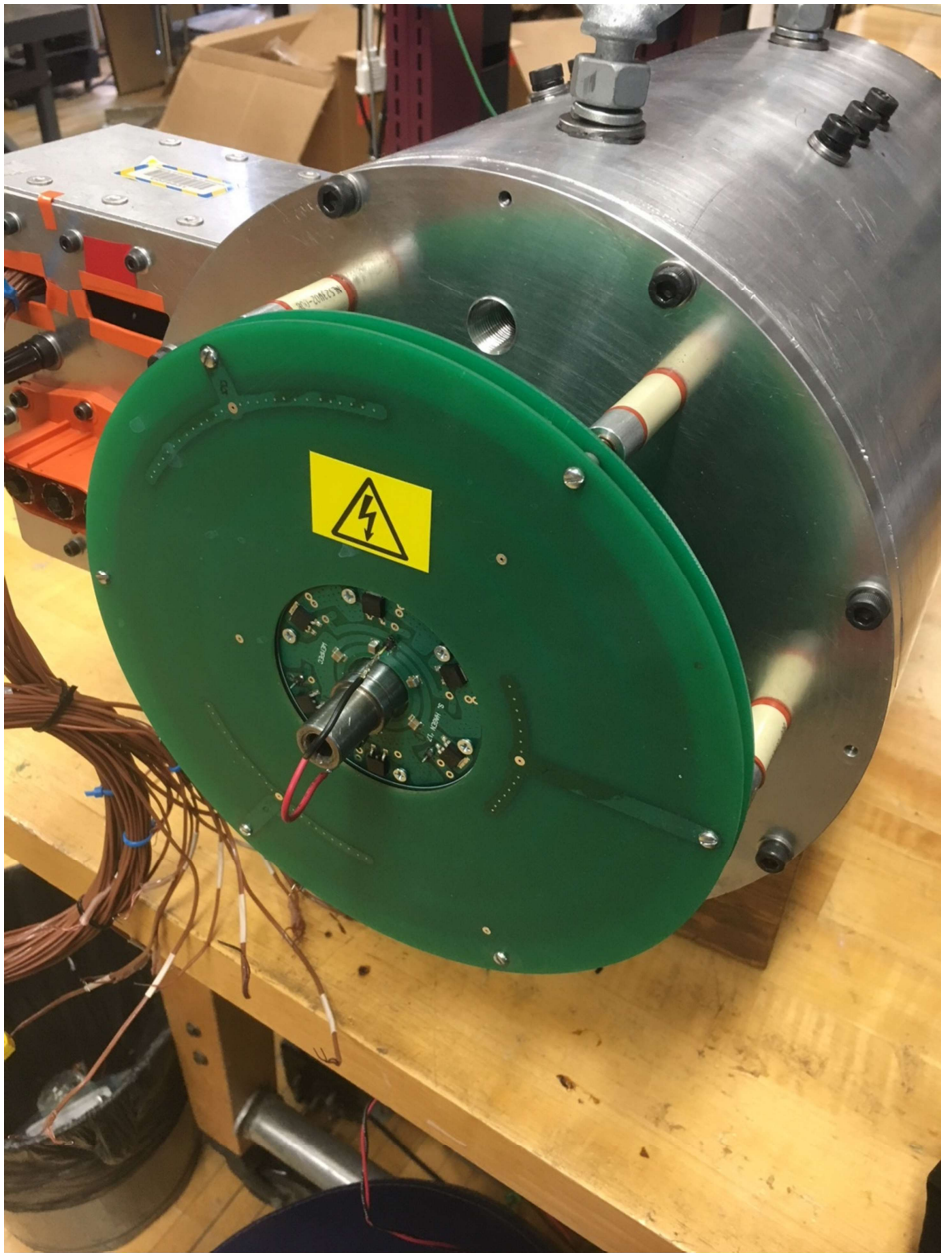

Fig. 2.4.4-7. Three phase Rev 1 PCB CPC mounted on WFSM non-drive end bell with insulating standoffs and press-fit rotor hub.

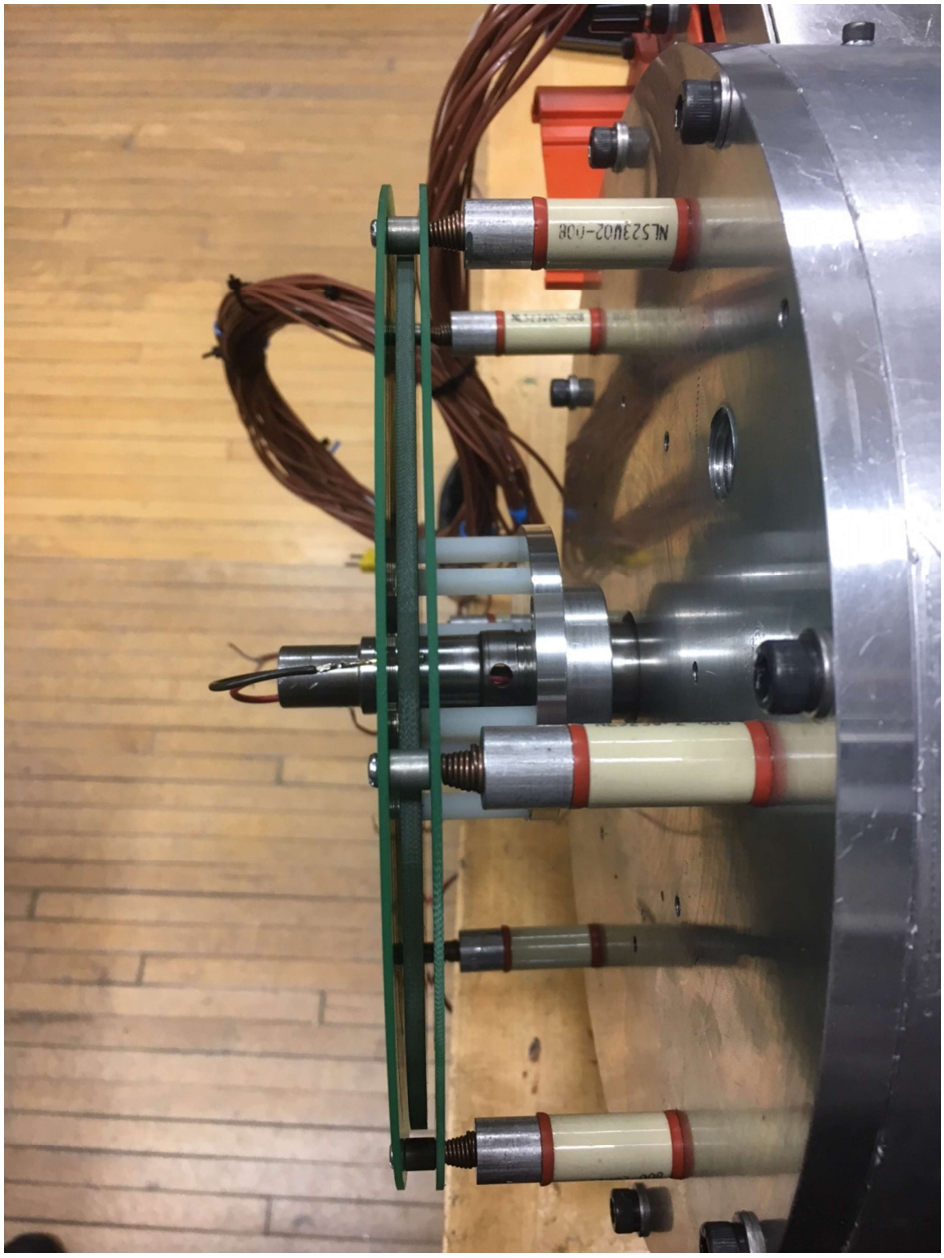

Fig. 2.4.4-8. Three phase Rev 1 PCB CPC mounted on WFSM non-drive end bell with insulating standoffs and press-fit rotor hub.

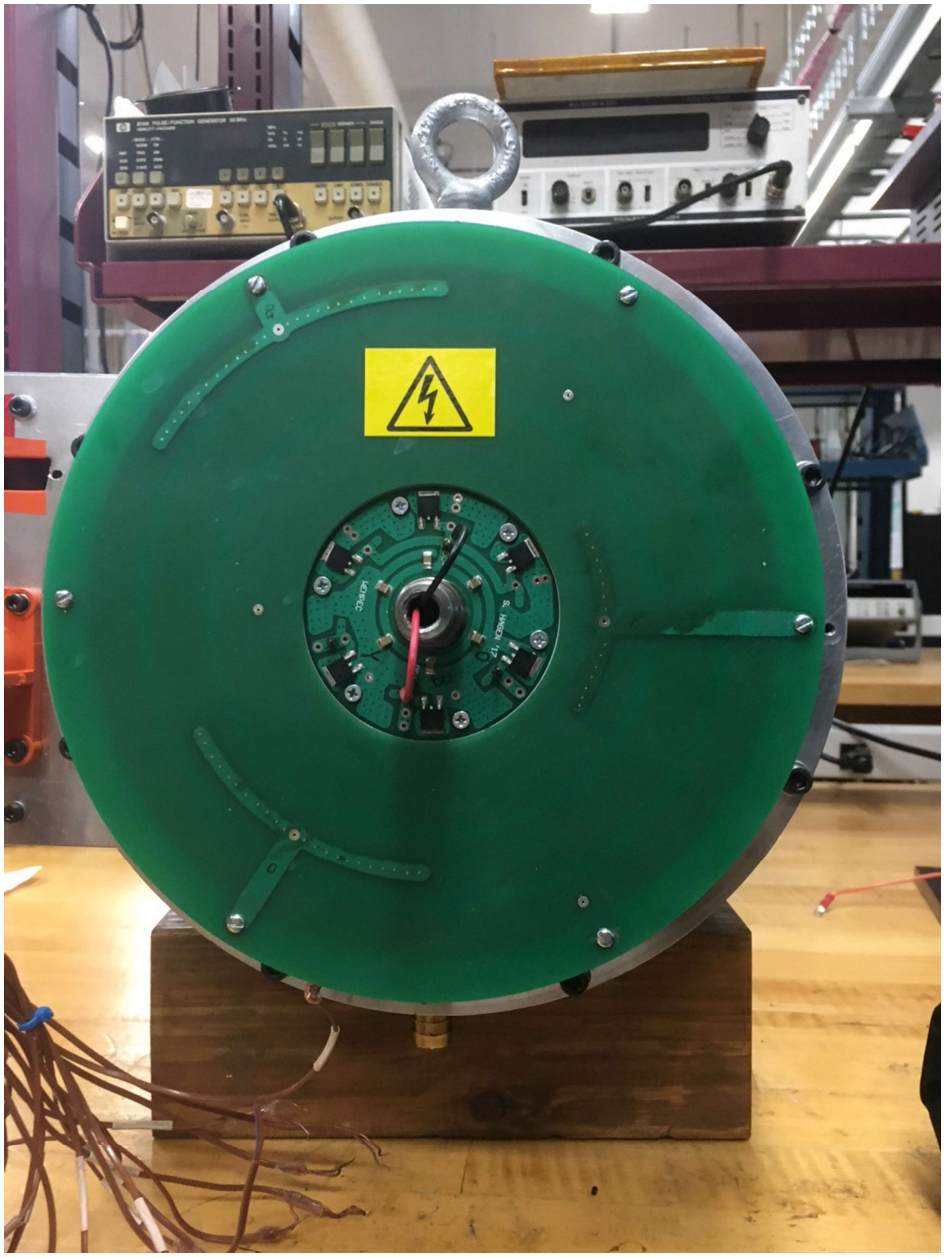

Fig. 2.4.4-9. Three phase Rev 1 PCB CPC mounted on WFSM non-drive end bell with insulating standoffs and press-fit rotor hub.

During power testing of this first three phase CPC prototype, hereafter referred to as “Rev.1” the efficiency was poor (~70%) due to the die electric losses and excessive current circulating in the stray capacitances between electrodes of adjacent capacitor sections.

Revised Three Phase Large Gap Capacitive Power Transfer System

The dielectric material between the traces in standard PCBs is FR4 a glass-filled composite. In areas between the electrodes with high AC electric fields the dielectric losses may be high due to alternating re-polarization of the electric dipoles at high frequency. If FR4 is removed and replaced with air where possible the dielectric loss may be substantially reduced as air has negligible dielectric loss. Extensive finite element analysis was carried out to remove FR4 and improve trace routing where losses are highest. Two design changes were undertaken to reduce the dielectric loss including slotting away of dielectric material, “FR4” between adjacent electrodes of opposite polarity and elimination of overlapping traces by switching from a 4 layer board to a 2 layer board.

The high dielectric losses between adjacent electrode surfaces can be reduced by slotting out the FR4 subject to mechanical constraints. The losses in the FR4 between adjacent electrodes and the effect of slotting can be estimated using finite element analysis, Fig. 2.4.4-10. Slotting between adjacent electrodes on a CPC board can be seen in Fig. 2.4.4-11.

The dielectric losses can further be significantly reduced by elimination of overlapping traces of differing phase/polarity. Instead of using inner trace layers, gaps are left in inner electrode rings to allow traces to pass through to connect the rectifier components near the inner radius of the CPC. Finite element analysis of the electric field displacement intensity with overlapping 4-layer traces and non-overlapping 2-layer traces, Fig. 2.4.4-12. An example gap in the inner electrode and trace passing through it are shown in Fig. 2.4.4-13.

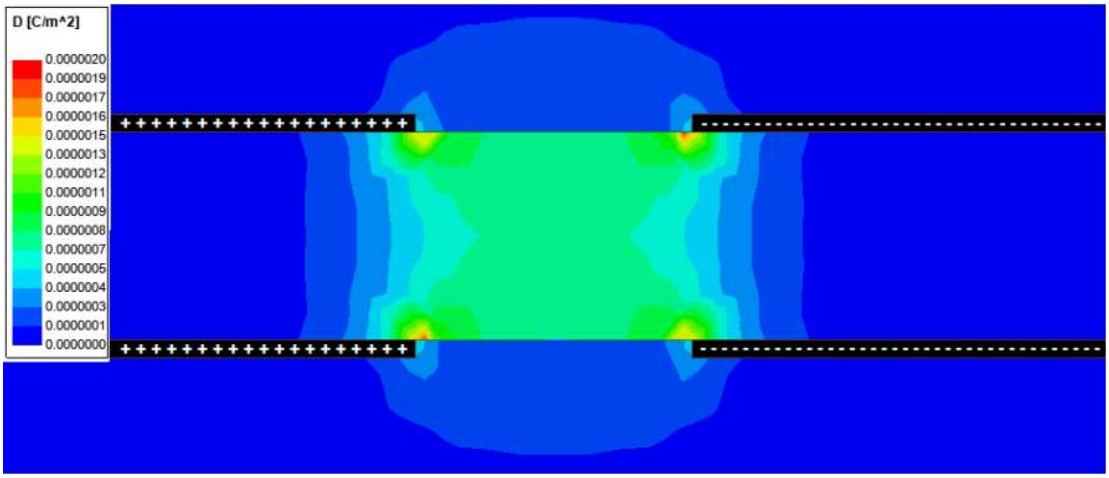

(a)

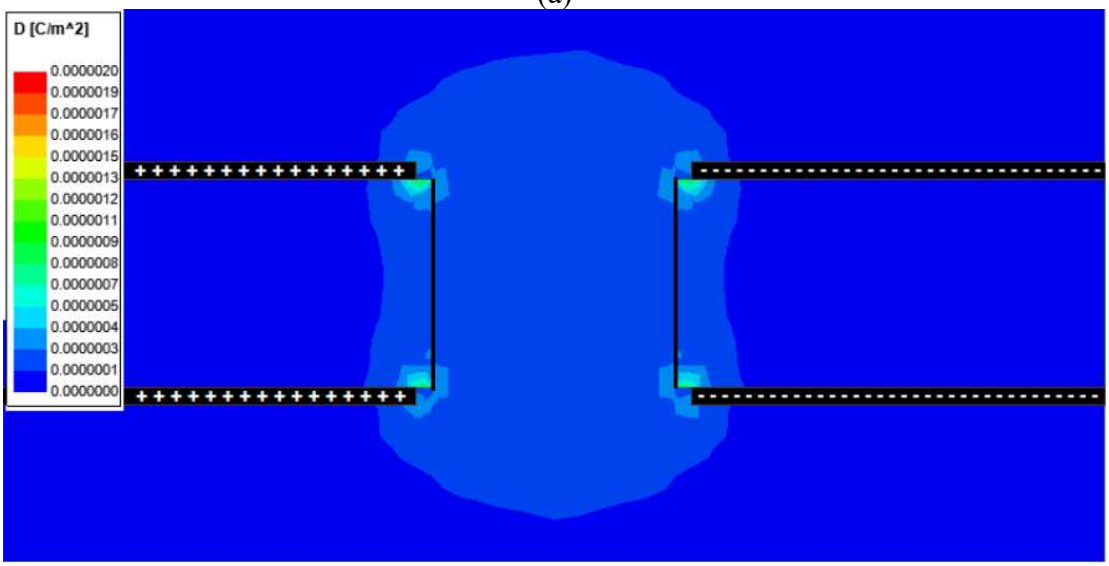

(b)

Fig. 2.4.4-10. Finite element analysis electric field displacement intensity with (a) FR4 between adjacent electrodes and (b) air due to slotting.

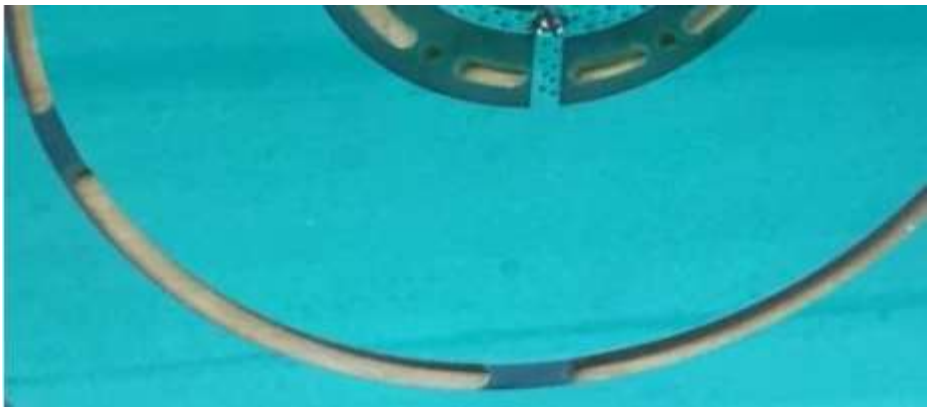

Fig. 2.4.4-11. Example slotting between adjacent CPC electrodes to reduce dielectric losses.

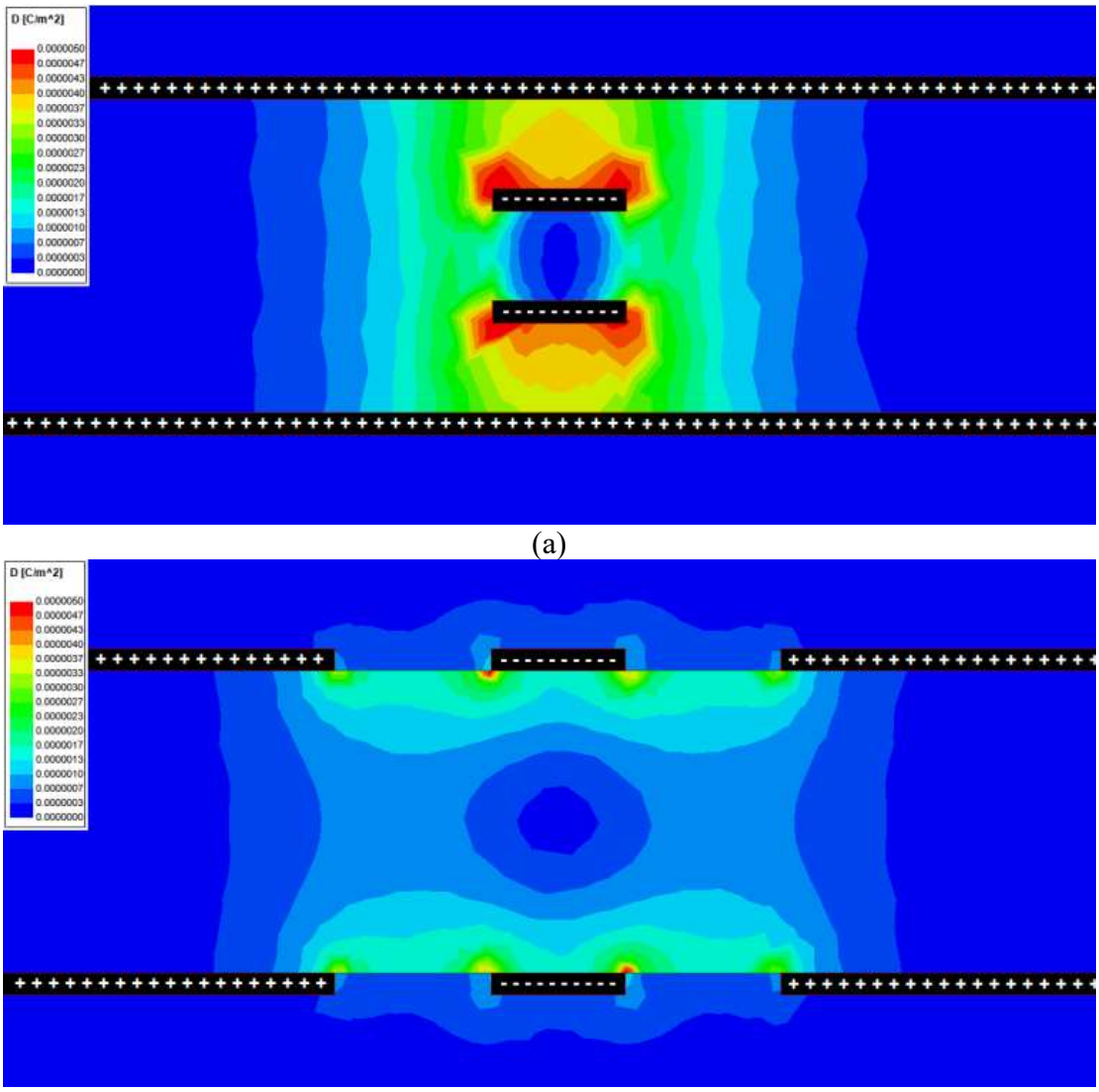

(a)

(b)

Fig. 2.4.4-12. Finite element analysis electric field displacement intensity in (a) overlapping 4-layer traces and (b) non-overlapping 2-layer traces.

Fig. 2.4.4-13. Example 2-layer rotor CPC with connection from outer electrode through gap in inner electrode to rectifier near inner radius.

Two iterations of the printed circuit board (PCB) capacitive power coupler (CPC) are shown below in Fig. 2.4.4-13 below. These PCB CPCs are integrated on the shaft on the wound field synchronous machine (WFSM). Both versions constitute a three-phase capacitive interface wherein the coupling surfaces are integrated into the rotating rectifier board using low cost PCBs. The two versions of the PCB CPC will be referred to as “Rev. 1” and “Rev. 2” going forward in this report.

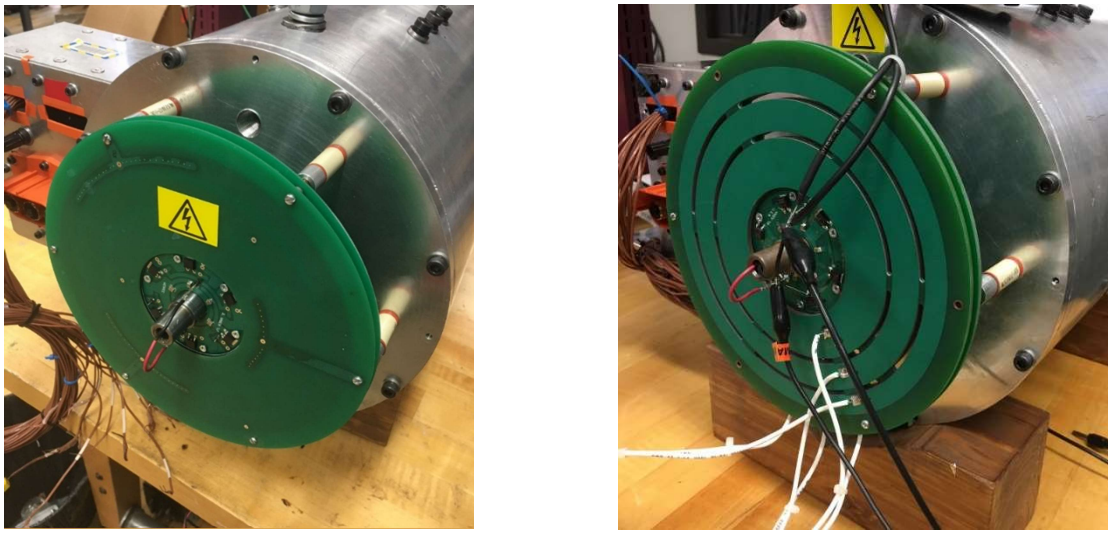

(a) (b)

(c)

Fig. 2.4.4-14. Revisions of PCB CPCs integrated on the a WFSM, (a) – Rev. 1 with no slits and overalpping traces, (b) – Rev. 2 with slits and no overlapping traces, (c) – Rev. 2 with slits and no overlapping traces.

Bench testing of the two CPC revisions revealed the characteristic circuit of the CPCs. Previous journal bearing incarnations had large electrical distances between the coupling surfaces making cross coupling leakage nearly zero. The three phase PCB CPCs have coupling surfaces integrated into a single structure, and the leakage terms are not negligible. These leakage capacitances create paths for circulating displacement currents within the tank, thereby increasing loss, lowering the quality factor and decreasing efficiency. The effective coupling capacitances at 2 MHz were measured for Rev. 1 and Rev. 2 PCBs and are shown in Fig. 2.4.4-15 and 2.4.4-16. The desired coupling from the same phase on one board to another are shown in black. Undesired stray or parasitic phase to phase capacitive couplings on the same PCB board are shown in green. Board to board stray phase to phase capacitive couplings are shown in red. The changes to the coupling capacitances are summarized in Table 2.4.4-II.

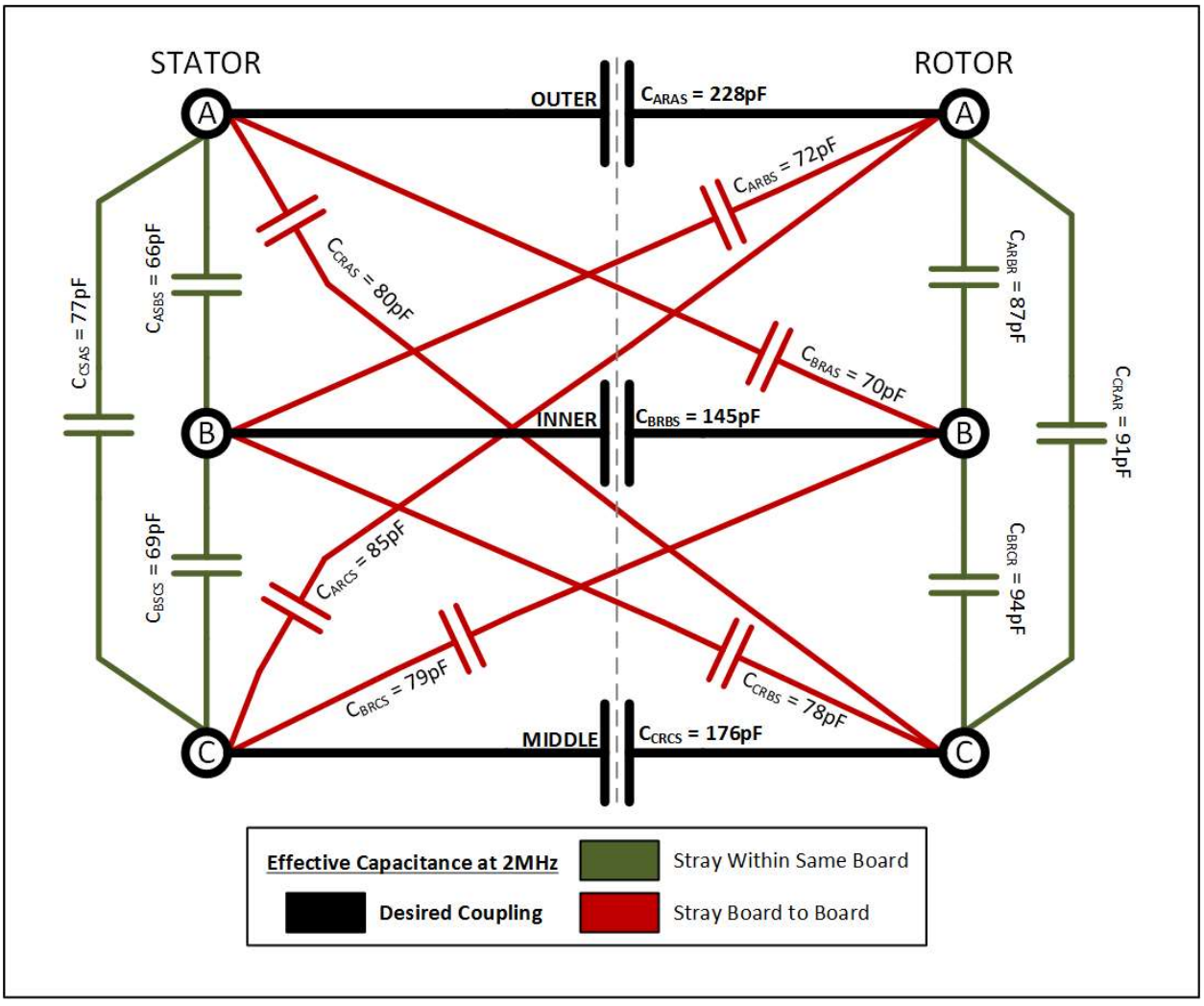

Fig. 2.4.4-15. Rev. 1 PCB effective coupling capacitiances between phases on the same board and the board across the airgap.

Note that the Rev. 1 board has leakage capacitances of the same order of magnitude as the intended (desired) mutual coupling. Also note that the coupling capacitance is not balanced, despite equal gap size and area for each phase. Rev. 2 was created to alleviate these problems. The primary improvements in the Rev. 2 CPC are:

1. No overlapping traces on different PCB layers to reduce phase to phase leakage.
2. Slits have been milled into the boards to introduce an air gap between the phases, thereby decreasing the effective permittivity of the region between conductors residing on a common rotor or stator. This does not diminish the desired mutual coupling between stators and rotors.

The actual surface areas of the boards are no longer equal, but have been scaled according to the different fringing that occurs at each radius. This serves to balance the coupling capacitances.
The modifications to the Rev. 2 board over Rev. 1 are clearly demonstrated in the circuit diagram below and the following Table 2.4.4-II.

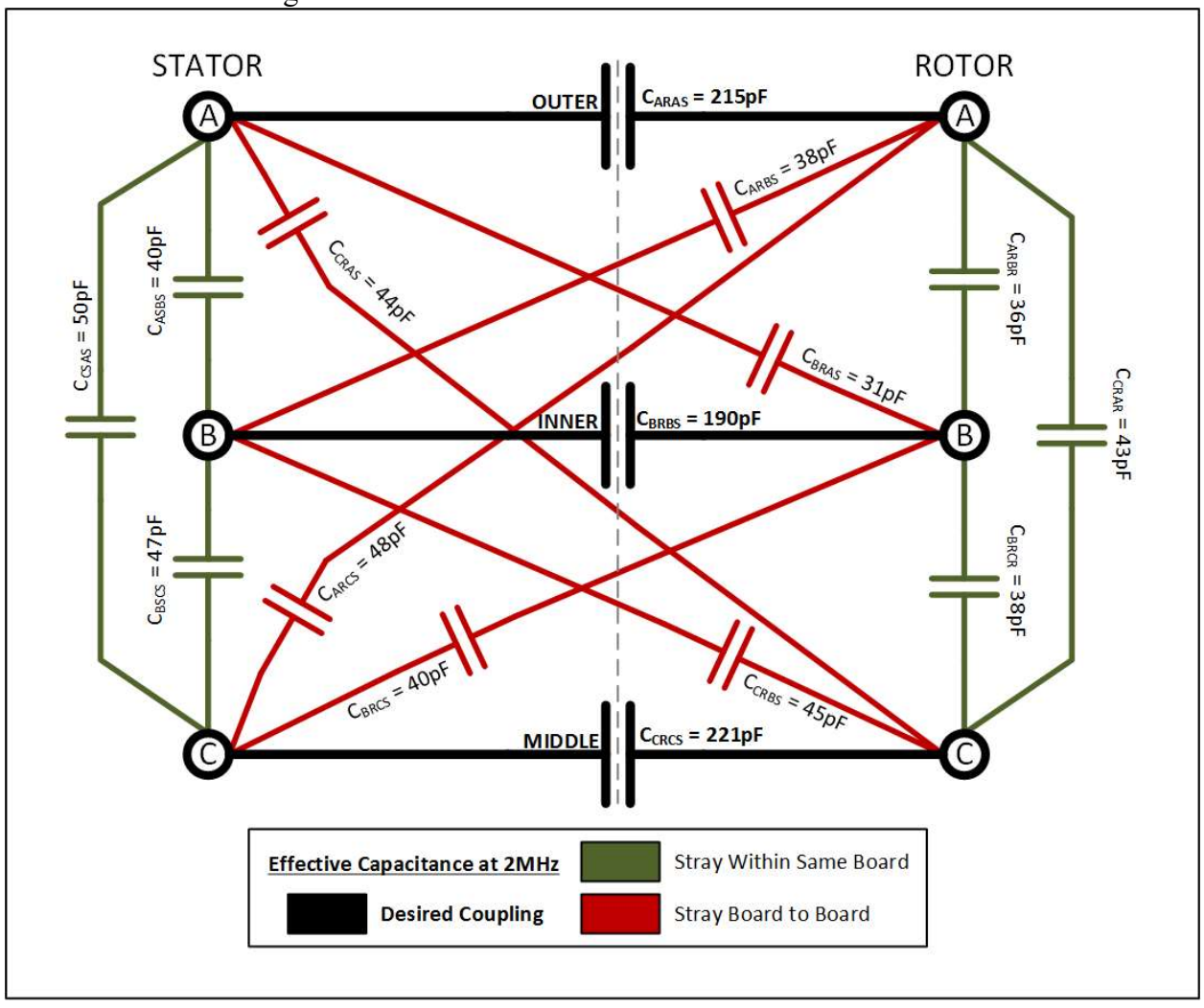

Fig. 2.4.4-16. Rev. 2 PCB effective coupling capacitiances between phases on the same board and the board across the airgap.

TABLE 2.4.4-II: SUMMARY TABLE OF COUPLING CAPACITANCE CHANGE BETWEEN REV. 1 AND REV. 2 PCBS.

CLASS	CAPACITANCE	REV 1 [μμfd]	REV 2 [μμfd]	Δ%
DESIRED COUPLING	C_{ARAS}	228 (+25% from mean)	215 (+3% from mean)	-
	C_{BRBS}	145 (-21% from mean)	190 (-9% from mean)	-
	C_{CRCS}	176 (-4% from mean)	221(+6% from mean)	-
STATOR/ROTOR PARASITIC	C_{ARBS}	72	38	-47%
	C_{ARCS}	85	48	-44%
	C_{BRAS}	70	31	-56%
	C_{BRCS}	79	40	-49%
	C_{CRAS}	80	44	-45%
	C_{CRBS}	78	45	-42%
STATOR SELF PARASITIC	C_{ASBS}	66	40	-39%
	C_{BSCS}	69	47	-32%
	C_{CSAS}	77	50	-35%
ROTOR SELF PARASITIC	C_{ARBR}	87	36	-59%
	C_{BRCR}	94	38	-60%
	C_{CRAR}	91	43	-53%

From Table 2.4.4-II it can be seen that the desired coupling capacitance from the same phase on one board to the same phase on another board remained roughly the same in magnitude or even increased in the average sense from Rev. 1 to Rev. 2. Additionally, the variation from phase to phase was significantly reduced. The stray or parasitic coupling capacitances were significantly reduced from Rev. 1 to Rev. 2. The resonant impedance of the Rev. 1 and Rev. 2 PCB couplers was also measured and plotted in Fig. 2.4.4-17. The equivalent series resistance or impedance of the Rev. 2 coupler is 58% smaller than the Rev. 1 coupler. The reduction in ESR increased the efficiency of the excitation system from 70% (Rev. 1) to 84% (Rev. 2).

The voltage across one of the switches in the 3 phase GaN inverter and the phase output current have also been measured, Fig. 2.4.4-18. Resonant zero-voltage switching is observable. A peak phase current of 6 A has also been captured. The initial target current at the DC output of the rectifier is 5 A for the Generation I WFSM.

The PCB CPC Rev 2 was tested on the bench while mounted to the machine. A DC power supply fed the inverter while the CPC fed the DC rotor winding. Selected measured results are provided in Table 2.4.4-III.

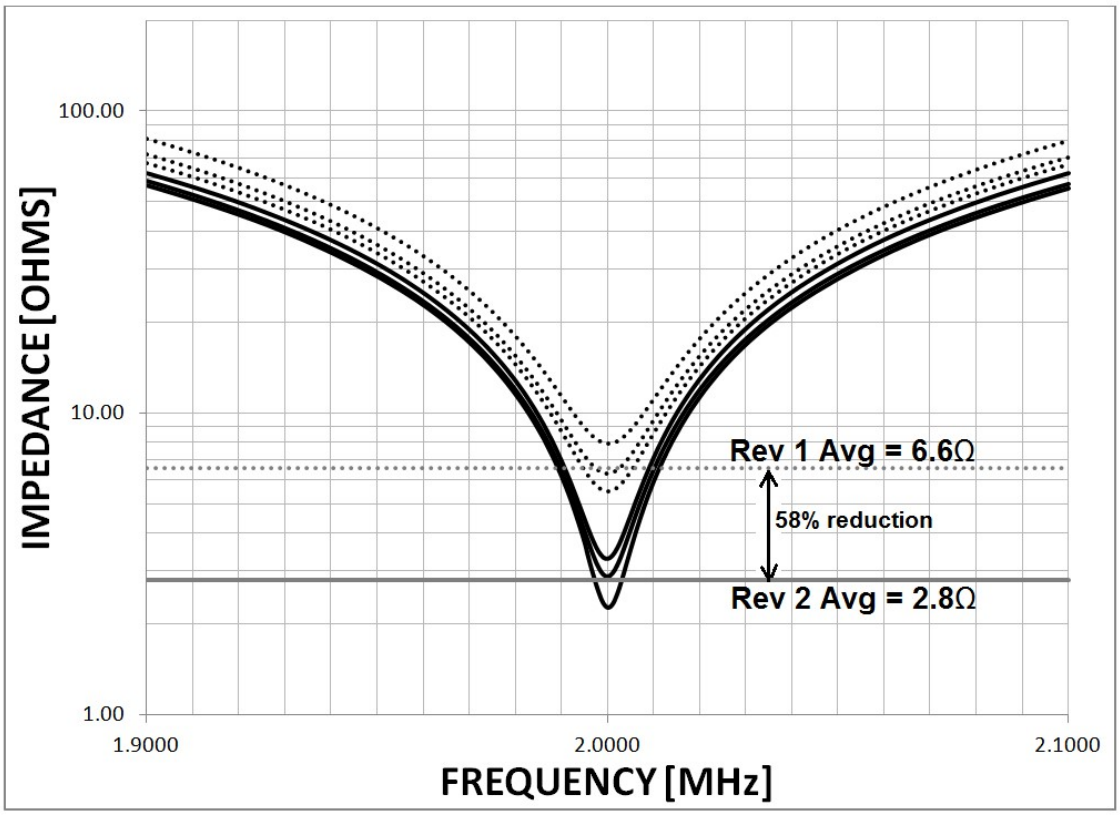

Fig. 2.4.4-17. Bode plots of impedance of each phase to phase connection vs. frequency. Dashed lines (higher ESR) are prototype 1, while solid lines (lower ESR) represent prototype 2, with reduced stray capacitance between phases.

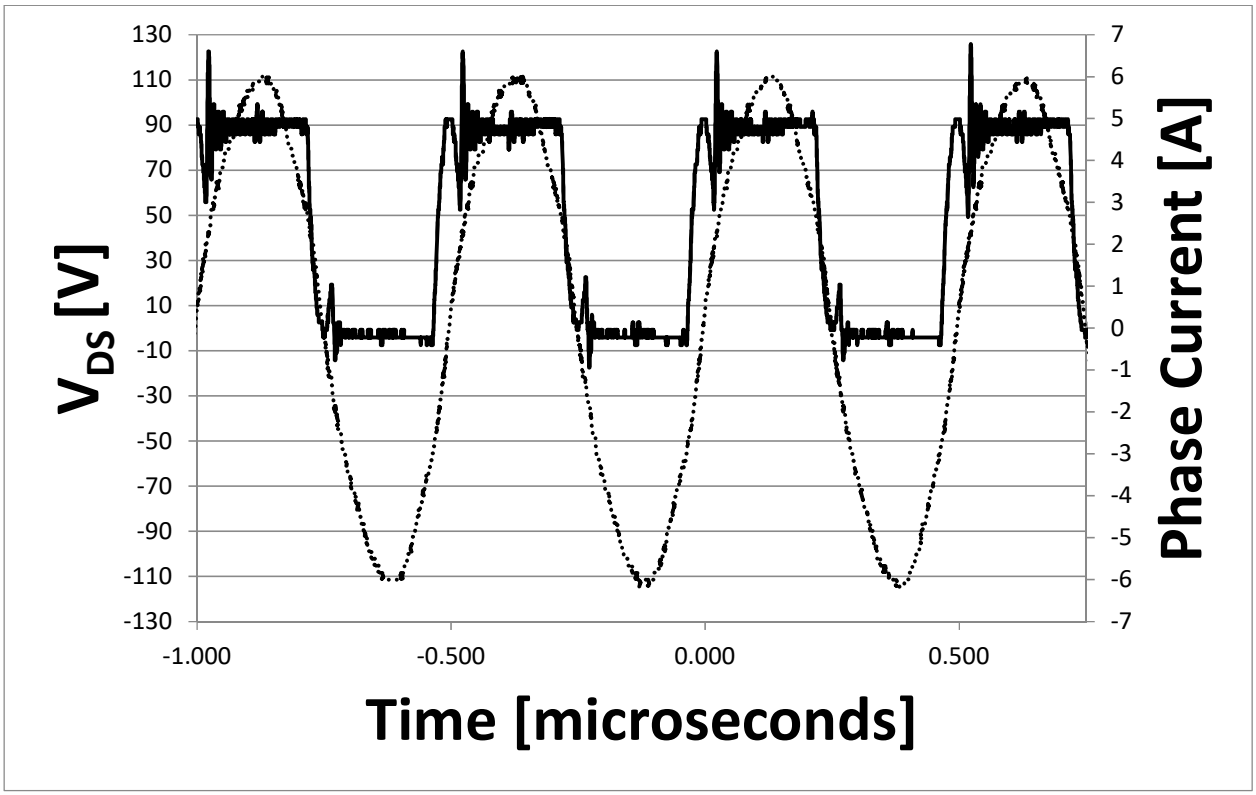

Fig. 2.4.4-18. GaN inverter drain source voltage (single switch) and phase current measurements.

TABLE 2.4.4-III. BENCH TEST DATA OF INTEGRATED REV 2 PCB CPC: DC POWER IN AND OUT

I_{IN}	V_{IN} [v]	I_{OUT} [A]	V_{OUT} [v]	R_{LOAD} [Ω]	P_{IN} [W]	P_{OUT} [W]	EFF %
1.77	**26.9**	**1**	**38.2**	**38.2**	**47.6**	**38.2**	**80.2**
2.62	**41.8**	**1.5**	**58.8**	**39.2**	**109.5**	**88.2**	**80.5**
3.39	**56.8**	**2**	**78.9**	**39.5**	**192.5**	**157.8**	**82.0**
4.14	**72.2**	**2.5**	**99.6**	**39.8**	**298.9**	**249.0**	**83.3**
4.88	**90.3**	**3**	**123.3**	**41.1**	**440.7**	**369.9**	**84.0**
5.7	**105.9**	**3.5**	**145**	**41.4**	**603.0**	**507.0**	**84.1**

Single Phase Large Gap Capacitive Power Transfer System

Benchtop testing of the PCB based 3 phase CPC demonstrated the necessary operation, but throughput power and efficiency were limited by the ESR of the coupler and circulating current/tuning issues associated with imbalance among the three phases. Since the bottle neck was the CPC and not the GaN inverter, the decision was made to go to a single-phase CPC. Although from power transfer first principles perspective 3 phases should deliver more power, the implementation issues associated with leakage and imbalance (in the current CPC form factor) are a drawback. Additionally, the switches of the GaN inverter are underutilized and the elimination of a phase leg will save cost without degrading the capability of the inverter for the intended application. Tradeoffs between the single phase and three phase CPC coupling structures are detailed in the table below. A comparison of the single-phase CPC rotor board and Rev. 2 three phase CPC rotor board are shown in Fig. 2.4.4-19. The single-phase CPC was measured to have lower ESR and less leakage per unit coupling capacitance than its three-phase counterpart as plotted in Fig. 2.4.4-20.

TABLE 2.4.4-IV. COMPARISON OF SINGLE PHASE AND THREE PHASE CAPACITIVE POWER TRANSFER SYSTEMS

	Capacitance Utilization	Drive Electronics & Passive Components	Leakage Capacitance and Dielectric Loss	Tuning Difficulty and Circulating Current Issues
Single Phase	**Worse**	**Simpler**	**Better**	**Simpler**
Three Phase	**Better**	**More complex**	**Worse**	**More complex**

The prototyped single-phase CPC coupling structure is pictured beside its three-phase counterpart in Fig. 2.4.4-19.

Fig. X.XX-19. Single phase CPC rotor board (left) and three phase CPC rotor board (right)

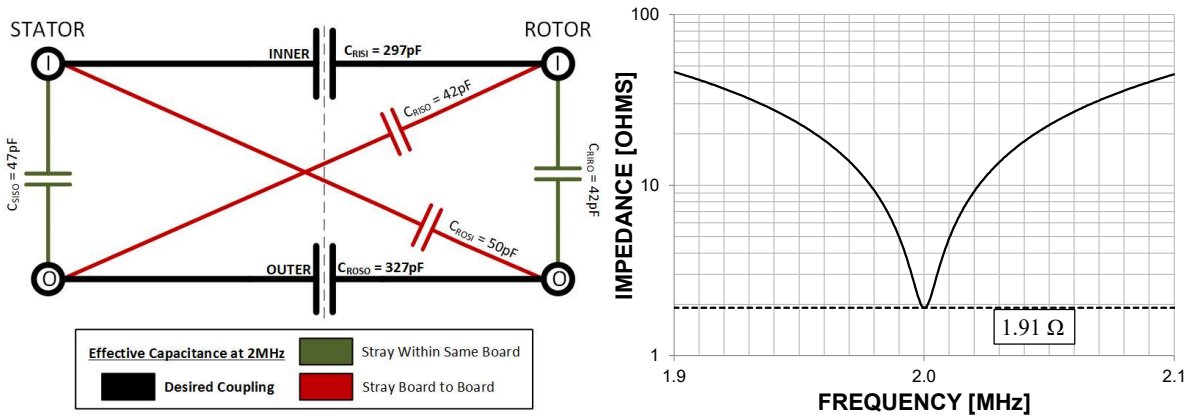

Fig. 2.4.4-20. Measured single phase CPC capacitive coupling (left) and tank impedance (right)

Single Phase GaN Inverter

The inverter to drive the system was reduced from three phase legs to two, making it a single-phase inverter, Fig. 2.4.4-21. The inverter design itself is largely the same as before, except the control board has become analog, rather than digital. The switching frequency of the inverter is generated by a voltage-controlled oscillator (VCO) which will form the backbone of a Phase Lock Loop (PLL) to track the resonance of the rotor.

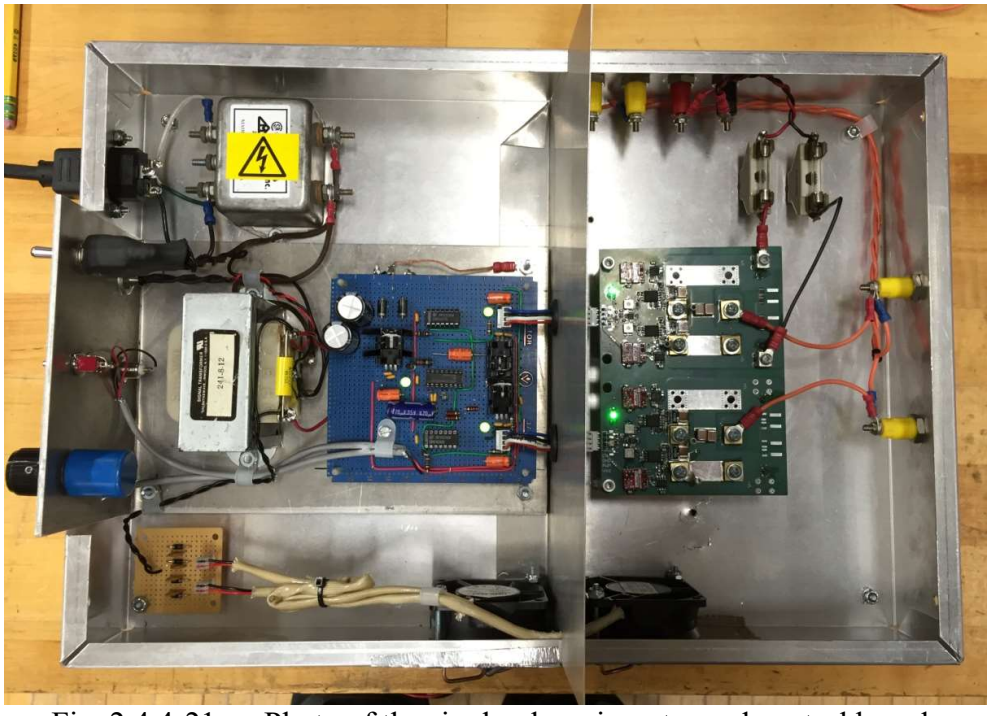

Fig. 2.4.4-21. – Photo of the single-phase inverter and control board.

Additionally, the air core inductors of the tank have been replaced by those with distributed gapped ferrite cores to minimize core loss, minimize conduction loss, minimize the volume, and withstand kV peak voltages within the resonant tank circuit. The basic idea for the distributed gapped ferrite core is based on:

> R. S. Yang, A. J. Hanson, D. J. Perreault and C. R. Sullivan, "A low-loss inductor structure and design guidelines for high-frequency applications,"*2018 IEEE Applied Power Electronics Conference and Exposition (APEC)*, San Antonio, TX, 2018, pp. 579-586.

The CAD design of the core design for the resonant tank inductor is shown in Fig. 2.4.4-22. The distributed gap ferrite core inductor and the equal value air core inductors are shown in Fig. 2.4.4-23.

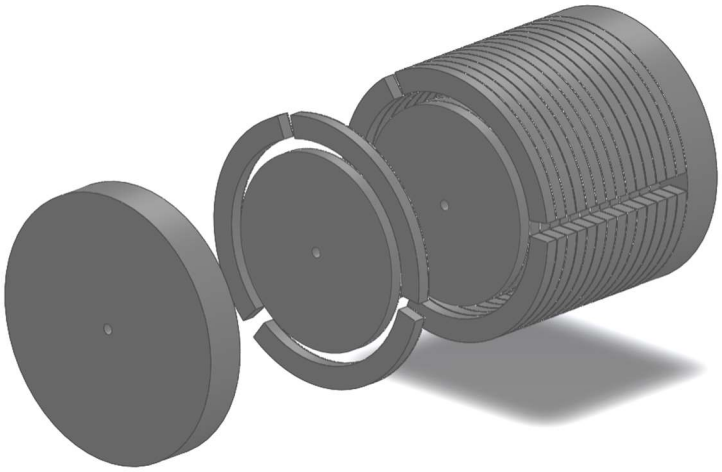

Fig. 2.4.4-22. CAD design for ferrite core resonant tank inductors.

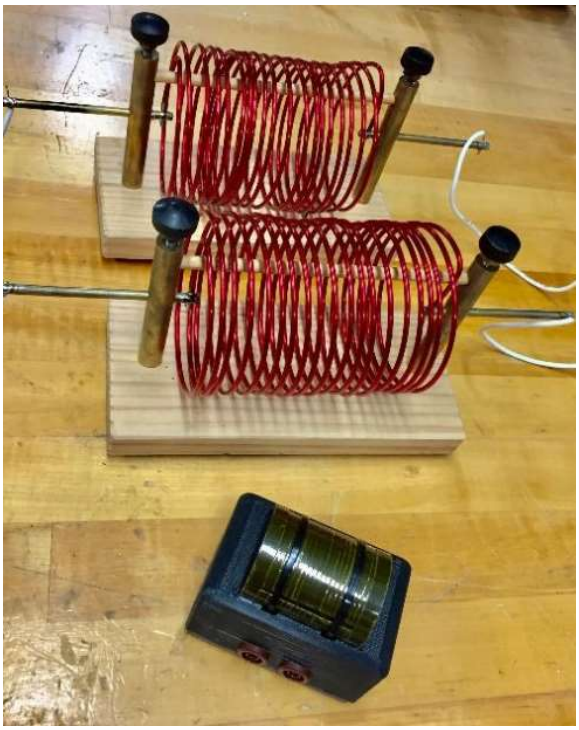

Fig. 2.4.4-23. Distributed gap ferrite core inductor (bottom) and air core inductors (top) of equal value.

Bench Testing of Single-Phase Large Gap CPC

The bench testing of the single-phase CPC is summarized in the two tables below, Table 2.4.4-V and Table 2.4.4-VI for different field resistances. Input DC power to the inverter and output DC power to the field winding were recorded. The CPC tank was driven at 2MHz. Tests with a rotor field resistance of 38.5 Ω generated excessive loss in the CPC due to ESR currents. During testing with the lower field resistance, efficiency was limited to 83%. To meet the necessary power requirement efficiently, the rotor resistance was increased to 92 Ω, thereby reducing the ESR losses of the CPC via reduced current and increased voltage. In some cases, it is difficult to wind the WFSM field winding with a sufficient number of turns to increase the field resistance.

TABLE 2.4.4-V. SINGLE-PHASE CPC BENCH TESTING DATA AT 2MHZ,

FIELD RESISTANCE: 38.5 Ω

I_{IN}	V_{IN}	I_{OUT}	V_{OUT}	P_{IN}	P_{OUT}	EFF %
0.681	18.60	0.50	20.74	12.65	10.37	81.98
1.35	36.37	1.00	40.26	49.10	40.26	82.00
1.96	57.20	1.49	61.49	112.11	91.62	81.72
2.59	77.62	2.00	81.21	201.04	162.42	80.79
3.17	95.00	2.51	100.58	301.15	252.46	83.83

TABLE 2.4.4-VI. SINGLE-PHASE CPC BENCH TESTING DATA AT 2MHZ,

FIELD RESISTANCE: 92 Ω

I_{IN}	V_{IN}	I_{OUT}	V_{OUT}	P_{IN}	P_{OUT}	EFF %
1.30	85.54	1.05	96.19	111.20	101.00	90.83
1.83	121.77	1.47	136.51	222.84	200.67	90.05
2.25	151.72	1.82	169.54	341.37	308.56	90.39
2.66	185.19	2.25	206.36	492.61	464.31	94.26
3.06	216.43	2.58	238.94	662.28	616.47	93.08

Buck Converter Integrated into the Rotating Rectifier

As seen in Table 2.4.4-V and 2.4.4-VI additional resistance, field resistance in the WFSM, provides a more desirable high-Z load for the CPC. However, by including one additional power transistor and a simple fixed duty ratio gate control on the CPC rotor board, a rotor buck converter can be formed as shown in Fig. 2.4.4-24. The resulting impedance matching would allow the CPC (better suited for high-Z loads) to feed a low-Z field winding. The advantage of a buck converter on the rotor will be that the wire gauge on the rotor may be heavier, providing more mechanical robustness and easier winding. The fixed duty cycle buck converter has been integrated into the single-phase CPC, Fig. 2.4.4-25 and Fig. 2.4.4-26.

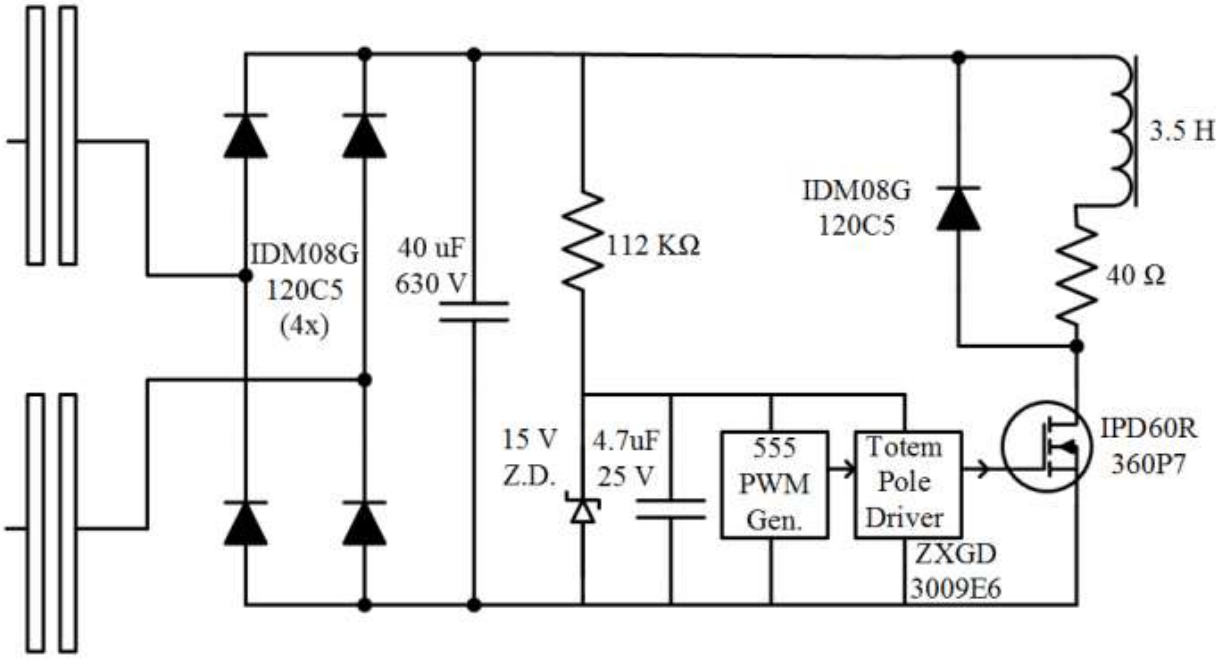

Fig. 2.4.4-24. Fixed duty cycle Buck converter integrated into the rotating rectifier.

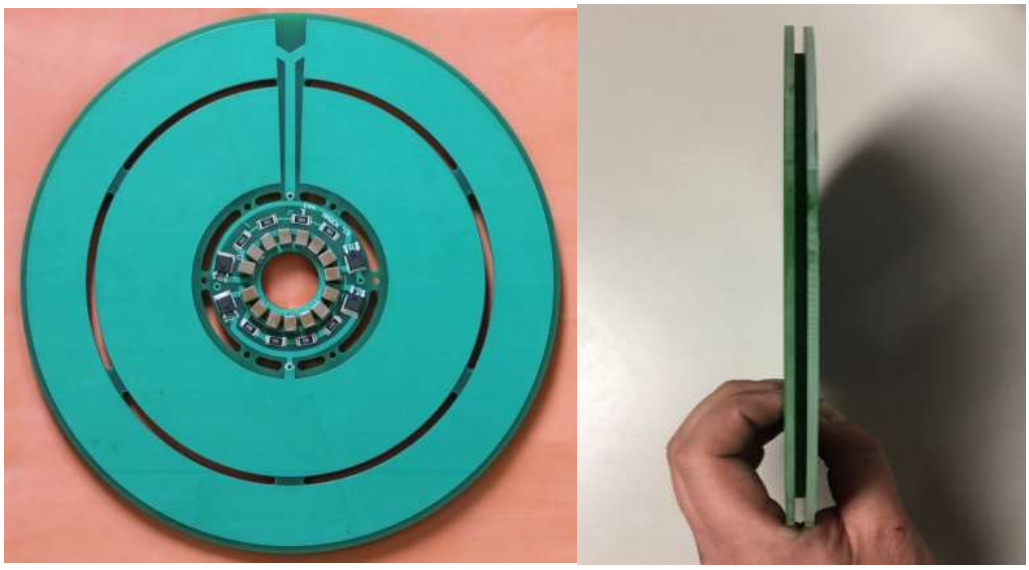

Fig. 2.4.4-25. Single-phase CPC with integrated fixed duty cycle buck converter.

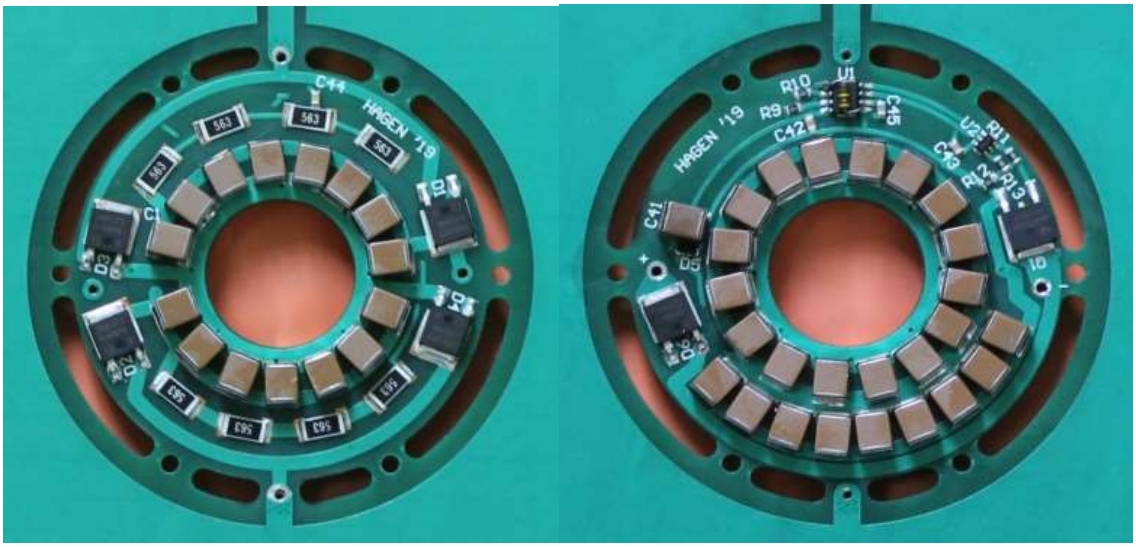

Fig. 2.4.4-26. Fixed duty cycle buck converter and rotating rectifier.

High Frequency Current Sensing and PLL to Maintain Soft-Switching Resonant Operation

An automatic frequency control system for the GaN inverter has been constructed based on conventional phase locked loop (PLL) methods, which holds the GaN inverter at the resonant frequency of the tuned circuit which is made up of the coupling capacitors and their series resonant inductors, Fig. 2.4.4-27.

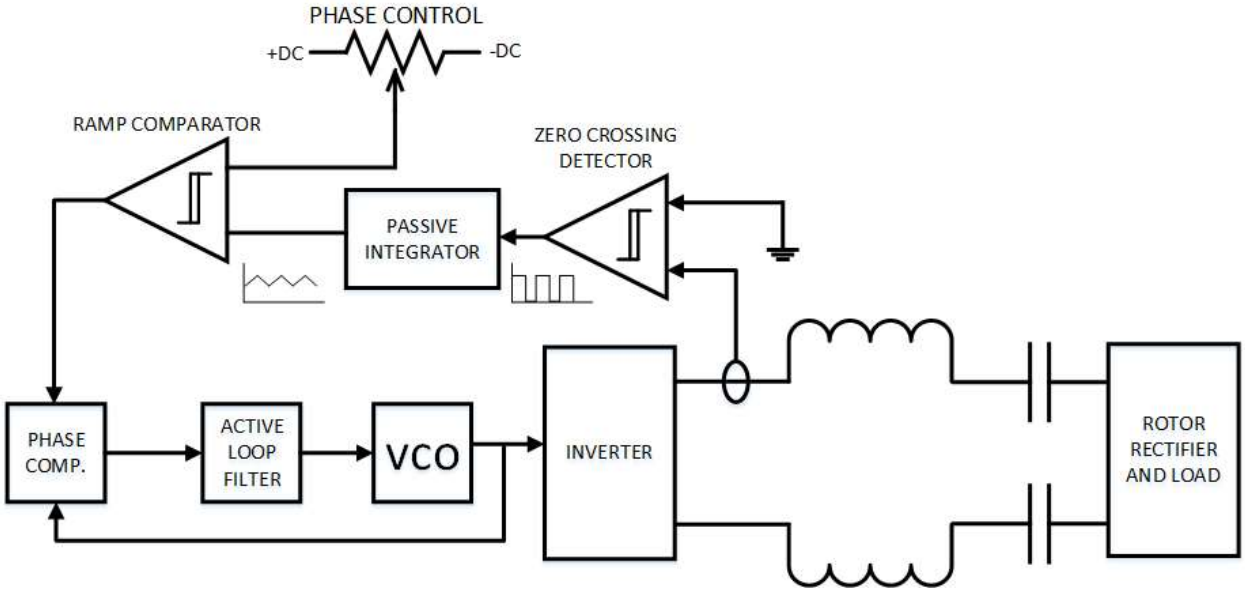

Fig. 2.4.4-27. Inverter control system overview, showing the use of a DC control voltage to adjust the phase relationship between inverter output voltage and current.

A radio frequency current transducer was constructed to allow measurement of inverter output current, Fig. 2.4.4-28. A powdered iron toroid is wound with 25 turns of 24AWG magnet wire. A grounded copper tube passing through the center provides electrostatic shielding. RG58 coaxial cable is brought to a 50 Ω termination in the inverter controller, developing 2 volts/amp at the input terminals of the zero-crossing detector. A comparator converts the zero crossing of the

measured sinusoidal current into a 50% duty cycle square wave. The square wave is passed through a passive RC integrator, converting it into a triangle wave. A second comparator is triggered when the linearly rising edge of the triangle wave crosses an adjustable DC threshold voltage, allowing a linearly adjustable phase delay to be inserted in the phase feedback path.

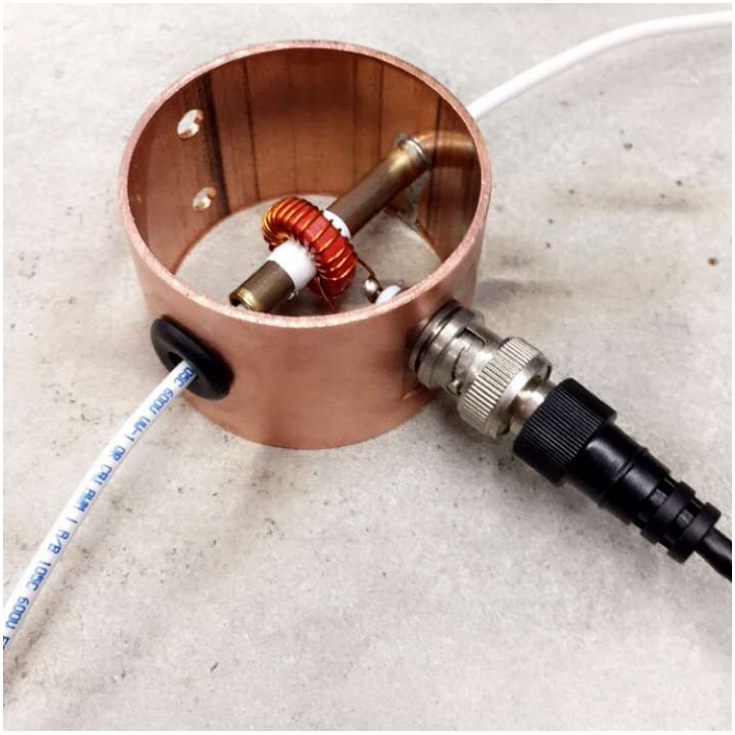

Fig. 2.4.4-28. Photo of RF current transducer (Transformer).

Finally, phase timing of the measured current (with added adjustable delay) is compared with the phase of the voltage-controlled oscillator which controls the GaN inverter gates. By varying the phase relationship between inverter output voltage and current, the system can be tuned for near-zero current switching, thus maximizing efficiency. Once this phase relationship is set, the PLL maintains the proper phase relationship for maximum efficiency over whatever range of switching frequency is required to accommodate slight variations in coupler capacitance, during rotation of the WFSM or other environmental changes in the system which would affect its resonant frequency.

The voltage-controlled oscillator gate control of the GaN inverter was tested to determine the proper phase relationship for minimum power loss in the inverter through soft switching. Fig. 2.4.4-29 demonstrates the impact of phase control on the phase relationships between the voltage and current. Proper soft switching is demonstrated in the middle plot of the Figure. The new control scheme allows for variations in the coupling and tank circuits to be adjusted for on the fly.

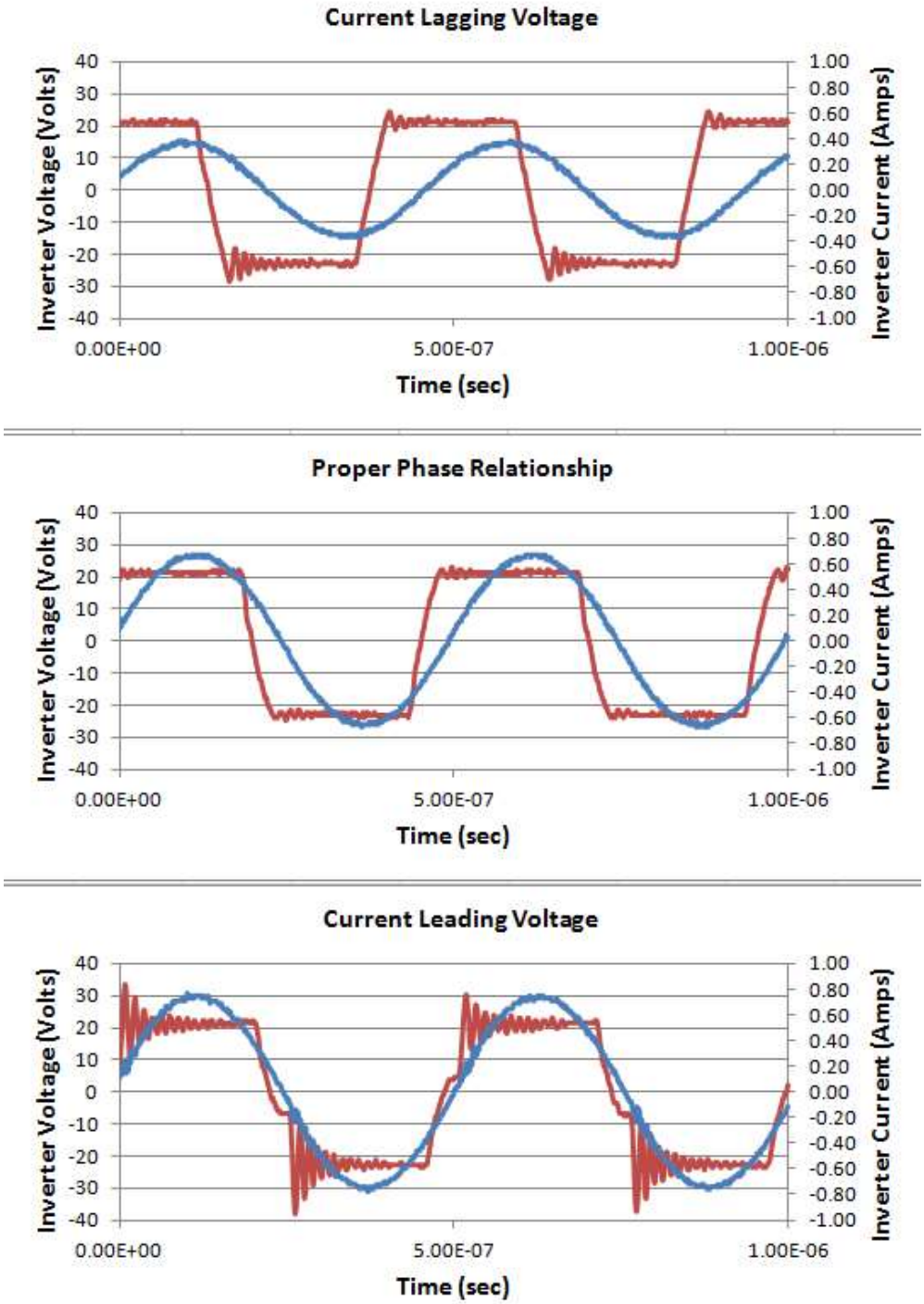

Fig. 2.4.4-29. The above plots show the effect of the phase angle control. The center plot is the point at which peak efficiency is obtained. Soft switching is evidenced by clean voltage and current waveforms. Upper and lower images show effects of shifting the phase relationship either direction from its optimum value.

Overall Capacitive Power Transfer System with First Generation Single Phase GaN Inverter

The overall capacitive power transfer system which incorporates the developments mentioned previously is shown in Fig. 2.4.4-30. The overall system can also be seen in Fig. 2.4.4-31 with the CPC and a fixed duty cycle buck converter mounted on the 1st generation WFSM. Bench test experimental results for this system measuring DC in and DC out are listed in Table 2.4.4-VII. The system is capable of brushless transferring more than 600 W of power at an efficiency of slightly more than 90%.

This system uses what will be termed the first-generation single phase GaN inverter. Another single phase GaN inverter developed as part of DE-EE0008869 and capable of 7 MHz switching frequencies was also tested with WFSMs developed as part of this project. This GaN inverter will be referred to as the second generation GaN inverter. Certain developments such as the fixed duty ratio buck converter and PLL soft-switching controller were not tested in combination with the 2nd generation GaN inverter and the WFSMs developed as part of this project.

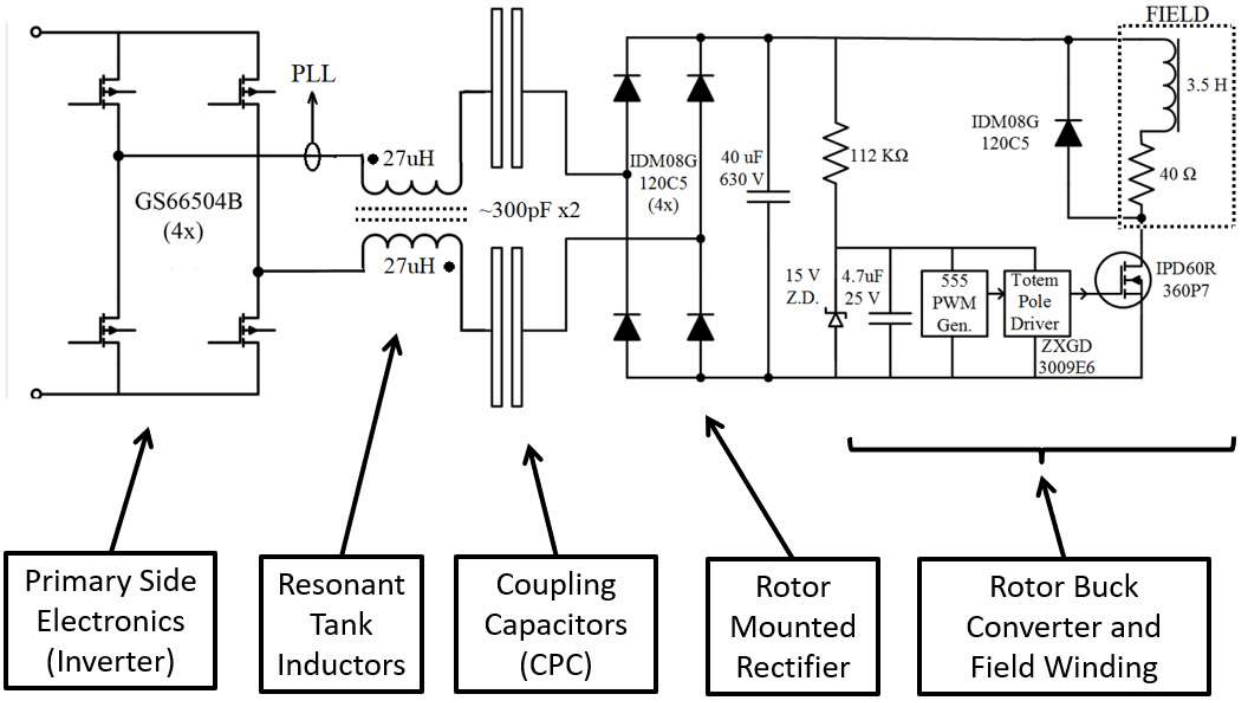

Fig. 2.4.4-30. The overall system architecture of the single phase capacitive power transfer system with first generation GaN inverter and fixed duty cycle buck converter on the rotor CPC PCB.

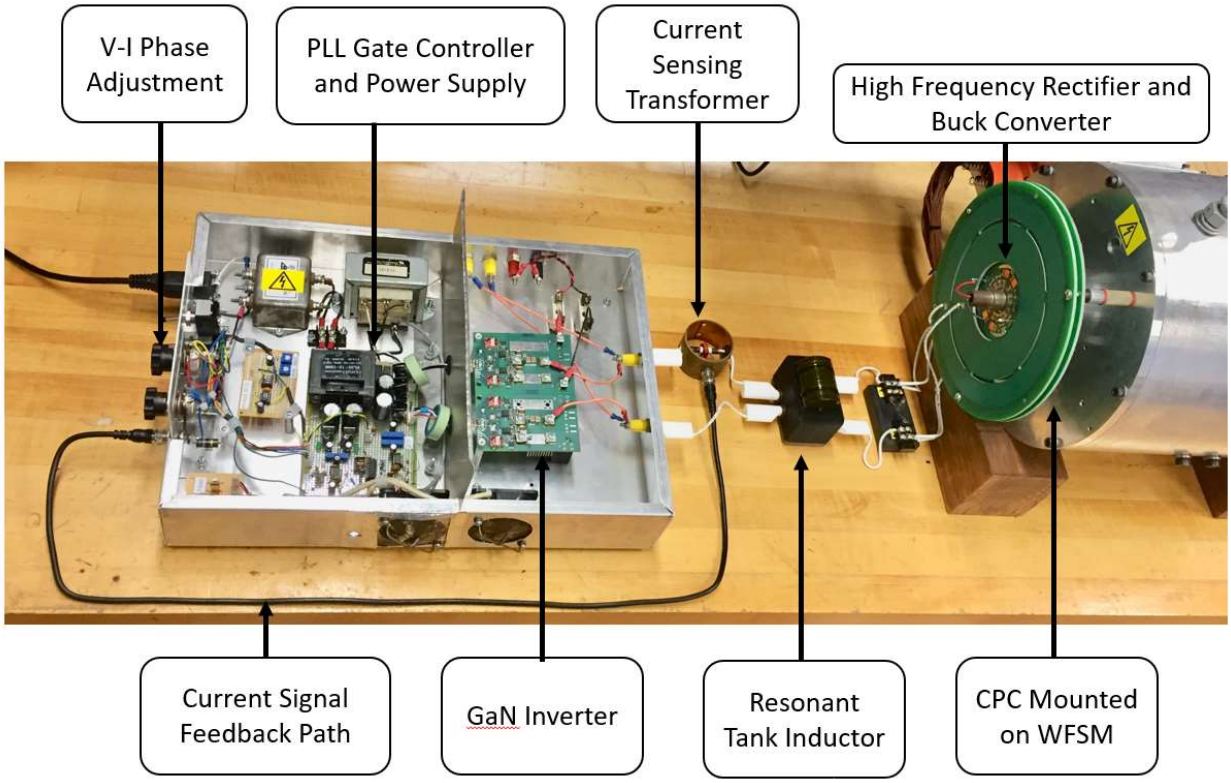

Fig. 2.4.4-31. Capacitive power transfer system with first generation single phase GaN inverter with CPC PCBs mounted on first generation WFSM.

Table 2.4.4-VII. Bench Test Data of Capacitive Power Transfer System with First Generation GaN Inverter with CPC Rotor Buck Converter: DC Power In and Out at 1.68 MHz

$V_{in,dc}$	$I_{in,dc}$	$V_{out,dc}$	$I_{out,dc}$	P_{in}	P_{out}	Eff	$I_{ac,rms}$	$V_{L,rms}$
(volts)	*(amps)*	*(volts)*	*(amps)*	*(watts)*	*(watts)*	*(%)*	*(amps)*	*(volts)*
108.27	1.03	65.27	1.53	111.52	99.86	89.55	1.614	465
152.06	1.47	88.84	2.26	223.53	200.78	89.82	2.346	676
189.59	1.76	110.01	2.74	333.68	301.43	90.33	3.090	890
219.41	2.02	126.98	3.15	443.21	399.99	90.25	2.869	826
247.80	2.24	142.55	3.51	555.07	500.35	90.14	3.436	989
269.54	2.48	159.57	3.77	668.46	601.58	89.99	3.680	1060
282.42	2.65	168.89	4.00	748.41	675.56	90.27	3.974	1144

Bench Testing Capacitive Power Transfer System with Second Generation Single Phase GaN Inverter on First Generation WFSM

A second-generation single phase GaN inverter has also been bench tested with a first generation WFSM. This GaN inverter was developed as part of DE-EE0008869 and is capable of switching at 7 MHz. This bench testing was completed without the fixed duty ratio buck converter and without the PLL circuit to maintain soft-switching. The bench measurements are listed in Table 2.4.4-VIII. With this second generation GaN inverter over 1.1 kW can be transferred to the field winding of the first generation WFSM.

TABLE 2.4.4-VIII. BENCH TESTING OF SECOND GENERATION GAN INVERTER WITH FIRST GENERATION WFSM WITHOUT CPC ROTOR BUCK CONVERTER OR PLL TO MAINTAIN SOFT-SWITCHING

V_{in}	I_{in}	V_{out}	I_{out}	P_{in}	P_{out}	$Efficiency$	I_{ac}
$[V]$	$[A]$	$[V]$	$[A]$	$[W]$	$[W]$	[%]	$[A_{RMS}]$
150	3.74	139.8	3.61	561	504.96	90.01	5.69
160	3.98	148.9	3.84	636.8	572.37	89.88	6.02
170	3.85	150.7	3.90	654.5	587.73	89.80	6.33
170	4.17	157.1	4.05	708.9	636.41	89.77	6.13
180	4.35	169	4.16	783	702.20	89.68	6.48
190	4.65	175.4	4.51	883.5	790.18	89.44	6.95
200	4.89	184.5	4.70	978	867.15	88.67	7.31
210	5.13	193.3	4.90	1077.3	947.36	87.94	7.65
220	5.36	202.5	5.19	1179.2	1050.98	89.13	8.01
230	5.6	210.5	5.41	1288	1138.59	88.40	8.31

2.5 Dynamometer Testing of Generation I WFSM with Generation I CPC

2.5.1 Introduction

The capacitive power transfer system using the large gap CPC and generation I single phase high frequency inverter was dynamometer tested with a generation I WFSM. The testing was carried out in generating mode with the stator connected to a three-phase load bank.

2.5.2 Setup of Generation I WFSM and Capacitive Power Transfer Inverter

A three-phase resistive load bank was connected to the WFSM stator. Measurements of the WFSM stator terminal voltages and currents were made with an oscilloscope with power analyzer capability. A schematic showing the test configuration and stator measurement points is shown in Fig. 2.5.2-1.

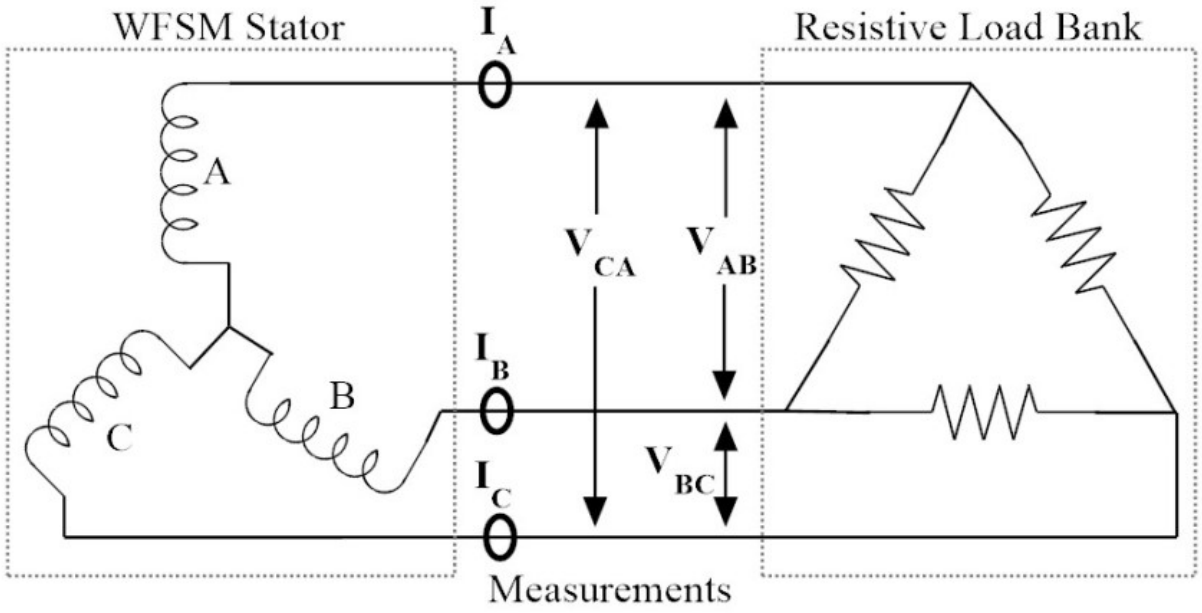

Fig. 2.5.2-1. Generator operation WFSM stator and resistive load connection and stator measurement points.

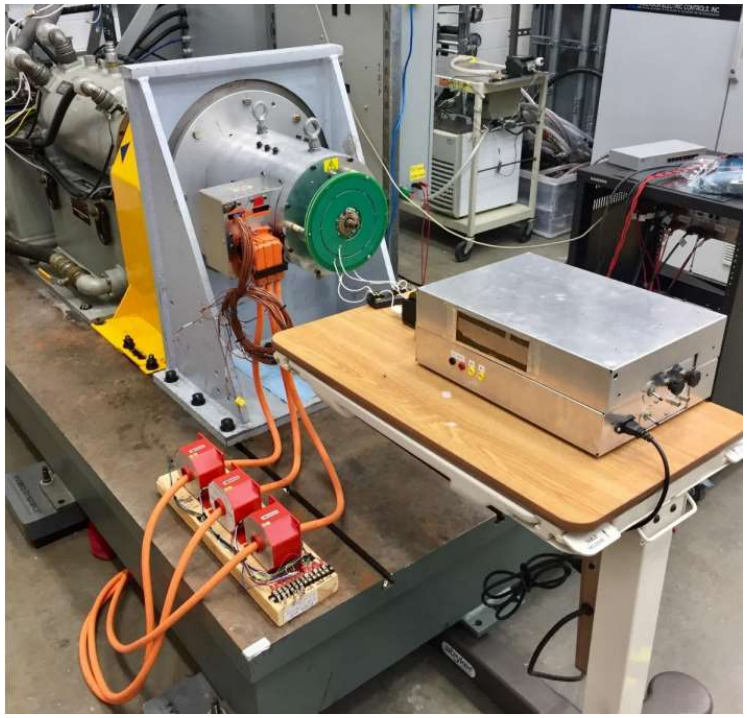

Fig. 2.5.2-2. Dynamometer test setup for CPC field excitation on generation I WFSM at rated speed. The generation I inverter is in the silver box on the adjustable table.

2.5.3 Dynamometer Testing of Generation I WFSM and Capacitive Power Transfer Inverter

The CPC tank current, I_{RF}, WFSM load power, and WFSM stator line to line voltages were measured for a range of speeds and tank currents up to a rated generation I WFSM speed of 4000 rpm and tank current of 4 A, Fig. 2.5.3-1 and Fig. 2.5.3-2. The load resistance was also reduced slightly at 4,000 RPM and a CPC tank current of 4 A to generate 30 kW of power.

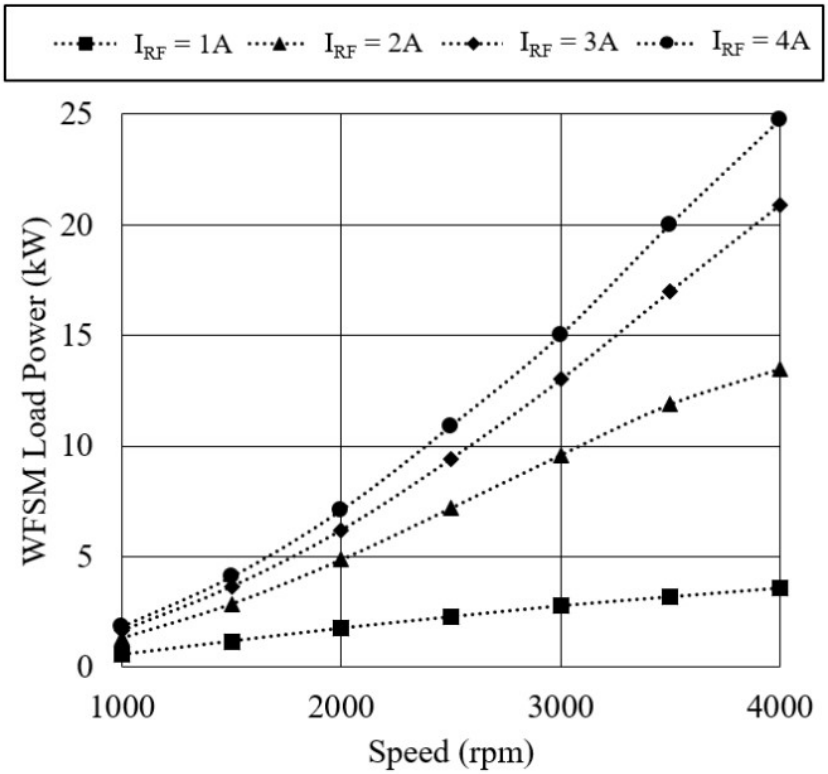

Fig. 2.5.3-1. WFSM load power transfer as a function of rotational speed and CPC tank current.

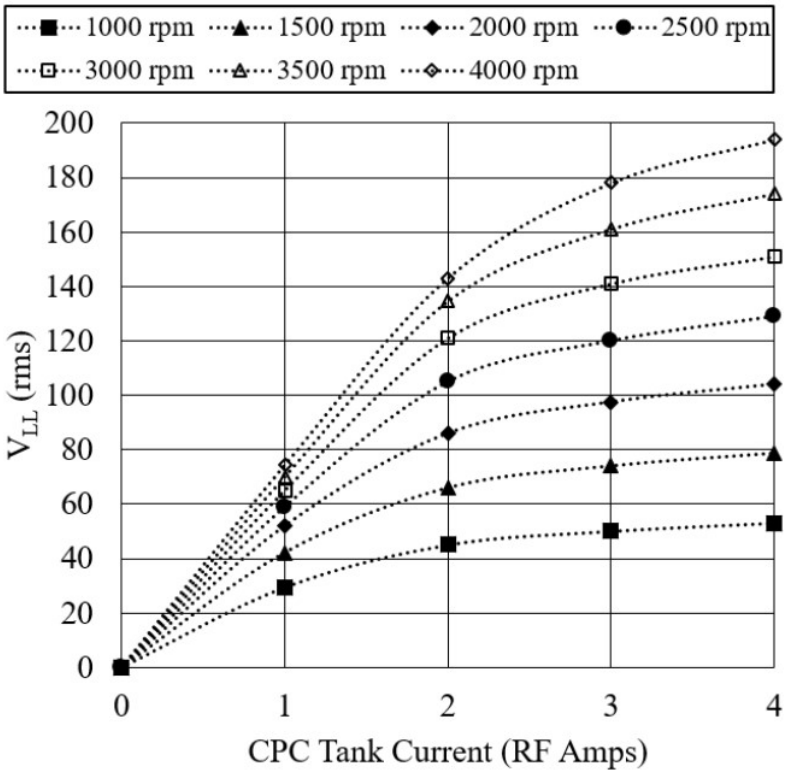

Fig. 2.5.3-2. WFSM line to line voltage as a function of CPC tank current and WFSM speed.

2.6 Dynamometer Testing of Generation III WFSM

2.6.1 Introduction

The generation III WFSM with bobbin wound square magnet wire winding was dynamometer tested with brushes and slip rings, and capacitive power transfer systems. Two different high frequency single phase GaN inverters switching at ~1.6 MHz and ~7.1 MHz were used with the same PCB capacitive power coupler. The WFSM prototype was tested up to the current limit of the device under test (DUT) Semikron inverter which was connected to the stator. The measured and predicted performance of the WFSM agreed closely.

2.6.2 Setup of Generation III WFSM on Dynamometer

The generation III WFSM prototype with bobbin wound square magnet wire winding had the motor frame mounted on the dynamometer, Fig. 2.6.2-1, rotor inserted, Fig. 2.6.2-2 and Fig. 2.6.2-3, coupler reattached, Fig. 2.6.2-4, overall shafts aligned, Fig. 2.6.2-5, and the rear ATF supply and ATF return lines attached, Fig. 2.6.2-5. Because of the current limit of the Semikron inverter used to drive the stator, only one high voltage safety terminal was used, Fig. 2.6.2-6. Because of the high currents, multiple magnet lead wires are used and an ATF jet also flows coolant over the terminal leads, Fig. 2.6.2-6. Initial dynamometer tests of the generation III WFSM were carried out with brushes and slip rings, Fig. 2.6.2-7. The generation III WFSM test setup is shown in Fig. 2.6.2-8 except for the encoder. The inverter, field supply, and ATF cooling loop are located in the blue cabinet to the left in Fig. 2.6.2-9. The encoder mounted on the rear of brushes and slip rings is also visible.

During initial testing and parameter identification the dynamometer absorber cabinet failed. Without the absorber the WFSM prototype could not be tested. After extensive debugging the failure was traced back to the main control PLC in the Anderson Electric absorber, Fig. 2.6.2-10. The PLC was removed and overnight shipped back to Anderson Electric. They were able to repair the PLC and the PLC was reinstalled and brought back online. Dynamometer testing with brushes and slip rings resumed with the repair of the PLC.

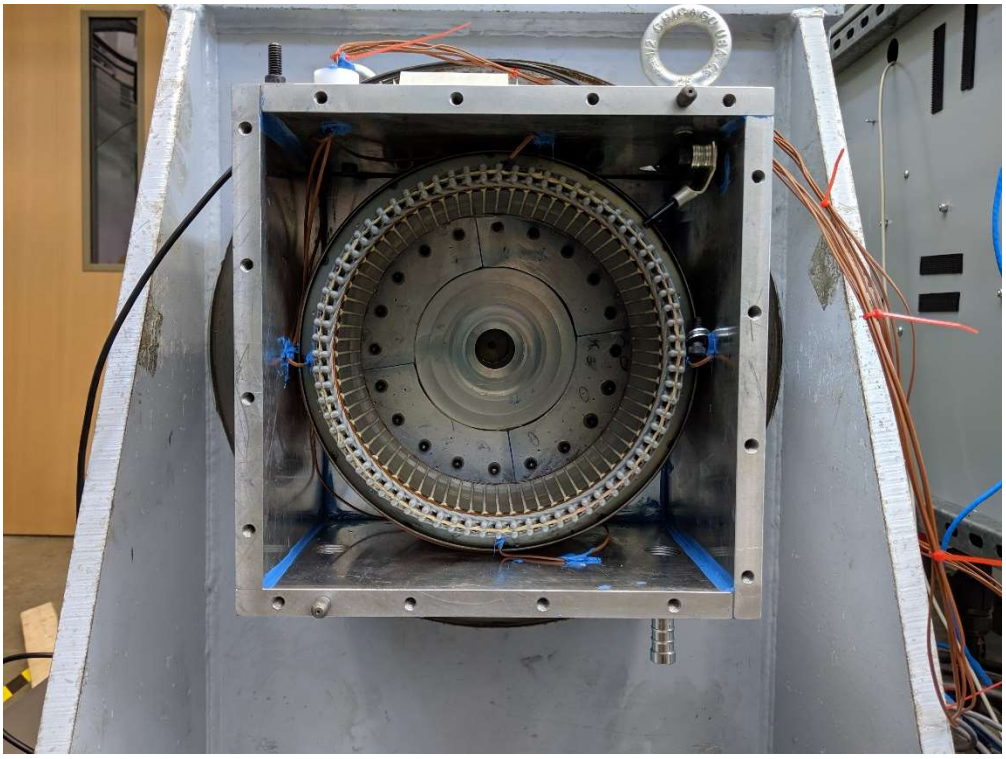

Fig. 2.6.2-1. Mounting of WFSM stator and housing onto dynamometer and installation of thermocouples and wireless bore scope. The drive end spray cooling plates can be seen in through the inner diameter of the stator.

Fig. 2.6.2-2: Preparing to insert the rotor assembly into the housing.

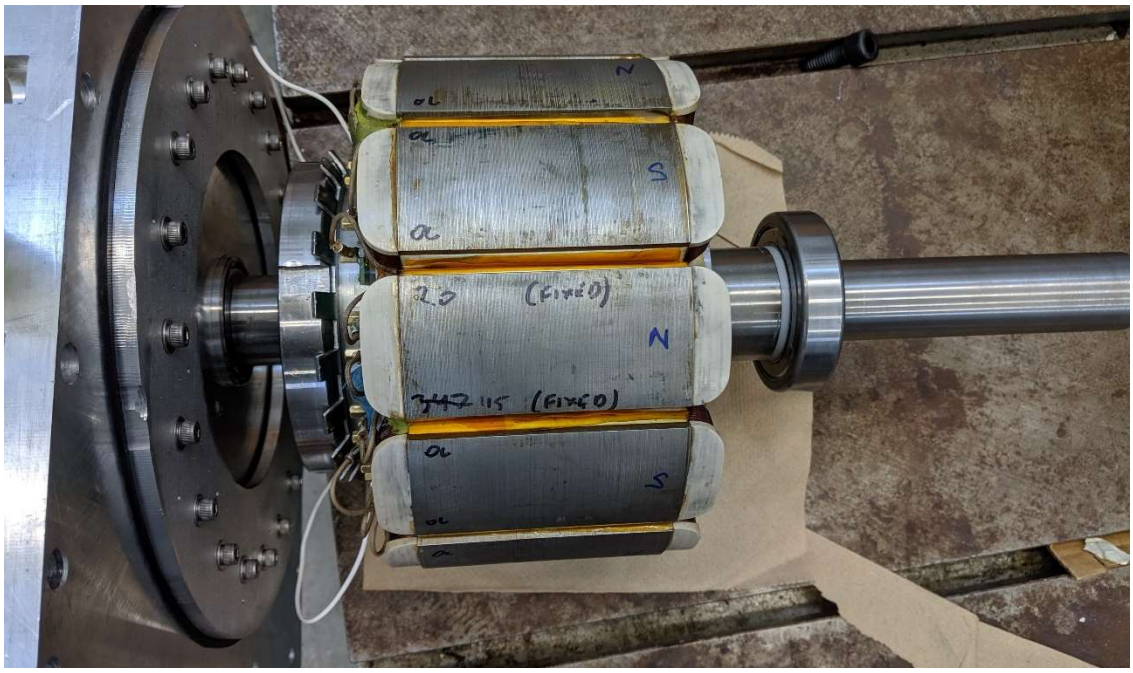

Fig. 2.6.2-3. Installation of the rotor assembly into the housing. The non-drive end plate is visible.

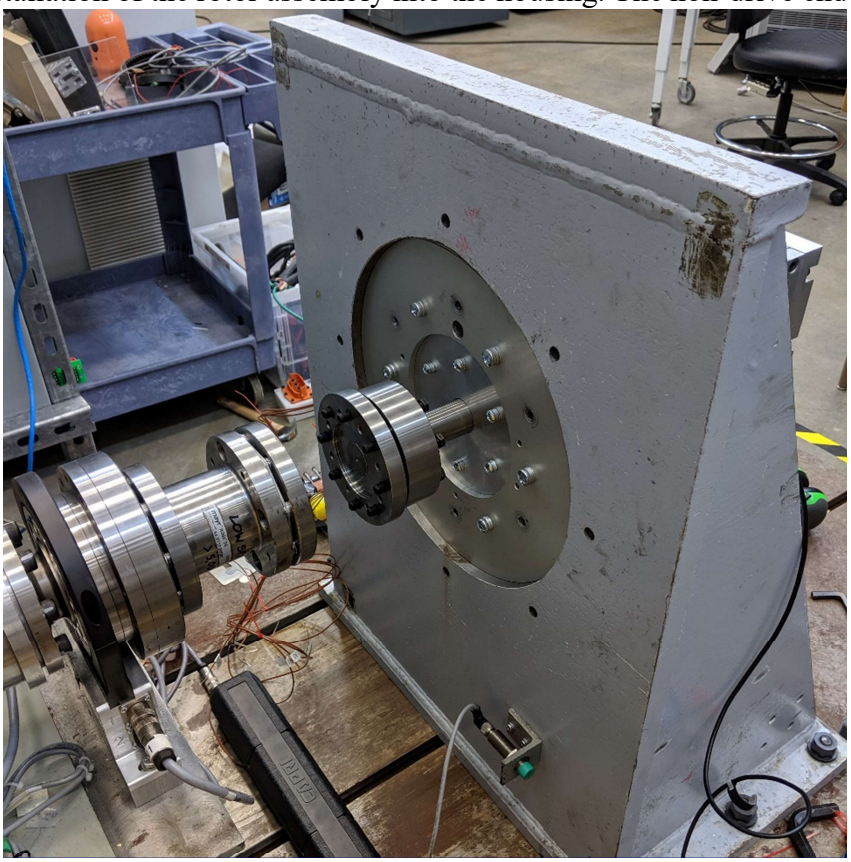
Fig. 2.6.2-4. Initial steps of connecting the flexible coupler and WFSM alignment.

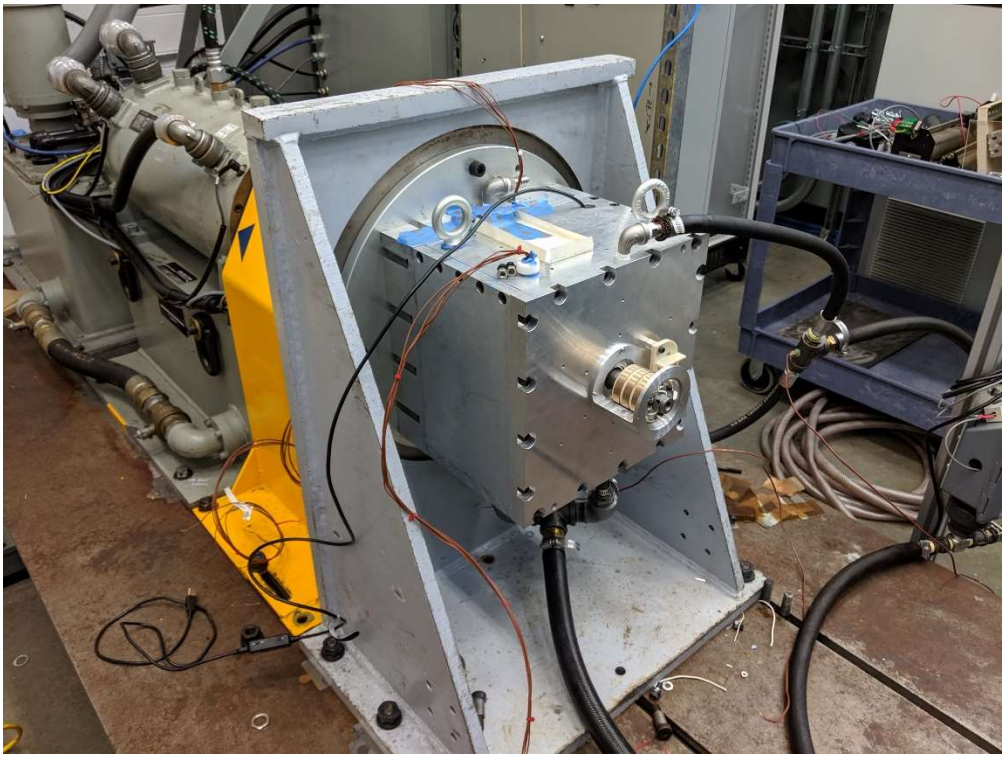

Fig. 2.6.2-5. WFSM prototype mounted and aligned with partial cooling system connections and encoder mount installed.

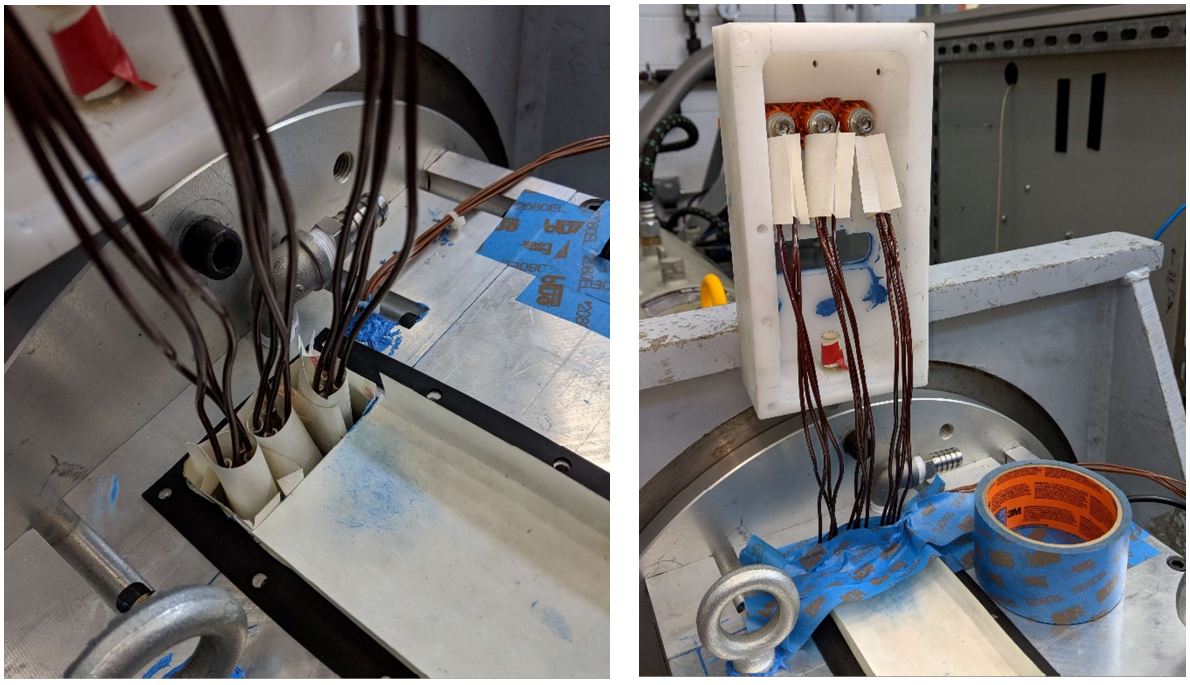

Fig. 2.6.2-6. Installation of stator terminals and lead connections. Because of the very high currents the stator leads are liquid cooled with ATF flow in the terminal box.

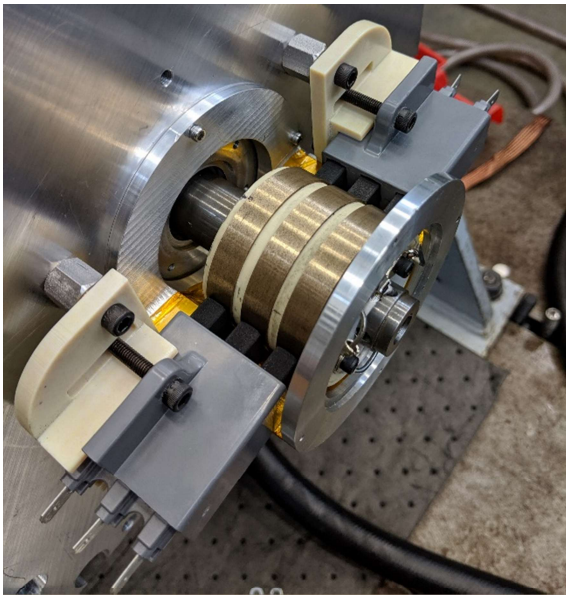

Fig. 2.6.2-7: Installation of brushes

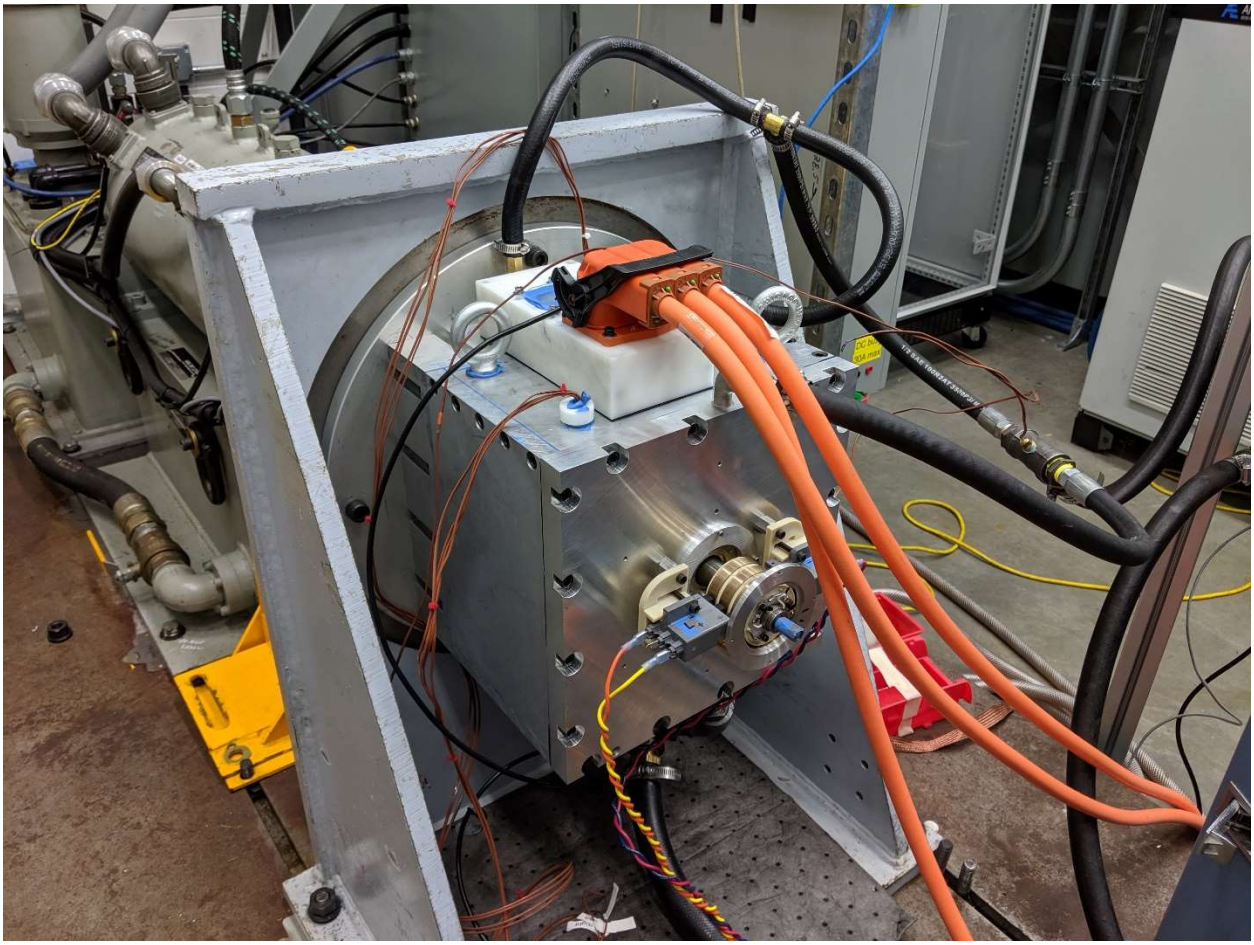

Fig. 2.6.2-8. Generation III WFSM prototype motor installed on dynamometer except for the encoder.

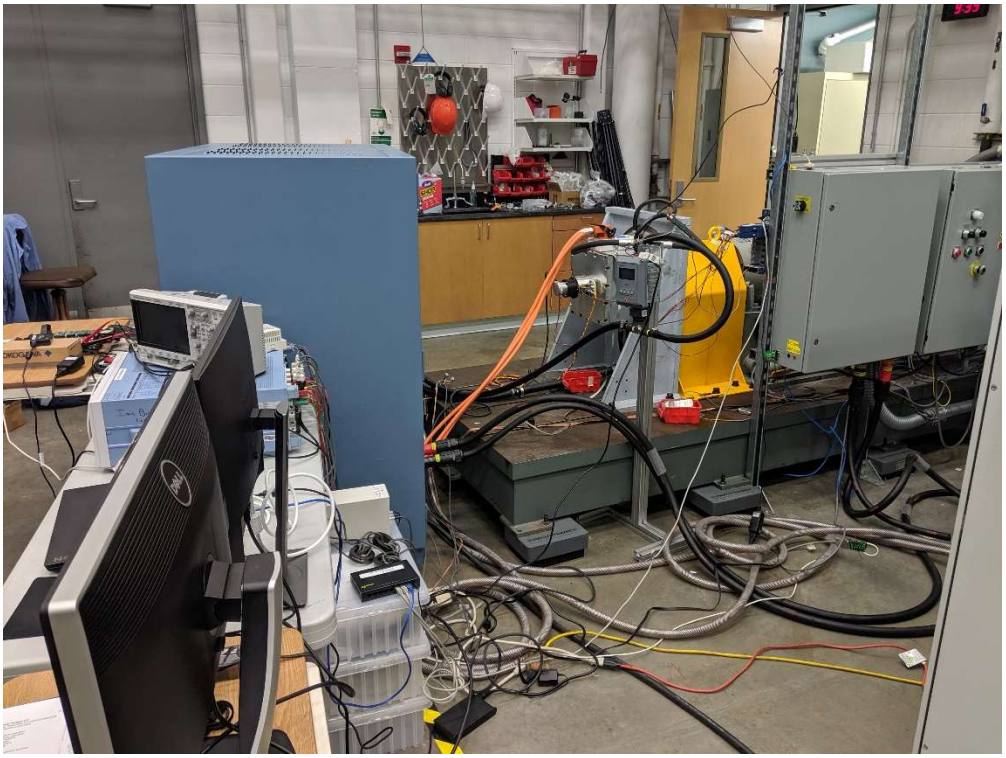

Fig. 2.6.2-19. Final testing setup with brushes and slip rings

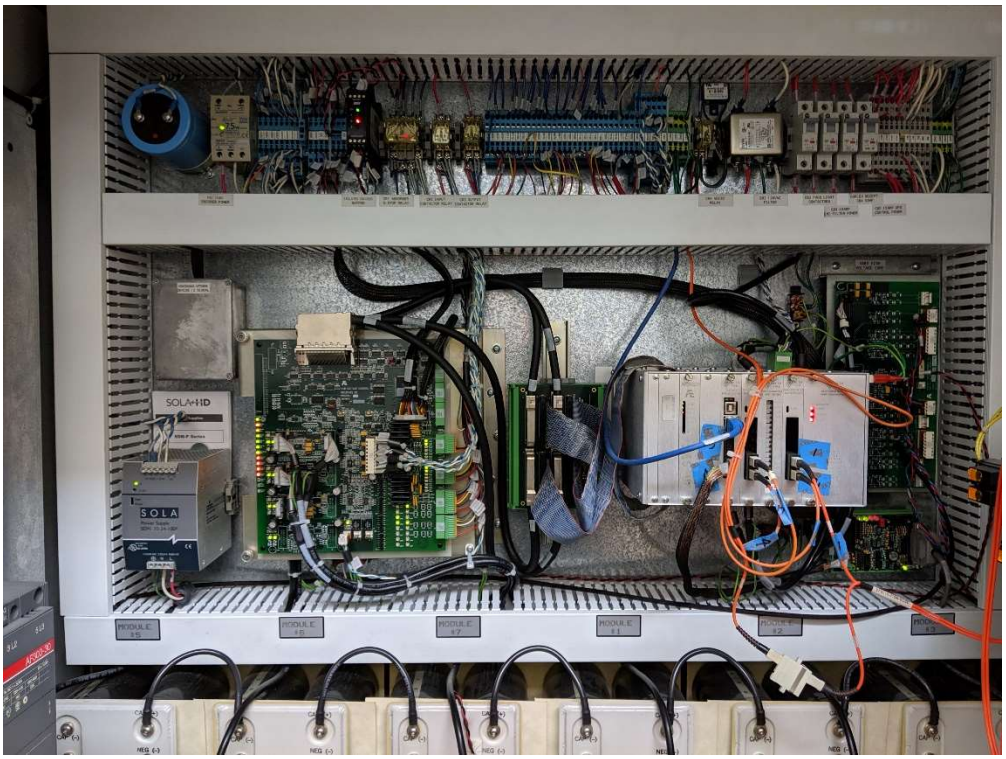

Fig. 2.6.2-9. Anderson Electric dynamometer drive control PLC failure. The failed PLC has the blue tape on it to mark connections to it.

2.6.3 Dynamometer Testing of Generation III WFSM with Brushes and Slip Rings

Ultimately the limit to testing the power capability of the prototype is the stator inverter which has a maximum current rating of 230 A_{rms}/325 A_{peak} at a switching frequency at 10 kHz. The peak rated current of the WFSM prototype is ~427 A_{rms}. Load point 3 is well within the capabilities of the inverter and the WFSMs measured performance can be compared to its predicted performance. A screen capture from a Yokogawa WT1800 power analyzer is shown in Fig. 2.6.3-1. Relevant performance metrics for comparison are highlighted in red boxes including the stator current, power factor, torque and efficiency. The predicted performance for this operating point is listed in Table 2.6.3-1.

Fig. 2.6.3-1. Yokogawa WT1800 power analyzer screen capture of operation near load point 3 conditions. The first three elements are the stator phases. The sigma element is the aggregated behavior of the three elements and the fourth element is the field excitation. The fifth element is the DC link voltage from the power interface unit.

TABLE 2.6.3-1. PREDICTED LOAD POINT 3 PERFORMANCE

Load Point	Speed (RPM)	Torque (Nm)	I_s (A_{peak})	I_f (A_{dc})	Power Factor	Eff (%)
3	2000	119.68	134.55	5.66	0.95	93.85

The predicted and measured torque and stator current are very close. Slightly more field excitation current is needed. This may be due to offsets in the current sensor or additional MMF drops in the segmented rotor laminations. It is a relatively small difference though of only 0.3 A_{dc}. The power factor and efficiency predictions and measurements agree closely. The correspondence between the predicted and measured performance lends evidence that the performance predictions from the finite element model are accurate.

Another representative Yokogawa WT1800 power analyzer screen capture of operation at 77.5 kW and 4,000 RPM is shown in Fig. 2.6.3-2. This operating point is near the current limit of the stator inverter (~230 A_{rms}). This operating point demonstrates a power output at greater than 55 kW.

Fig. 2.6.3-2. Screen capture from Yokogawa WT1800 power analyzer at an output torque of 184.91 Nm, 4,000 RPM, and power output of 77.5 kW. The first three elements are the stator phases. The sigma element is the aggregated behavior of the three elements and the fourth element is the field excitation. The fifth element is the DC link voltage from the power interface unit.

2.6.4 Dynamometer Testing of Generation III WFSM with Capacitive Power Transfer Systems

Testing of the generation III WFSM prototype with the large gap PCB capacitive power coupler (CPC) and two different high frequency single phase inverters was carried out. Several modifications to the CPC mounting hub where made to remove runout and reduce capacitance variation. The field winding resistance of the generation III WFSMs is lower than ideal for the design of the capacitive power transfer system. To wind the field poles with more turns would have required using a higher gauge wire making the winding much more difficult. In future work it is recommended to redesign the capacitive power transfer system for lower field resistances.

After arcing occurred in the airgap between printed circuit boards, potentially due to the voltage level reached and/or ATF intrusion into the gaps, the surfaces of the PCBs serving as electrodes were coated with Kapton. The setup of the PCB CPC is shown in Fig. 2.6.4-1. The rotating rectifier is visible in the center of the CPC. The setup for testing with the generation I inverter is shown in

Fig. 2.6.4-2. This inverter was switched at approximately 1.6 MHz. The latest generation II inverter developed as part of another DOE project is shown in Fig. 2.6.4-3. The testing setup with the generation II inverter is shown in Fig. 2.6.4-4. This inverter switches at ~7.1 MHz allowing for higher current transfer across the CPC to the field winding. The overall size of the generation II inverter and resonant tank is considerably smaller. Oscilloscope captures of the inverter output voltage and field current for the generation I inverter, Fig. 2.6.4-5 and generation II inverter, Fig. 2.6.4-6, were captured. In Fig. 2.6.4-5 and 2.6.4-6 the field currents were 2.75 A and 4 A respectively. A screen capture from the Yokogawa WT1800 power analyzer during operation is shown in Fig. 2.6.4-7 at a field current of 2 A. The power analyzer current probe has trouble with accurate measurement of the field current due to the high switching frequency of the inverter.

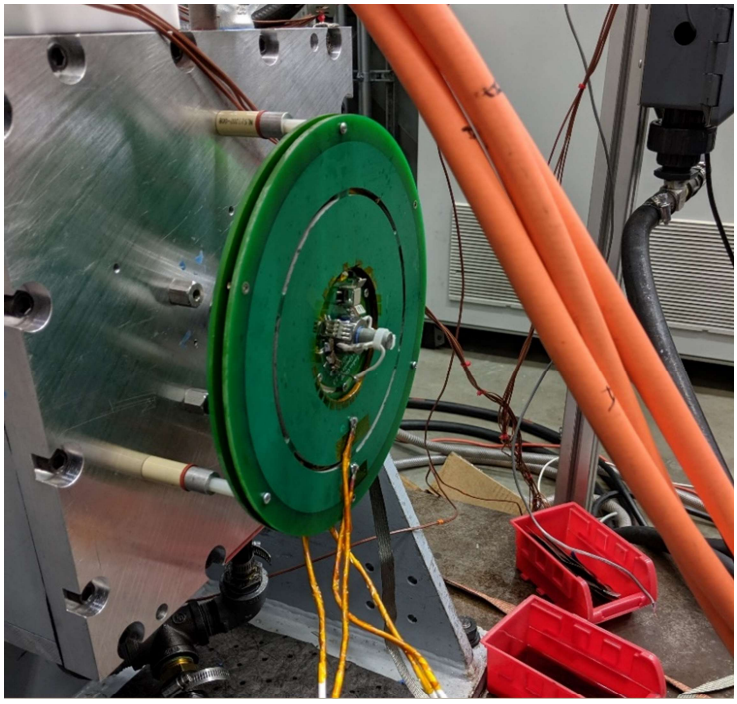

Fig. 2.6.4-1: Capacitive power coupler printed circuit boards mounted on the generation III WFSM prototype.

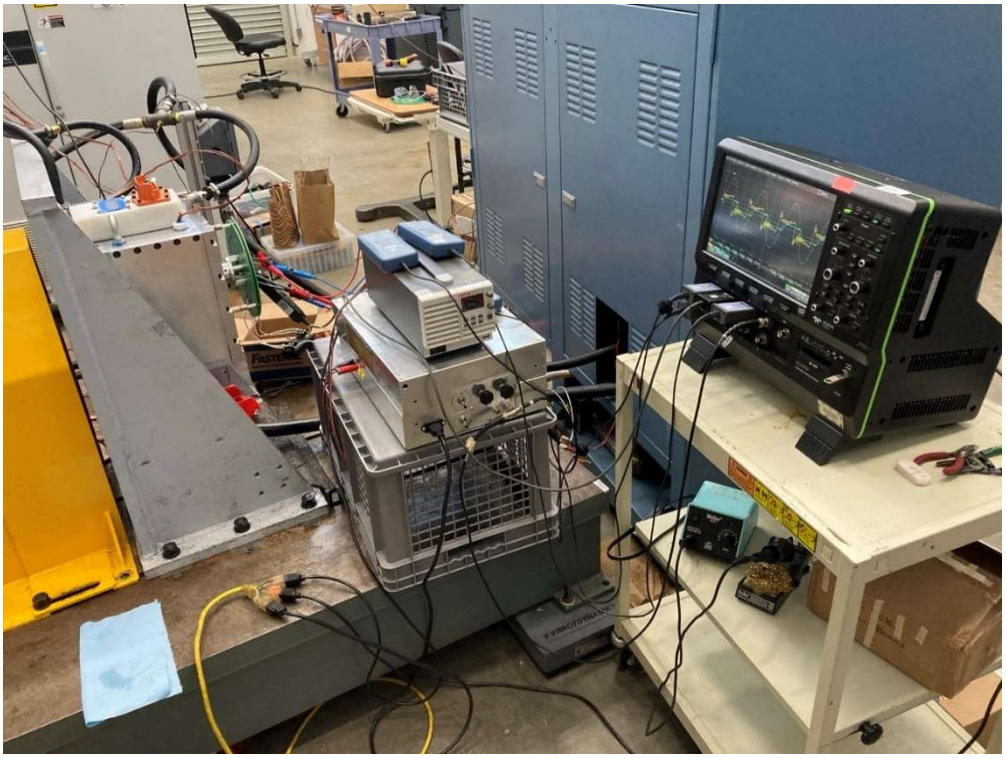

Fig. 2.6.4-2: Testing of the WFSM with CPC excited by generation I single phase inverter at ~1.6 MHz.

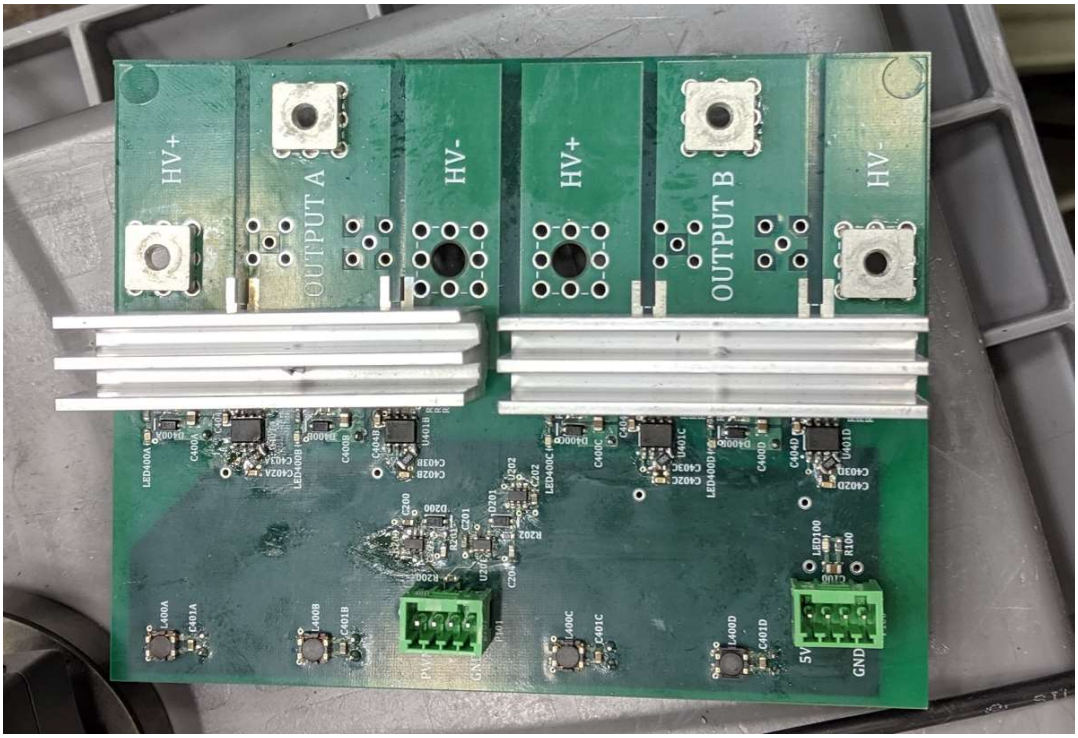

Fig. 2.6.4-3: Generation II single phase inverter used for testing at ~7.1 MHz and higher field currents.

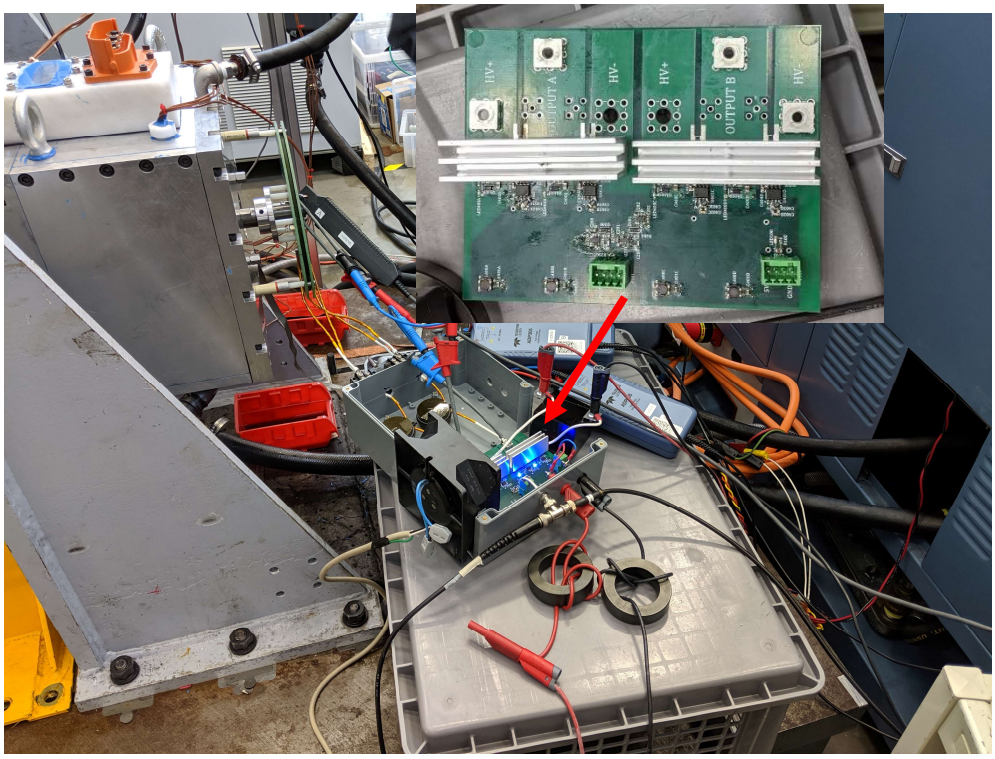

Fig. 2.6.4-4. Generation II single phase inverter test setup. The second-generation inverter is significantly smaller.

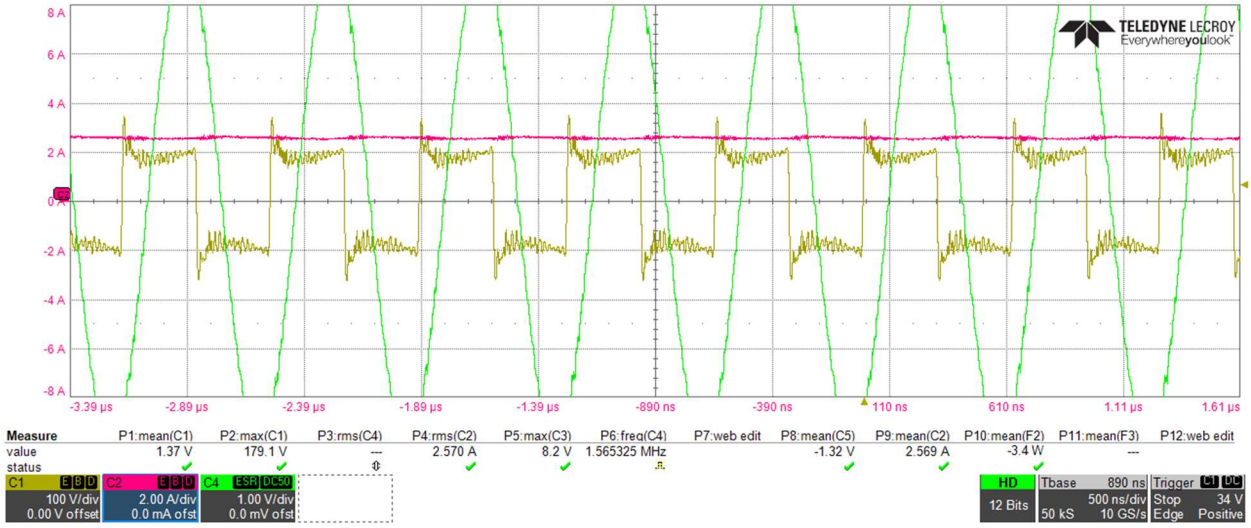

Fig. 2.6.4-5. Operation of the CPC powering the WFSM field at a switching frequency of ~1.6 MHz and a 2.75 A field current. The CPC was powered by the generation I single phase inverter. The yellow trace is the inverter output voltage and the pink trace is the field current.

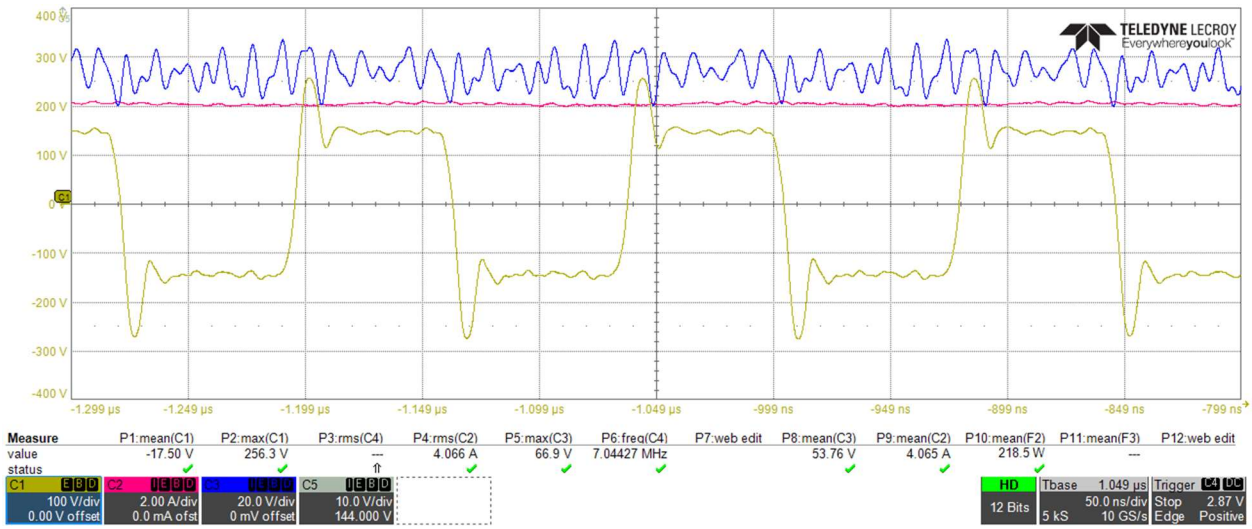

Fig. 2.6.4-6. Operation of the CPC powering the WFSM field at a switching frequency of ~7.1 MHz and 4 A field current with the generation II high frequency single phase inverter. The yellow trace is the inverter output voltage and the pink trace is the field current.

Fig. 2.6.4-7. Representative operation with the CPC.

While attempting to push the field current to 5 A, damage was sustained to the latest generation inverter. An apparent shoot through event occurred potentially due to dV/dt between the upper and lower gate drives and power switches or because one of the pole field winding connections pulled loose from its crimped connection and created an open circuit. Damage to the WFSM rotor was also noticed when attempting to push to higher power levels after the brushes and slip rings were reinstalled. It is unclear if the damage occurred to the WFSM rotor due to the inverter faulting or for mechanical reasons. The damage is consistent with either an inverter fault or if the field current was interrupted. For example, if one of the pole terminals disconnected due to centrifugal forces. The damage to the rotor included destroyed traces and varistors on the connection PCB, two broken leads, and shorts to the laminations at 2 poles. The damaged rotor poles have since been repaired. For future WFSMs, an improved pole connection scheme is desirable.

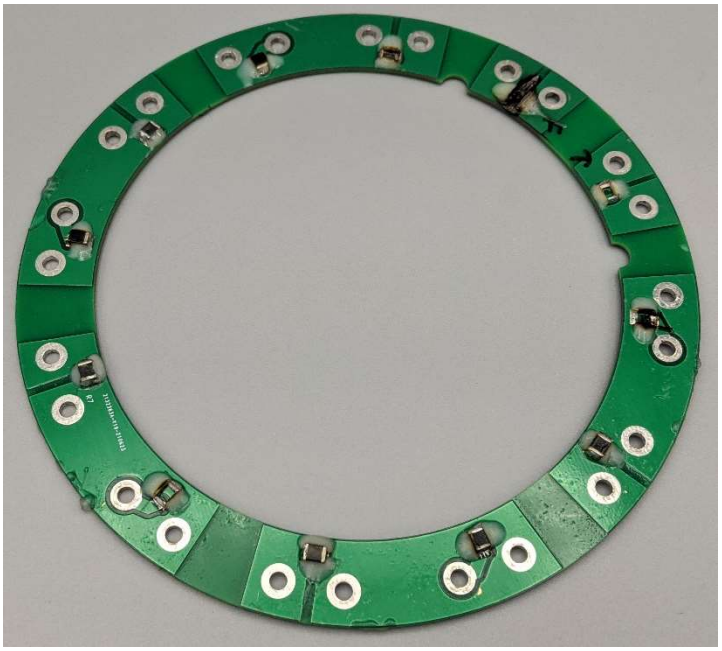

Fig. 2.6.4-8. Damaged PCB connection board. Destroyed or damaged varistors are evident.

Fig. 2.6.4-9. Evidence of arc flash damage to rotor pole and laminations after extraction of damaged rotor pole.

2.7 Hybrid Excitation Synchronous Machines

2.7.1 Introduction

A number of efforts were undertaken in the context of hybrid excitation synchronous machines (HESMs). The field excitation in hybrid excitation machines is provided by a combination of permanent magnets and field windings. HESMs have the potential to lower the field power excitation requirements while maintaining very good field weakening capabilities. In the course of this project analytical and finite element design tools were developed for the design of hybrid excitation machines. The analytical sizing equations that were developed are summarized in

A. Di Gioia, I.P. Brown, F. Giulii-Capponi, "Analytical Sizing of Radial Flux Hybrid Excitation Synchronous Machines" 2018 IEEE Energy Conversion Congress and Exposition (ECCE), Portland OR, Sept. 23rd-27th, 2018.

Based on the analytical design equations and finite element optimization routines a radial flux dual rotor HESM was developed. Its design and characterization are described in the following paper. The rotor of this hybrid excitation machine is shown in Fig. 2.7.1-1.

A. Di Gioia, I.P. Brown, F. Giulii-Capponi, "Design and Characterization of a Radial Flux Wound Field and Permanent Magnet Hybrid Excitation Synchronous Machine," 2018 IEEE Energy Conversion Congress and Exposition (ECCE), Portland OR, Sept. 23rd-27th, 2018.

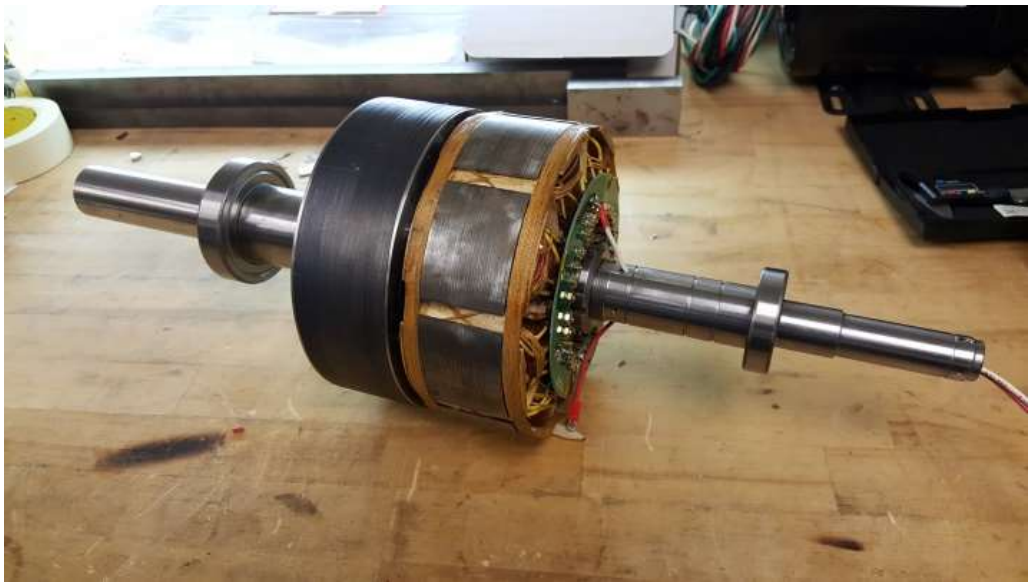

Fig. 2.7.1-1. Rotor of radial flux dual rotor hybrid excitation synchronous machine.

An additional an invention disclosure was filed for another hybrid excitation machine concept.

2.8 Control of Wound Field Synchronous Machines

2.8.1 Introduction

The main advancement in the control of WFSMs during the course of this project was the development of deadbeat direct torque and flux controllers for WFSMs. Deadbeat direct torque and flux control effectively decouples the cross-coupled d, q, and f axes and allows for independent control of the torque, stator flux linkage, and field flux linkage. A single pulse width modulation cycle torque response is possible. Manipulation of the field applied volt-sec allows the torque line to be shifted, an extra control degree of freedom, compared interior permanent magnet synchronous machines. The field flux linkage can also be commanded to achieve unity power factor during steady state. Two deadbeat direct torque and flux control variants for WFSMs were developed. One for high switching to fundamental frequency ratios and one for low switching to fundamental frequency ratios. Complete descriptions of the two variants are contained in the following papers.

Y. Nie, I.P. Brown, D.C. Ludois, "Deadbeat-Direct Torque and Flux Control for Wound Field Synchronous Machines," *IEEE Transactions on Industrial Electronics*, Vol. 65, No. 3, 2018. DOI: 10.1109/TIE.2017.2739696.

Y. Nie, D.C. Ludois, I.P. Brown, "Deadbeat-Direct Torque and Flux Control of Wound Field Synchronous Machine at Low Sampling to Fundamental Frequency Ratios," IEEE Transactions on Industrial Applications, Vol. 55, No. 4, 2019. DOI: 10.1109/TIA.2019.2914681.

3.1 Publications Associated with this Project

S. Hagen, M. Tisler, J.J. Dai, I.P. Brown, D.C. Ludois, "Use of the Rotating Rectifier Board as a Capacitive Power Coupler for Brushless Wound Field Synchronous Machines," to appear in IEEE Journal of Emerging and Selected Topics in Power Electronics, 2021. DOI: 10.1109/JESTPE.2020.3039497.

F. Guo, M. Salameh, M. Krishnamurthy, I.P.Brown, "Multi-Material Magneto-Structural Topology Optimization of Wound Field Synchronous Machine Rotors," *IEEE Transactions on Industrial Applications*, Vol. 56, No. 4, 2020. DOI: 10.1109/TIA.2020.2989682.

Y. Nie, I.P. Brown, D.C. Ludois, "Deadbeat-Direct Torque and Flux Control for Wound Field Synchronous Machines," *IEEE Transactions on Industrial Electronics*, Vol. 65, No. 3, 2018. DOI: 10.1109/TIE.2017.2739696.

Y. Nie, D.C. Ludois, I.P. Brown, "Deadbeat-Direct Torque and Flux Control of Wound Field Synchronous Machine at Low Sampling to Fundamental Frequency Ratios," IEEE Transactions on Industrial Applications, Vol. 55, No. 4, 2019. DOI: 10.1109/TIA.2019.2914681.

J.J. Dai, S. Hagen, D.C. Ludois, I.P. Brown, "Synchronous Generator Field Excitation Via Capacitive Coupling Through a Journal Bearing," *IEEE Transactions on Industrial Applications*, 2017, Vol. 53, No. 4, 2017. DOI: 10.1109/TIA.2017.2681621.

N. Tang, D. Sossong, I.P. Brown, "Design and Metamodel-Based Optimization of a High-Power Density Wound Field Traction Motor," Proceedings of the *2021 Energy Conversion Congress and Exposition (ECCE)*, Vancouver, CA, Oct. 10^{th}-14^{th}, 2021. DOI: 10.1109/ECCE47101.2021.9595403.

F. Guo, I.P. Brown, "Multi-Material Topological Optimization of Synchronous Electric Machines," Proceedings of *the 2019 Energy Conversion Congress and Exposition (ECCE)*, Baltimore, MD, Sep. 29^{th} – Oct 3^{rd}, 2019. DOI: 10.1109/ECCE.2019.8913309.

M. Salameh, T. Spillman, M. Krishnamurthy, D.C. Ludois, I.P. Brown, "Wound Field Synchronous Machine with Segmented Rotor Laminations and Die Compressed Field Winding," Proceedings of *the 2019 Energy Conversion Congress and Exposition (ECCE)*, Baltimore, MD, Sep. 29^{th} – Oct 3^{rd}, 2019. DOI: 10.1109/ECCE.2019.8912601

S. Hagen, D. Jiejian, I.P. Brown, D.C. Ludois, "Low-Cost, Printed Circuit Board Construction, Capacitively Coupled Excitation System for Wound Field Synchronous Machines," Proceedings of the *2019 Energy Conversion Congress and Exposition (ECCE)*, Baltimore, MD, Sep. 29^{th} – Oct 3^{rd}, 2019. DOI: 10.1109/ECCE.2019.8913084

Y. Nie, I.P. Brown, D.C. Ludois, “Low Switching Frequency Deadbeat-Direct Torque and Flux Control of Wound Field Synchronous Machines,” in *Proceedings of the 2018 IEEE Energy Conversion Congress and Exposition (ECCE)*, Portland, OR, September 23 – 27, 2018. DOI: 10.1109/ECCE.2018.8557780

A. Di Gioia, I.P. Brown, F. Giulii-Capponi, “Design and Characterization of a Radial Flux Wound Field and Permanent Magnet Hybrid Excitation Machine,” in *Proceedings of the 2018 IEEE Energy Conversion Congress and Exposition (ECCE)*, Portland, OR, September 23 – 27, 2018. DOI: 10.1109/ECCE.2018.8558335

A. Di Gioia, I.P. Brown, F. Giulii-Capponi, “Analytical Sizing of Radial Flux Hybrid Excitation Synchronous Machines,” in *Proceedings of the 2018 IEEE Energy Conversion Congress and Exposition (ECCE)*, Portland, OR, September 23 – 27, 2018. DOI: 10.1109/ECCE.2018.8558393

M. Salameh, A. Di Gioia, I.P. Brown, M. Krishnamurthy, “Evaluating the Feasibility of Single-Rotor Topologies in Hybrid Excitation Synchronous Machines for Automotive Traction Applications,” in *Proceedings of the 2018 IEEE Transportation Electrification Conference and Expo (ITEC)*, Long Beach, CA, June 13 – 15, 2018 DOI: 10.1109/ITEC.2018.8450099

J. Dai, S. Hagen, D.C. Ludois, and I.P. Brown, “Synchronous Generator Field Excitation Via Capacitive Coupling Through a Journal Bearing,” in *Proceedings of the 2016 IEEE Energy Conversion and Conservation Expo (ECCE)*, Milwaukee, WI, September 18 – 22, 2016 DOI: 10.1109/ECCE.2016.7855488.